CFD Simulation of Electrostatic Charging in Gas-Solid Fluidized Beds: Model Development Through Fundamental Charge Transfer Experiments

Fahad Al-Amin Chowdhury

uOttawa

Thesis submitted in partial fulfillment of the requirements for

Doctor of Philosophy in Chemical Engineering

Department of Chemical and Biological Engineering
Faculty of Engineering
University of Ottawa

Abstract

The triboelectrification of particles by contact or frictional charging is known to be an operational challenge in the polyolefin industry. Particularly in polyethylene production, gas-solid fluidized bed reactors are known to be susceptible to electrostatic charging due to the rigorous mixing of polyethylene and catalyst particles in a dry environment. The presence of charged particles coupled with a highly exothermic polymerization reaction results in sheet formation on the reactor walls. This behaviour can decrease reactor performance and obstruct the system, consequently forcing a shutdown for reactor maintenance. The generation of electrostatic charge in fluidized beds has been widely studied throughout the years; however, limited attention has been paid to the simulation and modeling of this phenomenon. Since it is difficult to accurately quantify the charge generation in industrial fluidized beds, developing an electrostatic model based on material properties would considerably aid in providing insight on this occurrence and its effects. A computational fluid dynamics (CFD) model that incorporates this electrostatic model can then be used as a predictive tool in research and development. Simulating electrostatic charging in gas-solid fluidized beds would be a cost-effective alternative to running experiments on them, especially for industrial-scale test runs.

In this thesis, an electrostatic charging model was developed to be used in conjunction with an Euler-Euler Two-Fluid CFD model to simulate triboelectrification and its effects in gas-solid flows. The electrostatic model was first established for mono-dispersed gas-particle flows and was validated using past experimental findings of particle charging for gas-solid fluidization runs. With the goal of providing a realistic representation of gas-solid fluidization of polyethylene resins with a wide particle-size distribution, the electrostatic model was extended to consider bi-dispersed particulate flow systems. Simulation results using this model show the prediction of bipolar charging when the particles have different sizes, even though they are made of the same material. This phenomenon is analyzed and is shown to be driven by the electric field produced by the charge accumulated on the particles. Experimental studies of particle-wall and particle-particle contact charging were performed to investigate the electrostatic and mechanical parameters that are crucial for modeling the magnitude and direction of charge transfer in gas-solid flow systems. Particle-wall contact charging due to single and repeated collisions were tested with various particles, including commercial linear low-density polyethylene, to determine their rates of

charging as well as their charge saturation limits when colliding with a metal surface. Plotting the charge saturation value of the particles against their respective surface areas revealed a linear trend which could be used to calculate the charge saturation of the particle for a given particle size. Additional particle-wall charging studies include the effect of initial charge, collision frequency, particle type, impact angle, impact velocity and the presence of impurities on particle charging. To study particle-particle contact charging, a novel apparatus was designed, built, and tested to determine the magnitude and direction of charge transfer due to the individual particle-particle collisions of insulator particles. This apparatus was the first of its kind, and it ensured that the measured charge transfer for each experimental trial was solely due to the binary collision between the particles. It was observed that the direction of charge transfer in identical particle collisions is not dictated by the net initial charges of the particles, but the localized charge difference at the particles' contacting surface. Moreover, particle-particle collisions of nylon particles of varying sizes confirmed the bipolar charging phenomena, where the direction of charging was dictated by the relative size of the colliding particles. These findings, among others, contradict the charge transfer behavior predicted by electrostatic charging models currently proposed for particle-particle collisions. As such, it was concluded that an empirically accurate charge transfer model needs to be established to simulate the electrostatic charging of particles in poly-dispersed gas-solid flow systems.

Résumé

La triboélectrification des particules par mise en charge, soit par contact ou par friction, est connue comme un défi opérationnel dans l'industrie des polyoléfines. En particulier dans la production de polyéthylène, les réacteurs à lit fluidisé gaz-solide sont sensibles à une mise en charge électrostatique en raison du mélange rigoureux de polyéthylène et de particules de catalyseur dans l'environnement sec du réacteur. La présence de particules chargées, combinées avec une réaction de polymérisation hautement exothermique, résulte en la formation d'une couche de particules sur les parois du réacteur. Ce phénomène peut diminuer la performance du réacteur et obstruer le système, forçant par conséquent un arrêt pour l'entretien du réacteur. La génération de charge électrostatique dans les lits fluidisés a été largement étudiée au fil des années. Cependant, une attention limitée a été accordée à la simulation et à la modélisation de la génération de charges électrostatiques dans les lits fluidisés gaz-solide. Puisqu'il est difficile de quantifier avec précision la génération de charge dans les lits fluidisés industriels, le développement d'un modèle électrostatique basé sur les propriétés des matériaux aiderait considérablement à fournir des informations sur ce phénomène et ses effets. Un modèle de mécanique des fluides numérique (MFN) qui incorpore ce modèle électrostatique peut ensuite être utilisé comme outil prédictif en recherche et développement. La simulation de la mise en charge électrostatique dans des lits fluidisés gaz-solide serait une alternative rentable à la réalisation d'expériences, en particulier pour les essais à l'échelle industrielle.

Un modèle pour la mise en charge électrostatique a été développé pour être utilisé en conjonction avec un modèle MFN Euler-Euler à deux fluides pour simuler la triboélectrification et ses effets dans les écoulements gaz-solide. Le modèle électrostatique a été d'abord développé pour des écoulements de particules monodispersés dans un gaz et a été validé à l'aide des résultats expérimentaux antérieurs de la mise en charge de particules lors des essais de fluidisation gaz-solide. Dans le but de fournir une représentation réaliste de la fluidisation gaz-solide des résines de polyéthylène ayant une large distribution granulométrique, le modèle électrostatique a été étendu pour prendre en considération des systèmes d'écoulement de particules bi-dispersées. Les résultats de simulation obtenus en utilisant ce modèle prédisent une mise en charge bipolaire lorsque les particules ont des tailles différentes, même si elles sont constituées du même matériau. Ce phénomène a été analysé et il a été démontré qu'il est généré par le champ électrique produit

par la charge qui est accumulée sur les particules. Des études expérimentales de la mise en charge par contacts particule-paroi et particule-particule ont été effectuées pour étudier les paramètres électrostatiques et mécaniques qui sont importants pour modéliser la grandeur et la direction du transfert de charge dans les systèmes à écoulement gaz-solide. La mise en charge par contact particule-paroi due à des collisions uniques et répétées a été testée avec diverses particules, y compris du polyéthylène linéaire commercial à basse densité, pour déterminer leurs taux de charge ainsi que leurs limites de saturation de charge lors d'une collision avec une surface métallique.

Une représentation graphique de la valeur de saturation de charge des particules par rapport à leurs surfaces respectives a révélé une tendance linéaire qui pourrait être utilisée pour calculer la saturation de charge de la particule pour une taille de particule donnée. Des études supplémentaires sur la mise en charge par contact particule-paroi ont établi l'effet de la charge initiale, la fréquence de collision, le type de particule, l'angle d'impact, la vitesse d'impact et la présence d'impuretés sur la mise en charge des particules. Pour étudier la mise en charge par contact particule-particule, un nouvel appareil a été conçu, construit et testé pour déterminer la grandeur et la direction du transfert de charge lors des collisions particule-particule individuelles de particules isolantes. Cet appareil était le premier du genre et garantissait que le transfert de charge mesuré pour chaque essai expérimental était uniquement dû à la collision binaire entre les particules. Il a été observé que la direction du transfert de charge dans des collisions de particules identiques n’est pas dictée par les charges initiales nettes des particules, mais par la différence de charge localisée à la surface de contact des particules. De plus, les collisions particule-particule de particules de nylon de différentes tailles ont confirmé les phénomènes de mise en charge bipolaire, où la direction du transfert de charge était dictée par la taille relative des particules en collision. Ces résultats, entre autres, contredisent le comportement de transfert de charge prédit par les modèles de mise en charge électrostatique actuellement proposés pour les collisions particule-particule. En tant que tel, un modèle de transfert de charge empiriquement précis doit être établi pour simuler la mise en charge électrostatique de particules dans des systèmes d'écoulement gaz-solide poly-dispersé.

Statement of Contributions of Collaborators

This thesis is part of the collaborative effort between the research groups under Dr. Poupak Mehrani (University of Ottawa, Canada) and Dr. Alberto Passalacqua (Iowa State University, USA). The experimental work in this collaboration was done solely by me at the University of Ottawa, while the contributions to the CFD modeling were distributed between myself and Dr. Manjil Ray, who recently completed his doctoral studies under Dr. Alberto Passalacqua.

Chapters 1 and 8 were written solely by me with editorial comments provided by Dr. Mehrani and Dr. Sowinski.

Chapter 2 is a manuscript published in a peer-reviewed academic journal, based on CFD modeling work performed in collaboration with Dr. Passalacqua and Dr. Ray of Iowa State University. The derivation of the electrostatic charging model and its implementation into the Eulerian CFD model was performed by Dr. Ray, which was a major component of his dissertation, with assistance from Dr. Passalacqua. The coding of the model into OpenFOAM®, the design and testing of the simulation cases, and the analysis and validation of the simulation results were equally distributed between me and Dr. Ray. I am the second author of this chapter, with Dr. Ray as the first, and my writing contribution to this work is approximately 40%. Editorial comments were provided by Dr. Mehrani, Dr. Sowinski, and Dr. Passalacqua who are also listed as co-authors.

Chapter 3 is a manuscript published in a peer-reviewed academic journal. I designed the particle-wall collision apparatus and performed all contact experiments and charge measurements. I also performed the data analyses with assistance on the theories and discussion from Dr. Sowinski and Dr. Mehrani. I am the first author and sole writer of this chapter, with editorial comments provided by the co-authors on the manuscript: Dr. Mehrani, Dr. Sowinski, Dr. Passalacqua, and Dr. Ray.

Chapter 4 is a manuscript published in a peer-reviewed academic journal. I designed the particle-particle collision apparatus, performed all contact experiments, and analyzed the charge measurements with assistance from an engineering co-op student, Bilal Elchamaa, who is mentioned as a co-author. I am the first author and sole writer of this chapter, with editorial comments provided by the remaining co-authors on the manuscript: Dr. Mehrani, Dr. Sowinski, Dr. Passalacqua, and Dr. Ray.

Chapter 5 is a manuscript published in a peer-reviewed academic journal. I performed all contact experiments and analyzed the charge measurements with assistance from Dr. Mehrani and Dr. Sowinski. I am the first author and sole writer of this chapter, with editorial comments provided by the co-authors on the manuscript: Dr. Mehrani, Dr. Sowinski, Dr. Passalacqua, and Dr. Ray.

Chapter 6 is a manuscript under review for publication in a peer-reviewed academic journal. I performed all the validation and analysis of the charge transfer model with assistance from Dr. Mehrani and Dr. Sowinski. I am the first author and sole writer of this chapter, with editorial comments provided by the co-authors on the manuscript: Dr. Mehrani, Dr. Sowinski, Dr. Passalacqua, and Dr. Ray.

Chapter 7 is a manuscript under review for publication in a peer-reviewed academic journal. It is a review article written in collaboration with Dr. Passalacqua and Dr. Ray of Iowa State University. I am the first author of this chapter, with Dr. Ray as the second, and my writing contribution is approximately 60%. The research, analysis, and discussion tasks were equally distributed between the two of us. I am the creator of all original schematics presented in this chapter. Editorial comments were provided by Dr. Mehrani, Dr. Sowinski, and Dr. Passalacqua who are also listed as co-authors.

Appendix A is a manuscript published in a peer-reviewed academic journal, based on CFD modeling work performed in collaboration with Dr. Passalacqua and Dr. Ray of Iowa State University. Dr. Ray is the first author and primary writer of this work with my writing contribution being approximately 10%, mainly on the introduction and literature review section. I also contributed to the set-up of the simulation cases and the analysis and discussion of the simulation results. Editorial comments were provided Dr. Mehrani, Dr. Sowinski, and Dr. Passalacqua who are also listed as co-authors.

Acknowledgements

First and foremost, I would like to express my deepest gratitude to my supervisors, Professors Poupak Mehrani and Andrew Sowinski. I was fortunate to have two caring supervisors who were deeply invested in my research, who dedicated so much of their time to help me achieve my goals. Their guidance and support throughout my years at the University of Ottawa, both during my undergraduate and graduate studies, had a profound impact on my academic, professional, and personal development.

I would also like to acknowledge Professor Alberto Pascalacqua and fellow colleague Manjil Ray of Iowa State University, who were collaborators and essential contributors in this research. I am particularly grateful to Professor Pascalacqua for hosting me at ISU as a visiting scholar, allowing me to work closely with his lab group and learn from experts in Computational Fluid Dynamics.

I wish to acknowledge the funding support from Univation Technologies through the Queen Elizabeth II Graduate Student of Science & Technology Scholarship. I am grateful for the awards I received through the Ontario Graduate Scholarship (OGS) and the NSERC Postgraduate Scholarship (PGS D) programs. I am also grateful for the funding I received from the Mobility Scholarship and the International Experience Scholarship from the University of Ottawa, as well as the Mitacs Globalink Research Award, which enabled me to attend Iowa State University as a visiting scholar on two separate occasions.

I am incredibly thankful to the Chemical & Biological Engineering technical staff (Louis Tremblay, Franco Ziroldo, Gérard Nina and James Macdermid). The experimental work performed in this research was only possible due to their invaluable assistance in designing and building the novel apparatuses. A special thanks also goes to the department's administrative staff (Francine Pétrin and Sylvie Saindon) for their support in all administrative matters over the years.

I would also like to thank the many friends I have made over the last ten years at the University of Ottawa. Those from my undergraduate studies continue to have a strong impact in my life to this day – Shazadi, Sophie, Russell, Aaraf, Sam, Lina, and many more. Thank you for always being there for me. I have also been fortunate to be surrounded by many remarkable colleagues during my graduate studies. To Charbel, Milad, Emily, Geraldine, Yasmine, Dean, Sean, Katrina, Di, Alex, Shidan, Farhad, Amir, Vida, David, Shazadi (again), Mohsen, Chris P., Chris M., Curtis, Sam, and so many more; thank you all for making this the best time of my life.

Lastly, I wish to thank my family all over the world, who helped shape me into the person I am today. My mother, Momotaz, for her unconditional love and support throughout my life. My sister, Wahida, for inspiring me to tackle any and all obstacles set before me. My brother, Adel, for being my first friend, guardian, and lifeline. Finally, I wish to thank my amazing wife, Kayla, for her love, support, and incredible patience. Thank you, for everything.

Dedication

This thesis is dedicated to my late father, Ruhul Amin Chowdhury.

Born in 1949 into a large family in rural Bangladesh, then known as East Pakistan, my father always had a strong calling for duty to his family, community, and country. After earning a Bachelor's in Commerce, he first worked as a schoolteacher in his small village. The Bangladesh Liberation War took place during this time and my father, along with his family, sheltered many displaced families as they fled their homes from major cities. He also joined the conflict as a freedom fighter, to help claim Bangladesh's independence.

Fueled with a sense of adventure, my father and his elder brother found themselves in Singapore in his late 20s to work for a construction company. Once there, he found an opportunity to go to Japan and work in a transport ship, which travelled between Australia and Saudi Arabia. During a stop in Saudi Arabia, he disembarked to make a pilgrimage to Mecca. After interacting with the Bangladeshi community there, he decided to stay and work in Saudi Arabia. This is where he worked for most of his life, all the while providing financial support to his family back home.

My father always cared for his family, returning to Bangladesh every year to visit them. He married my mother, Momotaz Begum, during one of these visits, in 1982. Together, they raised three children in Jeddah as he continued to build his career, where he earned a management role in a food production facility. He was also a keen entrepreneur, founding and investing in businesses in Bangladesh with the friends he made in Jeddah. Thanks to his efforts, we led a happy and comfortable childhood.

As we grew older, my parents wanted to ensure that my siblings and I could receive the best education possible, and so they set their sights on Canada. After an arduous process, and using the greater part of his life savings, my father managed to get us settled in Ottawa in 2005. Here, he fulfilled his dream of owning a restaurant, which had become a core part of our lives. He worked at the restaurant every day to earn for his family, so all three of his children could pursue opportunities they were passionate about. Unfortunately, the lifetime of hard work had taken its toll, and his body could no longer keep up with him. He passed in 2013 from pulmonary fibrosis, surrounded by family and the many friends he made in Ottawa.

I am eternally grateful for everything my father has done for us. He endured many challenges and made many sacrifices to give my family a better future.

Thank you so much Abbu. You may have left this world too soon, but I can only dream to live a life as full as yours. This thesis is dedicated to you, because without you, it would not have been possible.

I hope I made you proud.

Table of Contents

Abstract ii
Résumé iv
Statement of Contributions of Collaborators vi
Acknowledgements viii
Dedication ix
Table of Contents x
List of Figures xv
List of Tables xxi
Nomenclature xxii
Chapter 1. Introduction 1
1.1. Principles of Electrostatics 1
1.1.1. Charge Generation in Insulators 2
1.1.2. Charge Transfer Modeling 5
1.2. Electrostatic Charging in Gas-Solid Fluidized Beds 7
1.2.1. Effect of Operating Parameters on Electrostatics 9
1.3. Modeling & Simulation of Gas-Solid Fluidized Beds 10
1.3.1. Electrostatic Modeling 12
1.4. Thesis Objective 13
1.5. Thesis Outline 14
References 17
Chapter 2. An Euler-Euler model for mono-dispersed gas-particle flows incorporating electrostatic charging due to particle-wall and particle-particle collisions 22
Abstract 22
2.1. Introduction 23
2.2. Multiphase hydrodynamic model 26
2.3. Electrostatic model 29
2.3.1. Transport equation for particle charge 30
2.3.2. Particle number density function 31

2.3.3. Rate of change of particle charge due to particle-wall collisions 32
2.3.4. Rate of change of particle charge due to particle-particle collisions 33
2.3.5. Derivation of charge-velocity covariance 36
2.3.6. Derivation of expression for the charge variance 37
2.3.7. Wall boundary condition for particle charge density 38
2.4. Model implementation 39
2.5. Simulation and validation 40
2.5.1. Description of the test case 40
2.5.2. Numerical setup 43
2.5.3. Results 46
2.5.3.1. Grid convergence 46
2.5.3.2. Simulation Results 47
2.6. Conclusion 53
Appendix - Derivation of the interparticle collisional rate of change of charge 54
References 64
Chapter 3. Charge Generation and Saturation on Polymer Particles due to Single and Repeated Particle-Metal Contacts 70
Abstract 70
3.1. Introduction 71
3.2. Theory 72
3.2.1. Numerical model for particle-wall contact charging 73
3.3. Material and methods 74
3.4. Results and discussion 77
3.4.1. Effect of initial charge 77
3.4.2. Effect of collision frequency 78
3.4.3. Effect of particle type 80

3.4.4. Effect of particle size 81
3.4.5. Application of the numerical model 83
3.4.6. Effect of impurities (experimental observation) 84
3.5. Conclusions 85
References 86
Chapter 4. Apparatus Design for Measuring Electrostatic Charge Transfer due to Particle-Particle Collisions 89
Abstract 89
4.1. Introduction 90
4.2. Theory 90
4.3. Design and Methodology 93
4.3.1. Apparatus Design 94
4.3.2. Particle Collision Detection and Tracking 95
4.3.3. Charge Measurement Technique 96
4.4. Results and Discussion 98
4.4.1. Conventional Charge Transfer 100
4.4.2. Anomalous Charging 103
4.5. Conclusions and Future Work 104
References 105
Chapter 5. Electrostatic charging due to individual particle-particle collisions 108
Abstract 108
5.1. Introduction 109
5.1.1. Particle-Particle Charging Experiments 110
5.2. Design & Methodology 111
5.2.1. Apparatus Design 111
5.2.2. Collision Detection & Particle Tracking 113

5.2.2.1. Impact Velocity & Impact Angle 115
5.2.3. Materials and Operating Conditions 116
5.2.4. Particle Charging in Airflow 117
5.2.5. Reproducibility of Charge Measurements 120
5.3. Results & Discussion 121
5.3.1. Different-Material Collisions 121
5.3.1.1. Comparing particle-particle and particle-plate charge transfer 122
5.3.2. Same-Material Collisions 125
5.3.2.1. Same-Sized Collisions 126
5.3.2.2. Different-Sized Collisions 128
5.3.2.3. Effect of Initial Charge Difference 130
5.3.2.4. Effect of Impact Velocity & Angle 132
5.3.3. Summary of Particle-Particle Charge Transfer 134
5.4. Conclusions 136
References 137
Chapter 6. Evaluating the electrostatic charge transfer model for particle-particle interactions 140
Abstract 140
6.1. Introduction 141
6.1.1. Particle-particle charge transfer model 142
6.2. Model Evaluation 143
6.2.1. Rolling contact area 144
6.2.2. Different-material, same-sized particle collisions 145
6.2.3. Same-material, same-sized particle collisions 149
6.2.4. Same-material, different-sized collisions 152
6.3. Conclusion 156

References 157
Chapter 7. A review on modeling approaches for the electrostatic charging of particles 160
Abstract 160
7.1. Introduction 161
7.2. Charge transfer mechanisms and models 162
7.2.1. Condenser model 163
7.2.1.1. Effective work function difference 165
7.2.1.2. Critical gap 166
7.2.1.3. Saturation charge 166
7.2.1.4. Surface area of contact 167
7.2.1.5. Effect of the electric field 168
7.2.2. Ion transfer and material transfer models 169
7.2.3. Particle-particle charge transfer model 171
7.2.3.1. Dipole amplification mechanism 172
7.2.4. Charge relaxation model 173
7.3. Gas-solid flow models with electrostatic effects 175
7.3.1. CFD-DEM 176
7.3.2. Two-fluid models 178
7.4. Considerations for future electrostatic models 180
7.4.1. Finite duration of contact during impacts 180
7.4.2. Nonuniform surface charge density 183
7.4.3. Bipolar charging of granular materials 185
7.4.3.1. Bipolar charging in simulations 186
7.4.4. Operating conditions of gas-solid flow systems 189
7.5. Summary and Outlook 190

References 192

Chapter 8. Conclusions and Recommendations 198

8.1. Conclusions 198

8.2. Recommendations for Future Work 201

References 203

Appendix A. Eulerian modeling of charge transport in bi-disperse particulate flows due to triboelectrification 204

Appendix B. Supplemental Apparatus Images 240

List of Figures

Figure 1-1: Triboelectric charging by contact (top) and friction (bottom). 2

Figure 1-2: Charging by induction, generating a positive charge on a metal object. 3

Figure 1-3: Electron potential energy for metal-metal contacts 4

Figure 1-4: 2D and 3D Potential maps of a PC surface contact-charged by a PDMS surface 5

Figure 1-5: (a) Electrostatic probe measurement technique, (b) Faraday cup measurement technique. 8

Figure 1-6: Visual representation of the models listed in Table 1-2 11

Figure 1-7: Comparison of wall-fouling observed in a) experiments and b) simulation 13

Figure 2-1: Computational model framework. 40

Figure 2-2: Schematic of the experimental setup (and a snapshot of the bed simulation). 41

Figure 2-3: Two-dimensional grid layout: (left) across the bed width (with upper and lower blocks), (right) grid grading near the right wall 44

Figure 2-4: Plots illustrating grid convergence through comparison of deviation of (a) coefficient of variance, (b) maximum electric potential and total charge in the bed, w.r.t. the most refined grid. 46

Figure 2-5: Evolution of total bed charge. 47

Figure 2-6: Contour plots of (a) particle volume fraction, (b) electric potential, (c) electric field strength, and (d) vertical component of particle phase velocity, at T = 10s. 48

Figure 2-7: Contour plots of particle volume fraction as the particles settle. 49

Figure 2-8: Variation of electric potential across (a) the bed width, and (b) near the left wall. . 50

Figure 2-9: Variation of particle charge density across the bed: (a) full bed width and entire range of magnitude, (b) full bed width with one order lower magnitude (c) up to 1 mm from the left wall, (d) between 1 mm and 5 mm from the left wall. 51

Figure 2-10: (a) Particle layer thickness on the wall as a function of height for different diameters; Comparison of (a) mass percentage of particles sticking to the wall (loosely and tightly bound represent experimental results), (b) q/m ratio of wall particles in the simulation and loosely bound particles in the experiments, and (c) q/m ratio of bulk particles in the simulation and dropped particles in the experiments. 52

Figure 3-1: Array of particles used for the charge generation experiments. 75

Figure 3-2: Apparatus for single particle contact tests. 76

Figure 3-3: Effect of initial charge on the % change in charge of 3.18 mm PTFE spheres due to varying numbers of wall collisions. 78

Figure 3-4: Effect of collisional frequency on the repeated particle-metal charging of LLDPE #4. 79

Figure 3-5: Charge generated on HDPE and PTFE particles by a single plate collision. 80

Figure 3-6: Average saturated charge for various particle types. 81

Figure 3-7: Charge generated by 2.38 and 3.18 mm PTFE spheres after a single metal collision normalized by surface area. 82

Figure 3-8: Average charge normalized by surface area of various sizes of LLDPE resins with increasing number of particle-wall collisions. 82

Figure 3-9: Average charge saturation of LLDPE resins with increasing surface area. 83

Figure 3-10 Fitting the numerical model to the experimental data for particle charging of various sizes of LLDPE resins due to repeated wall collisions. 84

Figure 3-11: Effect of dust contamination on the charge of LLDPE #4 after 120 and 180 collisions. 85

Figure 4-1: Particle-particle collision apparatus. The arrows depict the particles' pathway as they are released during a collision trial. 93

Figure 4-2: Side and top view of the particle holder and release mechanism. 94

Figure 4-3: Snapshots from a particle-particle collision video, taken at 0.21 s intervals. 95

Figure 4-4: Composite image of two particles undergoing an elastic collision. 96

Figure 4-5: Charge readings of one particle dropping through its top Faraday cage before the particle-particle collision, and then landing in its bottom Faraday cage after the collision. 97

Figure 4-6: Initial charge comparison of paired particles measured for all trials. 99

Figure 4-7: Comparing the charge differences between two particles before and after their collision. 99

Figure 4-8: Ideal charge transfer trials where (a) the collided particles exhibited conventional charging with near-perfect collisional charge transfer; (b) the charge transfer trials were sorted by increasing discrepancy in the charging of the paired particles. 101

Figure 4-9: Imbalanced charge transfer trials where (a) the collided particles exhibited a charge transfer discrepancy beyond the truncated reading accuracy of the electrometers; (b) the trials were sorted by increasing net change in charge. 102

Figure 4-10: The effect of each particle's initial particle charge on its change in charge after experiencing a particle-particle collision. 103

Figure 5-1: Bottom view of the particle holder and release mechanism, showcasing the two sliding trapdoors. 112

Figure 5-2: Video frames of three sample collision trials: direct contact, angled contact, and tangential contact. 114

Figure 5-3: Procedure for identifying the normal velocity at the point of impact: (a) Original Coordinates: Determine the particles' cell-center coordinates as well as their velocities before collision. (b) Shifted Coordinates: Shift the coordinates of both particles and adjust the frame of reference such that the larger particle is at rest at the point of origin. (c) Rotated Coordinates: Rotate the particles about the origin until the moving particle horizontally approaches the resting particle. 115

Figure 5-4: Change in particle charge as a function of initial charge for single 3.2 mm PTFE particles dropped with and without airflow. 118

Figure 5-5: Change in particle charge as a function of initial charge for single HDPE and Nylon particles dropped with airflow. 119

Figure 5-6: Charge transferred to 4.0 mm particles in 4.0 mm-3.2 mm nylon collision trials over multiple days. The particles were washed and blow-dried for at least 24 hours prior to their use in each day. Notes: particles were used directly from storage and not pre-washed in Day 1. Newly purchased batch of non-washed particles were used in Day 4, which were then washed, dried, and reused for Day 5. 121

Figure 5-7: Charge transfer measurements for each particle in PTFE-Aluminum (left) and PTFE-Nylon (right) collision trials. (a) Change in charge, ΔQ, where PTFE-Nylon collisions exhibited

greater charge transfer than PTFE-Aluminum collisions. (b) A net change in charge, $\Delta Qnet$, close to zero implies near-perfect charge transfer between particles with negligible external influences. The error bars represent the truncated measurement errors from each electrometer. 122

Figure 5-8: The average charge transferred to 3.2 mm PTFE particles after colliding with an inclined aluminum plate. The charge measurements are grouped by the particles' impact velocities and angles, which are defined as shown in the inset. 123

Figure 5-9: Effect of impact angle and velocity on charge transfer to PTFE due to PTFE-aluminum particle collisions. The PTFE's impact angle, ϕ, and velocity, u, are defined as shown in the inset. 124

Figure 5-10: Sample of charge transfer measurements for nylon particles undergoing same-sized particle-particle collisions, using 3.2 mm (left) and 4.0 mm (right) nylon. The error bars represent the truncated measurement errors from each electrometer. Charge data is presented for two airflow rates for each set of collision trials. (a) Change in charge was higher in 4.0 mm nylon collisions than in 3.2 mm nylon collisions. (b) The net change in charge shows mostly negligible discrepancies in the charging of the paired particles. 127

Figure 5-11: Sample particle-particle charge transfer measurements of 3.2-4.0 mm nylon collisions with the flowrates set at 100 and 125 SLPM (left), and 3.2-4.8 mm nylon collisions at 125 SLPM (right). The error bars represent the truncated measurement errors from each electrometer. Note the difference in the scale of the two plots. (a) Change in charge on 3.2 mm nylon was greater when colliding with 4.0 mm nylon than with 4.8 mm nylon. (b) The net change in charge highlighted the minor to negligible discrepancies in the charging of the paired particles. 129

Figure 5-12: Sample Particle-particle charge transfer measurements due to collisions between 4.0 mm and 4.8 mm nylon. The error bars represent the truncated measurement errors from each electrometer. (a) 4.0 mm nylon charged positively in most collisions, contrary to previous charging direction based on particle size. Negative charging of the smaller particle was only observed for tangential contacts. (b) Near-perfect charge transfer observed for most collision trials. 129

Figure 5-13: Change in particle charge on 3.2 mm nylon after colliding with 3.2, 4.0 and 4.8 mm nylon as a function of the colliding particles' net initial surface charge densities, $\Delta\sigma i$. The initial surface charge density σi of the reference particle is also color-mapped for each collision trial. 130

Figure 5-14: Change in particle charge on 4.0 mm nylon after colliding with 3.2, 4.0 and 4.8 mm nylon as a function of the colliding particles' net initial surface charge densities, $\Delta\sigma i$. The initial surface charge density σi of the reference particle is also color-mapped for each collision trial. 131

Figure 5-15: Change in particle charge on 3.2 mm nylon after colliding with 3.2, 4.0 and 4.8 mm nylon as functions of impact velocity and angle. 133

Figure 5-16: Change in particle charge on 4.0 mm nylon after colliding with 3.2, 4.0 and 4.8 mm nylon as functions of impact velocity and angle. 133

Figure 5-17: Average charge transferred per contact area for all particle-particle collision scenarios, where n is the number of collision trials tested for every scenario. The data points in each set were determined by grouping the particles based on their material type and particle size and averaging their charge transfer values. For the identical particle-particle collision scenarios, the particles from each trial were instead grouped based on their charge transfer direction. ... 135

Figure 6-1: Contact area in particle-particle collisions as a function of impact velocity at varying contact angles. The dashed lines represent the total contact area when including particle rolling. 145

Figure 6-2: Surface plot of the charge transferred, ΔQ, as a function of the contact area, Sc, and the difference in initial charges, ΔQi, as described in Eq. 6-6 and using input parameters based on 3.2 mm same-sized PTFE-nylon collisions. 146

Figure 6-3: Comparing the experimentally measured change in charge for PTFE, $\Delta QPTFE$, with that calculated using the charge transfer model. kc values of 0.188 and 0.061 were used for PTFE-Aluminum (blue) and PTFE-nylon (red) collisions, respectively, to minimize their residual standard errors visualized along the 45 degree line..... 147

Figure 6-4: The effect of the initial charge difference, ΔQi, on the measured and modelled charge data for PTFE in (a) PTFE-Aluminum and (b) PTFE-Nylon collisions. The residual plots highlight the discrepancies between the measured and modelled data for each (c) PTFE-Aluminum and (d) PTFE-Nylon collision trial. 148

Figure 6-5: The effect of the surface area of contact, Sc, on the measured and modelled charge data for PTFE in (a) PTFE-Aluminum and (b) PTFE-Nylon collisions. The residual plots highlight the discrepancies between the measured and modelled data for each (c) PTFE-Aluminum and (d) PTFE-Nylon collision trial. 148

Figure 6-6: Surface plot of the charge transferred, ΔQ, as a function of the contact area, Sc, and the difference in initial charges, ΔQi, as described in Eq. (7) and using input parameters based on 3.2 mm same-sized nylon particle collisions..... 149

Figure 6-7: Comparing the experimentally measured charge transferred to nylon particles with a relatively negative initial charge with that calculated using the charge transfer model. While the model predicted positive charging for particles with a relatively negative initial charge, experimental data showed both positive and negative charging. Focusing on the magnitude of charge transfer instead of its direction, kc values of 0.188 and 0.061 were respectively used for the 3.2 mm (blue) and 4.0 mm (red) same-sized nylon particle collisions to minimize their absolute residual standard errors. 150

Figure 6-8: The effect of the initial charge difference, ΔQi, on the measured and modelled charge data for nylon particles with a relatively negative initial charge in (a) 3.2 mm and (b) 4.0 mm same-sized nylon particle collisions. Presented in logarithmic scale. The residual plots highlight

the significant discrepancies between the measured and modelled data for each (c) 3.2 mm and (d) 4.0 mm collision trial. 151

Figure 6-9: The effect of the surface area of contact, Sc, on the measured and modelled charge data for nylon particles with a relatively negative initial charge in (a) 3.2 mm and (b) 4.0 mm same-sized nylon particle collisions. The residual plots highlight the significant discrepancies between the measured and modelled data for each (c) 3.2 mm and (d) 4.0 mm collision trial. 152

Figure 6-10: Surface plot of the charge transferred, ΔQ, as a function of the contact area, Sc, and the difference in initial surface charge densities, $\Delta\sigma i$, as described in Eq. 6-8 and using input parameters based on 4.0-3.2 mm nylon collisions. 153

Figure 6-11: Comparing the experimentally measured charge transferred to 4.0 mm nylon particles with that calculated using the charge transfer model. The model generally predicted charge transfer in the opposite direction of the experimental data. Focusing on the magnitude of charge transfer instead of its direction, kc values of 64.33 and 46.98 were respectively used for the 4.0-4.8 mm (blue) and 4.0-3.2 mm (red) nylon collisions to minimize their reflected residual standard errors. 154

Figure 6-12: The effect of the difference in initial surface charge density, $\Delta\sigma i$, on the measured and modelled charge data for 4.0 mm nylon particles in (a) 4.0-4.8 mm and (b) 4.0-3.2 mm nylon collisions. The residual plots highlight the significant discrepancies between the measured and modelled data for each (c) 4.0-4.8 mm and (d) 4.0-3.2 mm collision trial. 155

Figure 6-13: The effect of the surface area of contact, Sc, on the measured and modelled charge data for 4.0 mm nylon particles in (a) 4.0-4.8 mm and (b) 4.0-3.2 mm same-sized nylon particle collisions. The residual plots highlight the significant discrepancies between the measured and modelled data for each (c) 4.0-4.8 mm and (d) 4.0-3.2 mm collision trial. 155

Figure 7-1: Condenser model schematic (Adapted from [19]). 164

Figure 7-2: Ion transfer mechanism (Adapted from [23]). 170

Figure 7-3: Dipole amplification model (adapted from [11]). 172

Figure 7-4: Mechanism of charge relaxation during separation (adapted from [19]). 174

Figure 7-5: Variation in collision outcome with coefficient of restitution [77]. 181

Figure 7-6: Residual particle velocity at the wall of a fluidized bed with relative humidity [32] 181

Figure 7-7: Temporal variation of residual velocity at the wall (simulation results for different relative humidity) [32]..... 182

Figure 7-8: Non-uniform charge transfer as a function of initial charge (The open circles are experimental results of Matsuyama and Yamamoto [79], and the solid circles are simulation predictions by Grosshans et al. [78]). 183

Figure 7-9: Evolution of particle charge due to non-uniform charging (copied from [78]). 184

Figure 7-10: Temporal evolution of charge in a box coated with PE particles (copied from [86]). 186

Figure 7-11: Distribution of charge for different equilibrium charge-to-mass ratios [31] (a charging acceleration factor of 12.86 was used). 187

Figure 7-12: Distribution of charge for different equilibrium charge-to-mass ratios a) e/g = 8, b) e/g = 4, and charging acceleration factors *a* [32]. 188

Figure 7-13: Bipolar charging when diameter ratio is varied (volume fraction = 0.3 for both particle phases) [58]. 189

List of Tables

Table 1-1: Work functions of various polymers [16]. 4

Table 1-2: Various models for simulating gas-solid fluidized beds [59]. 11

Table 2-1: Material properties of polyethylene particles. 41

Table 2-2: Experiment operating conditions and measured particles charge densities. 42

Table 2-3: Charge generation model parameters 43

Table 2-4: Simulation boundary conditions 45

Table 2-5: Simulation boundary conditions 48

Table 3-1: Average diameter and surface area of tested LLDPE resins. 75

Table 3-2: Summary of numerical model parameters and error compared to the experimental data. 84

Table 5-1: Densities, sizes, and airflow rates used for all successfully tested particles. 117

Table 6-1: Particle properties and model parameters used in the charge transfer model. 144

Table 7-1: Various proposed relationships for the general charge transfer equation. 163

Nomenclature

$\mathbf{B}$	Magnetic field (T)
$\langle \mathbf{C}q' \rangle$	Charge-velocity covariance ($C \cdot m \cdot s^{-1}$)
$\mathbb{C}$	Collisional rate of change of a property ($unit \cdot m^{-3} \cdot s^{-1}$)
$\mathbf{C}$	Particle fluctuation velocity ($m \cdot s^{-1}$)
C	Wall-particle interaction coefficient ($A \cdot s$)
$\mathbf{c}$	Velocity of particle moving in a field ($m \cdot s^{-1}$)
$\mathbf{D}$	Electric displacement ($C \cdot m^{-2}$)
d	Diameter (m)
$\mathbf{E}_q$	Electric potential (V)
$\mathbf{E}$	Electric field ($V \cdot m^{-1}$)
$\mathrm{E_c}$	Electric field acting on contact point ($V \cdot m^{-1}$)
E	Young's modulus (Pa)
e	Coefficient of restitution (-)
$\mathbf{F}$	Force term (N)
f	Frequency of collisions (Hz)
f^2	Pair distribution function (-)
f_p	Particle number density function (-)
$\mathbf{g}$	Gravitational acceleration vector ($m \cdot s^{-2}$)
g_0	Radial distribution function (-)
$\mathbf{I}$	Unit stress tensor (-)
J	Rate of change of granular energy due to phase interactions ($m^2 \cdot s^{-3}$)
K_d	Drag function model (N)
k	Elasticity parameter (Pa^{-1})
k_c	Charging efficiency (-)
k_e	Image charge constant ($V \cdot C^{-1}$)
k_r	Charge relaxation constant (s^{-1})
$k_{s,p}$	Constant for contact area between two particles ($m^{6/5} \cdot s^{4/5}$)
$k_{s,w}$	Constant for contact area between a particle and wall ($m^{6/5} \cdot s^{4/5}$)
$\mathbf{k}$	Unit vector from the center of the first particle to the center of the second (-)

$\mathbf{M}$	Momentum exchange term (N)
m	Mass (kg)
N	Number of particles per unit volume ($N_p \cdot m^{-3}$)
n, n_c	Number of collisions (-)
$\mathbf{n}$	Wall-normal unit vector (-)
$\mathbf{P}$	Induced polarization ($C \cdot m^{-2}$)
p	Shared pressure (Pa)
$\langle q \rangle$	Mean particle charge density ($C \cdot m^{-3}$)
q'	Fluctuation of charge (C)
q_∞	Particle saturation charge (C)
q	Particle charge (C)
q_i	Initial charge (C)
q_f	Final charge (C)
$\mathbf{r}$	Particle position vector (m)
$\mathbf{S}$	Deformation rate tensor (s^{-1})
S_c	Contact area (m^2)
$\mathbf{U}$	Mean phase velocity ($m \cdot s^{-1}$)
$\boldsymbol{u}$	Particle velocity vector ($m \cdot s^{-1}$)
$\boldsymbol{u_{impact}}$	Impact velocity vector ($m \cdot s^{-1}$)
$\boldsymbol{u^*_{impact}}$	Rotated impact velocity vector ($m \cdot s^{-1}$)
V_c	Difference of work functions of two impacting surfaces (V)
V	Volume (m^3)
v	Wall-normal magnitude of particle velocity ($m \cdot s^{-1}$)
z_0	Critical gap (m)

Subscripts

1	Term related to particle 1
2	Term related to particle 2
fr	Term related to friction
g	Term related to gas phase

kt	Term related to kinetic and collisional contributions
p	Term related to a particle
s	Term related to particle phase
q	Term related to electrostatic charge
w	Term related to wall interactions

Greek letters

α	Phase volume fraction (-)
Γ	Gamma function (-)
γ	Dissipation rate ($m^2 \cdot s^{-3}$)
ε_0	Electric permittivity of vacuum ($F \cdot m^{-1}$)
ε_m	Relative permittivity of multiphase mixture (-)
ε_r	Relative electric permittivity (-)
Θ_s	Granular energy ($m^2 \cdot s^{-2}$)
κ	Conductivity ($m^2 \cdot s^{-1}$)
λ	Bulk viscosity ($Pa \cdot s$)
μ	Shear viscosity ($Pa \cdot s$)
ν	Poisson ratio (-)
ρ	Thermodynamic density ($kg \cdot m^{-3}$)
σ	Surface charge density ($C \cdot m^{-2}$)
τ	Stress tensor (-)
φ_E	Electric potential (V)
ϕ	Impact angle (°)
χ_e	Electric susceptibility (-)
χ_q	Source term in the rate of change of particle charge ($C \cdot m^{-3} \cdot s^{-1}$)

Subscripts

Θ_s	Term related to granular energy
φ	Term related to the generic phase

Chapter 1

Introduction

When a gas or liquid vertically flows through a bed of solid particles at a sufficient flow velocity, the solid particles start exhibiting fluid-like behaviour. This is known as fluidization, and it occurs when the drag force exerted by the fluid counteracts the weight of the solid particles [1]. Fluidization has been an influential technological innovation in the chemical and petrochemical process industry. Gas-solid fluidized beds have been developed for a large variety of industrial applications, including polymerization, fluid catalytic cracking, combustion, mixing, coating and drying. One of the modern applications of gas-solid fluidized beds is the catalytic polymerization of ethylene gas to produce polyethylene. While the process has many advantages in terms of productivity, the solid particles in this flow system can face problems with electrostatic charge generation due to particle-particle and particle-wall interactions. Electrostatic effects on gas-solid fluidized beds have been investigated since its first application in 1942 with catalytic cracking [1], and since then many electrostatic measurement techniques have been developed for their study [2]. These investigations have led to concentrated efforts in reducing the electrostatic charge generation and in turn the wall fouling in fluidized beds [3,4]. As a part of this on-going effort, Computational Fluid Dynamic (CFD) simulation and modeling studies have gained recent attention to investigate the electrostatic charging in gas-solid fluidized beds. Through the collaborative efforts between two research groups at the University of Ottawa and Iowa State University, a CFD model was developed to simulate the effect of fixed particle charges on laboratory-scale fluidization experiments [5]. As a continuation of this effort, the objective of this thesis is to develop and implement an electrostatic charging model that simulates charge transfer due to particle-particle and particle-wall interactions. This would allow the particles' charge to be updated over time, thereby providing a more realistic simulation of the fluidized bed.

1.1. Principles of Electrostatics

Electrostatics is the study of charge accumulation in solids and liquids. While electrostatics can be a nuisance for everyday life, research on this topic led to the rapid development of industrial applications such as electrostatic powder coating and electrostatic photocopying [6]. In electrostatics, a neutral object can become either positively or negatively charged by losing or

gaining electrons. Two charged particles share an attraction if oppositely charged, or a repulsion if similarly charge. The magnitude of this attraction/repulsion, or the electrostatic force between them, can be described using Coulomb's law:

$$F_q = \frac{1}{4\pi\varepsilon_0\varepsilon_r}\frac{q_1 q_2}{r^2} \qquad 1\text{-}1$$

F_q is the electrostatic force; ε_0 is the permittivity of a vacuum; ε_r is the relative permittivity of the medium (such as air); r is the distance between two point sources (which in this case are two particles); and q_1 and q_2 are the charges on the two point sources. Equation 1-1 considers only two charges; the force acting on a charge due to multiple surrounding charges is simply the summation of the individual forces acting between the charge and each surrounding charge. The electric field (E) generated due to the electrostatic force is defined as electrostatic force per unit charge. As such, the magnitude of the electric field due to a point charge q can be calculated as:

$$E = \frac{q}{4\pi\varepsilon_0\varepsilon_r r^2} \qquad 1\text{-}2$$

1.1.1. Charge Generation in Insulators

Electrostatic charging can usually be classified into contact charging and frictional charging, as shown in Figure 1-1. In contact charging, two surfaces can exchange some of their charge due to the difference in surface energies. Frictional charging is very similar, except it involves an extended surface contact due to sliding or rolling. Due to their similarity, both charging methods are grouped together as triboelectric charging [7].

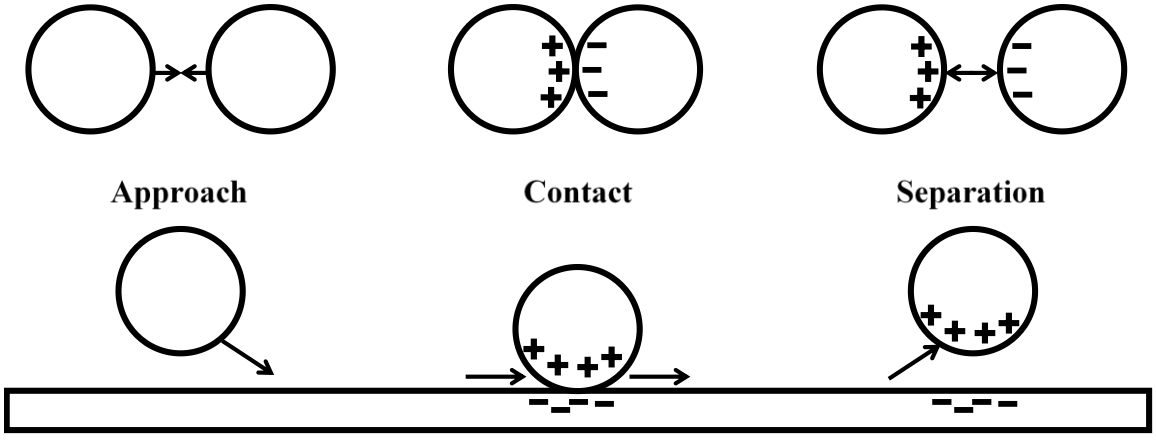

Figure 1-1: Triboelectric charging by contact (top) and friction (bottom).

Charging can also occur without any actual contact between the two objects, with a mechanism known as induction charging. When an already charged object comes near another uncharged conductive object, its electric field makes the uncharged object become polarized by shifting all the electrons to one side of the object. This is known as image charging since the charged particle leaves an oppositely charged "image" on the surface of the uncharged object (Figure 1-2). If the uncharged object is initially grounded, it will be left with a net charge if the ground is removed. In theory, induction charging can only happen with conductive materials since they have mobile electrons. Thus, the charge separation shown in Figure 1-2 should not occur for insulators; the electrons would be immobile and grounding cannot occur [6]. However, recent studies have shown that this mechanism is possible even for non-conductive materials, provided the two materials are close to each other for an extended period of time [8].

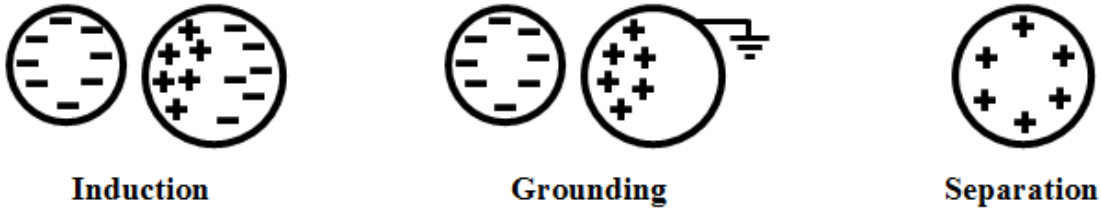

Figure 1-2: Charging by induction, generating a positive charge on a metal object.

The concepts of charging are well-studied and understood for conductive materials because of their low resistivity to current flow, which allows the transfer (and generation) of charge. Insulators, however, are more difficult to study since they have low charge mobility. This limits the triboelectric charging to localised surfaces of an object, usually in the microscopic range. This localised charging nature of insulators makes it very difficult to predict the electrostatic effects on non-spherical particles, such as polymers [9].

Extensive studies have been performed on the triboelectric charging tendencies of many materials by comparing their charge polarities [6,10–12]. These findings are usually arranged as a triboelectric series, where the materials with the highest tendency to become positively charged are placed on top, and the materials with the highest tendency to become negatively charged are placed on the bottom. The series is also analogous to the work functions of conductors, which is an inherent material property describing the amount of thermodynamic work required to eject an electron from the material surface to a neutral point in vacuum near the surface. A material with a

higher work function has a higher probability of holding electrons at its surface. The difference in work functions between two contacting metal objects is well known to be the driving force for electron transfer from one surface to another. The flow of electrons across the contacting interface occurs until equilibrium is reached [13], and the contact potential difference, V_C, can be determined as follows:

$$V_C = \frac{(\phi_1 - \phi_2)}{e} \qquad 1\text{-}3$$

where ϕ_1 and ϕ_2 are the work functions of the two metals/conductors, and e is the elementary charge. A visual representation of this equation is shown in Figure 1-3.

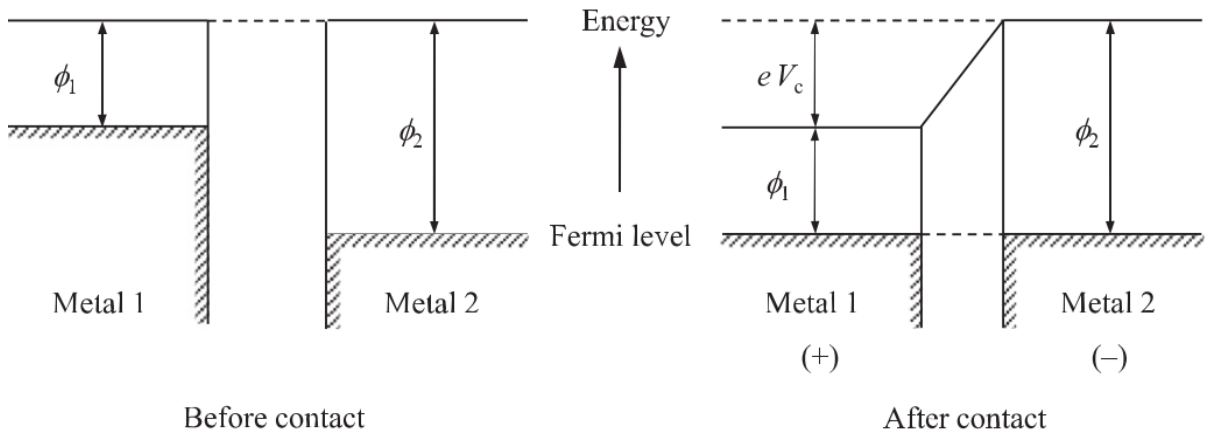

Figure 1-3: Electron potential energy for metal-metal contacts [7].

While this work function model should not be applicable for metal-insulator or insulator-insulator contacts due to the lack of "free electrons" in insulators, clear evidence of electron transfer in such contacts have been experimentally observed [14,15]. Thus, it was possible to determine the "effective" work function for polymers, shown in Table 1-1 via metal-polymer contacts [16].

Table 1-1: Work functions of various polymers [16].

Material	Work Function (eV)
Polyethylene	5.24 ± 0.24
Polyethylene (var.)	6.04 ± 0.47
Polytetrafluoroethylene	6.71 ± 0.26
Polypropylene	5.43 ± 0.16
Nylon 6/6	4.08 ± 0.06

In order to explain this charge transfer due to metal-insulator contacts, the surface state model has been proposed where it is assumed that the available energy levels of electrons are only on the surface as opposed to the bulk of the object [17]. As such, an insulator metal contact, and similarly an insulator-insulator contact, would result in electrons moving from the filled surface states of one material to the empty surface states of the other. This means the driving force for electron transfer is still the difference in work functions of the two contacting surfaces. The surface of insulators can be composed of positively or negatively charged nanoscopic regions, where the surface charge in a specific region is much larger than the net charge of the insulator [18]. This mosaic nature of surface charge has been observed in contact electrification experiments as shown in Figure 1-4, where a polycarbonate (PC) surface obtained a net negative charge after contacting a polydimethylsiloxane (PDMS) surface. Another possible explanation for electron transfer with insulator contact is the presence of impurities including side groups, surface impurities and ends of molecular chains. This conclusion was made based on a study where pure samples of crystalline insulators showed no charging when contacted by metals [19]. Impurities or surface/chemical defects on a material surface can therefore alter its effective work function, which would result in a range of values for any given material based on its production process.

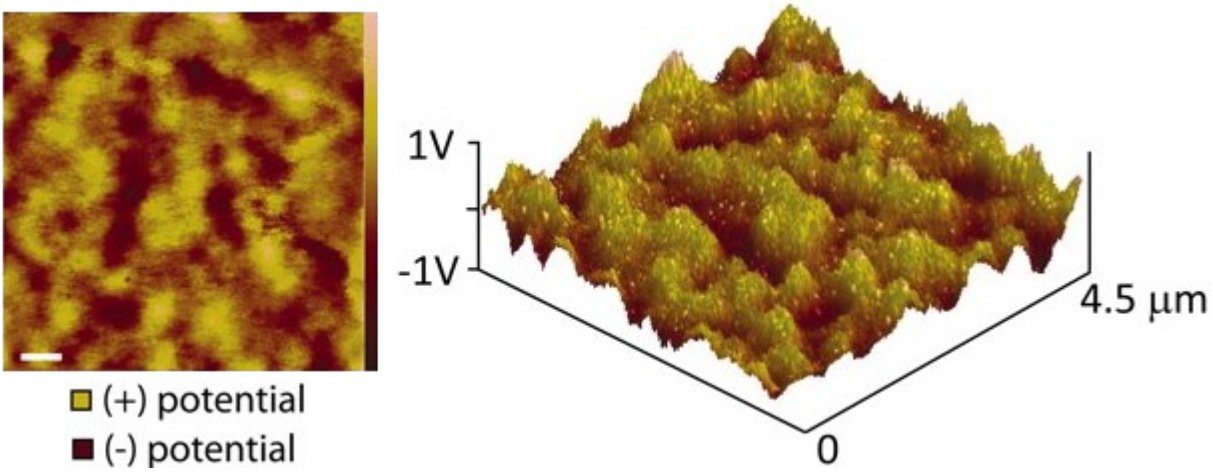

Figure 1-4: 2D and 3D Potential maps of a PC surface contact-charged by a PDMS surface [18].

1.1.2. Charge Transfer Modeling

The electrostatic charging tendencies of various materials have been extensively studied in bench-scale insulator-metal contact experiments [20–25]. In addition to effective work function differences, other factors were found to be involved in charge transfer include impact velocity and

angle, initial charge, particle size, temperature, and relative humidity [7]. The effects of varying operating conditions have only been analyzed qualitatively thus far, whereas the material properties and collision characteristics have been incorporated into charge transfer models to estimate the rate of charge transfer per collision or contact duration. One widely utilized charge transfer model is the condenser (or capacitor) model, which assumes that the contact area between two surfaces, S_c, can be regarded as a capacitor. It uses the effective work function difference, V_c, as the fixed driving force for the magnitude and direction of charge transfer on one particle [26]:

$$\Delta q = k_c \frac{\varepsilon_0 \varepsilon_r}{z_c} V_c \left(1 - \frac{q_i}{q_\infty}\right) S_c \qquad 1\text{-}4$$

Here, k_c is the charging efficiency, ε_0 is the absolute permittivity, ε_r is the relative permittivity of the medium, z_c is the critical gap, q_i is the particle's initial charge, and q_∞ the charge saturation point or the maximum charge a particle can hold. This model as well as other proposed charging models will be reviewed in Chapter 7. Charging models were found to provide a reasonable description of electrostatic charge transfer in insulator-metal contacts. However, this is only possible if one could identify the effective work functions and charge saturation points of the concerned materials through bench-scale charge transfer experiments.

Unlike insulator-metal contact charging, the charging behaviour of insulator-insulator collisions is still poorly understood, especially for the case of collisions in granular flows. Lacks and Shinbrot (2019) reviewed the complexity of triboelectric charging in granular materials, which sometimes even defied our qualitative understanding of electrostatics [27]. This means that while the condenser model could be utilized to model particle-particle collisions of different materials, additional model considerations are needed for collisions between particles made of the same material, as further highlighted in Chapter 6. As such, particle-particle contact charging experiments must be performed to develop an empirical charging model that better represents the inter-particle charging behaviour of granular insulators. Charge transfer experiments for particle-particle collisions were performed with bulk particle systems which highlighted the segregation of charge based on particle size [28–31]. However, individual particle-particle collision experiments have not been explored, which are necessary to identify the material or electrostatic properties responsible for the complex particle-particle charging behaviours discussed in-depth in Chapter 7.

1.2. Electrostatic Charging in Gas-Solid Fluidized Beds

Electrostatic charge generation is an inherent and economically detrimental issue in gas-solid fluidized beds, particularly in the production of polyethylene. Triboelectric charging in fluidized beds occurs due to the continuous particle-wall and particle-particle contacts during the fluidization process. In the case of the polyethylene reactors, polyethylene and catalyst particles can become highly charged very quickly, which results in them adhering to the reactor wall. As the adhered particles accumulate, the poor circulation of these particles and the highly exothermic reaction on the catalyst surface causes localised temperature spikes that melts the polyethylene particles into large sheets. Such sheets can be up to a 1 cm thick, over 50 cm wide and up to 1.5 m long [3]. They are found to form at approximately half the diameter of the fluidizing column above the distributor plate, where the drag forces along the column wall are at a minimum, and are also found to droop off the dome of the reactor [32]. These sheets can break off the reactor walls and obstruct the distributor plate, forcing a reactor shut-down even within a few hours of operation for clean-up [3]. The downtime due to the clean-up can result in significant economical loss due to reduced production. The reactor shut-down may take up to 30 days or even more depending on the severity of the sheeting. To put in perspective the magnitude of missed revenue due to such a lengthy reactor shut-down, a rudimentary cost analysis was considered. A single polymerization reactor can have a production capacity of at least 600,000 tons per year [33]. In 2011, when the polyethylene market (specifically LLDPE, or linear low-density polyethylene) was quite weak, the profit margin for producing and selling LLDPE was reported to be 374 USD per ton [34]. A 30-day reactor shutdown could therefore result in at least 18,700,000 USD in missed profits.

Extensive studies have been performed to understand the cause of wall fouling in gas-solid fluidized beds. This has lead to the development of various charge measurement techniques [35–37] as well as methods for controlling the electrostatic charge and its effects in the fluidized bed [4,38,39]. Current measurement techniques employed in labs as well as the industry use either electrostatic probes or Faraday cups (Figure 1-5). Electrostatic probes are widely used in industry as a means of measuring the charge at specific points in gas-solid fluidization columns. When a charged object is brought in close proximity to an electrostatic probe, the object can induce an image charge of itself on the probe. This induced signal is measured using an electrometer as an electric potential, current, or charge. In order to detect the onset of wall sheeting on the polyethylene reactor described earlier, electrostatic probes are inserted into the column at locations

which are prone to sheet formation [4]. However, this method of charge detection is still unreliable since the probe measurements can be distorted by contacts between the probe and the particles, and even due to particle accumulation on the probe itself.

Faraday cups are used to measure the net charge of objects that are placed inside it. They consist of two metal cups which are electrically isolated from each other with an insulative material. The outer cup is grounded to shield the inner cup from any external electric field, and by connecting the inner cup to an electrometer the charge of any object that interacts with it can be measured [6]. Faraday cup measurement techniques can be used to measure the bulk net charge of sampled particles in gas-solid fluidized beds. While the net charge measurements are generally reliable, it is difficult to measure the charge of the fluidizing particles in real-time. Sampling ports would only provide a local measurement, which may not reflect the overall charging within the entire bed. Faraday cup measurement techniques are thus better suited for use in experimental studies.

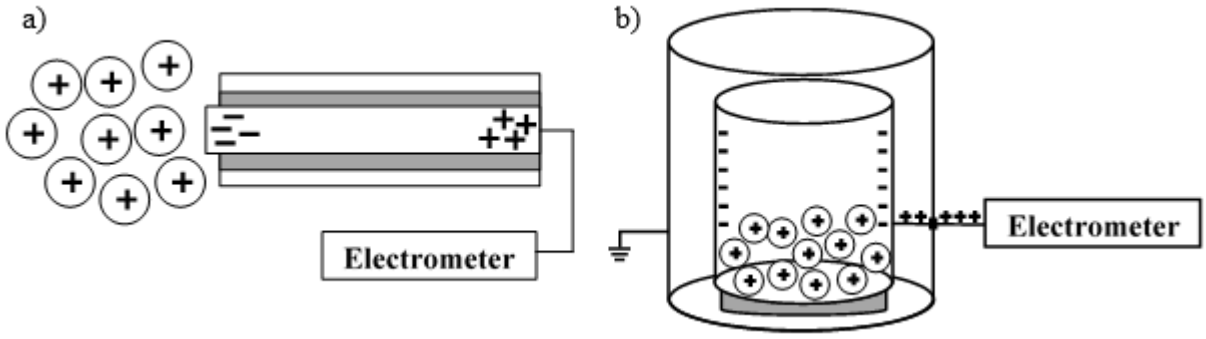

Figure 1-5: (a) Electrostatic probe measurement technique, (b) Faraday cup measurement technique.

There are currently two main methods used in the industry to control electrostatic charging: coating the inner column wall with polymer films [3,4], and injecting the charged bed with an inert, charge neutralizing additive (e.g. positive charging agent into a negatively charged bed) [35]. While both methods have helped combat sheeting on the reactor walls, they have their disadvantages. The coating method requires intermittent reactor shut-downs to reapply the film, whereas the injection method does not actually stop sheeting from happening as it is a reactionary measure; the additive required is dependent on the electrostatic state of the bed.

1.2.1. Effect of Operating Parameters on Electrostatics

The operating parameters of a fluidized bed system, such as the fluidizing gas velocity, particle size, temperature, pressure, and relative humidity, can affect the amount of charge generation in the bed. The fluidizing gas velocity has a significant effect on the degree of charge generation in a fluidized bed, as it directly correlates with the rate of particle-wall and particle-particle interactions [40,41]. It was observed that the bubbling flow regime generated the most amount of particle charge in the fluidized bed, as the rising bubbles induced particle mixing [32,38]. As such, larger bubble sizes and rising velocities, which comes with increasing fluidizing gas velocities, induce more particle mixing and thereby increase the amount of charge measured in the bed [41–43]. This aligns with the finding that, with increasing gas velocity, a maximum degree of bed electrification is reached at the onset of the slug-flow regime, after which, the degree of electrification starts to decline [44]. However, recent studies have shown that increasing the fluidizing gas velocity all the way to the turbulent flow regime significantly increases charging in a bed of polyethylene particles compared to a bubbling flow regime [45]. Apart from the increased frequency of particle-wall impacts in the turbulent flow regime, the lack of bubbles to induce particle-particle collisions is compensated by the increased entrainment rate of fine particles. These entrained fines tended to charge negatively, and so their entrainment left the bulk of the bed in a net positive charge and resulted in increased wall fouling [45].

Particle sizes as well as particle size distributions have been studied to understand their impact on fluidized bed electrification. In mono-sized particle systems, i.e. systems with a very narrow particle size distribution, it was observed that an increase in particle size directly correlated to an increase in charge generated in the fluidized bed [41,46,47]. However, in polymerization fluidized bed reactors the fluidizing particles generally have a large size distribution, which leads to a phenomenon known as bipolar charging. This occurs when particles of the same material, but different sizes, become oppositely charged during fluidization [8]. In a charged particle separation study performed by this research group on fluidized polyethylene particles, narrow particle size ranges which charged predominantly in one direction still exhibited some bipolar charging [48]. The mechanism to describe bipolar charging is unclear, since the studies on poly-sized particle systems have shown conflicting results; some noted that the smaller particles charged negatively and the larger particles charged positively [8,49,50], while others have reported the opposite

[37,43,51]. Nonetheless, this phenomenon is an important factor in the positive-negative particle charge layering on the column wall.

Temperature studies have shown that electrostatic charges in the bed decreased when increasing the temperature from 25°C to up to 75°C [52,53]. This is in agreement with single particle charging experiments where the particle consistently measured less charge at higher temperatures [54]. The effects of pressure on charging is more difficult to assess in a fluidized bed while controlling the other parameters since pressurizing has a complex impact on the hydrodynamics of the bed [43]. Nonetheless, pressure controlled experiments have shown that there is an increase in charge generation with increasing pressures from 100 to 800 kPa [52], which justifiably leads to an increase in wall fouling in pressurized (up to 2500 kPa) fluidized beds [55,56]. Finally, single particle impact experiments with a control on the relative humidity have shown that the amount of charge generated is reduced with increasing relative humidity, regardless of the particle temperature [54]. This direct correlation was not observed in a study with glass beads fluidized in an acrylic column which showed a reduction in charging after a certain relative humidity [41]. In agreement to this study, another fluidization study on humidity effects using polyethylene in a stainless steel column showed that, at the bubbling flow regime, the degree of wall fouling only started to reduce after a relative humidity of 60% [57].

1.3. Modeling & Simulation of Gas-Solid Fluidized Beds

With the continuous advances in computing technology, CFD modeling has become essential in the systematic investigation and development of fluid flow processes [58]. CFD simulations are an excellent tool for analyzing fluid flows in industrial processes, since the alternative would be to perform all the necessary testing in pilot-scale systems, driving up costs and greatly increasing the time needed for scale-up. Industrial fluidized beds tend to be very large units, their size being of the order of cubic meters. However, the vital particle-particle and fluid-particle interactions in these devices occur at scales of the order of millimeters or smaller. It is therefore clear that a multiscale approach must be developed, based on the required level of detail [59].

There are two ways to describe the dynamics of the phases in a system: Eulerian models that describe the phases as continua, using conservation equations; and Lagrangian models, which describe the phases as a collection of discrete particles that obey Newton's Second Law of Motion.

When modeling gas-solid fluidized beds, the solid and gas phases are considered separately, and so the available coupled-system models can be classified based on all the possible combinations of these two models. Table 1-2 lists the widely recognized models used for simulating gas-solid fluidized beds.

Table 1-2: Various models for simulating gas-solid fluidized beds [59].

Model Name	Gas Phase	Solid Phase
1. Two-Fluid Model	Eulerian	Eulerian
2. Unresolved Discrete Particle Model	Eulerian (unresolved)	Lagrangian
3. Resolved Discrete Particle Model	Eulerian (resolved)	Lagrangian

A visual representation of the models is shown in Figure 1-6. The two-fluid model (TFM) is an Euler-Euler (EE) method that uses the continuum description for both the solid and gas phases; for each phase a continuity equation and a momentum equation need to be solved. The fluid-dynamic properties of the granular phase are usually determined by means of closures obtained from the kinetic theory of granular flow. Since the model is constituted by a set of coupled partial differential equations, its solution is typically obtained with numerical methods, particularly the finite volume method, to guarantee conservation of the transported quantities [60].

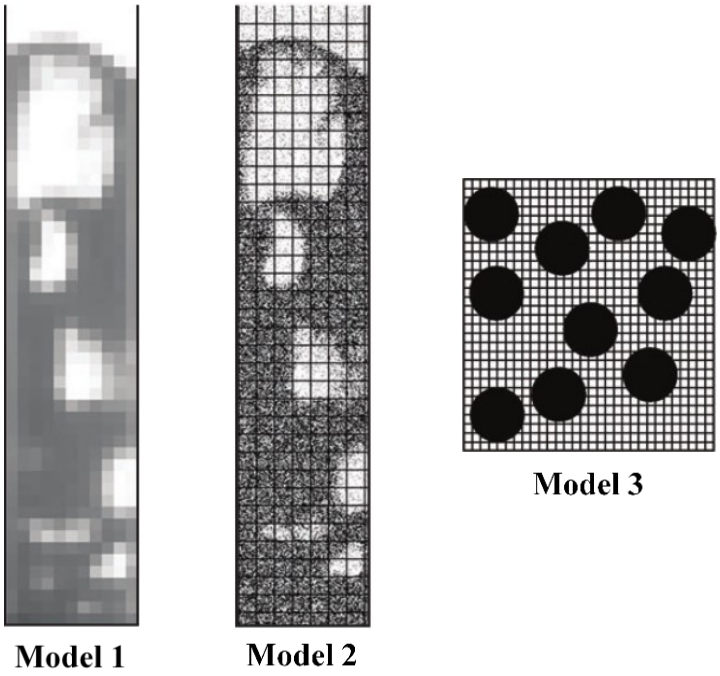

Figure 1-6: Visual representation of the models listed in Table 1-2 [59].

While TFM models the particle-particle or particle-gas interactions in terms of momentum transfer between both phases, the Discrete Particle Models (DPM) describe the solid phase as actual particles. The solid phase is solved using Newton's Second Law of Motion, where the interaction with the continuous gas phase is dependent on the size of the particles with respect to the Eulerian grid. In the Unresolved Discrete Particle Model (UDPM), also known as the discrete element model (DEM), the grid is at least 10 times larger than the particles. In terms of the gas-particle interactions, this reduces the particles to point sources and momentum sinks and gas-solid interaction correlations similar to the TFM method is needed [59]. In the Resolved Discrete Particle Model (RDPM), also known as the direct numerical simulation (DNS) model, the grid is at least 10 times smaller than the particles, allowing the calculation of the flow between the particles. No correlations are required in this case since the gas-particle interactions are handled by boundary conditions at the solid particle surfaces. The modeling of gas-solid fluidized beds is currently most developed for TFM [61,62], UDPM [63,64] and RDPM [65].

1.3.1. Electrostatic Modeling

Electrostatic effects in gas-solid flow have been studied using both Euler-Lagrange and Euler-Euler models. The effect of electrostatic charge on particle elutriation was investigated using an Euler-Lagrange model with a fixed charge input [66]. The study showed that electrostatic charges on particles suppressed or even eliminated particle elutriation due to the agglomeration caused by electrostatic attraction. An Euler-Lagrange model was developed to study the effect of electrostatic forces between mono-charged and bipolar charged particles on fluidization hydrodynamics [67]. Mono-charged particles showed a decrease in bubble sizes and increase in bed voidage, which is in good agreement with experimental results [64], whereas bipolar charged particles exhibited the same hydrodynamics as a neutral bed. An Euler-Euler model was developed to investigate the influence of electrostatic charges on bubbles in freely-bubbling fluidized beds with charged mono-sized glass beads [68]. The simulation results predicted that electrostatic charges decrease bubble size and influence the bubble spatial distribution as well as the time-average solid velocities. Another Euler-Euler model was developed for a pilot-scale gas-solid fluidized bed that incorporated electrostatic effects [69]. Using a fixed charge-to-mass ratio for particles obtained from experimental results of this research group [51], the model reproduced trends in particle segregation, entrainment and wall fouling, as shown in Figure 1-7, due to electrostatic charges as

seen in the fluidized bed experiments [5]. All these simulation studies used a fixed charge value to study the electrostatic interactions in gas-solid fluidized beds.

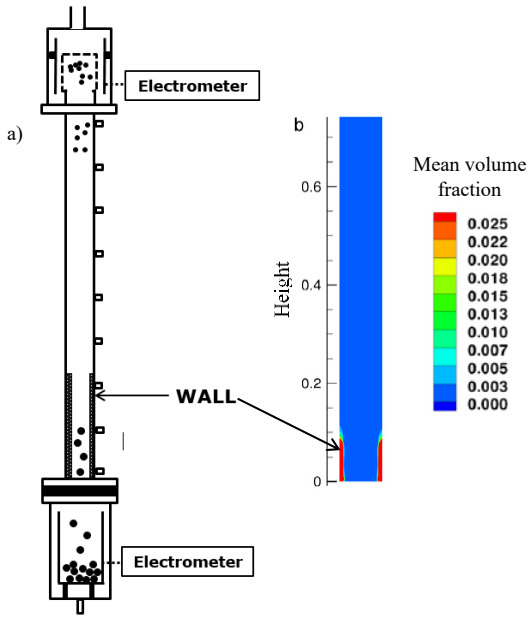

Figure 1-7: Comparison of wall-fouling observed in a) experiments and b) simulation [51,69].

To simulate the transient case for these systems, which is necessary for the model's development as a predictive tool, a charge transfer model is needed to update the electrostatic charge in the system upon any particle-particle and particle-wall contacts. Several studies have implemented the widely accepted condenser model for charge transfer into Euler-Lagrange simulations of particle-particle and particle-wall interactions [70–73]. However, these CFD models are only computationally feasible for millimeter-scale domains and cannot be used to simulate industrial-scale or even laboratory-scale gas-solid fluidized beds. As such the charge transfer model needs to be incorporated into the less computationally intensive Euler-Euler model.

1.4. Thesis Objective

The overall objective for this study was to develop an Euler-Euler CFD model to study the electrostatic charging of industrial-scale gas-solid fluidized beds, with particular interest in the polyethylene production process. Such a model could also be used as a predictive tool in any application of gas-solid flows, including pneumatic conveying and duct flow systems. The primary challenge of developing this Eulerian model is that the charge transfer model currently used in numerical studies is tailored for discrete particles; the charge is transferred only between two

distinct particles at a time. Since Eulerian models do not have a discrete particle phase, a solution is needed to determine the change in the volume-averaged particle charge densities over time within every cell of the simulation domain. Moreover, many charge transfer studies over the years have reported that the charging model currently used in CFD simulations cannot accurately predict the observed particle charging behaviours in gas-solid flows, particularly for particle-particle collisions [27]. The charge transfer model thus needs to be modified and validated using fundamental particle-wall and particle-particle contact charging experiments. Once confirmed, it can be implemented into the Euler-Euler CFD model to study the electrostatic charging of industrial-scale gas-solid fluidized beds. Thus, the specific objectives of this study were to:

1. Develop an electrostatic charging model compatible with Euler-Euler Two-Fluid CFD models for gas-solid flow systems.
    a. Determine a solution using the existing charge transfer model to determine the change in volume-averaged particle charge densities over time in an Eulerian context.
    b. Validate the CFD model by simulating laboratory-scale fluidization experiments and evaluating the predicted degree of charging and bed behaviour.
2. Develop novel apparatus designs and perform bench-scale particle collision experiments to observe the charging behaviour of insulative particles in various collision scenarios.
    a. Perform single and repeated particle-wall collision experiments to validate the particle-wall charge transfer model and extract the necessary input parameters for simulation.
    b. Perform single particle-particle collision experiments to confirm whether the charge transfer model currently used in CFD simulations is acceptable for predicting experimentally observed inter-particle charging behaviour.

1.5. Thesis Outline

The thesis is divided into eight chapters, where six chapters are prepared in manuscript form for publication in refereed journals. These chapters describe the experimental studies and model development process in chronological order. A publication relevant to the research is also included in Appendix A, and additional supporting information is presented in Appendix B.

The second chapter presents the Euler-Euler CFD model developed to consider electrostatic charging and its effects on bed hydrodynamics for mono-dispersed, or single-sized, particles. Provided with the input parameters from experiments, such as charge saturation values for particles of varying sizes, the model was validated using past laboratory-scaled fluidization studies on the charging and wall fouling behaviour of polyethylene resins sieved into narrow particle-size distributions. This chapter is a manuscript published in Chemical Engineering Science (*Ray M, Chowdhury F, Sowinski A, Mehrani P, Passalacqua A. An Euler-Euler model for mono-dispersed gas-particle flows incorporating electrostatic charging due to particle-wall and particle-particle collisions. Chem Eng Sci. 2019; 197:327-344*).

The third chapter describes the single and repeated particle-wall collision experiments performed to validate the particle-wall charging model and extract input parameters needed to perform the abovementioned CFD studies. This chapter is a manuscript published in Journal of Electrostatics (*Chowdhury F, Sowinski A, Ray M, Passalacqua A, Mehrani P. Charge generation and saturation on polymer particles due to single and repeated particle-metal contacts. J Electrostat. 2018; 91:9-15*).

The fourth chapter describes a novel particle-particle collision apparatus designed and tested to perform particle-particle charging experiments. This apparatus was the first of its kind and allowed the analysis of particle charging behaviour due to individual particle collisions. This chapter is a manuscript published in Powder Technology (*Chowdhury F, Elchamaa B, Ray M, Sowinski A, Passalacqua A, Mehrani P. Apparatus design for measuring electrostatic charge transfer due to particle-particle collisions. Powder Technol. 2020; 361:860-866*). This work was motivated by the simulation results observed in the Eulerian model for mono-dispersed particles, which highlighted the importance of developing an empirical particle-particle charging model. The study was performed in parallel to the continued development of the electrostatic model to also consider bi-dispersed particle flows (i.e., two particle phases of varying sizes). As presented in Appendix A, this developed model is discussed in a manuscript published in Physics of Fluids (*Ray M, Chowdhury F, Sowinski A, Mehrani P, Passalacqua A. Eulerian modeling of charge transport in bi-disperse particulate flows due to triboelectrification. Phys Fluids. 2020; 32(2):023302*).

The fifth chapter presents the continued development of the particle-particle collision apparatus, with particular improvements to the particle release mechanism. Charge transfer observations are

discussed based on various particle collision scenarios, including collisions between different-sized particles made of the same material. The results are further evaluated with respect to the initial charge, impact velocity and angle for each collision trial. This chapter is a manuscript published in Powder Technology (*Chowdhury F, Ray M, Passalacqua A, Mehrani P, Sowinski A. Electrostatic charging due to individual particle-particle collisions. Powder Technol. 2021; 381:352-365*). Images of the apparatus is presented in Appendix B.

The sixth chapter describes the evaluation of the particle-particle charge transfer model currently proposed in CFD simulations as it is used to predict the charge transfer behaviour observed in different particle collision scenarios based on work function differences, initial charges, and effective contact areas. It highlights the major discrepancies in the direction of charge transfer between the modeled and measured results, confirming the necessity for developing a more accurate particle-particle charging model. This chapter is a manuscript under review for publication in the Journal of Electrostatics (*Chowdhury F, Ray M, Passalacqua A, Mehrani P, Sowinski A. Evaluating the electrostatic charge transfer model for particle-particle interactions. J Electrostat. Manuscript ID: ELSTAT-S-21-00078*).

The seventh chapter provides an overview of the research progress made over the years, and particularly during the timeline of this research, on the modelling of electrostatic charging in gas-solid flows. The review highlights the different charging behaviours observed due to varying impact conditions and solids surface properties that need to be included in the model, such as bipolar charging in same material collisions. The Euler-Lagrange and Euler-Euler electrostatic models developed by multiple research groups are also discussed, providing insights on factors such as simulation setup and input parameters to consider for the simulation while highlighting shortcomings that need to be addressed. This chapter is a manuscript under review for publication in Powder Technology (*Chowdhury F, Ray M, Sowinski A, Mehrani P, Passalacqua A. A review on the modeling of electrostatic charging in gas-solid flows, Powder Technol. Manuscript ID: POWTEC-D-20-03376R1*).

The final chapter, chapter eight, presents the overall conclusions of this research and provides recommendations for future work on experimental studies as well as model development for electrostatic charging.

References

[1] D. Kunii, O. Levenspiel, Fluidization Engineering., Second, Butterworth-Heinemann, Newton, USA, 1991.

[2] P. Mehrani, M. Murtomaa, D.J. Lacks, An overview of advances in understanding electrostatic charge buildup in gas-solid fluidized beds, J. Electrostat. 87 (2017) 64–78.

[3] B.D. Fulks, S.P. Sawin, C.D. Aikman, J.M. Jenkins, Process for reducing sheeting during polymerization of alpha-olefins, US 4532311 A, 1985.

[4] R.O. Hagerty, M.E. Muhle, A.K. Agapiou, C.-T.I. Kuo, M.G. Goode, F.D. Hussein, R.B. Pannell, J.F. Szul, Method for Controlling Sheeting in Gas Phase Reactors, 2005/0148742 A1, 2011.

[5] R.G. Rokkam, a. Sowinski, R.O. Fox, P. Mehrani, M.E. Muhle, Computational and experimental study of electrostatics in gas-solid polymerization fluidized beds, Chem. Eng. Sci. 92 (2013) 146–156.

[6] J. Cross, Electrostatics: Principles, Problems and Applications, Adam Hilger, Bristol, 1987.

[7] S. Matsusaka, H. Maruyama, T. Matsuyama, M. Ghadiri, Triboelectric charging of powders: A review, Chem. Eng. Sci. 65 (2010) 5781–5807.

[8] F. Sharmene Ali, M. Adnan Ali, R. Ayesha Ali, I.I. Inculet, Minority charge separation in falling particles with bipolar charge, J. Electrostat. 45 (1998) 139–155.

[9] M. Sow, R. Widenor, A. Kumar, S.W. Lee, D.J. Lacks, R.M. Sankaran, Strain-Induced Reversal of Charge Transfer in Contact Electrification, Angew. Chemie Int. Ed. 51 (2012) 2695–2697.

[10] D.J. Montgomery, Static Electrification of Solids, Solid State Phys. 9 (1959) 139–197.

[11] V.J. Webers, Measurement of triboelectric position, J. Appl. Polym. Sci. 7 (1963) 1317–1323.

[12] M.W. Williams, Effect of Polymer Structure on its Triboelectric Properties, IEEE Trans. Ind. Appl. IA-12 (1976) 213–219.

[13] W.R. Harper, The Volta Effect as a Cause of Static Electrification, Proc. R. Soc. A Math. Phys. Eng. Sci. 205(1080) (1951) 83–103.

[14] D.K. Davies, Charge generation on dielectric surfaces, J. Phys. D. Appl. Phys. 2 (1969) 1533–1537.

[15] Y. Murata, S. Kittaka, Evidence of Electron Transfer as the Mechanism of Static Charge Generation by Contact of Polymers with Metals, Japanese J. Appl. Physics, Part 1 Regul. Pap. Short Notes Rev. Pap. 18 (1979) 421.

[16] K. Tanoue, H. Masuda, Electrostatic Separation, in: Powder Technol. Handb., 3rd ed., CRC Press LLC, 2006.

[17] G.S.P.S.P.P. Castle, L.B.B. Schein, General model of sphere-sphere insulator contact electrification, J. Electrostat. 36 (1995) 165–173.

[18] H.T. Baytekin, A.Z. Patashinski, M. Branicki, B. Baytekin, S. Soh, B.A. Grzybowski, The mosaic of surface charge in contact electrification, Science (80-.). 333 (2011) 308–312.

[19] J. Lowell, A.C.C. Rose-Innes, Contact Electrification, Adv. Phys. 29 (1980) 947–1023.

[20] T. Matsuyama, H. Yamamoto, Impact charging of particulate materials, Chem. Eng. Sci. 61 (2006) 2230–2238.

[21] T. Itakura, H. Masuda, C. Ohtsuka, S. Matsusaka, The contact potential difference of powder and the tribo-charge, J. Electrostat. 38 (1996) 213–226.

[22] S. Matsusaka, H. Masuda, Electrostatics of particles, Adv. Powder Technol. 14 (2003) 143–166.

[23] A. Ema, D. Yasuda, K. Tanoue, H. Masuda, Tribo-charge and rebound characteristics of particles impact on inclined or rotating metal target, Powder Technol. 135–136 (2003) 2–13.

[24] P.M. Ireland, Triboelectrification of particulate flows on surfaces: Part I — Experiments, Powder Technol. 198 (2010) 189–198.

[25] H. Watanabe, M. Ghadiri, T. Matsuyama, Y.L. Ding, K.G. Pitt, H. Maruyama, S. Matsusaka, H. Masuda, Triboelectrification of pharmaceutical powders by particle impact, Int. J. Pharm. 334 (2007) 149–155.

[26] S. Matsusaka, M. Ghadiri, H. Masuda, Electrification of an elastic sphere by repeated impacts on a metal plate, J. Phys. D. Appl. Phys. 33 (2000) 2311–2319.

[27] D.J. Lacks, T. Shinbrot, Long-standing and unresolved issues in triboelectric charging, Nat. Rev. Chem. 3 (2019) 465–476.

[28] M.A. Bilici, J.R. Toth, R.M. Sankaran, D.J. Lacks, Particle size effects in particle-particle triboelectric charging studied with an integrated fluidized bed and electrostatic separator system, Rev. Sci. Instrum. 85 (2014).

[29] K.M. Forward, D.J. Lacks, R. Mohan Sankaran, Methodology for studying particle-particle triboelectrification in granular materials, J. Electrostat. 67 (2009) 178–183.

[30] S.R. Waitukaitis, V. Lee, J.M. Pierson, S.L. Forman, H.M. Jaeger, Size-dependent same-material tribocharging in insulating grains, Phys. Rev. Lett. 112 (2014) 1–5.

[31] A. Sowinski, A. Mayne, P. Mehrani, Effect of fluidizing particle size on electrostatic charge generation and reactor wall fouling in gas–solid fluidized beds, Chem. Eng. Sci. 71 (2012) 552–563.

[32] G. Hendrickson, Electrostatics and gas phase fluidized bed polymerization reactor wall sheeting, Chem. Eng. Sci. 61 (2006) 1041–1064.

[33] I. Burdett, New innovations drive gas phase PE technology, Hydrocarb. Eng. 13 (2008) 67–76.

[34] J. Richardson, Polyethylene Pricing, Profits In 2017: Three Scenarios (2016). http://www.icis.com/blogs/asian-chemical-connections/2016/12/polyethylene-pricing-profits-in-2017-three-scenarios (accessed August 22, 2017).

[35] M.G. Goode, D.M. Hasenberg, T.J. Mcneil, E. Spriggs, Method for reducing sheeting during polymerization of alpha-olefins, 1989.

[36] M. Murtomaa, E. Räsänen, J. Rantanen, A. Bailey, E. Laine, J.-P. Mannermaa, J. Yliruusi, Electrostatic measurements on a miniaturized fluidized bed, J. Electrostat. 57 (2003) 91–106.

[37] P. Mehrani, H.T. Bi, J.R. Grace, Electrostatic charge generation in gas–solid fluidized beds, J. Electrostat. 63 (2005) 165–173.

[38] A.H. Park, H. Bi, J.R. Grace, Reduction of electrostatic charges in gas-solid fluidized beds, Chem. Eng. Sci. 57 (2002) 153–162.

[39] K. Dong, Q. Zhang, Z. Huang, Z. Liao, J. Wang, Y. Yang, Experimental investigation of electrostatic reduction in a gas-solid fluidized bed by an in situ corona charge eliminator, Ind. Eng. Chem. Res. 53 (2014) 14217–14224.

[40] J. Ciborowski, A. Wlodarski, On electrostatic effects in fluidized beds, Chem. Eng. Sci. 17 (1962) 23–32.

[41] J. Guardiola, V. Rojo, G. Ramos, Influence of particle size, fluidization velocity and relative humidity on fluidized bed electrostatics, J. Electrostat. 37 (1996) 1–20.

[42] V. Rojo, J. Guardiola, A. Vian, A capacitor model to interpret the electric behaviour of fluidized beds. Influence of apparatus geometry, Chem. Eng. Sci. 41 (1986) 2171–2181.

[43] Z. Liu, X.T. Bi, J.R. Grace, Electrostatic charging behaviour of dielectric particles in a pressurized gas-solid fluidized bed, J. Electrostat. 68 (2010) 321–327.

[44] A. Gajewski, Investigation of the electrification of polypropylene particles during the fluidization process, J. Electrostat. 16 (1985) 219.

[45] D. Song, P. Mehrani, Comparison of electrostatic charge generation in gas-solid fluidized beds in turbulent versus pre-turbulent flow regime, Powder Technol. 319 (2017) 426–433.

[46] D. Boland, D. Geldart, Electrostatic charging in gas fluidised beds, Powder Technol. 5 (1972) 289–297.

[47] L. Fasso, B.T. Chao, S.L. Soo, Measurement of electrostatic charges and concentration of particles in the freeboard of a fluidized bed, Powder Technol. 33 (1982) 211–221.

[48] A. Sowinski, The Study of Reactor Wall Fouling in Gas-Solid Fluidized Beds Caused by Electrostatic Charge Generation, University of Ottawa, 2012.

[49] K.M. Forward, D.J. Lacks, R.M. Sankaran, Triboelectric charging of granular insulator mixtures due solely to particle - Particle interactions, Ind. Eng. Chem. Res. 48 (2009) 2309–2314.

[50] H. Zhao, G.S.P. Castle, I.I. Inculet, A.G. Bailey, Bipolar charging of poly-disperse polymer powders in fluidized beds, IEEE Trans. Ind. Appl. 39 (2003) 612–618.

[51] A. Sowinski, L. Miller, P. Mehrani, Investigation of electrostatic charge distribution in gas–solid fluidized beds, Chem. Eng. Sci. 65 (2010) 2771–2781.

[52] W.O. Moughrabiah, J.R. Grace, X.T. Bi, Effects of pressure, temperature, and gas velocity on electrostatics in gas-solid fluidized beds, Ind. Eng. Chem. Res. 48 (2009) 320–325.

[53] T.A. Alsmari, J.R. Grace, X.T. Bi, Effects of superficial gas velocity and temperature on entrainment and electrostatics in gas-solid fluidized beds, Chem. Eng. Sci. 123 (2015) 49–56.

[54] W.D. Greason, Investigation of a test methodology for triboelectrification, J. Electrostat. 49 (2000) 245–256.

[55] D. Song, F. Salama, J. Matta, P. Mehrani, Implementation of Faraday cup electrostatic charge measurement technique in high-pressure gas-solid fluidized beds at pilot-scale, Powder Technol. 290 (2016) 21–26.

[56] D. Song, Study of Electrostatic Charging and Particle Wall Fouling in a Pilot-scale Pressurized Gas-Solid Fluidized Bed up to Turbulent Flow Regime, (2017).

[57] A. Giffin, P. Mehrani, Effect of gas relative humidity on reactor wall fouling generated due to bed electrification in gas-solid fluidized beds, Powder Technol. 235 (2013) 368–375.

[58] T.G. Dobre, J.G.S. Marcano, Chemical Engineering: Modeling, Simulation and Similitude, Wiley, 2007.

[59] M. a. van der Hoef, M. van Sint Annaland, N.G. Deen, J. a. M. Kuipers, Numerical Simulation of Dense Gas-Solid Fluidized Beds: A Multiscale Modeling Strategy, Annu. Rev. Fluid Mech. 40 (2008) 47–70.

[60] D. Gidaspow, Multiphase Flow and Fluidization: Continuum and Kinetic Theory Descriptions, First, Academic Press, 1994.

[61] R. Fan, R.O. Fox, Segregation in polydisperse fluidized beds: Validation of a multi-fluid model, Chem. Eng. Sci. 63 (2008) 272–285.

[62] L. Huilin, H. Yurong, D. Gidaspow, Y. Lidan, Q. Yukun, Size segregation of binary mixture of solids in bubbling fluidized beds, Powder Technol. 134 (2003) 86–97.

[63] B.P.B. Hoomans, J. a. M. Kuipers, W.J. Briels, W.P.M. van Swaaij, Discrete particle simulation of bubble and slug formation in a two-dimensional gas-fluidised bed: A hard-sphere approach, Chem. Eng. Sci. 51 (1996) 99–118.

[64] G.A. Bokkers, M. van Sint Annaland, J.A.M. Kuipers, Mixing and segregation in a

bidisperse gas–solid fluidised bed: a numerical and experimental study, Powder Technol. 140 (2004) 176–186.

[65] T.-W. Pan, D.D. Joseph, R. Bai, R. Glowinski, V. Sarin, Fluidization of 1204 spheres: simulation and experiment, J. Fluid Mech. 451 (2002) 169–191.

[66] Y. Yang, C. Zi, Z. Huang, J. Wang, M. Lungu, Z. Liao, Y. Yang, H. Su, CFD-DEM investigation of particle elutriation with electrostatic effects in gas-solid fluidized beds, Powder Technol. 308 (2016) 422–433.

[67] M.A. Hassani, R. Zarghami, H.R. Norouzi, N. Mostoufi, Numerical investigation of effect of electrostatic forces on the hydrodynamics of gas–solid fluidized beds, Powder Technol. 246 (2013) 16–25.

[68] F. Jalalinejad, X.T. Bi, J.R. Grace, Effect of electrostatics on freely-bubbling beds of mono-sized particles, Int. J. Multiph. Flow. 70 (2015) 104–112.

[69] R.G. Rokkam, R.O. Fox, M.E. Muhle, Computational fluid dynamics and electrostatic modeling of polymerization fluidized-bed reactors, Powder Technol. 203 (2010) 109–124.

[70] J.C.C. Laurentie, P. Traoré, L. Dascalescu, Discrete element modeling of triboelectric charging of insulating materials in vibrated granular beds, J. Electrostat. 71 (2013) 951–957.

[71] M.W. Korevaar, J.T. Padding, M.A. Van der Hoef, J.A.M. Kuipers, Integrated DEM-CFD modeling of the contact charging of pneumatically conveyed powders, Powder Technol. 258 (2014) 144–156.

[72] C. Pei, C.Y. Wu, M. Adams, DEM-CFD analysis of contact electrification and electrostatic interactions during fluidization, Powder Technol. 304 (2016) 208–217.

[73] J. Kolehmainen, A. Ozel, C.M. Boyce, S. Sundaresan, A hybrid approach to computing electrostatic forces in fluidized beds of charged particles, AIChE J. 62 (2016) 2282–2295.

Chapter 2

An Euler-Euler model for mono-dispersed gas-particle flows incorporating electrostatic charging due to particle-wall and particle-particle collisions

M. Ray[a], F. Chowdhury[b], A. Sowinski[b], P. Mehrani[b], A. Passalacqua[a,]

[a] Department of Chemical and Biological Engineering, University of Ottawa, 161 Louis Pasteur, Ottawa, ON, Canada, K1N 6N5
[b] Department of Mechanical Engineering, Iowa State University, 2025 Black Engineering Building Ames, IA, 50011-2161, USA

This chapter is a manuscript published in Chemical Engineering Science (2019; 197:327-344)

Abstract

A computational model for the prediction of triboelectric charging in gas-solid fluidized beds is developed in the context of the Euler-Euler two-fluid model with kinetic theory closures for the description of the particulate phase. Sub-model for charge transfer due to particle-wall collisions is obtained consistently with the boundary conditions of Johnson and Jackson (1987) [1], and assuming the model of Matsusaka et al. (2000) [2] for charge transfer during a single collision. Similarly, a sub-model for charge diffusion due to particle-particle collisions is developed based on the kinetic theory of granular flow of Jenkins and Savage (1983) [3], and the aforementioned charging model. The Eulerian charging model is then coupled to the two-fluid model, with kinetic theory closures which are available in the OpenFOAM® computational toolbox for fluid dynamics. The model is tested to simulate the effect of polyethylene particle size (362, 462, 550 μm) in the electrification process, and is validated against past experimental findings. The order of magnitude of charge densities in different regions of the bed, predicted by the model, was coherent with the experimental results. The model also predicted that particles larger than 425 μm would not stick to the column wall, which acceptably agreed with the experimental observation that particles larger than 600 μm did not adhere to the wall surface.

2.1. Introduction

Gas-solid fluidized beds have been employed in a variety of industrial applications including polymerization, fluid catalytic cracking, mixing, coating and drying, to name just a few. One of the applications of gas-solid fluidized beds is the catalytic polymerization of ethylene gas to produce polyethylene [4]. An operational challenge faced in such processes is the generation of electrostatic charges, which is an inherent issue in gas-solid fluidized beds. Charging in fluidized beds occur due to particle-particle and particle-wall contact charging, a phenomenon known as triboelectrification [5–7]. In polymerization reactors for polyethylene production, the polymer or catalyst particles used in these fluidized bed reactors can, once charged, adhere to the reactor wall. As the adhered particles accumulate, the highly exothermic reaction causes localized temperature spikes that melt the particles into large sheets. The sheets can detach from the reactor walls and obstruct the distributor plate after only a few hours of operation, forcing a reactor shut-down for clean-up operations.

A widely adopted approach to investigate the hydrodynamics in fluidized beds [8–12] is the Euler-Euler two-fluid model [13–16] with kinetic theory closures for the disperse granular phase [3,10,17–21]. Compared to Euler-Lagrange models [22–28], the Euler-Euler model allows to lower the cost of simulations, particularly for large-scale systems operating with dense particle-laden flow. However, the incorporation of models to predict triboelectric charging in models for computational fluid dynamics only started recently. Hassani et al. (2013) [29] developed an Euler-Lagrange model to study the effect of electrostatic forces between mono-charged and bipolar-charged particles on the hydrodynamics of fluidization. Mono-charged particles showed a decrease in bubble sizes and an increase in bed voidage, which was in agreement with experimental results [30]; in the case of bipolar-charged particles, the net charge, which was essentially neutral, governed the hydrodynamics of the system. Yang et al. (2016) [28] investigated the effect of electrostatic charge on particle elutriation using an Euler-Lagrange model with a fixed charge input. Jalalinejad et al. (2015) [31] investigated the influence of electrostatic charges on bubbles in freely-bubbling fluidized beds using an Euler-Euler model with charged mono-sized glass beads. Rokkam et al. (2010, 2010, 2013) [32–34] developed an Euler-Euler model for a pilot-scale gas-solid fluidized bed to study the effect of electrostatics. Using a fixed charge-to-mass ratio for particles obtained from experimental results from Sowinski et al. (2010) [35], the model reproduced trends in particle segregation and entrainment due to electrostatic charges as seen in

the fluidized bed experiments results [34]. All the simulations studies performed by Rokkam et al. used a fixed charge value to study electrostatic interactions in gas-solid fluidized beds. For a more realistic representation of these systems, however, a model accounting for charge generation and transport is needed to describe the triboelectric charge generation due to collisions between a particle and a solid wall, and with other particles.

Matsuyama and Yamamoto (2006) [36] proposed a contact charging model called the charge relaxation model. The model suggests that the separation process of two contacting bodies, rather than the contact itself, dictates the amount of charging experienced by the two bodies. Ireland (2010) [37] proposed a model that considers contact time, velocity, and mode of contact (i.e. bouncing, sliding, and rolling) as the main contributors to the particle-wall charging mechanism. Matsusaka et al. (2010) [38] proposed that the contact region between a particle and a wall can be regarded as a capacitor, and so a short contact time is sufficient to experience charge transfer. According to their model, repeated particle-wall contacts cause the particle to reach a maximum charge value, after which no more charge is acquired. This value is indicated as saturation charge of the particle. This model [38], known as the *condenser model*, while not fundamentally justified, is commonly used to calculate particle-wall charge transfer, due to its agreement with experimental results. Korevaar et al. (2014) [24] proposed a model for contact charging based on the condenser model for pneumatically conveyed powders in an Euler-Lagrange CFD-DEM framework. Their reported simulation results revealed the significant influence of particle-wall interactions on both the spatial distribution of powder in the duct and the acquired charge of the particles [24]. Pei et al. (2013, 2015, 2016) [39–41] performed several studies to analyze contact electrification and electrostatic interactions in an Euler-Lagrange model. Charge generation was determined using the condenser model, the numerical results of which agreed with the experimental work by Matsusaka et al. (2000) [2]. Based on their results, charge transfer is proportional to the maximum contact area, and repeated contacts result in charge accumulation up to a maximum point [39], corresponding to the saturation charge mentioned above. Simulations showed that particles of different material properties can acquire charges of opposite polarity and form agglomerates, which can result in de-fluidization at low superficial gas velocities [40]. A study on long-range electrostatic interactions in this model implied that even long-range contributions are necessary for accurate modeling of charged particle systems [41].

Laurentie et al. (2013) [42] proposed a charge transfer model inspired by the charge relaxation model, and incorporated it into a CFD-DEM approach. In this model, charge transfer occurs based on the difference between the effective work functions of the contacting objects [42]. The model suggests that the charge transfer is not only dependent on the effective work function of the two contacting bodies, but also on the total electric field, i.e. both short-range and long-range, acting on the contact point. Values for the effective work function needs to be calibrated based on experimental data to perform an accurate simulation of charge transfer. Kolehmainen et al. (2016a, 2016b) [43,44] used the charge transfer model of [42] in their Euler-Lagrange model for laboratory-scale vibrated granular beds and fluidized beds. Their study [43,44] revealed that bed height oscillations in small fluidized beds of mono-charged particles decreases with increasing charge due to the lateral segregation of particles. Simulations with a small work function difference resulted in minor electrostatic charge effects on the hydrodynamics of the fluidized bed. The average charge saturated at a value much lower than expected based on the work function difference [44].

As reviewed above, Euler-Lagrange models have been developed to study electrostatic charging and its effects in laboratory-scaled systems. The objective of this work is to develop a triboelectrification model to simulate industrial-scale gas-solid fluidized bed reactors. To this purpose, an Euler-Euler model for gas-particle flows, incorporating electrostatic charging due to particle-particle and particle-wall contacts is formulated in this work. As a first step towards the formulation of a general Euler-Euler model, this effort focuses on mono-disperse particles. Closures for charge generation and transport due to particle-particle collisions are found in accordance to the kinetic theory of Jenkins and Savage (1983) and Lun et al. (1984) [3,45]. Charge generation due to collisions of particles with a solid wall is described by means of a boundary condition obtained following the work of Johnson and Jackson (1987) [1]. A similar derivation was performed by [46], who adapted the self-diffusion coefficient found by [47] for heat transfer to the self-diffusion of charge. The computational model is implemented into the open-source software for computational fluid dynamics OpenFOAM® [48], and validated against experimental results [35].

2.2. Multiphase hydrodynamic model

The two-fluid model approach [13–15,49] is used to describe the gas-particle flow considered in this work. Since species transport and chemical reactions are neglected, and both the fluid and particulate phase are considered to be incompressible and isothermal, only continuity and momentum equations for each phase are solved.

The continuity equation for the generic phase φ is

$$\frac{\partial}{\partial t}\left(\alpha_\varphi \rho_\varphi\right) + \nabla \cdot \left(\alpha_\varphi \rho_\varphi \mathbf{U}_\varphi\right) = 0, \tag{2-1}$$

where α_φ is the phase fraction, ρ_φ is the thermodynamic density of the phase, and $\mathbf{U}_\varphi$ is the phase velocity.

The phase momentum equation for the fluid phase is

$$\frac{\partial}{\partial t}\left(\alpha_\mathrm{g} \rho_\mathrm{g} \mathbf{U}_\mathrm{g}\right) + \nabla \cdot \left(\alpha_\mathrm{g} \rho_\mathrm{g} \mathbf{U}_\mathrm{g} \otimes \mathbf{U}_\mathrm{g}\right) = \nabla \cdot \boldsymbol{\tau}_\mathrm{g} - \alpha_\mathrm{g} \nabla p + \alpha_\mathrm{g} \rho_\mathrm{g} \mathbf{g} + \mathbf{M}_\mathrm{sg}, \tag{2-2}$$

and for the particle phase is

$$\frac{\partial}{\partial t}\left(\alpha_\mathrm{s} \rho_\mathrm{s} \mathbf{U}_\mathrm{s}\right) + \nabla \cdot \left(\alpha_\mathrm{s} \rho_\mathrm{s} \mathbf{U}_\mathrm{s} \otimes \mathbf{U}_\mathrm{s}\right) = \nabla \cdot \boldsymbol{\tau}_\mathrm{s} - \alpha_\mathrm{s} \nabla p - \nabla p_s + \alpha_\mathrm{s} \rho_\mathrm{s} \mathbf{g} + \mathbf{M}_\mathrm{gs} + \mathbf{F}_q, \tag{2-3}$$

where $\boldsymbol{\tau}_\varphi$ is the phase stress tensor, p is the shared pressure, p_s is the particle pressure, $\mathbf{g}$ the gravitational acceleration vector, $\mathbf{M}_\mathrm{sg} = -\mathbf{M}_\mathrm{gs}$ is the momentum exchange term, and $\mathbf{F}_q$ is the electrostatic force.

The stress tensor for the generic phase φ is

$$\tau_\varphi = \alpha_\varphi \mu_\varphi \left(\nabla \mathbf{U}_\varphi + \nabla^\mathrm{T} \mathbf{U}_\varphi\right) + \alpha_\varphi \left(\lambda_\varphi - \frac{2}{3}\mu_\varphi\right)\left(\nabla \cdot \mathbf{U}_\varphi\right)\mathbf{I}, \tag{2-4}$$

in which λ_φ is the phase bulk viscosity, μ_φ the phase shear viscosity and $\mathbf{I}$ the unit stress tensor.

Since the focus of the present work is on gas-particle flows involving highly inertial particles, only the drag force is considered in the momentum exchange term, because it is dominant compared to lift and virtual mass. As a consequence, it is assumed that

$$\mathbf{M}_{\mathrm{gs}} = K_{\mathrm{d}}\left(\mathbf{U}_{\mathrm{s}} - \mathbf{U}_{\mathrm{g}}\right), \tag{2-5}$$

being K_d the drag function model.

The particulate phase is described according to the kinetic theory of granular flows [10,45,50,51]. According to this approach, the phase pressure, shear viscosity and bulk viscosity of the particulate phase are expressed as a function of the granular energy Θ_{s}, determined by solving the transport equation:

$$\begin{aligned}\frac{3}{2}\left[\frac{\partial}{\partial t}(\alpha_{\mathrm{s}}\rho_{\mathrm{s}}\Theta_{\mathrm{s}}) + \nabla\cdot(\alpha_{\mathrm{s}}\rho_{\mathrm{s}}\Theta_{\mathrm{s}}\mathbf{U}_{\mathrm{s}})\right] \\ = (\boldsymbol{\tau}_{\mathrm{s}} - p_{\mathrm{s}}\mathbf{I}):\nabla\mathbf{U}_{\mathrm{s}} + \nabla\cdot\left(\kappa_{\Theta_{\mathrm{s}}}\nabla\Theta_{\mathrm{s}}\right) - \gamma_{\Theta_{\mathrm{s}}} + J_{\mathrm{gs}}\,.\end{aligned} \tag{2-6}$$

The particle phase pressure is calculated as the sum of the kinetic and collisional contributions p_{kt}, provided by the kinetic theory model [45], and the frictional pressure p_{fr} [1,52,53]:

$$p_{\mathrm{s}} = p_{\mathrm{kt}} + p_{\mathrm{fr}}, \tag{2-7}$$

where [45]

$$p_{\mathrm{kt}} = \alpha_{\mathrm{s}}\rho_{\mathrm{s}}\Theta_{\mathrm{s}} + 2\alpha_{\mathrm{s}}^2\rho_{\mathrm{s}}\Theta_{\mathrm{s}}g_0(1+e_{\mathrm{s}}), \tag{2-8}$$

and [54]

$$g_0(\alpha_{\mathrm{s}}) = \left[1 - \left(\frac{\alpha_{\mathrm{s}}}{\alpha_{\mathrm{s,max}}}\right)^{\frac{1}{3}}\right]^{-1}. \tag{2-9}$$

The frictional pressure is modeled following [1]:

$$p_{\mathrm{fr}} = 0.05\frac{\left(\alpha_s - \alpha_{s,\mathrm{fr,min}}\right)^2}{\left(\alpha_{s,\mathrm{max}} - \alpha_{\mathrm{f}}\right)^5}. \tag{2-10}$$

In analogy to the particle pressure, the particle viscosity is given by the sum of the contributions obtained from the kinetic theory (kinetic + collisional) and the frictional contribution [1]

$$\mu_{\mathrm{s}} = \mu_{\mathrm{kt}} + \mu_{\mathrm{fr}}, \tag{2-11}$$

where [10]

$$\mu_{kt} = \frac{4}{5}\alpha_s^2 \rho_s d_p g_0 (1+e_s)\sqrt{\frac{\Theta_s}{\pi}} + \frac{10\rho_s d_p \sqrt{\pi\Theta_s}}{96\, g_0(1+e_s)}\left[1+\frac{4}{5}(1+e_s)\alpha_s g_0\right]^2, \quad 2\text{-}12$$

and [52]

$$\mu_{fr} = p_{fr}\frac{\sqrt{2}\sin\phi_{fr}}{2\sqrt{\mathbf{S}_s : \mathbf{S}_s}}, \quad 2\text{-}13$$

in which ϕ_{fr} is the angle of internal friction, and $\mathbf{S}_s$ is the deformation rate tensor of the particle phase.

The particle phase bulk viscosity is given by the equation [10,45]

$$\lambda_s = \frac{4}{3}\alpha_s^2 \rho_s d_p g_0 (1+e_s)\sqrt{\frac{\Theta_s}{\pi}}. \quad 2\text{-}14$$

The conductivity and the dissipation rate of the granular energy are modeled according to Gidaspow (1994) [10]:

$$\kappa_{\Theta_s} = \frac{150\rho_s d_p \sqrt{\pi\Theta_s}}{384\, g_0(1+e_s)}\left[1+\frac{6}{5}\alpha_s g_0(1+e_s)\right]^2 + 2\alpha_s^2 \rho_s d_p g_0 (1+e_s)\sqrt{\frac{\Theta_s}{\pi}}, \quad 2\text{-}15$$

$$\gamma_{\Theta_s} = 3\alpha_s^2 \rho_s g_0 (1-e_s^2)\Theta_s\left[\frac{4}{d_p}\sqrt{\frac{\Theta_s}{\pi}} - \nabla\cdot\mathbf{U}_s\right]. \quad 2\text{-}16$$

The rate of change of granular energy due to the interaction between the fluid and particle phases is also described according to Gidaspow (1994) [10]:

$$J_{gs} = -3K_d\Theta_s. \quad 2\text{-}17$$

Different kinetic theory formulations could be selected [10,55,56]. The formulation summarized above [3] was chosen because it is considered adequate for the flow conditions of interest in

bubbling fluidized beds, and has been widely tested in these applications, showing satisfactory results for what concerns the prediction of hydrodynamic parameters [10–12,57].

2.3. Electrostatic model

The force acting on a particle carrying a charge q due to electromagnetic effects is given by the definition of Lorentz's force:

$$\mathbf{F}_q = q(\mathbf{E} + \mathbf{c} \times \mathbf{B}), \tag{2-18}$$

where **E** and **B** are, respectively, the electric field and the magnetic field in which the particle is moving with velocity **c**. Observing that the velocities of particles in gas-particle flows are moderate, the contribution of the magnetic field to Lorentz's force is neglected [32,33], leading to $\mathbf{F}_q = q\mathbf{E}$.

The electric field can be found introducing the electric displacement:

$$\mathbf{D} = \varepsilon_0 \mathbf{E} + \mathbf{P}, \tag{2-19}$$

where ε_0 is the permittivity of the vacuum, and **P** is the induced polarization, which can be expressed as:

$$\mathbf{P} = \varepsilon_0 \chi_e \mathbf{E}, \tag{2-20}$$

with χ_e the electric susceptibility of the medium. More conveniently, the electric displacement field can be rewritten as:

$$\mathbf{D} = \varepsilon_0 \varepsilon_r \mathbf{E}, \tag{2-21}$$

in which ε_r represents the relative electric permittivity of the medium, with $\varepsilon_r = 1 + \chi_e$.

According to Gauss' law,

$$\nabla \cdot \mathbf{D} = \rho_q, \tag{2-22}$$

where ρ_q is the charge density (amount of charge per unit of total volume).

Introducing the electric potential φ_E, which is related to the electric field by

$$\mathbf{E} = -\nabla\varphi_E, \tag{2-23}$$

Eq. 2-22 yields:

$$\nabla \cdot (\varepsilon_0 \varepsilon_m \nabla\varphi_E) = \rho_q, \tag{2-24}$$

in which ε_m is the relative permittivity of the multiphase mixture.

Focusing on the case of mono-disperse particles leads to $\rho_q = \alpha_s q$, and to

$$\mathbf{F}_q = -q\alpha_\mathrm{s}\nabla\varphi_E. \tag{2-25}$$

The charge density of the particle phase q depends on position and time, since particles may acquire or dissipate charge when impacting walls or other particles [58]. Only the charging processes due to particle-particle and particle-wall collisions are considered in this work.

2.3.1. Transport equation for particle charge

A transport equation for the particle charge can be obtained following [3], and observing that the charge carried by a solid particle and the particle velocity are correlated. Under this assumption, the following evolution equation for the mean particle charge density $\langle q \rangle$ is obtained:

$$\frac{\partial}{\partial t}(\alpha_\mathrm{s}\rho_\mathrm{s}\langle q\rangle) + \nabla \cdot (\alpha_\mathrm{s}\rho_\mathrm{s}\langle \mathbf{c}q\rangle) = m_p \mathbb{C}(q) \tag{2-26}$$

or

$$\frac{\partial}{\partial t}(\alpha_\mathrm{s}\rho_\mathrm{s}\langle q\rangle) + \nabla \cdot (\alpha_\mathrm{s}\rho_\mathrm{s}\langle q\rangle \mathbf{U}_\mathrm{s}) + \nabla \cdot (\alpha_\mathrm{s}\rho_\mathrm{s}\langle \mathbf{C}q'\rangle) = m_p \mathbb{C}(q) \tag{2-27}$$

where $\mathbb{C}(q)$ is the mean collisional rate of change of particle charge due to binary collisions between particles, and $\langle \mathbf{C}q' \rangle$ is the expected value of the charge-velocity covariance. It is worth remembering at this point that the following derivation accounts for particle charging due to contact between two particles. The effect of enduring contact and of collisions among more than two particles is neglected. Eq. 2-27 can be solved once a boundary condition describing the evolution of particle charge due to particle-wall interactions (Sec. 2.3.3 and 2.3.7), and expressions for $\mathbb{C}(q)$ (Sec. 2.3.4) and $\langle \mathbf{C}q' \rangle$ (Sec. 2.3.5) are specified.

2.3.2. Particle number density function

The one particle number density function (NDF) is assumed to have the following form

$$f_p = \frac{N}{(2\pi\Theta_s)^{3/2}\sqrt{2\pi Q^2}} \exp\left[-\frac{1}{2}\left(\frac{C^2}{\Theta_s} + \frac{q'^2}{Q^2}\right)\right], \quad 2\text{-}28$$

where a Maxwellian and a Gaussian distribution have been assumed for the particle velocity and charge respectively such that N is the number of particles per unit volume and Θ_s is the uncorrelated particle fluctuating energy (granular temperature) [3,10,19], defined as

$$\Theta_s = \frac{1}{3}\langle \mathbf{C}^2 \rangle, \quad 2\text{-}29$$

and Q^2 is the variance of charge expressed as

$$Q^2 = \langle q'q' \rangle = \langle q'^2 \rangle. \quad 2\text{-}30$$

$\mathbf{C}$ and q' are defined as follows in the above equations and in the rest of the paper

$$\mathbf{c} = \mathbf{U}_s + \mathbf{C} \quad 2\text{-}31$$

$$q = \langle q \rangle + q', \quad 2\text{-}32$$

where $\mathbf{c}$ is the particle velocity, $\mathbf{U}_s$ is the mean particle velocity, $\mathbf{C}$ is the particle fluctuation velocity, q is the particle charge, and q' is the fluctuation of charge. The charge-velocity covariance $\langle \mathbf{C}q' \rangle$ is defined as

$$\langle \mathbf{C}q' \rangle = \int_{\mathbb{R}^3} \int_{\mathbb{R}} (\mathbf{c} - \mathbf{U}_s)(q - \langle q \rangle) f_p \, \mathrm{dq} \, \mathrm{d}\mathbf{c} = \int_{\mathbb{R}^3} \int_{\mathbb{R}} \mathbf{C}q' \, f_p \mathrm{dq} \, \mathrm{d}\mathbf{c}, \quad 2\text{-}33$$

and is assumed to be a constant while evaluating integrals such that

$$\mathbf{C}_1 q'_1 = \mathbf{C}_2 q'_2 = \langle \mathbf{C}q' \rangle \quad 2\text{-}34$$

On the other hand, the fluctuations of velocity of particle 1 and that of charge of particle 2 are assumed to be uncorrelated, and vice versa. On assuming that this is true over every dimension of space and time, it implies

$$\mathbf{C}_1 q'_2 = \mathbf{C}_2 q'_1 = 0. \quad 2\text{-}35$$

2.3.3. Rate of change of particle charge due to particle-wall collisions

The flux of $\langle q \rangle$ due to collisions of a particle with a wall is given by the integral [17,18]

$$\begin{aligned} \mathbb{C}_w(q) &= -g_0 \int_{\mathbf{c}\cdot\mathbf{n}<\mathbf{0}} (q' - q) f(\mathbf{c})(\mathbf{c}\cdot\mathbf{n}) \mathrm{d}\mathbf{c} \\ &= -g_0 \int_{\mathbf{c}\cdot\mathbf{n}<\mathbf{0}} \frac{\mathrm{d}q}{\mathrm{d}\mathbf{n}_{c,w}} f(\mathbf{c})(\mathbf{c}\cdot\mathbf{n}) \mathrm{d}\mathbf{c}, \end{aligned} \tag{2-36}$$

where $\mathbf{n}$ is the wall-normal unit vector, and g_0 is a function that accounts for the presence of other particles (Eq. 2-9).Following Matsusaka et al. (2000) and Matsusaka and Masuda (2003) [2,58], the change of charge during the collision of a particle with a wall, accounting for the effect of repeated collisions, can be calculated as

$$\frac{\mathrm{d}q}{\mathrm{d}\mathbf{n}_{c,w}} = -k_c \varepsilon_0 \varepsilon_r \left[\frac{V_c}{z_0} \left(1 - \frac{q}{q_\infty} \right) + \mathbf{E}_q \cdot \mathbf{n} \right] S, \tag{2-37}$$

where V_c is the difference of the work functions of the two impacting surfaces, k_c is the charging efficiency, ε_r is the relative electrical permittivity of the gaseous medium, z_0 is the critical gap, q is the particle charge, q_∞ is the particle saturation charge, $\mathbf{E}_q$ the electric potential at the contact point, and S is the contact area.

The contact area is computed according to the Hertzian theory as

$$S = 1.364 d_\mathrm{p}^2 v^{4/5} \left[\rho_\mathrm{s} \frac{1-\nu}{E} \right]^{2/5} = k_{s,w} v^{4/5}, \tag{2-38}$$

where ν and E are, respectively, the Poisson ratio and the Young's modulus of the material forming the particle, and v is the magnitude of the wall-normal component of the particle velocity.

Since the objective of the present work is to develop a boundary condition for electrostatic charging to be paired to the partial slip conditions of Johnson and Jackson (1987) [1], we assume a Maxwellian velocity distribution for the particle velocity as described by Eq. 2-28.

The integral in Eq. 2-36 can be calculated by observing that the norm of the particle velocity in the wall-normal direction is

$$v = \mathbf{c} \cdot \mathbf{n} \,. \tag{2-39}$$

By choosing a frame of reference in spherical coordinates with the x axis aligned with the particle slip velocity at the wall, and the z axis perpendicular to the wall surface (parallel to $\mathbf{n}$) [17], the following identity is obtained [1,17]:

$$\begin{cases} C_x = C\sin\phi\cos\theta \\ C_y = C\sin\phi\sin\theta \\ C_z = C\cos\phi \end{cases}. \tag{2-40}$$

Since the Jacobian of the transformation from Cartesian to spherical coordinates is $J = C^2\sin\phi$, and observing that

$$\mathbf{u}\cdot\mathbf{n} = 0, \tag{2-41}$$

because the wall is impenetrable, leads to

$$\mathbf{c}\cdot\mathbf{n} = (\mathbf{C}+\mathbf{u})\cdot\mathbf{n} = \mathbf{C}\cdot\mathbf{n}. \tag{2-42}$$

The following expression for the flux of charge due to collisions with the wall is ultimately obtained:

$$\begin{aligned} \mathbb{C}_w(q) &= g_0 k_c k_{s,w}\varepsilon_0\varepsilon_r \int_0^{\frac{\pi}{2}}\int_{-\pi}^{\pi}\int_0^{+\infty} f(C)C^{\frac{19}{5}}\sin\phi\cos^{\frac{9}{5}}\phi \mathrm{d}C\mathrm{d}\theta\mathrm{d}\phi \\ &= \frac{5}{7}g_0 N\frac{1}{2^{\frac{1}{10}}\sqrt{\pi}}\Gamma\left(\frac{12}{5}\right)\Theta_{\mathrm{s}}^{\frac{9}{10}}k_c k_{s,w}\varepsilon_0\varepsilon_r\left[\frac{V_c}{z_0}\left(1-\frac{q}{q_\infty}\right)+\mathbf{E}_q\cdot\mathbf{n}\right]. \end{aligned} \tag{2-43}$$

2.3.4. Rate of change of particle charge due to particle-particle collisions

The rate of change of charge of a particle $\mathbb{C}(q)$, identified by the index 1, due to a binary collision with another particle, identified by the index 2 is found from the collision integral [3,50]:

$$\mathbb{C}(q) = \int_{\mathbf{c}_{12}\cdot\mathbf{k}>0}\int_{\mathbb{R}^6}\int_{\mathbb{R}^2}(q_1'-q_1)f^{(2)}d_{\mathrm{p}}^2(\mathbf{c}_{12}\cdot\mathbf{k})\mathrm{d}q_1\mathrm{d}q_2\mathrm{d}\mathbf{c}_1\mathrm{d}\mathbf{c}_2\mathrm{d}\mathbf{k}, \tag{2-44}$$

in which q_1 and q_1' are the charge densities before and after collisions of particle 1, $\mathbf{r}_i$ is the position vector of particle i, $\mathbf{c}_i$ is the velocity of particle i, $\mathbf{c}_{12} = \mathbf{c}_1 - \mathbf{c}_2$ is the particle relative velocity vector, and $\mathbf{k}$ is the unit vector directed from the center of the first particle to the center

of the second particle at contact [3]. Following the same procedure explained in Jenkins and Savage (1963) [3], and expanding the pair velocity-charge number density function as

$$f^{(2)}\left(\mathbf{c}_1, \mathbf{r}_1, q_1, \mathbf{c}_2, \mathbf{r}_2 + d_\mathrm{p}\mathbf{n}_\mathrm{p}, q_2\right) = f^{(2)}(\mathbf{c}_1, \mathbf{r}_1, q_1, \mathbf{c}_2, \mathbf{r}_2, q_2) + d_\mathrm{p}\mathbf{n}_\mathrm{p} \cdot \nabla f^{(2)}(\mathbf{c}_1, \mathbf{r}_1, q_1, \mathbf{c}_2, \mathbf{r}_2, q_2), \quad 2\text{-}45$$

the integral of Eq. 2-44 can be rewritten as

$$\mathbb{C}(q) = \chi_q - \nabla \cdot \boldsymbol{\theta}_q, \quad 2\text{-}46$$

where

$$\chi_q = \frac{\mathrm{d}_\mathrm{p}^2}{2} \int\limits_{\mathbf{c}_{12}\cdot\mathbf{k}>0} \int\limits_{\mathbb{R}^6} \int\limits_{\mathbb{R}^2} (q'_2 + q'_1 - q_2 - q_1) \times (\mathbf{c}_{12} \cdot \mathbf{k}) f^2 \, \mathrm{d}q_1 \mathrm{d}q_2 \mathrm{d}\mathbf{c}_1 \mathrm{d}\mathbf{c}_2 \mathrm{d}\mathbf{k} \quad 2\text{-}47$$

and

$$\boldsymbol{\theta}_q = \frac{\mathrm{d}_\mathrm{p}^3}{2} \int\limits_{\mathbf{c}_{12}\cdot\mathbf{k}>0} \int\limits_{\mathbb{R}^6} \int\limits_{\mathbb{R}^2} \mathbf{k}\left(q'_1 - q_1\right)(\mathbf{c}_{12} \cdot \mathbf{k}) \, f^2 \mathrm{d}q_1 \mathrm{d}q_2 \mathrm{d}\mathbf{c}_1 \mathrm{d}\mathbf{c}_2 \mathrm{d}\mathbf{k}. \quad 2\text{-}48$$

The pair distribution function is then rewritten as the product of the marginal distributions [3,50]

$$f^2 = g_0 f_p(\mathbf{c}_1, q_1, \mathbf{r}_1) f_p(\mathbf{c}_2, q_2, \mathbf{r}_2) = g_0 f_{p1} f_{p2} = \frac{g_0 N^2}{(2\pi\Theta_s)^3 2\pi Q^2} \exp\left[-\frac{1}{2}\left(\frac{C_1^2 + C_2^2}{\Theta_s} + \frac{q'^2_1 + q'^2_2}{Q^2}\right)\right]. \quad 2\text{-}49$$

In the case of mono-disperse particles, the source term χ_q in Eq. 2-47 is null because particles are identical, and the total charge belonging to a single phase during a collision is conserved. Consequently, only the integral in Eq. 2-48 needs to be calculated.

The difference $q'_1 - q_1$ can be calculated, as:

$$q'_1 - q_1 = \frac{dq_1}{dn_c} = \left\{K_1(q_2 - q_1) + K_2\left(\mathbf{E}_q \cdot \mathbf{k}\right)\right\}(\mathbf{c}_{12} \cdot \mathbf{k})^{4/5}, \quad 2\text{-}50$$

where

$$K_1 = \frac{k_c k_s}{\pi d_p^2}, \tag{2-51}$$

and

$$K_2 = k_c k_s \varepsilon_0 \varepsilon_r, \tag{2-52}$$

with

$$k_s = 0.783 d_{\mathrm{p}}^2 \left(\rho_{\mathrm{s}} \frac{1-\nu}{E}\right)^{2/5}, \tag{2-53}$$

based on the Hertzian theory of contact deformation between two identical particles.

Eq. 2-50 which describes the rate of charge exchange between two particles, is based on the theoretical model of Schein et al. (1992) [59] which is similar to Matsusaka's model given by Eq. 2-37 but has no work function dependency since charge exchange takes place between surfaces made of identical materials. The effective electric field between the two surfaces is the superposition of the electric field due to the overall distribution of charge in the bed and the localized field imposed by difference in the charge densities of the two surfaces. This model has already been used in previous modelling attempts of [42] and [46].

To include the contribution to particle-particle charging due to difference of particle charge densities, f^2 must be expanded to include the finite particle-size effect. Thus following the same procedure as [3] and including spatial derivatives up to first order, we have

$$\begin{aligned} f^2 &= g_0 f_{p1} f_{p2} \left(1 + \frac{\mathrm{d_p}}{2}(\mathbf{k}\cdot\nabla)\ln\frac{f_{p2}}{f_{p1}}\right) \\ &= \frac{g_0 N^2}{(2\pi\Theta_s)^3 2\pi Q^2} \exp\left[-\frac{1}{2}\left(\frac{C_1^2 + C_2^2}{\Theta_s} + \frac{{q'}_1^2 + {q'}_2^2}{Q^2}\right)\right] \\ &\times \left[1 + \frac{\mathrm{d_p}}{2}\left(\frac{1}{2Q^4} q_{12}(q_2 + q_1)(\mathbf{k}\cdot\nabla\langle q'q'\rangle) - \frac{q_{12}}{Q^2}(\mathbf{k}\cdot\nabla\langle q\rangle)\right.\right. \\ &\qquad \left.\left. + \frac{1}{2\theta_s^2}\left(\mathbf{c}_{12}\cdot(\mathbf{c}_2 + \mathbf{c}_1)\right)(\mathbf{k}\cdot\nabla\Theta_s) - \frac{1}{\theta_s}\mathbf{c}_{12}\cdot(\mathbf{k}\cdot\nabla\mathbf{U}_{\mathrm{s}})\right)\right]. \end{aligned} \tag{2-54}$$

Based on the assumptions described above, the term $\boldsymbol{\theta}_q$ of Eq. 2-48 then becomes (see Appendix)

$$\boldsymbol{\theta}_q = g_0\alpha_{\mathrm{s}}N \times \left[\left(\frac{60}{19}2^{9/5}\Gamma\left(\frac{19}{10}\right)\frac{1}{\sqrt{\pi}}K_1{\Theta_s}^{2/5}\right)\langle \mathbf{C}q'\rangle \right.$$
$$+\left(\frac{5}{9}2^{9/5}\Gamma\left(\frac{12}{5}\right)\frac{1}{\sqrt{\pi}}K_2{\Theta_s}^{9/10}\right)\mathbf{E}_q \qquad 2\text{-}55$$
$$\left.+\left(\frac{5}{21}2^{9/5}\Gamma\left(\frac{12}{5}\right)\frac{1}{\sqrt{\pi}}K_1{\Theta_s}^{9/10}\mathrm{d_p}\right)\left(\frac{\langle q\rangle}{\langle q'q'\rangle}\nabla\langle q'q'\rangle - \nabla\langle q\rangle\right)\right].$$

The charge transport equation, Eq. 2-18, can then be written as

$$\frac{\partial}{\partial t}(\alpha_{\mathrm{s}}\rho_{\mathrm{s}}\langle q\rangle) + \nabla\cdot(\alpha_{\mathrm{s}}\rho_{\mathrm{s}}\langle q\rangle\mathbf{U}_{\mathrm{s}}) + \nabla\cdot\mathbf{q}_q = 0, \qquad 2\text{-}56$$

where

$$\mathbf{q}_q = g_0{\alpha_{\mathrm{s}}}^2\rho_{\mathrm{s}}\left[\left(\frac{1}{g_0\alpha_{\mathrm{s}}} + \frac{60}{19}2^{9/5}\Gamma\left(\frac{19}{10}\right)\frac{1}{\sqrt{\pi}}K_1{\Theta_s}^{\frac{2}{5}}\right)\langle \mathbf{C}q'\rangle \right.$$
$$+\left(\frac{5}{9}2^{9/5}\Gamma\left(\frac{12}{5}\right)\frac{1}{\sqrt{\pi}}K_2{\Theta_s}^{\frac{9}{10}}\right)\mathbf{E}_q \qquad 2\text{-}57$$
$$\left.+\left(\frac{5}{21}2^{9/5}\Gamma\left(\frac{12}{5}\right)\frac{1}{\sqrt{\pi}}K_1{\Theta_s}^{\frac{9}{10}}\mathrm{d_p}\right)\left(\frac{\langle q\rangle}{\langle q'q'\rangle}\nabla\langle q'q'\rangle - \nabla\langle q\rangle\right)\right].$$

2.3.5. Derivation of charge-velocity covariance

To derive an expression for $\langle \mathbf{C}q'\rangle$, which is responsible for self-diffusion, we investigate the transport equation of $\langle \mathbf{c}q\rangle$ given by [46]

$$\frac{\partial}{\partial t}(\alpha_{\mathrm{s}}\rho_{\mathrm{s}}\langle \mathbf{c}q\rangle) + \nabla\cdot(\alpha_{\mathrm{s}}\rho_{\mathrm{s}}\langle \mathbf{cc}q\rangle) = m_p\mathbb{C}(\mathbf{c}q) + \alpha_{\mathrm{s}}\rho_{\mathrm{s}}\left\langle\frac{\partial \mathbf{c}q}{\partial \mathbf{c}}\frac{\mathrm{d}\mathbf{c}}{\mathrm{dt}}\right\rangle + \alpha_{\mathrm{s}}\rho_{\mathrm{s}}\left\langle\frac{\partial \mathbf{c}q}{\partial q}\frac{\mathrm{dq}}{\mathrm{dt}}\right\rangle, \qquad 2\text{-}58$$

which simplifies to (see Appendix)

$$\frac{\partial}{\partial t}(\alpha_{\mathrm{s}}\rho_{\mathrm{s}}\langle \mathbf{c}q\rangle) + \nabla\cdot(\alpha_{\mathrm{s}}\rho_{\mathrm{s}}\langle \mathbf{cc}q\rangle) = m_p\mathbb{C}(\mathbf{c}q) + \alpha_{\mathrm{s}}\rho_{\mathrm{s}}\left\langle q\frac{\mathbf{F}}{m_p}\right\rangle. \qquad 2\text{-}59$$

If the following assumptions are made in this context:

1. $\langle \mathbf{c}q\rangle$ is a quasi-steady variable,
2. $\langle \mathbf{CC}q'\rangle = 0$
3. Divergence of terms containing $\mathbf{U}_{\mathrm{s}}$ is negligible
4. Gradients of $\alpha_{\mathrm{s}}, \rho_{\mathrm{s}}, \langle \mathbf{CC}\rangle$ are considered negligible compared to gradients of $\langle q\rangle$,

then we obtain (see Appendix)

$$m_p \mathbb{C}(\mathbf{c}q) = \alpha_s \rho_s \Theta_s \nabla\langle q\rangle - \alpha_s \rho_s \langle q \frac{\mathbf{F}}{m_p}\rangle, \tag{2-60}$$

where

$$m_p \mathbb{C}(\mathbf{c}q) = m_p\left(\boldsymbol{\chi}_{\mathbf{c}q} - \nabla \cdot \theta_{\mathbf{c}q}\right). \tag{2-61}$$

Evaluating the collision integrals for $\boldsymbol{\chi}_{\mathbf{c}q}$ and $\theta_{\mathbf{c}q}$ (see Appendix) and substituting the same in Eq. 2-60 gives

$$\begin{aligned}\langle \mathbf{C}q'\rangle = &-\frac{1}{(1+e)\sqrt{\pi\Theta_s}+} \\ &\times\left[\left(\frac{1}{2}(1+e)+\frac{\pi}{6g_0\alpha_s}\right)d_p\Theta_s\nabla\langle q\rangle - \frac{\pi d_p}{6g_0\alpha_s}\langle\frac{\mathbf{F}}{m_p}\rangle\langle q\rangle\right. \\ &\left.+\left(\frac{5}{57}-\frac{23}{264}(1+e)\right)2^{19/5}\Gamma\left(\frac{29}{10}\right)\sqrt{\pi}K_2{\Theta_s}^{7/5}\mathbf{E}_q\right].\end{aligned} \tag{2-62}$$

2.3.6. Derivation of expression for the charge variance

Here we use the same approach that was used for derivation of $\langle \mathbf{C}q'\rangle$ in the previous section. We first consider the transport equation for charge variance, which is given by

$$\begin{aligned}&\frac{\partial}{\partial t}(\alpha_s\rho_s\langle q'q'\rangle) + \nabla\cdot(\alpha_s\rho_s\langle \mathbf{c}q'q'\rangle) \\ &\qquad = m_p\mathbb{C}(q'q') + \alpha_s\rho_s\langle\frac{\partial q'q'}{\partial \mathbf{c}}\frac{\mathrm{d}\mathbf{c}}{\mathrm{dt}}\rangle + \alpha_s\rho_s\langle\frac{\partial q'q'}{\partial q}\frac{\mathrm{dq}}{\mathrm{dt}}\rangle.\end{aligned} \tag{2-63}$$

In addition to the assumptions used in Section 2.3.5, we also assume the following

1. $\langle q'q'\rangle$ is a quasi-steady variable,
2. $\langle \mathbf{C}q'q'\rangle = 0$
3. $\langle q'q'\rangle$ is not a function of particle velocity $\mathbf{c}$

This implies that

$$\mathbb{C}(q'q') = \chi_{q'q'} - \nabla\cdot\boldsymbol{\theta}_{q'q'} = 0 \tag{2-64}$$

Evaluating the collision integrals for $\chi_{q'q'}$ and $\boldsymbol{\theta}_{q'q'}$ (see Appendix) and substituting the same in Eq. 2-64 gives

$$\begin{aligned}\langle q'q'\rangle = \frac{1}{\frac{5}{9}2^{23/5}\Gamma\left(\frac{14}{5}\right)\sqrt{\pi}{K_1}^2{\Theta_s}^{13/10} - \frac{5}{7}2^{19/5}\Gamma\left(\frac{12}{5}\right)\sqrt{\pi}K_1{\Theta_s}^{9/10}} \\ \times\left\{\left(\frac{13}{35}2^{13/5}\Gamma\left(\frac{14}{5}\right)\sqrt{\pi}{K_2}^2{\Theta_s}^{13/10}\left|\mathbf{E}_q\right|^2\right)\right. \\ +\left[\left(\frac{5}{23}2^{23/5}\Gamma\left(\frac{23}{10}\right)\sqrt{\pi}K_1K_2{\Theta_s}^{4/5}\right)\right. \\ \left.\left.-\left(\frac{5}{57}2^{19/5}\Gamma\left(\frac{29}{10}\right)\sqrt{\pi}K_2{\Theta_s}^{2/5}\right)\right]\left(\mathbf{E}_q\cdot\langle\mathbf{C}q'\rangle\right)\right\}\end{aligned} \quad 2\text{-}65$$

It should be noted here that in deriving expressions for $\langle\mathbf{C}q'\rangle$ and $\langle q'q'\rangle$, the effect of the finite size of the particles has been ignored while considering the two-particle PDF f^2. Thus Eq. 2-49 has been used instead of Eq. 2-54 for the integrals in this section and section 2.3.5.

2.3.7. Wall boundary condition for particle charge density

A boundary condition for the particle charge q_w can be obtained by writing a differential balance equation for the particle charge exchanged at the wall, similar to what was done in [1,17,18] for particle momentum and fluctuating energy, leading to

$$-\mathbf{q}_q\cdot\mathbf{n} = \mathbb{C}_w(q_w). \quad 2\text{-}66$$

This condition is more easily suited for the incorporation into two-fluid models if $\mathbb{C}_w(q)$ is rewritten in terms of the particle volume fraction. Substituting $N = \alpha/V_p$, being V_p the particle volume, into Eq. 2-43 and then in Eq. 2-66, we obtain

$$\begin{aligned}-\mathbf{q}_q\cdot\mathbf{n} &= \mathbb{C}_{\mathrm{w}}(q_w) \\ &= g_0\alpha_{\mathrm{s}}\frac{k_c k_{s,w}\varepsilon_0\varepsilon_r}{d_{\mathrm{p}}^3}\left(\frac{15}{7}\frac{1}{2^{\frac{21}{10}}\pi^{3/2}}\Gamma\left(\frac{12}{5}\right)\right)\Theta_{\mathrm{s}}^{\frac{9}{10}}\left[\frac{V_c}{z_0}\left(1-\frac{q_w}{q_\infty}\right)+\mathbf{E}_q\cdot\mathbf{n}\right],\end{aligned} \quad 2\text{-}67$$

which gives the required boundary condition

$$q_w = q_\infty \left[1 + \frac{z_0}{V_c k_w}\left(\mathbf{E}_q + \mathbf{q}_q\right)\cdot \mathbf{n}\right], \tag{2-68}$$

where

$$k_w = g_0 \alpha_\mathrm{s} \frac{k_c k_{s,w} \varepsilon_0 \varepsilon_r}{d_\mathrm{p}^3}\left(\frac{15}{7}\frac{1}{2^{21/10}\pi^{3/2}}\Gamma\left(\frac{12}{5}\right)\right)\Theta_\mathrm{s}^{9/10}. \tag{2-69}$$

2.4. Model implementation

The model presented above was implemented in the computational code for fluid dynamics OpenFOAM® 6.x by adding it to the reactingTwoPhaseEulerFoam solver. The solver implements the two-fluid model and solves the momentum and continuity equations for the two phases as well as the granular energy transport (Figure 2-1). The algorithm used to discretize the hydrodynamic equations is based on the work of [60], who developed the partial elimination algorithm for the decoupling of momentum equations in iterative solvers. The reactingTwoPhaseEulerFoam solver uses an iterative approach, hybrid of the SIMPLE [61] and PISO methods [62]. The advection term in continuity equation for the granular phase was discretized using the MULES (Multidimensional Universal Limiter for Explicit Solution) implemented in OpenFOAM [63]. The treatment of the particle pressure is analogous to the one described in [64]. The pressure is treated by separating the hydrostatic contribution, as shown in [65]. The equation for charge transport was implemented as a transport equation in the solver, and was solved at the end of the iteration loop, in order to have a converged velocity flux in the equation. Thereafter, the Poisson equation, Eq. 2-24, was used to calculate the electric potential used to determine the electrostatic force on the particle phase. The electrostatic force term is discretized as a momentum flux term, and incorporated in the solution of the pressure equation, rather than directly treating it as a source term in the momentum equation for the granular phase. This procedure, detailed in [64,66], is adopted to stabilize the numerical solution when the electrostatic force term becomes large. The linear system originating from the discretization of the Poisson equation was solved with a conjugate gradient approach, while the linear system corresponding to the transport equation for charge was solved with a stabilized bi-conjugate gradient approach. A geometric-algebraic multi-grid method was chosen to solve the linear system for the pressure equation.

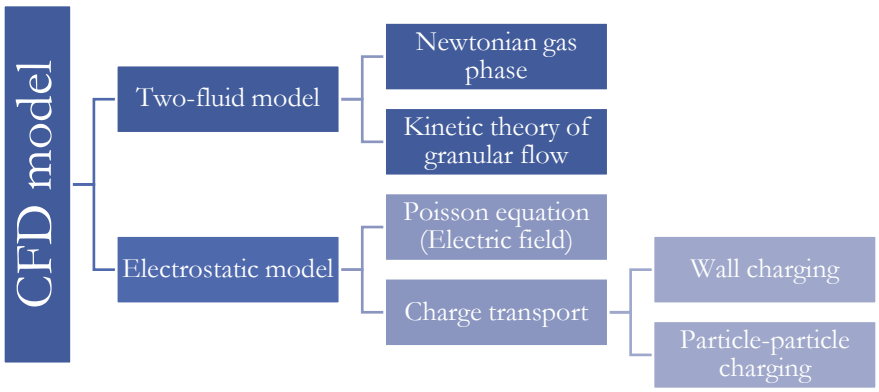

Figure 2-1: Computational model framework.

2.5. Simulation and validation

2.5.1. Description of the test case

The experimental results of [67,68] have been compared to those obtained from the simulations for validation purposes. The experimental setup in their study is shown in Figure 2-2. The fluidized bed in their tests was a grounded cylindrical carbon steel column, with a diameter of 0.1 m and a height of 1.27 m. The column was fluidized with air, which entered the column at the bottom through a knife gate valve. The column was initially filled with linear low-density polyethylene particles up to a height of 0.4 m. The bed was fluidized for 60 minutes, during which fine particles were elutriated to the top Faraday cup. Upon the completion of fluidization, the knife gate valve was opened, and the particles were allowed to drop into the bottom Faraday cup. However, not all the particles fell; a fraction of them remained attached to the column wall. When the column was tapped, most of the particles which had not fallen (*loosely bound*), dropped and were collected in a separate Faraday cup. A small number of particles (*tightly bound*) still held on to the wall and could be only removed by scraping. The loosely bound particles are expected to have charge density values lower than the equilibrium ones. It is also assumed that the tightly bound particles are close to or are at saturation levels.

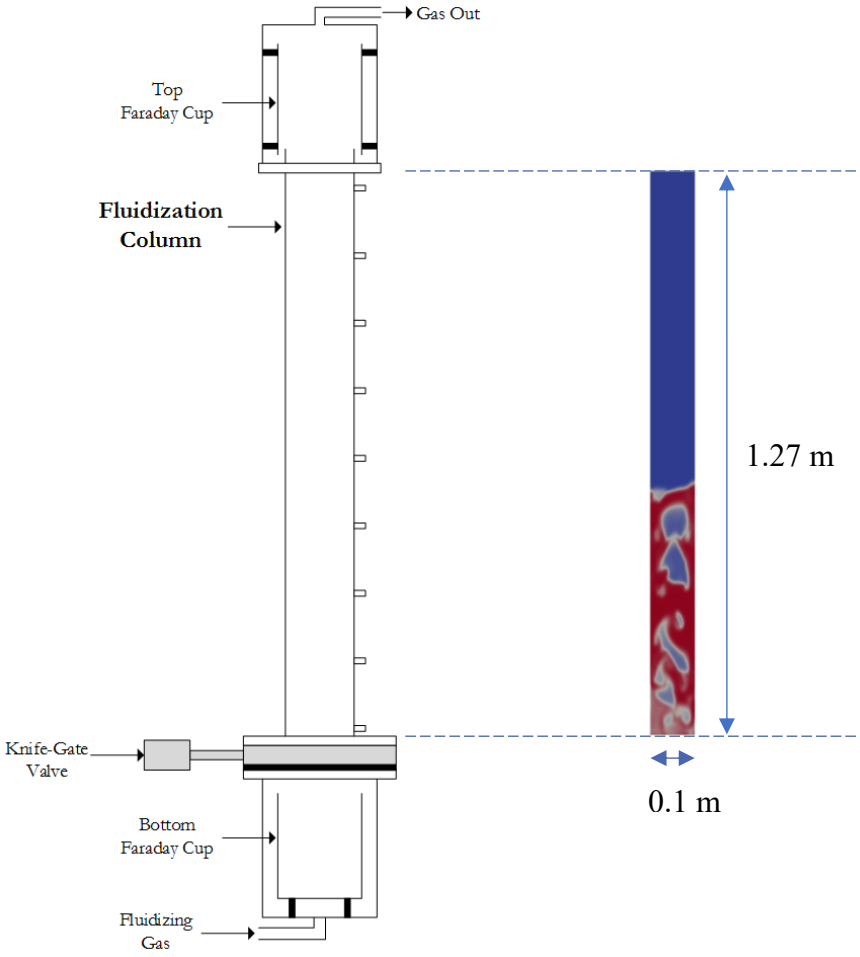

Figure 2-2: Schematic of the experimental setup [67] (and a snapshot of the bed simulation).

The material properties of the particles [67] required for the hydrodynamic and electrostatic model are provided in Table 2-1. The experimental fluidization velocities and particle charge-to-mass ratio q/m, values are summarized in Table 2-2. The initial charge density varied randomly between experiments of different particle sizes, however this is not expected to produce significant difference in the final outcome.

Table 2-1: Material properties of polyethylene particles.

Mass density	Young's modulus	Poisson's ratio	Angle of repose	Relative permittivity	Work function
(kg/m^3)	(MPa)	-	(deg)	-	(eV)
935	150	0.5	30	2.25	5.3

Table 2-2: Experiment operating conditions and measured particles charge densities.

Size Range	Average size	Minimum fluidization velocity U_{mf}	Experimental fluidization velocity ($1.5U_{mf}$)	Initial $\langle q/m \rangle$	Loosely bound $\langle q/m \rangle$	Dropped $\langle q/m \rangle$
(μm)	(μm)	(m/s)	(m/s)	(μC/kg)	(μC/kg)	(μC/kg)
300-425	362	0.0813	0.1220	-0.1	-38	-1.1
425-500	462	0.1420	0.2130	-0.6	-30	-2.0
500-600	550	0.1431	0.2147	-0.4	-30	-0.8
600-710	655	0.1960	0.2940	-0.7	-20	-3.0
710-1000	855	0.252	0.3780	-0.1	-30	-2.6

The fluidization velocities (1.5 U_{mf}) listed in Table 2-2 are used as input parameters in the simulation (Table 2-3) for the different particle sizes. Experiments conducted by Chowdhury et al. (2018) [69] showed that the equilibrium (saturation) charge density q/A was independent of the size of the particle. This advocates for the hypothesis that the electric charge is mostly confined to surface states of the insulator. The saturation q/A of the particles in Sowinski's experiments were not measured and have been assumed to have the same values as those seen in [69], which had a mean of -7 μC/m^2. This serves as an important input for assigning q_∞ (Eq. 2-68) used in the simulations (Table 2-3). The initial q/m is selected as the lower limit in Table 2-2, corresponding to which an initial q/V (Table 2-3) value is assigned to the particle phase. This is not significant for the simulations as it was found that the steady state was independent of the initial charge conditions. The value of z_0 is not exactly defined, however it is expected to of the order of 10 – 100 nm [70,71]. In our simulations, we assume it to be the higher limit of 100 nm, although this has to be verified through experimentation. The value of V_c is calculated from work function potential values of 4.4 V and 5.3 V for the column wall (carbon steel) [72] and polyethylene [67] respectively.

Table 2-3: Charge generation model parameters

Particle size	Saturated q_∞/A	Saturated q_∞/V	Initial q/V	V_c	z_0	k_c (Experiment)	k_c (Simulation)
(μm)	(μC/m^2)	(C/ m^3)	(C/ m^3)	(V)	(nm)	-	-
362	-7	-0.1159	$-1 \cdot 10^{-4}$	0.9	100	$5.6 \cdot 10^9$	$4.0 \cdot 10^{11}$
462	-7	-0.0908	$-1 \cdot 10^{-4}$	0.9	100	$5.6 \cdot 10^9$	$4.0 \cdot 10^{11}$
550	-7	-0.0764	$-1 \cdot 10^{-4}$	0.9	100	$5.6 \cdot 10^9$	$4.0 \cdot 10^{11}$
655	-7	-0.0641	$-1 \cdot 10^{-4}$	0.9	100	$5.6 \cdot 10^9$	$4.0 \cdot 10^{11}$
855	-7	-0.0491	$-1 \cdot 10^{-4}$	0.9	100	$5.6 \cdot 10^9$	$4.0 \cdot 10^{11}$

The value of k_c which determines the rate of charge diffusion was found out to be $5.6 \cdot 10^9$ (Table 2-3), independent of the particle size, based on the measurements of [69] and the particle material properties (Table 2-1). However, simulations using this value exhibited strong dominance of self-diffusion, which led to excessive bed charging (as compared to experiments), accompanied by very high electric potential and field strength. To undermine the effect of self-diffusion, k_c had to be significantly increased to a value of $4.0 \cdot 10^{11}$ for obtaining reasonable results. Computation was done for a simulation time of 10 s, which allowed steady state to be obtained well within this period. This further proves that the rate of diffusion predicted by the simulation is much higher as compared to experiments where a steady state of charge was only observed after a period of 15 minutes or more [73] for the fluidization regime considered, which is why the value of k_c had to be increased by a similar order of magnitude.

2.5.2. Numerical setup

A two-dimensional hexahedral grid, shown in Figure 2-3, is used in the simulations. While the flow in the fluidized bed is intrinsically three-dimensional, we have chosen to perform two-dimensional simulations to demonstrate the application of the model developed in this work, while limiting the computational cost. Several studies demonstrated that the use of two-dimensional simulations is suitable for parametric studies in fluidized bed systems [8,10–12,57,74–76], even if some limitations for what concerns the prediction of the bed expansion and of the bubble dynamics,

as discussed in [77,78]. Validation of the proposed model on three-dimensional calculations is left to future work.

The computational domain considered in the simulations was divided into two blocks in the vertical direction. The lower block, which accounted for 60% of the column height from the bottom, was decomposed into cells of uniform height such that 80% of the total number of cells were accommodated in this block. The upper block accounted for the remaining column height and cells. This ensured that the hydrodynamics of bubbling which is confined to the lower block was sufficiently resolved. The particle bed seldom reached the upper block and hence didn't require much resolution. The number of cell divisions in the vertical direction was fixed at 500, as this was found to predict consistent bubbles over time. In the horizontal direction, a graded grid refinement was applied to accurately capture the wall boundary layer. For this, 20% of the cells were assigned to a layer of 10 mm width at each of the two walls, such that the ratio of the widths of the narrowest and widest cells in this layer was 1:5 (Figure 2-3). For spatial convergence, the total number of cell divisions in the horizontal direction was varied, as explained in section 2.5.3.1.

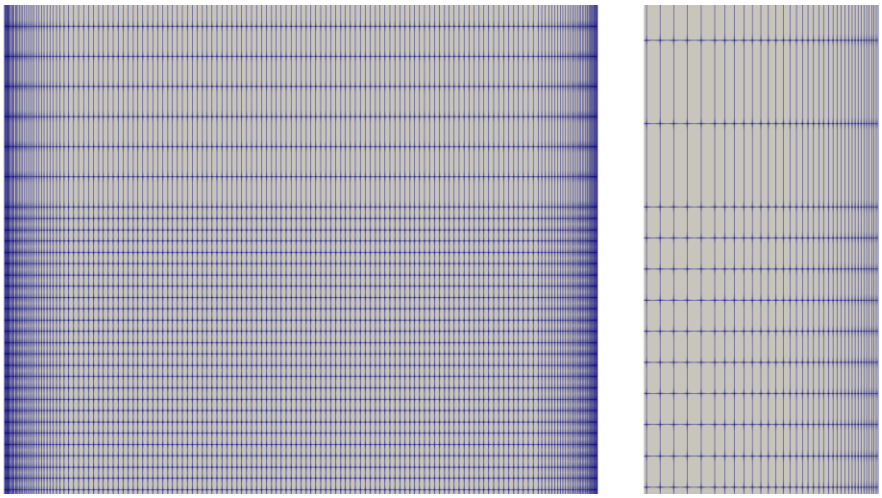

Figure 2-3: Two-dimensional grid layout: (left) across the bed width (with upper and lower blocks), (right) grid grading near the right wall

The transient simulation was performed using the backward Euler time integration scheme. The time step was adaptive to ensure that the maximum Courant flow number (CFL) is below 0.4. The time step was also restricted to a maximum value of 50 μs, as this provided improved stability when the regions at high particle concentration, where the electrostatic force is particularly intense,

formed. In cases of higher inlet air velocities, solution convergence was better with even smaller timesteps (the minimum value used as ceiling for the time stem was 25 μs). These restrictions on the integration time-step were imposed because simulations were stable during the transient, when particle charge was accumulating, but presented some stability problem when the local value of the electrostatic force was very intense. This stability problem is due to the fact that such a large force term needs to be counterbalanced by the particle pressure, in order to maintain the maximum packing limit of the granular phase. The strong non-linearity of the particle pressure, which drastically changes in nearly packed regions, as a consequence of small changes in particle volume fraction, is responsible for the observed numerical instabilities, which could be addressed only imposing a restriction on the time-step. A second-order scheme [79] was employed for spatial discretization, while gradients were calculated using the second-order least-squares method. A tolerance level of $1 \cdot 10^{-4}$ and $1 \cdot 10^{-6}$ was prescribed for the convergence criteria for pressure (and velocity) and volume fraction, respectively. The boundary conditions for the simulation are listed in Table 2-4. A restitution coefficient of 0.8, a specularity coefficient of 0.6 and a friction coefficient of 0.25 were assigned as the parameters for the Johnson and Jackson (1987) [1] particle slip boundary condition. The inlet air velocity has the same value as in Table 2-2 for each case. The thermal condition was isothermal with a fixed temperature of 300 K.

Table 2-4: Simulation boundary conditions

Variable	*Inlet*	*Outlet*	*Walls*
α_s	0	Inlet Outlet	$\nabla\alpha_s \cdot \mathbf{n} = 0$
Θ_s	$1 \cdot 10^{-4}$ m^2/s^2	$\nabla\Theta_s \cdot \mathbf{n} = 0$	Johnson and Jackson [1]
$\mathbf{U}_s$	No slip	$\nabla\mathbf{U}_s \cdot \mathbf{n} = 0$	Johnson and Jackson [1]
$\mathbf{U}_g$	$\mathbf{U}_g = U\frac{\mathbf{n}}{\lvert\mathbf{n}\rvert}$	$\nabla\mathbf{U}_g \cdot \mathbf{n} = 0$	No slip
p_g	$\nabla p_g \cdot \mathbf{n} = 0$	$1 \cdot 10^5$ Pa	$\nabla p_g \cdot \mathbf{n} = 0$
q	$\nabla q \cdot \mathbf{n} = 0$	$\nabla q \cdot \mathbf{n} = 0$	Charge BC (Eq. 2-68)
φ_E	$\nabla\varphi_E \cdot \mathbf{n} = 0$	$\nabla\varphi_E \cdot \mathbf{n} = 0$	0 V

2.5.3. Results

2.5.3.1. Grid convergence

To ensure grid-independence of the results, the computational domain was decomposed as per the discussion in Section 2.5.2. The total number of cell divisions in the horizontal direction (along the bed width) was varied from 60 to 160 in increments of 20, and the results are compared in Figure 2-4. For all the cases, the initial and boundary conditions corresponding to the 362 μm case (Table 2-2,Table 2-3) were used. The simulation was run up to 10 s and all the properties were time-averaged over the period between 4-10 s, when steady state was reached. Figure 2-4(a) indicates insignificant deviation in the coefficient of variance (COV), with electric potential as the exception. The deviation is calculated considering the values obtained in the most refined grid as the base. Figure 2-4(b) also shows that the deviation in maximum electric potential and total charge in the bed reduces with increased refinement. For satisfactory accuracy therefore, at least 140 cells would be required along the bed width, and hence 160 cells have been used for the rest of the simulations discussed in this paper. The total charge (Figure 2-4(b)) is calculated as per Eq. 2-70, which is the volume fraction weighted total charge in the system. This is not the true charge that would be measured in experiments, since the simulation is carried out in a two-dimensional domain, and the

$$Q_{total} = \int \alpha q d\mathbb{V} = \sum \alpha_i q_i \mathbb{V}_i \qquad 2\text{-}70$$

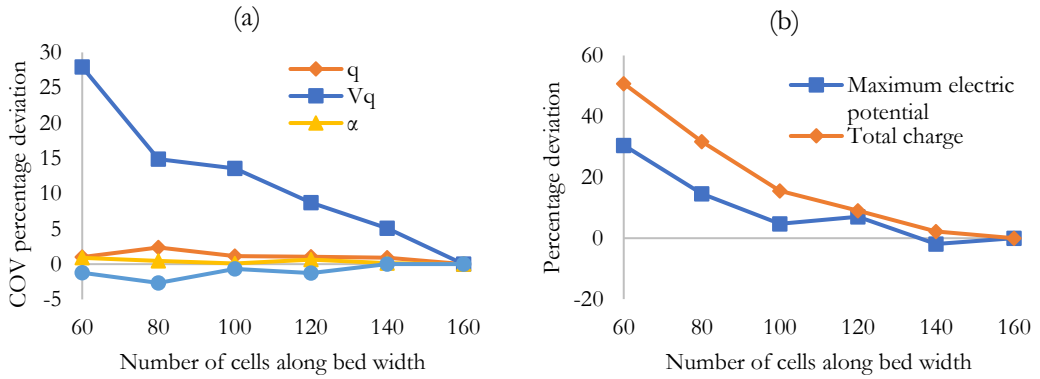

Figure 2-4: Plots illustrating grid convergence through comparison of deviation of (a) coefficient of variance, (b) maximum electric potential and total charge in the bed, w.r.t. the most refined grid.

2.5.3.2. Simulation Results

Using the grid decomposition and simulation settings described in the previous sections, the computation was allowed to run up to 10 s. The compiled code was executed using 16 parallel MPI processes and entailed a computation time of approximately 15-30 hours for each case, depending on the minimum time step. To check whether the system has reached steady state or not, the total bed charge was monitored (Figure 2-5), and it only seemed to fluctuate about some mean value after the initial 4s, for all cases. This therefore signified a steady state of electrification. However, it should be noted that a steady layer of particles on the wall was observed only after about 15 minutes of fluidization in experiments [73] and thus the results presented here are accelerated versions of the actual process. This difference may be due to the value of the selected parameters of the charging model, particularly the charging efficiency, but also to the fact that charge transport due to diffusion could be accelerated compared to the experiments. These aspects should be further investigated in future studies by performing a sensitivity analysis of the model to its parameters, and by considering the impact of the assumptions made in the derivation of the model, particularly those in Sec. 2.3.5 and 2.3.6 which led to the proposed formulation of the charge-velocity covariance and the charge variance. Figure 2-6 shows a snapshot of the particle volume fraction and velocity, and of the electric field properties for the particles of 362 µm diameter, at 10 s.

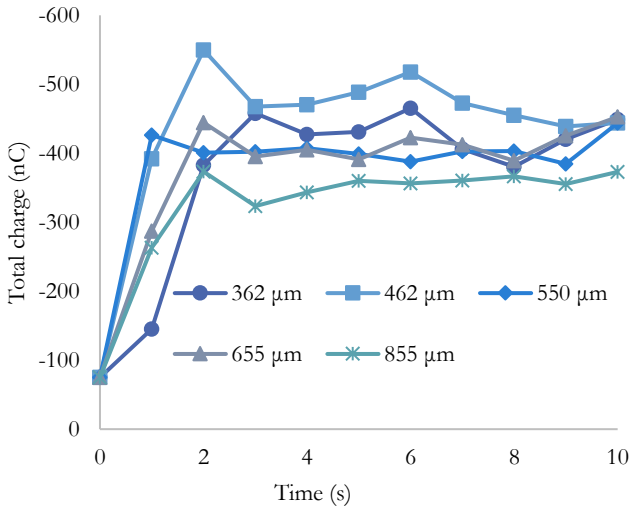

Figure 2-5: Evolution of total bed charge.

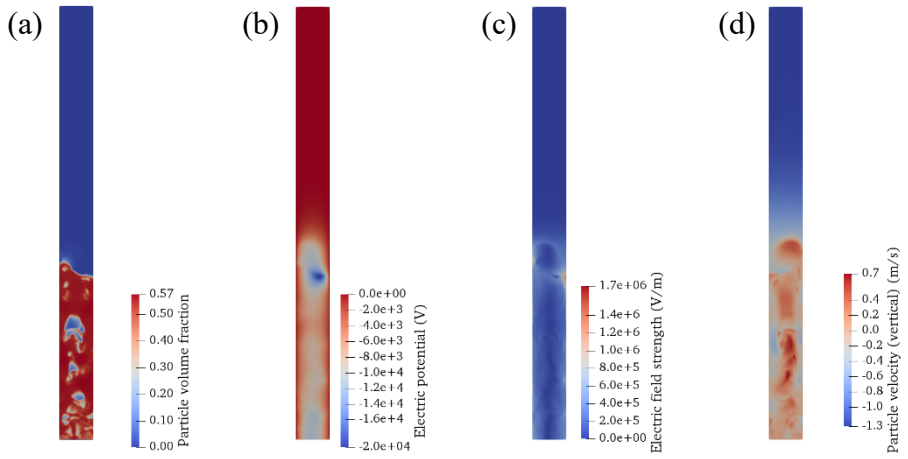

Figure 2-6: Contour plots of (a) particle volume fraction, (b) electric potential, (c) electric field strength, and (d) vertical component of particle phase velocity, at T = 10s.

As in the experiments, the particles in the bed were then allowed to settle by changing the inlet boundary conditions as per Table 2-5. All the boundary conditions at the inlet are simply changed to those at the wall, thus accounting for contact with the distributor plate. Figure 2-7 shows how the volume fraction changes as the particles settle, which become stationary after T = 12s. To compare experimental observations, the charge distribution and force field is now analyzed.

Table 2-5: Simulation boundary conditions

Variable	*Inlet (fluidization)*	*Inlet (settling)*
α_s	0	$\nabla\alpha_s \cdot \mathbf{n} = 0$
Θ_s	$1 \cdot 10^{-4}\ \mathrm{m}^2/\mathrm{s}^2$	Johnson and Jackson [1]
$\mathbf{U}_s$	No slip	Johnson and Jackson [1]
$\mathbf{U}_g$	$\mathbf{U}_g = U\frac{\mathbf{n}}{\lvert\mathbf{n}\rvert}$	$\mathbf{U}_g = \mathbf{0}$
p_g	$\nabla p_g \cdot \mathbf{n} = 0$	$\nabla p_g \cdot \mathbf{n} = 0$
q	$\nabla q \cdot \mathbf{n} = 0$	Charge BC (Eq. 2-68)
φ_E	$\nabla\varphi_E \cdot \mathbf{n} = 0$	0 V

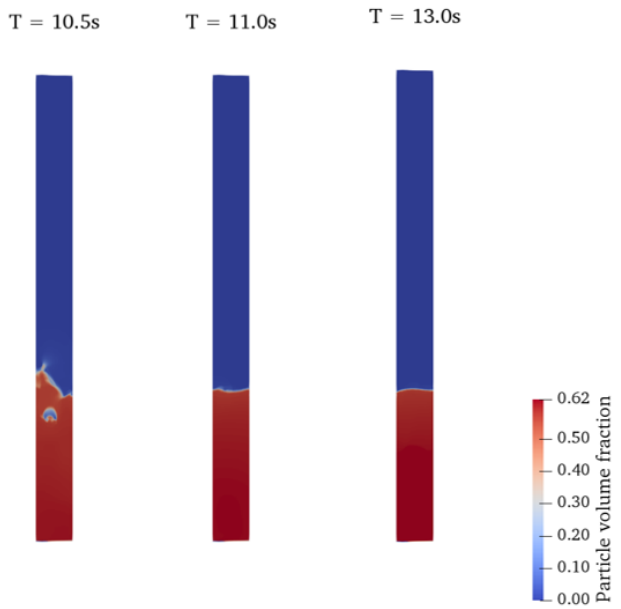

Figure 2-7: Contour plots of particle volume fraction as the particles settle.

First, we investigate the electric potential in the bed and look for signs of air ionization (breakdown). Figure 2-8 (a, b) show the electric potential profiles in relation to the Paschen's curve, which is explained in the context of the charged bed as follows. The Paschen's breakdown voltage signifies the minimum potential difference between two electrodes (or surfaces in this case) required for ionization of air and is a function of their separation distance. Since the wall is grounded, the electric potential at any location is the difference in potential between a charged particle at that location and the wall. This potential difference must be greater than the potential difference between any two particles at any location, since the gradient of potential (or the electric field strength) is maximum at the wall. Hence, the electric potential at any point can be implied as the maximum potential difference with any other point in the column. Thus, the Paschen's curve at STP has been plotted as a function of distance from the wall and if it envelopes the electric potential curve within its limits, it can be concluded there are no two points in the bed between which breakdown would occur. The profiles in Figure 2-8 (a, b) represent the maximum potential encountered at a given x-position (location along the bed width) at any height. Interestingly, in Figure 2-8 (b), the electric potential near the left wall for the 462 μm case crosses over the Paschen's curve, which points to increased probability of breakdown in this region. This difference is small, and its effect is assumed to be negligible. However, air ionization may need to be modeled to account for such occurrences in the future.

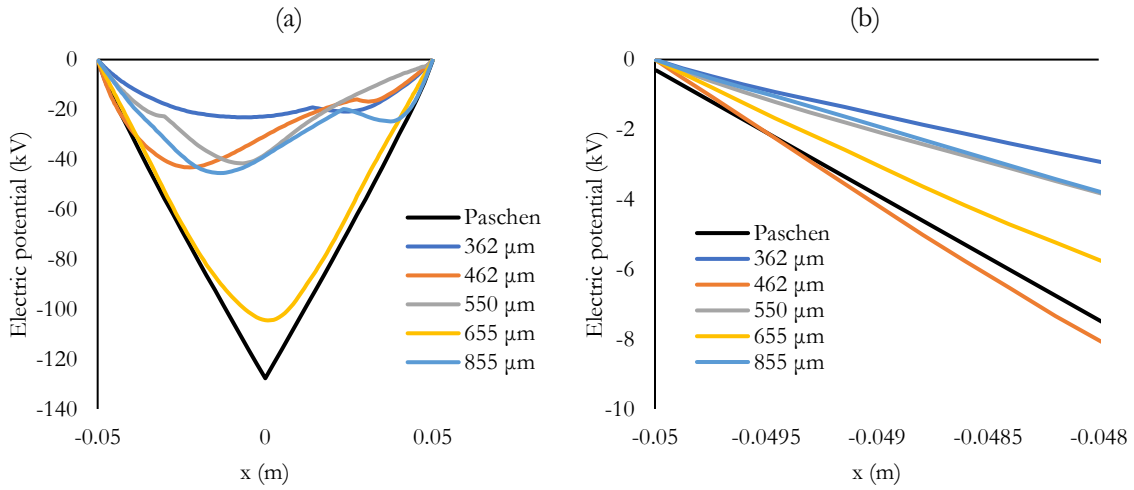

Figure 2-8: Variation of electric potential across (a) the bed width, and (b) near the left wall.

The variation of particle charge in the settled bed is shown in Figure 2-9, which similar to the electric potential (Figure 2-8) is the highest magnitude of charge for a given x-location (for all y-values). Figure 2-9(a, b) show the variation across the whole bed width, but with different ranges of magnitude, while Figure 2-9(c, d) highlight the steep gradients near the wall. To validate the usefulness of the model in predicting the formation of a layer of particles that stick to the wall surface, the simulation results are compared to those of the experiments [68] as illustrated in Figure 2-10. Ideally, the bed should have been allowed to drain out and the properties of the particles sticking to the wall after draining should have been analyzed. Such a simulation leads to the volume fraction becoming very low (tending to zero) due to the nature of the two-fluid model, which is not expected physically based on the charge density and the corresponding force field magnitudes. Hence the properties were approximately determined through analysis of the fields in the settled bed. Figure 2-10(a) shows the thickness of the particle layer on the wall, for each of the cases. To find the thickness, we had to determine if a particle placed in a location on the wall or a certain distance away from it would have enough electrostatic force acting on it such that friction could resist dropping due to gravity. For this, the average force acting over the width of a particle is calculated, and this is carried out by imagining the particle being placed a given distance away from the wall, and averaging the force profile across its width. The distance beyond which this force is lower than the threshold is assumed to be the wall layer thickness at that bed height, since beyond this any particle will have an increased probability of falling off.

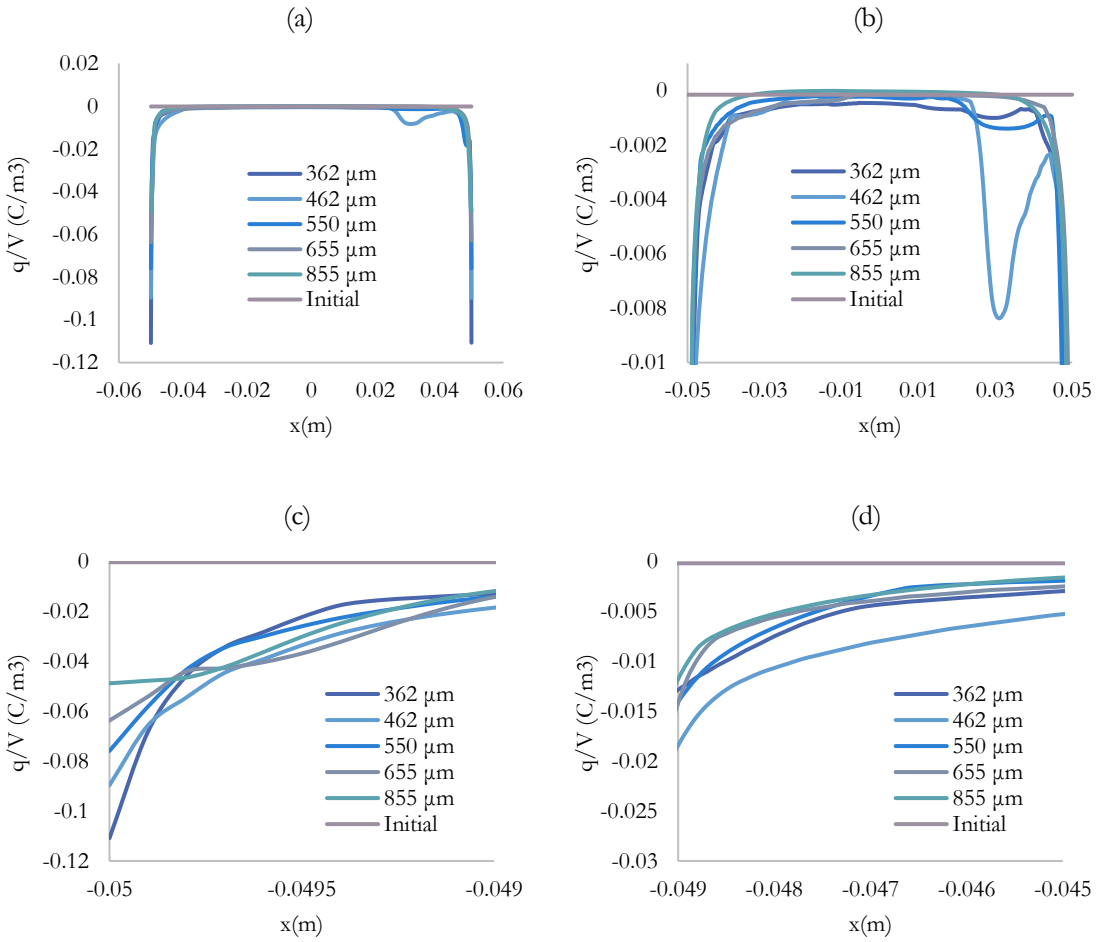

Figure 2-9: Variation of particle charge density across the bed: (a) full bed width and entire range of magnitude, (b) full bed width with one order lower magnitude (c) up to 1 mm from the left wall, (d) between 1 mm and 5 mm from the left wall.

The threshold electrostatic force density was found to be 16000 N/m3 base on Eq. 2-71 for an angle of repose of 30 degrees (Table 2-1). Using this threshold value, it was seen that the thickness (Figure 2-10 (a)) was not uniform along the bed axis. The maximum thickness was also not correlated to the particle size. However, with increasing diameter, a trend of decreasing tendency of sticking is observed. This corroborates to the experimental results as seen in Figure 2-10 (b) which shows that for 655 µm and 855 µm sizes, the fraction of particles on the wall is low. We observe higher percentages of particles on the wall for the other diameters in the simulation although these values are lower than those seen in the experiments. We also determined the average q/m ratio on the wall layer and this seemed to be coherent with the lab tests Figure 2-10 (c). The same is done for the remaining particles (bulk) in the bed, and the q/m ratios correspond closely

to the experimental values for sizes up to 550 µm (Figure 2-10 (d)). For the two largest sizes, there is a significant deviation, which can be caused due to several reasons. Sowinski had mentioned that some of the highly charged loosely bound particles fall off and causes an increase in the average dropped particle charge measurement [67].

$$F_{min} = \frac{Mg}{\mu} = \frac{Mg}{\tan\theta} \qquad 2\text{-}71$$

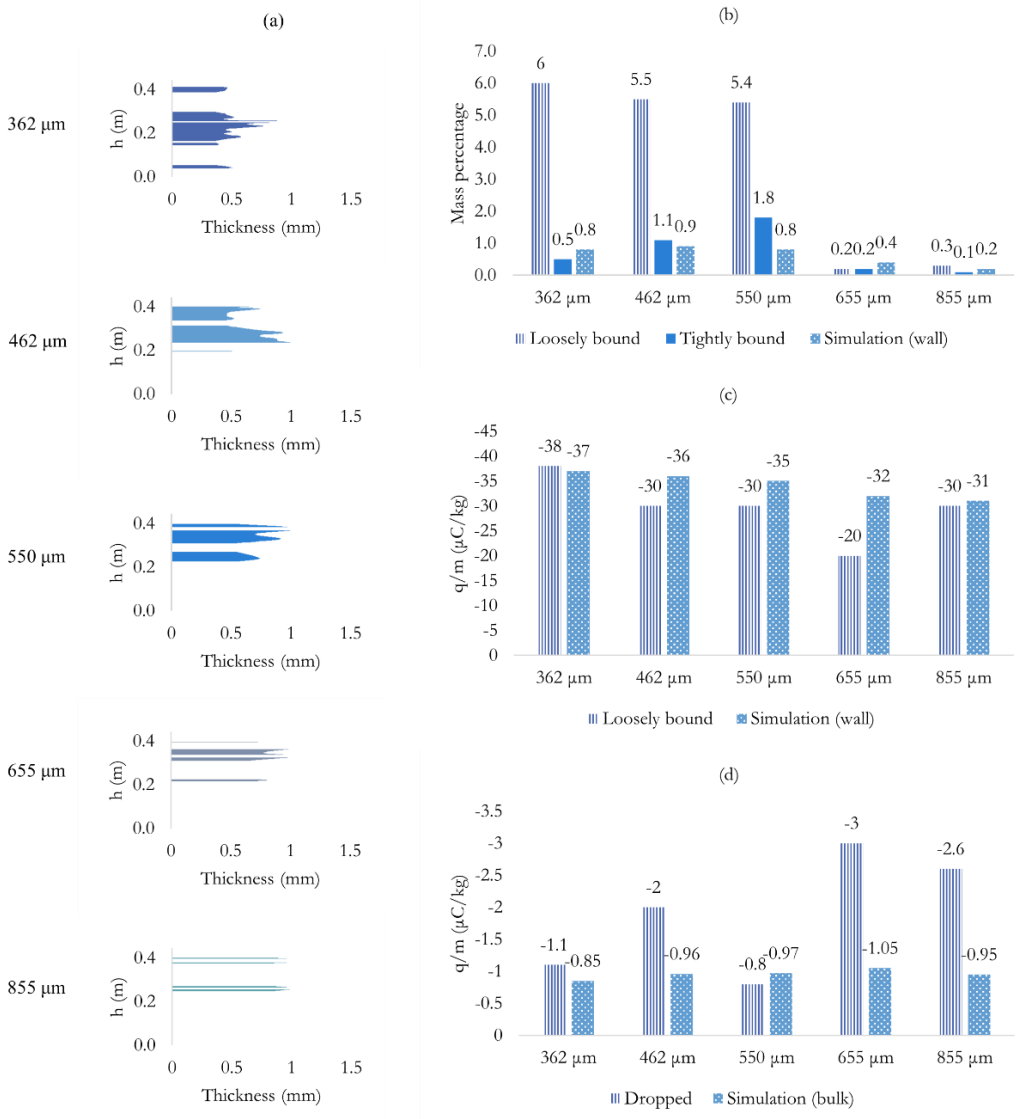

Figure 2-10: (a) Particle layer thickness on the wall as a function of height for different diameters; Comparison of (a) mass percentage of particles sticking to the wall (loosely and tightly bound represent experimental results), (b) q/m ratio of wall particles in the simulation and loosely bound particles in the experiments, and (c) q/m ratio of bulk particles in the simulation and dropped particles in the experiments.

2.6. Conclusion

A model describing contact charging due to collisions of particles with a solid wall was derived, consistent with the boundary conditions developed for the hydrodynamic model by Johnson and Jackson (1987) [1], and using the charging model of Matsusaka et al. (2000) [2]. A charge diffusion model for mono-disperse particles, based on the collisional theory of Jenkins and Savage (1983) [3] and on the charge transfer model of Matsusaka et al. (2000) [2], was developed and tested in this work. Charge and velocity were assumed to be correlated and an expression for the corresponding covariance was derived, which had a significant contribution to the diffusion rate. Employing these in conjunction with the Eulerian two-fluid model, the phenomenon of electrification in a fluidized bed of polyethylene particles was simulated with emphasis on the effect of particle size. The dimensions of the bed, fluidization parameters and particle size groups used in the simulation were the same as that used in the experiments [67,68], whose results were used for the model validation.

Based on the simulation results and observations, the process of electrification in the fluidized bed can be explicated as such. The initial uniform bed charge produces an electric field which is linear. The wall flux boundary condition imposes a steep gradient at the wall, which initiates charge diffusion into the fluidized bed. During fluidization, gradients of granular temperature and particle charge density diffuse the charge and cause an increase in the total bed charge as well as the potential energy of the system. This results in an increase of the electric field strength, while the gradient of charge density at the wall boundary fluctuates. The latter contributes to further diffusion while the former acts as a resistance to this process. This continues until a dynamic equilibrium is reached.

After steady state of total charge and electrical potential were observed, the bed was allowed to settle down and the properties at this state were analyzed. The electric potential in the bed was within the envelope of Panchen's curve for all cases except 462 μm, although no significant occurrence of ionization was expected based on the values. The average electrostatic force acting on a particle at different locations was calculated to determine the expected value of the wall layer thickness. The propensity of particles to stick on the wall was shown to attenuate with increasing size. This was confirmed by the same trend in the mass percentage of wall particles, which was consistent with laboratory observations. The q/m ratio of the wall particles in the simulation was

close to the corresponding values for the loosely bound particles in the experiments, although some differences were obtained when comparing the same between bulk particles in the simulation and dropped particles in the experiments, particularly for particle diameters 655 μm and 855 μm.

The steady state for all cases was achieved in 4 s, whereas it is expected to take at least 15 minutes based on experiments [73]. This large discrepancy may be attributed to the electrostatic parameters and also on the rate of self-diffusion which seems to overestimate the diffusion process. These need to be separately and thoroughly investigated. The experimental results also suggested variation in particle sticking and charge density magnitudes, when different fluidization velocities and wall materials were used [35,67]. These will be analyzed and discussed in future work.

Appendix - Derivation of the interparticle collisional rate of change of charge

Details of the derivation of the collisional rate of change of charge of a solid particle due to collisions with another particle are reported in this appendix for the interested reader.

Charge transport equation

The charge transport equation which needs to be solved is given as

$$\frac{\partial}{\partial t}(\alpha_s \rho_s \langle q \rangle) + \nabla \cdot (\alpha_s \rho_s \langle q \rangle \mathbf{U}_s) + \nabla \cdot (\alpha_s \rho_s \langle \mathbf{C} q' \rangle) = m_p \mathbb{C}(q) \qquad 2\text{-}72$$

To evaluate terms in the transport equation, we need to evaluate the associated collision integrals, for which we employ the assumptions described in sections (2.3.1-2.3.6). In all these integrals $\mathbf{C}_1 q'_1$, $\mathbf{C}_2 q'_2$, $\mathbf{C}_1 q'_2$ and $\mathbf{C}_2 q'_1$ are treated as independent variables. Henceforth, it should be noted that

$$\mathbf{c}_{12} = \mathbf{c}_2 - \mathbf{c}_1 = \mathbf{C}_2 - \mathbf{C}_1$$

and

$$q_{12} = q_2 - q_1 = q'_2 - q'_1$$

The following expression is also useful for evaluation of the integrals

$$\langle q_{12}\mathbf{c}_{12}\rangle = \langle (q_2 - q_1)(\mathbf{c}_2 - \mathbf{c}_1)\rangle = \langle \left(q'_2 - q'_1\right)(\mathbf{C}_2 - \mathbf{C}_1)\rangle$$
$$= \langle \mathbf{C}_1 q'_1 + \mathbf{C}_2 q'_2 - \mathbf{C}_1 q'_2 - \mathbf{C}_1 q'_2\rangle = 2\langle \mathbf{C}q'\rangle \quad \text{2-73}$$

Derivation of expression for $\langle \boldsymbol{C}q'\rangle$

For this we consider the transport equation for $\langle \mathbf{c}q\rangle$ which is

$$\frac{\partial}{\partial t}(\alpha_s \rho_s \langle \mathbf{c}q\rangle) + \nabla \cdot (\alpha_s \rho_s \langle \mathbf{cc}q\rangle) = m_p \mathbb{C}(\mathbf{c}q) + \alpha_s \rho_s \langle \frac{\partial \mathbf{c}q}{\partial \mathbf{c}} \frac{\mathrm{d}\mathbf{c}}{\mathrm{dt}}\rangle + \alpha_s \rho_s \langle \frac{\partial \mathbf{c}q}{\partial q} \frac{\mathrm{dq}}{\mathrm{dt}}\rangle, \quad \text{2-74}$$

simplifying to (since no charge is generated in the volume)

$$\frac{\partial}{\partial t}(\alpha_s \rho_s \langle \mathbf{c}q\rangle) + \nabla \cdot (\alpha_s \rho_s \langle \mathbf{cc}q\rangle) = m_p \mathbb{C}(\mathbf{c}q) + \alpha_s \rho_s \langle q \frac{\mathbf{F}}{m_p}\rangle. \quad \text{2-75}$$

If we consider $\langle \mathbf{c}q\rangle$ as a quasi-steady variable, we have

$$\nabla \cdot (\alpha_s \rho_s \langle \mathbf{cc}q\rangle) = m_p \mathbb{C}(\mathbf{c}q) + \alpha_s \rho_s \langle q \frac{\mathbf{F}}{m_p}\rangle \quad \text{2-76}$$

and also note that

$$\nabla \cdot (\alpha_s \rho_s \langle \mathbf{cc}q\rangle) = \nabla \cdot (\alpha_s \rho_s \mathbf{U}_s \langle \mathbf{c}q\rangle) + \nabla \cdot (\alpha_s \rho_s \langle \mathbf{Cc}q\rangle). \quad \text{2-77}$$

Treating divergence of terms containing $\mathbf{U}_s$ as negligible and neglecting the correlation between fluctuation velocity and charge variance $\langle \mathbf{CC}q'\rangle$ gives

$$\nabla \cdot (\alpha_s \rho_s \langle \mathbf{cc}q\rangle) = \nabla \cdot (\alpha_s \rho_s \langle \mathbf{Cc}q\rangle) = \nabla \cdot (\alpha_s \rho_s \langle q\rangle \langle \mathbf{CC}\rangle). \quad \text{2-78}$$

Also, if gradients of $\alpha_s, \rho_s, \langle \mathbf{CC}\rangle$ are considered negligible compared to gradients of $\langle q\rangle$, we get

$$\nabla \cdot (\alpha_s \rho_s \langle \mathbf{cc}q\rangle) = \alpha_s \rho_s \Theta_s \nabla \langle q\rangle. \quad \text{2-79}$$

Hence, the transport equation for $\langle \mathbf{c}q\rangle$ reduces to

$$m_p \mathbb{C}(\mathbf{c}q) = \alpha_s \rho_s \Theta_s \nabla \langle q\rangle - \alpha_s \rho_s \langle q \frac{\mathbf{F}}{m_p}\rangle. \quad \text{2-80}$$

Evaluation of collisional diffusion of $\mathbf{c}q$

$$m_p \mathbb{C}(\mathbf{c}q) = m_p\left(\boldsymbol{\chi}_{\mathbf{c}q} - \nabla \cdot \theta_{\mathbf{c}q}\right) \tag{2-81}$$

such that

$$\boldsymbol{\chi}_{\mathbf{c}q} = \frac{\mathrm{d_p^2}}{2} \int_{\mathbf{c}_{12}\cdot\mathbf{k}>0} \int_{\mathbb{R}^6} \int_{\mathbb{R}^2} \left((\mathbf{c}q)'_2 + (\mathbf{c}q)'_1 - (\mathbf{c}q)_2 - (\mathbf{c}q)_1\right) \times (\mathbf{c}_{12}\cdot\mathbf{k}) f^2 \, \mathrm{d}q_1 \mathrm{d}q_2 \mathrm{d}\mathbf{c}_1 \mathrm{d}\mathbf{c}_2 \mathrm{d}\mathbf{k} \tag{2-82}$$

and

$$\theta_{\mathbf{c}q} = \frac{\mathrm{d_p^3}}{2} \int_{\mathbf{c}_{12}\cdot\mathbf{k}>0} \int_{\mathbb{R}^6} \int_{\mathbb{R}^2} \mathbf{k}\left((\mathbf{c}q)'_1 - (\mathbf{c}q)_1\right)(\mathbf{c}_{12}\cdot\mathbf{k}) f^2 \, \mathrm{d}q_1 \mathrm{d}q_2 \mathrm{d}\mathbf{c}_1 \mathrm{d}\mathbf{c}_2 \mathrm{d}\mathbf{k}, \tag{2-83}$$

where

$$(\mathbf{c}q)'_1 - (\mathbf{c}q)_1 = q_1 \frac{d\mathbf{c}_1}{dn_c} + \mathbf{c}_1 \frac{dq_1}{dn_c} + \frac{dq_1}{dn_c}\frac{d\mathbf{c}_1}{dn_c}$$

and

$$(\mathbf{c}q)'_2 - (\mathbf{c}q)_2 = q_2 \frac{d\mathbf{c}_2}{dn_c} + \mathbf{c}_2 \frac{dq_2}{dn_c} + \frac{dq_2}{dn_c}\frac{d\mathbf{c}_2}{dn_c}$$

with

$$\frac{d\mathbf{c}_1}{dn_c} = -\frac{d\mathbf{c}_2}{dn_c} = \frac{1}{2}(1+e)(\mathbf{c}_{12}\cdot\mathbf{k})\mathbf{k}$$

and

$$\frac{dq_1}{dn_c} = -\frac{dq_2}{dn_c} = \left[K_1(q_2 - q_1) + K_2\left(\mathbf{E}_q \cdot \mathbf{k}\right)\right](\mathbf{c}_{12}\cdot\mathbf{k})^{4/5}$$

Evaluation of χ_{cq}

$$I_{\chi_{\mathbf{c}q,1}} = \frac{\mathrm{d_p}^2}{2} \int_{\mathbf{c}_{12}\cdot\mathbf{k}>0} \int_{\mathbb{R}^6} \int_{\mathbb{R}^2} \left(q_1 \frac{d\mathbf{c}_1}{dn_c} + q_2 \frac{d\mathbf{c}_2}{dn_c} \right) (\mathbf{c}_{12}\cdot\mathbf{k}) f^2 \, \mathrm{d}q_1 \mathrm{d}q_2 \mathrm{d}\mathbf{c}_1 \mathrm{d}\mathbf{c}_2 \mathrm{d}\mathbf{k}$$

$$= \frac{\mathrm{d_p}^2}{2} \int_{\mathbf{c}_{12}\cdot\mathbf{k}>0} \int_{\mathbb{R}^6} \int_{\mathbb{R}^2} \left(-\frac{1}{2}(1+e) q_{12} (\mathbf{c}_{12}\cdot\mathbf{k})\mathbf{k} \right) \times (\mathbf{c}_{12}\cdot\mathbf{k}) f^2 \, \mathrm{d}q_1 \mathrm{d}q_2 \mathrm{d}\mathbf{c}_1 \mathrm{d}\mathbf{c}_2 \mathrm{d}\mathbf{k} = -g_0 N^2 \mathrm{d_p}^2 (1+e) \sqrt{\pi \Theta_s} \langle \mathbf{C}q' \rangle \quad \text{2-84}$$

$$I_{\chi_{\mathbf{c}q,2}} = \frac{\mathrm{d_p}^2}{2} \int_{\mathbf{c}_{12}\cdot\mathbf{k}>0} \int_{\mathbb{R}^6} \int_{\mathbb{R}^2} \left(\mathbf{c}_1 \frac{dq_1}{dn_c} + \mathbf{c}_2 \frac{dq_2}{dn_c} \right) (\mathbf{c}_{12}\cdot\mathbf{k}) f^2 \, \mathrm{d}q_1 \mathrm{d}q_2 \mathrm{d}\mathbf{c}_1 \mathrm{d}\mathbf{c}_2 \mathrm{d}\mathbf{k}$$

$$= \frac{\mathrm{d_p}^2}{2} \int_{\mathbf{c}_{12}\cdot\mathbf{k}>0} \int_{\mathbb{R}^6} \int_{\mathbb{R}^2} \left(-K_1 q_{12} \mathbf{c}_{12} - K_2 (\mathbf{E}_q \cdot \mathbf{k}) \mathbf{c}_{12} \right) (\mathbf{c}_{12}\cdot\mathbf{k})^{4/5} \times (\mathbf{c}_{12}\cdot\mathbf{k}) f^2 \, \mathrm{d}q_1 \mathrm{d}q_2 \mathrm{d}\mathbf{c}_1 \mathrm{d}\mathbf{c}_2 \mathrm{d}\mathbf{k} \quad \text{2-85}$$

$$= -g_0 N^2 \mathrm{d_p}^2 \times \left[\left(\frac{5}{7} 2^{14/5} \Gamma\left(\frac{12}{5}\right) \sqrt{\pi} K_1 {\Theta_s}^{9/10} \langle \mathbf{C}q' \rangle \right) + \left(\frac{5}{57} 2^{19/5} \Gamma\left(\frac{29}{10}\right) \sqrt{\pi} K_2 {\Theta_s}^{7/5} \mathbf{E}_q \right) \right]$$

$$I_{\chi_{\mathbf{c}q,3}} = \frac{\mathrm{d_p}^2}{2} \int_{\mathbf{c}_{12}\cdot\mathbf{k}>0} \int_{\mathbb{R}^6} \int_{\mathbb{R}^2} \left(\frac{dq_1}{dn_c}\frac{d\mathbf{c}_1}{dn_c} + \frac{dq_2}{dn_c}\frac{d\mathbf{c}_2}{dn_c} \right) (\mathbf{c}_{12}\cdot\mathbf{k}) f^2 \, \mathrm{d}q_1 \mathrm{d}q_2 \mathrm{d}\mathbf{c}_1 \mathrm{d}\mathbf{c}_2 \mathrm{d}\mathbf{k}$$

$$= \frac{\mathrm{d_p}^2}{2} \int_{\mathbf{c}_{12}\cdot\mathbf{k}>0} \int_{\mathbb{R}^6} \int_{\mathbb{R}^2} (1+e) \left(K_1 q_{12} + K_2 (\mathbf{E}_q \cdot \mathbf{k}) \right) (\mathbf{c}_{12}\cdot\mathbf{k})^{9/5} \times (\mathbf{c}_{12}\cdot\mathbf{k}) f^2 \, \mathrm{d}q_1 \mathrm{d}q_2 \mathrm{d}\mathbf{c}_1 \mathrm{d}\mathbf{c}_2 \mathrm{d}\mathbf{k} \quad \text{2-86}$$

$$= g_0 N^2 \mathrm{d_p}^2 (1+e) \times \left[\left(\frac{5}{12} 2^{14/5} \Gamma\left(\frac{12}{5}\right) \sqrt{\pi} K_1 {\Theta_s}^{9/10} \langle \mathbf{C}q' \rangle \right) + \left(\frac{23}{264} 2^{19/5} \Gamma\left(\frac{29}{10}\right) \sqrt{\pi} K_2 {\Theta_s}^{7/5} \mathbf{E}_q \right) \right]$$

Therefore,

$$\boldsymbol{\chi}_{\mathbf{c}q} = -g_0 N^2 \mathrm{d_p}^2 \times \left\{ \left[(1+e)\sqrt{\pi\Theta_s} + \left(\frac{5}{7} - \frac{5}{12}(1+e) \right) 2^{14/5} \Gamma\left(\frac{12}{5}\right) \sqrt{\pi} K_1 {\Theta_s}^{9/10} \right] \langle \mathbf{C}q' \rangle + \left(\frac{5}{57} - \frac{23}{264}(1+e) \right) 2^{19/5} \Gamma\left(\frac{29}{10}\right) \sqrt{\pi} K_2 {\Theta_s}^{7/5} \mathbf{E}_q \right\} \quad \text{2-87}$$

Evaluation of θ_{cq}

$$I_{\theta_{\mathbf{c}q},1} = \frac{\mathrm{d_p}^3}{2} \int_{\mathbf{c}_{12}\cdot\mathbf{k}>0} \int_{\mathbb{R}^6} \int_{\mathbb{R}^2} \mathbf{k} \left(q_1 \frac{d\mathbf{c}_1}{dn_c} \right) (\mathbf{c}_{12}\cdot\mathbf{k}) f^2 \, \mathrm{d}q_1 \mathrm{d}q_2 \mathrm{d}\mathbf{c}_1 \mathrm{d}\mathbf{c}_2 \mathrm{d}\mathbf{k}$$

$$= \frac{\mathrm{d_p}^3}{2} \int_{\mathbf{c}_{12}\cdot\mathbf{k}>0} \int_{\mathbb{R}^6} \int_{\mathbb{R}^2} \mathbf{k} \left(\frac{1}{2}(1+e) q_1 (\mathbf{c}_{12}\cdot\mathbf{k}) \mathbf{k} \right) \times (\mathbf{c}_{12}\cdot\mathbf{k}) f^2 \, \mathrm{d}q_1 \mathrm{d}q_2 \mathrm{d}\mathbf{c}_1 \mathrm{d}\mathbf{c}_2 \mathrm{d}\mathbf{k} = \frac{1}{2} g_0 N^2 \mathrm{d_p}^3 (1+e) \langle q \rangle \Theta_s \mathrm{I} \quad \text{2-88}$$

$$I_{\theta_{\mathbf{c}q},2} = \frac{\mathrm{d_p}^3}{2} \int_{\mathbf{c}_{12}\cdot\mathbf{k}>0} \int_{\mathbb{R}^6} \int_{\mathbb{R}^2} \mathbf{k} \left(\mathbf{c}_1 \frac{dq_1}{dn_c} \right) (\mathbf{c}_{12}\cdot\mathbf{k}) f^2 \, \mathrm{d}q_1 \mathrm{d}q_2 \mathrm{d}\mathbf{c}_1 \mathrm{d}\mathbf{c}_2 \mathrm{d}$$

$$= \frac{\mathrm{d_p}^3}{2} \int_{\mathbf{c}_{12}\cdot\mathbf{k}>0} \int_{\mathbb{R}^6} \int_{\mathbb{R}^2} \mathbf{k} \left(\mathbf{c}_1 \left(K_1 q_{12} + K_2 (\mathbf{E}_q \cdot \mathbf{k}) \right) (\mathbf{c}_{12}\cdot\mathbf{k})^{4/5} \right) \times (\mathbf{c}_{12}\cdot\mathbf{k}) f^2 \, \mathrm{d}q_1 \mathrm{d}q_2 \mathrm{d}\mathbf{c}_1 \mathrm{d}\mathbf{c}_2 \mathrm{d}\mathbf{k} \quad \text{2-89}$$

$$= g_0 N^2 \mathrm{d_p}^3 \times \left[\left(\frac{5}{12} 2^{14/5} \Gamma\left(\frac{12}{5}\right) \sqrt{\pi} K_1 {\Theta_s}^{9/10} \langle \mathbf{C}q' \rangle \right) + \left(\frac{5}{108} 2^{14/5} \Gamma\left(\frac{12}{5}\right) \sqrt{\pi} K_2 {\Theta_s}^{7/5} \mathbf{E}_q \right) \right] \mathbf{U}_\mathrm{s}$$

$$I_{\theta_{cq},3} = \frac{\mathrm{d_p^3}}{2} \int_{\mathbf{c}_{12}\cdot\mathbf{k}>0} \int_{\mathbb{R}^6} \int_{\mathbb{R}^2} \mathbf{k}\left(\frac{dq_1}{dn_c}\frac{d\mathbf{c}_1}{dn_c}\right)(\mathbf{c}_{12}\cdot\mathbf{k}) f^2 \,\mathrm{d}q_1 \mathrm{d}q_2 \mathrm{d}\mathbf{c}_1 \mathrm{d}\mathbf{c}_2 \mathrm{d}\mathbf{k}$$

$$= \frac{\mathrm{d_p^3}}{2} \int_{\mathbf{c}_{12}\cdot\mathbf{k}>0} \int_{\mathbb{R}^6} \int_{\mathbb{R}^2} \mathbf{k}\left(\frac{1}{2}(1+e)\left(K_1 q_{12} + K_2(\mathbf{E}_q\cdot\mathbf{k})\right)(\mathbf{c}_{12}\cdot\mathbf{k})^{9/5}\mathbf{k}\right) \tag{2-90}$$

$$\times (\mathbf{c}_{12}\cdot\mathbf{k}) f^2 \,\mathrm{d}q_1 \mathrm{d}q_2 \mathrm{d}\mathbf{c}_1 \mathrm{d}\mathbf{c}_2 \mathrm{d}\mathbf{k} = 0$$

Hence,

$$\theta_{\mathbf{c}q} = g_0 N^2 \mathrm{d_p^3}\left\{\frac{1}{2}(1+e)\langle q\rangle \Theta_s \mathrm{I}\right.$$

$$+ \left[\left(\frac{5}{12} 2^{14/5}\Gamma\left(\frac{12}{5}\right)\sqrt{\pi} K_1 {\Theta_s}^{9/10}\langle \mathbf{C}q'\rangle\right)\right. \tag{2-91}$$

$$\left.\left. + \left(\frac{5}{108} 2^{14/5}\Gamma\left(\frac{12}{5}\right)\sqrt{\pi} K_2 {\Theta_s}^{7/5}\mathbf{E}_q\right)\right]\mathbf{U}_s\right\}.$$

Again, ignoring divergence of terms containing $\mathbf{U}_s$, we arrive at the following expression for the charge-velocity covariance:

$$\langle \mathbf{C}q'\rangle = -\frac{1}{(1+e)\sqrt{\pi\Theta_s} +}$$

$$\times \left[\left(\frac{1}{2}(1+e) + \frac{\pi}{6 g_0 \alpha_s}\right) d_p \Theta_s \nabla\langle q\rangle - \frac{\pi d_p}{6 g_0 \alpha_s}\langle\frac{\mathbf{F}}{m_p}\rangle\langle q\rangle\right. \tag{2-92}$$

$$\left. + \left(\frac{5}{57} - \frac{23}{264}(1+e)\right) 2^{19/5}\Gamma\left(\frac{29}{10}\right)\sqrt{\pi} K_2 {\Theta_s}^{7/5}\mathbf{E}_q\right].$$

Derivation of expression for charge variance

The transport equation of charge variance is given by

$$\frac{\partial}{\partial t}(\alpha_\mathrm{s}\rho_\mathrm{s}\langle q'q'\rangle) + \nabla\cdot(\alpha_\mathrm{s}\rho_\mathrm{s}\langle \mathbf{c}q'q'\rangle)$$

$$= m_p \mathbb{C}(q'q') + +\alpha_\mathrm{s}\rho_\mathrm{s}\langle\frac{\partial q'q'}{\partial \mathbf{c}}\frac{\mathrm{d}\mathbf{c}}{\mathrm{d}t}\rangle + \alpha_\mathrm{s}\rho_\mathrm{s}\langle\frac{\partial q'q'}{\partial q}\frac{\mathrm{d}q}{\mathrm{d}t}\rangle. \tag{2-93}$$

If it is assumed that $q'q'$ is not a function of $\mathbf{c}$ and that $\langle q'q' \rangle$ is a quasi-steady variable, we get

$$\nabla \cdot (\alpha_s \rho_s \langle \mathbf{c} q'q' \rangle) = m_p \mathbb{C}(q'q') \tag{2-94}$$

and also note that

$$\nabla \cdot (\alpha_s \rho_s \langle \mathbf{c} q'q' \rangle) = \nabla \cdot (\alpha_s \rho_s \mathbf{U}_s \langle q'q' \rangle) + \nabla \cdot (\alpha_s \rho_s \langle \mathbf{C} q'q' \rangle). \tag{2-95}$$

Here we assume that $\mathbf{C}$ and $q'q'$ are uncorrelated and we also neglect the divergence of terms containing $\mathbf{U}_s$ as before. Thus, it is simply arrived at

$$\mathbb{C}(q'q') = \chi_{q'q'} - \nabla \cdot \boldsymbol{\theta}_{q'q'} = 0, \tag{2-96}$$

where

$$\chi_{q'q'} = \frac{\mathrm{d_p^2}}{2} \int_{\mathbf{c}_{12} \cdot \mathbf{k} > 0} \int_{\mathbb{R}^6} \int_{\mathbb{R}^2} \left((q'q')'_2 + (q'q')'_1 - (q'q')_2 - (q'q')_1 \right) \times (\mathbf{c}_{12} \cdot \mathbf{k}) f^2 \, \mathrm{d}q_1 \mathrm{d}q_2 \mathrm{d}\mathbf{c}_1 \mathrm{d}\mathbf{c}_2 \mathrm{d}\mathbf{k} \tag{2-97}$$

and

$$\boldsymbol{\theta}_{q'q'} = \frac{\mathrm{d_p^3}}{2} \int_{\mathbf{c}_{12} \cdot \mathbf{k} > 0} \int_{\mathbb{R}^6} \int_{\mathbb{R}^2} \mathbf{k} \left((q'q')'_1 - (q'q')_1 \right) (\mathbf{c}_{12} \cdot \mathbf{k}) f^2 \, \mathrm{d}q_1 \mathrm{d}q_2 \mathrm{d}\mathbf{c}_1 \mathrm{d}\mathbf{c}_2 \mathrm{d}\mathbf{k}, \tag{2-98}$$

with

$$(q'q')'_1 - (q'q')_1 = 2q'_1 \frac{dq_1}{dn_c} + \left(\frac{dq_1}{dn_c} \right)^2,$$

$$(q'q')'_2 - (q'q')_2 = 2q'_2 \frac{dq_2}{dn_c} + \left(\frac{dq_2}{dn_c} \right)^2$$

and

$$(q'q')'_2 + (q'q')'_1 - (q'q')_2 - (q'q')_1 = -2q_{12} \frac{dq_1}{dn_c} + 2 \left(\frac{dq_1}{dn_c} \right)^2$$

Evaluation of $\chi_{q'q'}$

$$I_{\chi_{q'q',1}} = \frac{\mathrm{d_p}^2}{2} \int\limits_{\mathbf{c}_{12}\cdot\mathbf{k}>0} \int\limits_{\mathbb{R}^6} \int\limits_{\mathbb{R}^2} \left(-2q_{12}\frac{dq_1}{dn_c}\right)(\mathbf{c}_{12}\cdot\mathbf{k}) f^2 \,\mathrm{d}q_1 \mathrm{d}q_2 \mathrm{d}\mathbf{c}_1 \mathrm{d}\mathbf{c}_2 \mathrm{d}\mathbf{k}$$

$$= \frac{\mathrm{d_p}^2}{2} \int\limits_{\mathbf{c}_{12}\cdot\mathbf{k}>0} \int\limits_{\mathbb{R}^6} \int\limits_{\mathbb{R}^2} \left(-2q_{12}\left(K_1 q_{12} + K_2\left(\mathbf{E}_q\cdot\mathbf{k}\right)\right)(\mathbf{c}_{12}\cdot\mathbf{k})^{4/5}\right) \times (\mathbf{c}_{12}\cdot\mathbf{k}) f^2 \,\mathrm{d}q_1 \mathrm{d}q_2 \mathrm{d}\mathbf{c}_1 \mathrm{d}\mathbf{c}_2 \mathrm{d}\mathbf{k} \qquad 2\text{-}99$$

$$= -g_0 N^2 \mathrm{d_p}^2 \times \left[\left(\frac{5}{7}2^{19/5}\Gamma\left(\frac{12}{5}\right)\sqrt{\pi}K_1 {\Theta_s}^{9/10}\langle q'q'\rangle\right) + \left(\frac{5}{57}2^{19/5}\Gamma\left(\frac{29}{10}\right)\sqrt{\pi}K_2 {\Theta_s}^{2/5}\left(\mathbf{E}_q\cdot\langle\mathbf{C}q'\rangle\right)\right)\right]$$

$$I_{\chi_{q'q',2}} = \frac{\mathrm{d_p}^2}{2} \int\limits_{\mathbf{c}_{12}\cdot\mathbf{k}>0} \int\limits_{\mathbb{R}^6} \int\limits_{\mathbb{R}^2} 2\left(\frac{dq_1}{dn_c}\right)^2 (\mathbf{c}_{12}\cdot\mathbf{k}) f^2 \,\mathrm{d}q_1 \mathrm{d}q_2 \mathrm{d}\mathbf{c}_1 \mathrm{d}\mathbf{c}_2 \mathrm{d}\mathbf{k}$$

$$= \frac{\mathrm{d_p}^2}{2} \int\limits_{\mathbf{c}_{12}\cdot\mathbf{k}>0} \int\limits_{\mathbb{R}^6} \int\limits_{\mathbb{R}^2} \left({K_1}^2 {q_{12}}^2 + {K_2}^2\left(\mathbf{E}_q\cdot\mathbf{k}\right)^2 + 2K_1K_2q_{12}\left(\mathbf{E}_q\cdot\mathbf{k}\right)\right)(\mathbf{c}_{12}\cdot\mathbf{k})^{8/5} \times (\mathbf{c}_{12}\cdot\mathbf{k}) f^2 \,\mathrm{d}q_1 \mathrm{d}q_2 \mathrm{d}\mathbf{c}_1 \mathrm{d}\mathbf{c}_2 \mathrm{d}\mathbf{k} \qquad 2\text{-}100$$

$$= g_0 N^2 \mathrm{d_p}^2 \times \left[\frac{5}{9}2^{23/5}\Gamma\left(\frac{14}{5}\right)\sqrt{\pi}{K_1}^2 {\Theta_s}^{13/10}\langle q'q'\rangle + \frac{13}{35}2^{13/5}\Gamma\left(\frac{14}{5}\right)\sqrt{\pi}{K_2}^2 {\Theta_s}^{13/10}\left|\mathbf{E}_q\right|^2 + \frac{5}{23}2^{23/5}\Gamma\left(\frac{23}{10}\right)\sqrt{\pi}K_1K_2 {\Theta_s}^{4/5}\left(\mathbf{E}_q\cdot\langle\mathbf{C}q'\rangle\right)\right]$$

$$\boldsymbol{\theta}_{q'q'} = \frac{\mathrm{d_p}^3}{2} \int\limits_{\mathbf{c}_{12}\cdot\mathbf{k}>0} \int\limits_{\mathbb{R}^6} \int\limits_{\mathbb{R}^2} \mathbf{k}\left(2{q'}_1\frac{dq_1}{dn_c} + \left(\frac{dq_1}{dn_c}\right)^2\right) \times (\mathbf{c}_{12}\cdot\mathbf{k}) f^2 \,\mathrm{d}q_1 \mathrm{d}q_2 \mathrm{d}\mathbf{c}_1 \mathrm{d}\mathbf{c}_2 \mathrm{d}\mathbf{k} \qquad 2\text{-}101$$

$$= 0$$

Therefore,

$$\chi_{q'q'} = 0 \tag{2-102}$$

Which gives us the expression for $\langle q'q' \rangle$ as

$$\begin{aligned}\langle q'q' \rangle = \frac{1}{\frac{5}{9}2^{23/5}\Gamma\left(\frac{14}{5}\right)\sqrt{\pi}{K_1}^2{\Theta_s}^{13/10} - \frac{5}{7}2^{19/5}\Gamma\left(\frac{12}{5}\right)\sqrt{\pi}K_1{\Theta_s}^{9/10}} \\ \times\left\{\frac{13}{35}2^{13/5}\Gamma\left(\frac{14}{5}\right)\sqrt{\pi}{K_2}^2{\Theta_s}^{13/10}\left|\mathbf{E}_q\right|^2\right. \\ + \left[\frac{5}{23}2^{23/5}\Gamma\left(\frac{23}{10}\right)\sqrt{\pi}K_1K_2{\Theta_s}^{4/5}\right. \\ \left.\left. - \frac{5}{57}2^{19/5}\Gamma\left(\frac{29}{10}\right)\sqrt{\pi}K_2{\Theta_s}^{2/5}\right]\left(\mathbf{E}_q \cdot \langle \mathbf{C}q' \rangle\right)\right\}.\end{aligned} \tag{2-103}$$

Evaluation of collisional diffusion of q

$$\mathbb{C}(q) = -\nabla \cdot \boldsymbol{\theta}_q + \chi_q, \tag{2-104}$$

where

$$\chi_q = \frac{\mathrm{d_p}^2}{2}\int\limits_{\mathbf{c}_{12}\cdot\mathbf{k}>0}\int\limits_{\mathbb{R}^6}\int\limits_{\mathbb{R}^2}(q'_2 + q'_1 - q_2 - q_1)(\mathbf{c}_{12}\cdot\mathbf{k})f^2\,\mathrm{d}q_1\mathrm{d}q_2\mathrm{d}\mathbf{c}_1\mathrm{d}\mathbf{c}_2\mathrm{d}\mathbf{k} = 0 \tag{2-105}$$

and

$$\boldsymbol{\theta}_q = \frac{\mathrm{d_p}^3}{2}\int\limits_{\mathbf{c}_{12}\cdot\mathbf{k}>0}\int\limits_{\mathbb{R}^6}\int\limits_{\mathbb{R}^2}\mathbf{k}\left(q'_1 - q_1\right)(\mathbf{c}_{12}\cdot\mathbf{k})\,f^2\mathrm{d}q_1\mathrm{d}q_2\mathrm{d}\mathbf{c}_1\mathrm{d}\mathbf{c}_2\mathrm{d}\mathbf{k}. \tag{2-106}$$

The 2-particle PDF is given by

$$f^2 = g_0 f_{p1} f_{p2}\left(1 + \frac{\mathrm{d_p}}{2}(\mathbf{k}\cdot\nabla)\ln\frac{f_{p2}}{f_{p1}}\right), \tag{2-107}$$

where the effect of finite particle size has been included since it will allow for diffusion due to difference in particle charge as per the model of [59] given by Eq. 2-50.

$$(\mathbf{k}\cdot\nabla)\ln\frac{f_{p2}}{f_{p1}}=\frac{1}{2Q^4}q_{12}(q_2+q_1)(\mathbf{k}\cdot\nabla\langle q'q'\rangle)-\frac{q_{12}}{Q^2}(\mathbf{k}\cdot\nabla\langle q\rangle)+\frac{1}{2\theta_s^2}\big(\mathbf{c}_{12}\cdot(\mathbf{c}_2+\mathbf{c}_1)\big)(\mathbf{k}\cdot\nabla\Theta_s)-\frac{1}{\theta_s}\mathbf{c}_{12}\cdot(\mathbf{k}\cdot\nabla\mathbf{U}_\mathrm{s}),\tag{2-108}$$

and as previously assumed, if the gradients of θ_s and $\mathbf{U}_\mathrm{s}$ are neglected, we have

$$(\mathbf{k}\cdot\nabla)\ln\frac{f_{p2}}{f_{p1}}=\frac{1}{2Q^4}q_{12}(q_2+q_1)(\mathbf{k}\cdot\nabla\langle q'q'\rangle)-\frac{q_{12}}{Q^2}(\mathbf{k}\cdot\nabla\langle q\rangle).\tag{2-109}$$

Therefore,

$$\begin{aligned}\boldsymbol{\theta}_q=\frac{\mathrm{d_p}^3}{2}&\int_{\mathbf{c}_{12}\cdot\mathbf{k}>0}\int_{\mathbb{R}^6}\int_{\mathbb{R}^2}\mathbf{k}\Big(K_1q_{12}+K_2\big(\mathbf{E}_q\cdot\mathbf{k}\big)\Big)(\mathbf{c}_{12}\cdot\mathbf{k})^{4/5}\\&\times(\mathbf{c}_{12}\cdot\mathbf{k})\,f^2\mathrm{d}q_1\mathrm{d}q_2\mathrm{d}\mathbf{c}_1\mathrm{d}\mathbf{c}_2\mathrm{d}\mathbf{k}\\=g_0\alpha_\mathrm{s}N\Bigg[&\left(\frac{60}{19}2^{9/5}\Gamma\left(\frac{19}{10}\right)\frac{1}{\sqrt{\pi}}K_1{\Theta_s}^{2/5}\right)\langle\mathbf{C}q'\rangle\\&+\left(\frac{5}{9}2^{9/5}\Gamma\left(\frac{12}{5}\right)\frac{1}{\sqrt{\pi}}K_2{\Theta_s}^{9/10}\right)\mathbf{E}_q\\&+\left(\frac{5}{21}2^{9/5}\Gamma\left(\frac{12}{5}\right)\frac{1}{\sqrt{\pi}}K_1{\Theta_s}^{9/10}\mathrm{d_p}\right)\left(\frac{\langle q\rangle}{\langle q'q'\rangle}\nabla\langle q'q'\rangle-\nabla\langle q\rangle\right)\Bigg],\end{aligned}\tag{2-110}$$

and the charge transport equation finally becomes

$$\frac{\partial}{\partial t}(\alpha_s \rho_s \langle q \rangle) + \nabla \cdot (\alpha_s \rho_s \langle q \rangle \mathbf{U}_s)$$
$$+ \nabla \cdot \left\{ \alpha_s \rho_s \left[\left(1 + 2^{\frac{9}{5}} \Gamma\left(\frac{19}{10}\right) \frac{60 K_1 g_0 \alpha_s \Theta_s^{\frac{2}{5}}}{19\sqrt{\pi}} \right) \langle \mathbf{C} q' \rangle \right.\right.$$
$$+ \left(\frac{5}{9} 2^{9/5} \Gamma\left(\frac{12}{5}\right) \frac{1}{\sqrt{\pi}} K_2 g_0 \alpha_s \Theta_s^{\frac{9}{10}} \right) \mathbf{E}_q \qquad \text{2-111}$$
$$+ \left(\frac{5}{21} 2^{9/5} \Gamma\left(\frac{12}{5}\right) \frac{1}{\sqrt{\pi}} K_1 g_0 \alpha_s \Theta_s^{\frac{9}{10}} \mathrm{d_p} \right)$$
$$\left.\left. \times \left(\frac{\langle q \rangle}{\langle q' q' \rangle} \nabla \langle q' q' \rangle - \nabla \langle q \rangle \right) \right] \right\} = 0.$$

References

[1] P.C. Johnson, R. Jackson, Frictional-collisional constitutive relations for granular materials, with application to plane shearing, Journal of Fluid Mechanics. 176 (1987) 67–93.

[2] S. Matsusaka, M. Ghadiri, H. Masuda, Electrification of an elastic sphere by repeated impacts on a metal plate, Journal of Physics D: Applied Physics. 33 (2000) 2311–2319.

[3] J.T. Jenkins, S.B. Savage, A theory for the rapid flow of identical, smooth, nearly elastic, spherical particles, Journal of Fluid Mechanics. 130 (1983) 187–202.

[4] D. Kunii, O. Levenspiel, Fluidization Engineering., Second, Butterworth-Heinemann, Newton, USA, 1991.

[5] J. Cross, Electrostatics: Principles, Problems and Applications, Adam Hilger, Bristol, 1987.

[6] J.R. Mountain, M.K. Mazumder, R.A. Sims, D.L. Wankum, T. Chasser, P.H. Pettit, Triboelectric charging of polymer powders in fluidization and transport processes, IEEE Transactions on Industry Applications. 37 (2001) 778–784.

[7] P. Mehrani, H.T. Bi, J.R. Grace, Electrostatic charge generation in gas–solid fluidized beds, Journal of Electrostatics. 63 (2005) 165–173.

[8] D. Gidaspow, B. Ettahadieh, Fluidization in two-dimensional beds with a jet; 2. Hydrodynamic modeling, Industrial & Engineering Chemistry Fundamentals. 22 (1983) 193 – 201.

[9] Y.P. Tsuo, D. Gidaspow, Computation of flow patterns in circulating fluidized beds, AIChE Journal. 86 (1990) 886 – 896.

[10] D. Gidaspow, Multiphase Flow and Fluidization: Continuum and Kinetic Theory Descriptions, First, Academic Press, 1994.

[11] A. Boemer, H. Qi, U. Renz, Eulerian simulation of bubble formation at a jet in a two-dimensional fluidized bed, International Journal of Multiphase Flow. 23 (1997) 927 – 944.

[12] A. Boemer, H. Qi, U. Renz, Verification of Eulerian simulation of spontaneous bubble formation in a fluidized bed, Chemical Engineering Science. 53 (1998) 1835 – 1846.

[13] D.A. Drew, L.A. Segel, Averaged Equations for Two-Phase Flows, Studies in Applied Mathematics. 50 (1971) 205–231.

[14] D.A. Drew, Continuum modeling of two-phase flows, in: R. Meyer (Ed.), Theory of Dispersed Multiphase Flow, Academic Press, 1983: pp. 173–190.

[15] M. Ishii, Thermo-fluid dynamic theory of two-phase flow, Eyrolles, Paris, 1975.

[16] R.T. Lahey Jr., The simulation of multidimensional multiphase flows, Nuclear Engineering and Design. 235 (2005) 1043–1060.

[17] J.T. Jenkins, Boundary Conditions for Rapid Granular Flow: Flat, Frictional Walls, Journal of Applied Mechanics. 59 (1992) 120.

[18] J.T. Jenkins, M.Y. Louge, On the flux of fluctuation energy in a collisional grain flow at a flat, frictional wall, Physics of Fluids. 9 (1997) 2835.

[19] O. Simonin, Continuum modelling of dispersed two-phase flows, von Karman Institute, Belgium, 1996.

[20] V. Mathiesen, T. Solberg, B.H. Hjertager, Predictions of gas/particle flow with an Eulerian model including realistic particle size distribution, Powder Technology. 112 (2000) 34 – 45.

[21] B.H. Hjertager, Multi-fluid CFD analysis of chemical reactors, in: D.L. Marchisio, R.O. Fox (Eds.), Multiphase Reacting Flows: Modelling and Simulation, Springer, 2006: pp. 125 – 179.

[22] R. Garg, C. Narayanan, S. Subramaniam, A numerically convergent Lagrangian-Eulerian simulation method for dispersed two-phase flows, International Journal of Multiphase Flow. 35 (2009) 376–388.

[23] Y. Kaneko, T. Shiojima, M. Horio, DEM simulation of fluidized beds for gas-phase olefin polymerization, Chemical Engineering Science. 54 (1999) 5809 – 5821.

[24] M.W. Korevaar, J.T. Padding, M.A. Van der Hoef, J.A.M. Kuipers, Integrated DEM-CFD modeling of the contact charging of pneumatically conveyed powders, Powder Technology. 258 (2014) 144–156.

[25] X. Liu, Y. Chen, Y. Chen, Analysis of gas-particle flow characteristics in impinging streams, Chemical Engineering and Processing: Process Intensification. 79 (2014) 14–22.

[26] A.D. Rakotonirina, A. Wachs, Grains3D, a flexible DEM approach for particles of arbitrary convex shape - Part II: Parallel implementation and scalable performance, Powder Technology. 324 (2018) 18–35.

[27] C. Song, D. Liu, J. Ma, X. Chen, CFD-DEM simulation of flow pattern and particle velocity in a fluidized bed with wet particles, Powder Technology. 314 (2017) 346–354.

[28] Y. Yang, C. Zi, Z. Huang, J. Wang, M. Lungu, Z. Liao, Y. Yang, H. Su, CFD-DEM investigation of particle elutriation with electrostatic effects in gas-solid fluidized beds, Powder Technology. 308 (2016) 422–433.

[29] M.A. Hassani, R. Zarghami, H.R. Norouzi, N. Mostoufi, Numerical investigation of effect of electrostatic forces on the hydrodynamics of gas–solid fluidized beds, Powder Technology. 246 (2013) 16–25.

[30] G.A. Bokkers, M. van Sint Annaland, J.A.M. Kuipers, Mixing and segregation in a bidisperse gas–solid fluidised bed: a numerical and experimental study, Powder Technology. 140 (2004) 176–186.

[31] F. Jalalinejad, X.T. Bi, J.R. Grace, Effect of electrostatics on freely-bubbling beds of mono-sized particles, International Journal of Multiphase Flow. 70 (2015) 104–112.

[32] R.G. Rokkam, R.O. Fox, M.E. Muhle, Computational fluid dynamics and electrostatic modeling of polymerization fluidized-bed reactors, Powder Technology. 203 (2010) 109–124.

[33] R.G. Rokkam, R.O. Fox, M.E. Muhle, CFD Modeling of Electrostatic Forces in Gas-Solid Fluidized Beds, The Journal of Computational Multiphase Flows. 2 (2010) 189–205.

[34] R.G. Rokkam, A. Sowinski, R.O. Fox, P. Mehrani, M.E. Muhle, Computational and experimental study of electrostatics in gas–solid polymerization fluidized beds, Chemical Engineering Science. 92 (2013) 146–156.

[35] A. Sowinski, L. Miller, P. Mehrani, Investigation of electrostatic charge distribution in gas–solid fluidized beds, Chemical Engineering Science. 65 (2010) 2771–2781.

[36] T. Matsuyama, H. Yamamoto, Impact charging of particulate materials, Chemical Engineering Science. 61 (2006) 2230–2238.

[37] P.M. Ireland, Triboelectrification of particulate flows on surfaces: Part II—Mechanisms and models, Powder Technology. 198 (2010) 189–198.

[38] S. Matsusaka, H. Maruyama, T. Matsuyama, M. Ghadiri, Triboelectric charging of powders: A review, Chemical Engineering Science. 65 (2010) 5781–5807.

[39] C. Pei, D. England, S. Byard, H. Berchtold, M. Adams, C.Y. Wu, D. England, S. Byard, H. Berchtold, M. Adams, Numerical analysis of contact electrification using DEM–CFD, Powder Technology. 248 (2013) 34–43.

[40] C. Pei, C.-Y. Wu, D. England, S. Byard, H. Berchtold, M. Adams, DEM-CFD Modeling of Particle Systems with Long-Range Electrostatic Interactions, American Institute of Chemical Engineers Journal. 61 (2015) 1792–1803.

[41] C. Pei, C.-Y. Wu, M. Adams, DEM-CFD analysis of contact electrification and electrostatic interactions during fluidization, Powder Technology. In submiss (2016) 208–217.

[42] J.C.C. Laurentie, P. Traoré, L. Dascalescu, Discrete element modeling of triboelectric charging of insulating materials in vibrated granular beds, Journal of Electrostatics. 71 (2013) 951–957.

[43] J. Kolehmainen, A. Ozel, C. M. Boyce, S. Sundaresan, A Hybrid Approach to Computing Electrostatic Forces in Fluidized Beds of Charged Particles, American Institute of Chemical Engineers Journal. (2016).

[44] J. Kolehmainen, A. Ozel, C.M. Boyce, S. Sundaresan, Triboelectric charging of monodisperse particles in fluidized beds, American Institute of Chemical Engineers Journal. (2016).

[45] C.K.K. Lun, S.B. Savage, D.J. Jeffrey, N. Chepurniy, Kinetic theories of granular flows: inelastic particles in Couette flow and slightly inelastic particles in a general flow field, Journal of Fluid Mechanics. 140 (1984) 223–256.

[46] J. Kolehmainen, A. Ozel, S. Sundaresan, Eulerian modelling of gas–solid flows with triboelectric charging, Journal of Fluid Mechanics. 848 (2018) 340–369.

[47] S.S. Hsiau, M.L. Hunt, Kinetic Theory Analysis of Flow-Induced Particle Diffusion and Thermal Conduction in Granular Material Flows, J. Heat Transfer. 115 (1993) 541–548.

[48] OpenFOAM, The OpenFOAM Foundation, (2017). http://openfoam.org/.

[49] R. Jackson, Locally averaged equations of motion for a mixture of identical spherical particles and a Newtonian fluid, Chemical Engineering Science. 52 (1997) 2457–2469.

[50] S. Chapman, T.G. Cowling, The mathematical theory of non-uniform gases, 2nd ed., Cambridge University Press, Cambridge, {U.K.}, 1961.

[51] C.K.K. Lun, S.B. Savage, The effects of an impact velocity dependent coefficient of restitution on stresses developed by shear granular materials, (1986) 14–44.

[52] D.G. Schaeffer, Instability in the evolution equations describing incompressible granular flow, Journal of Differential Equations. 66 (1987) 19–50.

[53] A. Srivastava, S. Sundaresan, Analysis of a frictional-kinetic model for gas-particle flow, Powder Technology. 129 (2003) 72–85.

[54] S. Ogawa, A. Umemura, N. Oshima, On the equation of fully fluidized granular materials, Zeitschrift Fur Angewandte Mathematik Und Physik. (1980) 483–493.

[55] S. Benyahia, Verification and validation study of some polydisperse kinetic theories, Chemical Engineering Science. 63 (2008) 5672–5680.

[56] V. Garzó, S. Tenneti, S. Subramaniam, C.M. Hrenya, Enskog kinetic theory for monodisperse gas–solid flows, Journal of Fluid Mechanics. 712 (2012) 129–168.

[57] A. Passalacqua, L. Marmo, A critical comparison of frictional stress models applied to the simulation of bubbling fluidized beds, Chemical Engineering Science. 64 (2009) 2795–2806.

[58] S. Matsusaka, H. Masuda, Electrostatics of particles, Advanced Powder Technology. 14 (2003) 143–166.

[59] L.B. Schein, M. LaHa, D. Novotny, Theory of insulator charging, Physics Letters A. 167 (1992) 79–83.

[60] D.B. Spalding, Numerical Computation of Multi-phase fluid flow and heat transfer, in: C. Taylor (Ed.), Recent Advances in Numerical Methods in Fluids, Pineridge Press, 1980.

[61] S. Patankar, Numerical Heat Transfer and Fluid Flow, 1st ed., Taylor & Francis, 1980.

[62] R.I. Issa, Solution of the implicitly discretised fluid flow equations by operator-splitting, Journal of Computational Physics. 62 (1986) 40–65.

[63] H.G. Weller, Bounded Explicit and Implicit Second-Order Schemes for Scalar Transport, 2006.

[64] A. Passalacqua, R.O. Fox, Implementation of an iterative solution procedure for multi-fluid gas–particle flow models on unstructured grids, Powder Technology. 213 (2011) 174–187.

[65] P.J. Oliveira, R.I. Issa, Numerical aspects of an algorithm for the Eulerian simulation of two-phase flows, International Journal for Numerical Methods in Fluids. 43 (2003) 1177–1198.

[66] W.Z. Shen, J.A. Michelsen, J. N. Sørensen, Improved Rhie-Chow Interpolation for Unsteady Flow Computations, AIAA Journal. 39 (2001) 2406–2409.

[67] A. Sowinski, The study of reactor wall fouling in gas-solid fluidized beds caused by electrostatic charge generation, Thesis dissertation, University of Ottawa, 2012.

[68] A. Sowinski, A. Mayne, P. Mehrani, Effect of fluidizing particle size on electrostatic charge generation and reactor wall fouling in gas–solid fluidized beds, Chemical Engineering Science. 71 (2012) 552–563.

[69] F. Chowdhury, A. Sowinski, M. Ray, A. Passalacqua, P. Mehrani, Charge generation and saturation on polymer particles due to single and repeated particle-metal contacts, Journal of Electrostatics. 91 (2018) 9–15.

[70] J. Lowell, A.C. Rose-Innes, Contact electrification, Advances in Physics. 29 (1980) 947–1023.

[71] J. Lowell, Contact electrification of metals, Journal of Physics D: Applied Physics. 8 (1975) 53.

[72] R.G. Wilson, Vacuum Thermionic Work Functions of Polycrystalline Be, Ti, Cr, Fe, Ni, Cu, Pt, and Type 304 Stainless Steel, Journal of Applied Physics. 37 (1966) 2261–2267.

[73] A. Giffin, P. Mehrani, Comparison of influence of fluidization time on electrostatic charge build-up in the bubbling vs. slugging flow regimes in gas–solid fluidized beds, Journal of Electrostatics. 68 (2010) 492–502.

[74] L. Cammarata, P. Lettieri, G.D.M. Micale, D. Colman, 2D and 3D CFD simulations of bubbling fluidized beds using Eulerian-Eulerian models, International Journal of Chemical Reactor Engineering. 1 (2003).

[75] F. Taghipour, N. Ellis, C. Wong, Experimental and computational study of gas–solid fluidized bed hydrodynamics, Chemical Engineering Science. 60 (2005) 6857–6867.

[76] M. Ye, J. Wang, M.A. van der Hoef, J.A.M. Kuipers, Two-fluid modeling of Geldart A particles in gas-fluidized beds, Particuology. 6 (2008) 540–548.

[77] A. Bakshi, C. Altantzis, A. Bershanska, A.K. Stark, A.F. Ghoniem, On the limitations of 2D CFD for thin-rectangular fluidized bed simulations, Powder Technology. 332 (2018) 114–119.

[78] H. Lindborg, M. Lysberg, H.A. Jakobsen, Practical validation of the two-fluid model applied to dense gas-solid flows in fluidized beds, Chemical Engineering Science. 62 (2007) 5854–5869.

[79] P. Sweby, High resolution schemes using flux limiters for hyperbolic conservation laws, SIAM J. Numer. Anal. 21 (1984) 995–1011.

Chapter 3

Charge Generation and Saturation on Polymer Particles due to Single and Repeated Particle-Metal Contacts

F. Chowdhury[a], A. Sowinski[a], M. Ray[b], A. Passalacqua[b], P. Mehrani[a]

[a] Department of Chemical and Biological Engineering, University of Ottawa, 161 Louis Pasteur, Ottawa, ON, Canada, K1N 6N5
[b] Department of Mechanical Engineering, Iowa State University, 2025 Black Engineering Building Ames, IA, 50011-2161, USA

This chapter is a manuscript published in Journal of Electrostatics (2018; 91:9-15)

Abstract

The development of an electrostatic model for particle-wall contact charging requires a good understanding of the charge generation mechanism for insulative particles. Single and repeated-contact experiments were performed with various particles, including commercial linear low-density polyethylene, to determine their rates of charging as well as their charge saturation limits. Plotting the charge saturation value of the particles against their respective surface areas revealed a linear trend which could be used to calculate the charge saturation of the particle for a given particle size. Additional studies include the effect of initial charge, collision frequency, particle type and impurities on particle charging.

3.1. Introduction

The triboelectrification of particles, via contact or frictional charging, is known to be an operational hindrance in some gas-solid fluidized bed reactors in the polyolefin industry. Polyethylene resins and catalyst particles are particularly prone to charge generation due to the particle-particle and particle-reactor wall collisions that occur during the fluidization process [1,2]. The large frequency of such collisions results in highly charged polyethylene and catalyst particles that adhere to the reactor wall. As the adhered particles accumulate, the continuous and highly exothermic polymerization reaction causes local temperature spikes on the wall, leading to the formation of large sheets of melted particles that can break off and obstruct the gas flow. It has been reported that in such cases the reactors might operate for only a few hours before they must be shut down for clean-up [3]. The generation of electrostatic charge in fluidized beds has been widely studied throughout the years; however, limited attention has been paid to the simulation and modeling of electrostatic charge generation in gas-solid fluidized beds. Since it is difficult to accurately quantify the charge generation in industrial fluidized beds, an electrostatic model based on fundamental material properties would considerably aid in providing insight on this occurrence and its effects.

The successful development of an electrostatic model for polymer charging first requires a good understanding of the charging mechanism for such insulative particles. Although the triboelectrification of various types of particles has been studied and reviewed for many years [4–6], the variability in the reported charging results has made it difficult to establish the effect of different factors on the charge transfer process. Some of these factors include the physical, chemical and electrical properties of the particle, as well as environmental conditions [6]. Thus, charging experiments are necessary to evaluate these factors for any given particle type; and in turn, they can help obtain input parameters for the charging model in order to realistically simulate the rate of charging of the given particles, along with their charging limits.

In the present work, single particle contact charging tests were performed to determine the rate of charging as well as the charge saturation limit of various polymer particles due to collisions with a metal surface. Most importantly, various sizes of linear low-density polyethylene (LLDPE) resin, received directly from a commercial gas-solid fluidized bed reactor, were tested to obtain some insight in their charging tendencies in relation to their surface areas. These results can help in the

validation process for the electrostatic model being developed to simulate charging in industrial-scale fluidized bed reactors.

3.2. Theory

Extensive studies have been performed on the triboelectric charging tendencies of many materials by comparing their charge polarities [7–10]. The difference in work function has been determined to be the driving force for triboelectric charging even for insulators despite their lack of free electrons [11]. This allowed the development of "effective" work functions for polymers via metal-polymer contacts [12]. In order to explain the charge transfer due to metal-insulator contacts, the surface state model has been proposed where it is assumed that the available energy levels of electrons are only on the surface as opposed to the bulk of the object [13]. As such, electrons can move from the filled surface states of one material to the empty surface states of the other. It should be noted that the surface of insulators can be composed of positively or negatively charged nanoscopic regions, where the surface charge in a specific region is much larger than the net charge of the insulator [14]. Insulator charging can also be caused by the presence of impurities including side groups, surface impurities and ends of molecular chains, based on a study where pure samples of crystalline insulators showed no charging when contacted by metals [5]. Material transfer due to attrition can also emulate charge transfer, since the transferred material may be the charge carrier [5].

Many studies have been reported which observed the charging tendencies of insulative particles, ranging from single particle contacts with a metal plate [15–19] to bulk particle flow in pneumatic conveying [20–24] or fluidized beds [25–29]. Other than the work function difference of the colliding surfaces, some factors that can affect the rate of charge generation on an insulative particle contacting a metal wall include impact velocity and angle, particle size, temperature, relative humidity, and initial charge [6]. Kittaka et al. (1979) developed a method to measure the charging tendencies of powders in a pneumatic conveying system [24]. In their work, both the charge saturation limit and the initial rate of charge generation were reported to be dependent on the transport speed and pipe material. The increase in particle charging with increasing flow velocity, which implies a larger impact velocity, was also observed in several experiments using fluidized bed systems [27,30,31].

Watanabe et al. (2006) reported that, based on their single particle charging experiments, the amount of charge generated by a single particle-wall contact can be zero for a specific initial charge, independent of the impact velocity [32]. This implied that a charge limit exists for any given particle, where the particle no longer gains any charge regardless of the number of collisions or the impact velocity.

In fluidized beds with mono-sized particles, i.e. systems with a very narrow particle size distribution, it was observed that an increase in particle size directly correlated to an increase in charge generated in the fluidized bed [27,33,34]. This observation could be connected to the surface state theory; a larger surface area provides more available electron sites. The particle size should therefore affect both the rate of charge generation from a single wall contact, as well as the maximum amount of charge the particle can hold. A single-particle contact charging study on polymer particles of the same type but different sizes could help confirm the relationship between surface area and charging rate as well as charge saturation.

The phenomenon of charge saturation is consistently observed by other researchers [19,35–37] and is a key input parameter for most electrostatic charging models. Currently, the charge saturation limit of a particle of a specific material and size can only be determined experimentally. As such, to simulate the charging behaviour of polymers in a fluidized bed system due to particle-reactor wall collisions, it is necessary to perform particle collision experiments using those polymers to determine their charge saturation and rate of charging. By determining the charge saturation limit of the particles at varying sizes, it may be possible to obtain an equation that can estimate the charge saturation as a function of surface area.

3.2.1. Numerical model for particle-wall contact charging

Every time a collision occurs between a solid particle and a metal wall, the existing charge on the particle should change by a specified value due to charge generation. A charge limit must also be implemented to ensure that the particles do not constantly increase in charge every time a collision with the wall occurs. Matsusaka et al. (2000) proposed a charge generation model for particle charging by repeated wall contacts [35]. According to their model, the change in particle charge per collision with a wall is given by the following equation:

$$\frac{dq}{dn} = k_c \frac{\varepsilon_r \varepsilon_0 S}{z_0} (V_c - k_e q) - \frac{k_r}{f} q \quad 3\text{-}1$$

The contact area, *S*, can be approximated using the Hertzian deformation pattern [17]:

$$S = 1.364 k^{2/5} \rho_p^{2/5} d_p^2 v_{p,i}^{4/5} \quad 3\text{-}2$$

$$k = \frac{1 - v^2}{E} \quad 3\text{-}3$$

For dielectric materials such as rubber or plastic, the effects of charge relaxation in the proposed model is negligible ($k_r \approx 0$). Thus, the rate of charge generation per collision can be determined by the following simplified equation:

$$\frac{dq}{dn} = \mathrm{C}\left(1 - \frac{q}{q_\infty}\right) \quad 3\text{-}4$$

$$\mathrm{C} = \frac{V_c k_c \varepsilon_r \varepsilon_0 S}{z_0} \quad 3\text{-}5$$

$$q_\infty = \frac{V_c}{k_e} \quad 3\text{-}6$$

Here, q_∞ is the particle saturated charge, and *C* is an interaction coefficient that is based on the electrostatic relationship between the wall and the particle as well as the impact velocity. If the impact velocity is controlled, Eq. 3-4 can be used to find the charge saturation and the interaction coefficient using experimental data of charge generated with increasing number of collisions.

3.3. Material and methods

Contact charging experiments were performed with three types of polymer particles: spherical polytetrafluorethylene (PTFE) and spherical high-density polyethylene (HDPE) supplied by McMaster Carr (USA), and a commercially produced LLDPE resin. The LLDPE particles were first sieved to a narrow size range, after which a few particles were selected with sizes ranging between 1.2 to 3.6 mm. Table 3-1 lists the average diameter and surface area of the selected particles, and an image of all the particles is shown in Figure 3-1.

Table 3-1: Average diameter and surface area of tested LLDPE resins.

Material	Particle #	Avg. Diameter (mm)	Surface Area (mm^2)
LLDPE	1	1.24	4.8
	2	2.12	14.1
	3	2.48	19.3
	4	2.98	27.9
	5	3.35	35.2
	6	3.57	40.0
PTFE	1	2.38	17.8
	2	3.18	31.8
HDPE	1	3.18	31.8

Figure 3-1: Array of particles used for the charge generation experiments.

Two types of particle-metal collision experiments were performed for this study: single contact with a metal plate and repeated contacts in a metal container. The single contact experiments were performed with hundreds of PTFE and HDPE particles. Each respective set of these particles had nearly identical particles sizes and mass, and so each particle was used only once to minimize the risk of contaminants, such as dust or other impurities, affecting the charge generation results. PTFE is known to have a higher work function than HDPE [12], and the larger PTFE particle is expected to generate more charge from a single contact. Thus, obtaining these two results from the particle-metal single contact experiments would confirm the efficacy of the charge measurement technique.

Repeated particle-wall contact experiments were performed with all the particle types to determine the amount of charge generated in each of them over a controlled number of collisions. Unlike the PTFE and HDPE particles, the selected LLDPE resins were reused for all the repeated contact experiments. As such, since the presence of impurities may severely affect the charging rate of the particles, great care was needed during particle handling to minimize the particles' interaction with

possible contaminants. A comparison on the charge saturation values of the three particle types will provide some insight on the work function of the commercial LLDPE resin relative to the other particles.

Figure 3-2 depicts the experimental apparatus used for single particle-metal plate contact experiments. A single particle was dropped through Faraday Cup 1, which rested on a polyethylene board attached to a height-adjustable bar. The particle would then contact an aluminum plate attached to a rotating clamp, which can be adjusted to obtain the desired contact angle. Faraday Cup 2 was placed on the floor on top of an insulated mat. Two Keithley 6514 Electrometers were used to measure the charge in the Faraday cups. The data collection process was programmed into LabView, which was used to continuously retrieve charge values from both cups for the duration of each run.

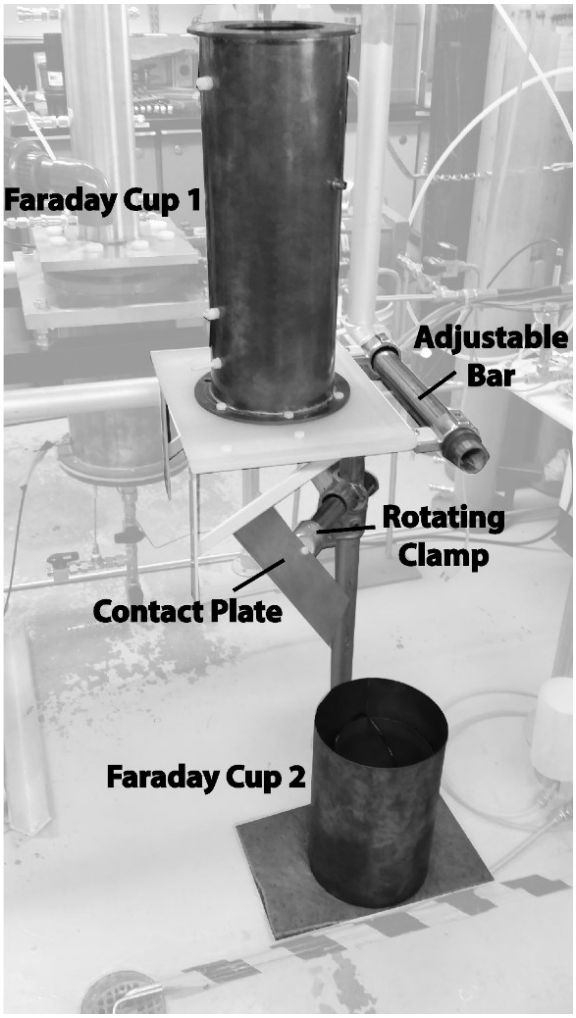

Figure 3-2: Apparatus for single particle contact tests.

For repeated contact charging tests, the contact plate was replaced by a cubic (3.5 cm) stainless-steel container to capture the falling particle after its initial charge measurement from Faraday Cup 1. Once retrieved, the container was closed and shaken vigorously to induce rapid particle-wall collisions for a set duration, after which the particle was dropped into Faraday Cup 2 for the final charge measurement. A charge neutralizer (MEB Shockless Static Neutralizing Bar, 5 mA) was used before every repeated collision test for the LLDPE particles to ensure their charges were as close to neutral as possible. A benefit of the charge neutralizer is that the initial charge is already known to be within a small range of values close to zero; so, only one Faraday Cup is required to measure the final charge. For PTFE and HDPE particles, however, the neutralizer was not used in order to study the effect of initial charge on the rate of charge generation.

The number of wall collisions experienced by each particle can be estimated by tracking the shake frequency of the container. It can be assumed that, on average, two particle-wall collisions occur in every shake sequence. Tracking the number of collisions experienced by the particle is vital for the success of this study, as it is directly related to the charge generation rate of the particle. As such, performing the shake manually, while susceptible to human error, was deemed the most reliable option for ensuring the appropriate number of collisions have occurred. It should be noted that the contact angle and velocity is expected to slightly vary for each collision in the repeated contact experiments. Thus, each test case was performed at least 10 times to ensure the observed effect of repeated collisions on particle charge is reproducible.

3.4. Results and discussion

3.4.1. Effect of initial charge

It has been well established that the charging trend for particle-wall contacts is a decreasing exponential function [38]. Watanabe et al. have also reported that a linear relationship exists between impact charge and initial charge of a particle [32]. This implies that a particle with a known charge trend should stay on the same path when starting at any given initial charge. Repeated particle-wall collision experiments performed with PTFE particles were organized based on their measured initial charge to observe this idea. Figure 3-3 shows the percent change in charge, $(q_f - q_i)/q_i$, due to varying numbers of particle-wall collisions experienced by 3.18 mm

PTFE particles as a function of their initial charge. Results are shown for a range of tests between 10 to 240 collisions.

It was observed that the percent change in charge decreased with increasing initial charge. While the higher collision number cases expectedly had relatively higher percent change, the number of collisions experienced by the particles ultimately carried little weight for particles with high initial charge. The characteristic charging line held true; less charge generation was observed the closer the particle was to the charge equilibrium point. This property creates a need to control the initial charge of the particles when attempting to identify their charging rate at specific impact velocities and operating conditions. Always starting from a reference charge, or at least from a narrow range of low charges obtained by charge neutralization, would help expedite this process.

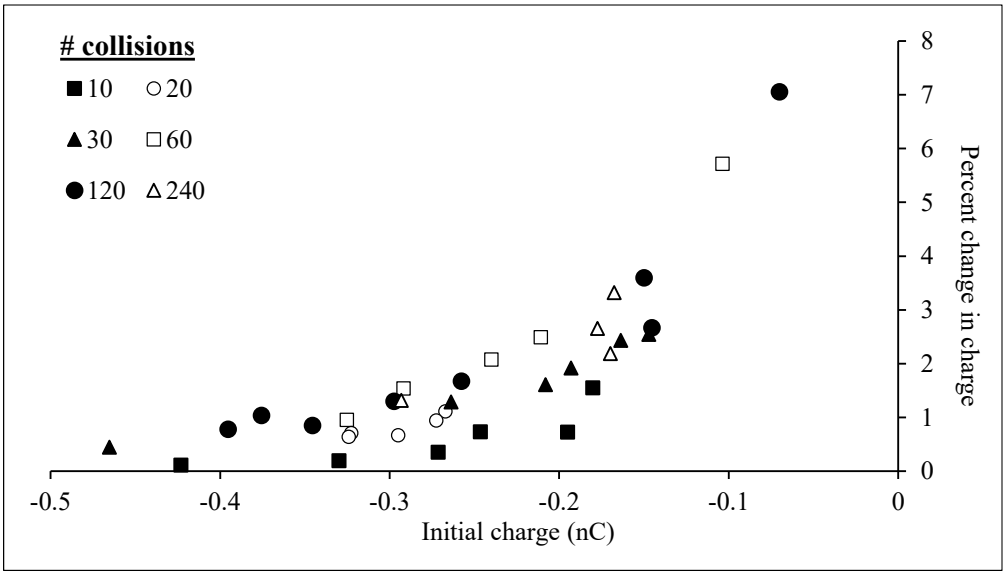

Figure 3-3: Effect of initial charge on the % change in charge of 3.18 mm PTFE spheres due to varying numbers of wall collisions.

3.4.2. Effect of collision frequency

Collision frequency was considered in this study as it is connected to the phenomenon of charge relaxation; at a sufficiently low collision frequency the rate of charge release may be greater than the rate of charge accumulation on a particle [16]. Generally, charge relaxation is considered negligible for dielectric materials such as rubber or other insulators. However, an observable decrease in charge was reported by Matsusaka et al. at lower collision frequencies in their repeated

impact experiments with a rubber ball [35]. As such, the effect of collision frequency on particle charge was briefly considered by performing repeated particle-wall collision experiments with LDPE resin #4.

For this study, it should be noted that a similar impact velocity had to be maintained while changing the shake frequency. It was deemed feasible to comfortably perform and maintain 4 shaking sequences in one second. The charge generation values can then be compared with performing 1 shaking sequence per second so long as they are performed with the same amount of force. The number of collisions from both shake frequency cases were aligned and presented in Figure 3-4. The error bars in this figure represent one standard deviation. Based on these results, the amount of charge generated in both cases were very similar up to 80 collisions. After this point, however, a lower collision frequency resulted in noticeably less charge generation. This implies that, over time, charge relaxation may become a contributing factor for the tested LLDPE resin, at least for those in the 3 mm or greater particle size range. Considering Eq. 3-1, this would mean the charge relaxation constant, k_r, is not negligible for this resin. Thus, it is necessary in this work to maintain a large enough collision frequency through vigorous shaking to minimize the effects of charge relaxation. It should be noted that since charge relaxation becomes negligible at sufficiently high collision frequencies, it would certainly not be a concern in fluidized bed systems.

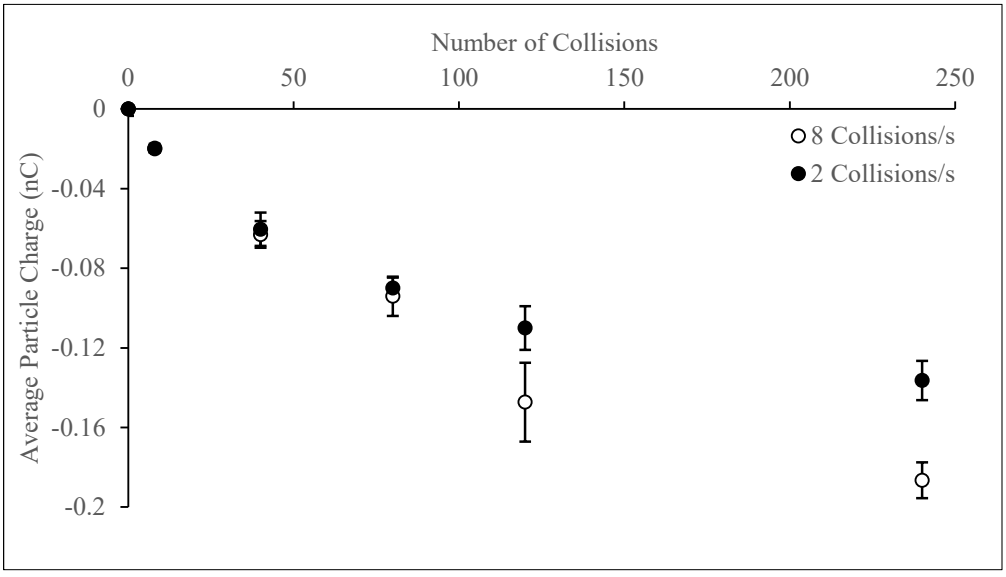

Figure 3-4: Effect of collisional frequency on the repeated particle-metal charging of LLDPE #4.

3.4.3. Effect of particle type

It is well established that the difference in work functions between two contacting objects is the driving force for electron transfer from one surface to another. The effective work function of any given material is unique, as it is dependent on the electrostatic and surface properties of the insulator. Thus, a range of work function values for common insulative materials, including polyethylene and PTFE, have been reported from various experimental studies [10]. PTFE has been consistently reported to be more electronegative than polyethylene [12]. This was also confirmed in this study, as shown in Figure 3-5 which presents the charge generated due to a single plate collision on same-sized HDPE and PTFE particles. The error bars in this figure is based on the measurement error of the electrometer. According to the numerical model, specifically Eq. 3-6, the work function of a material has a direct influence on the charge saturation limit.

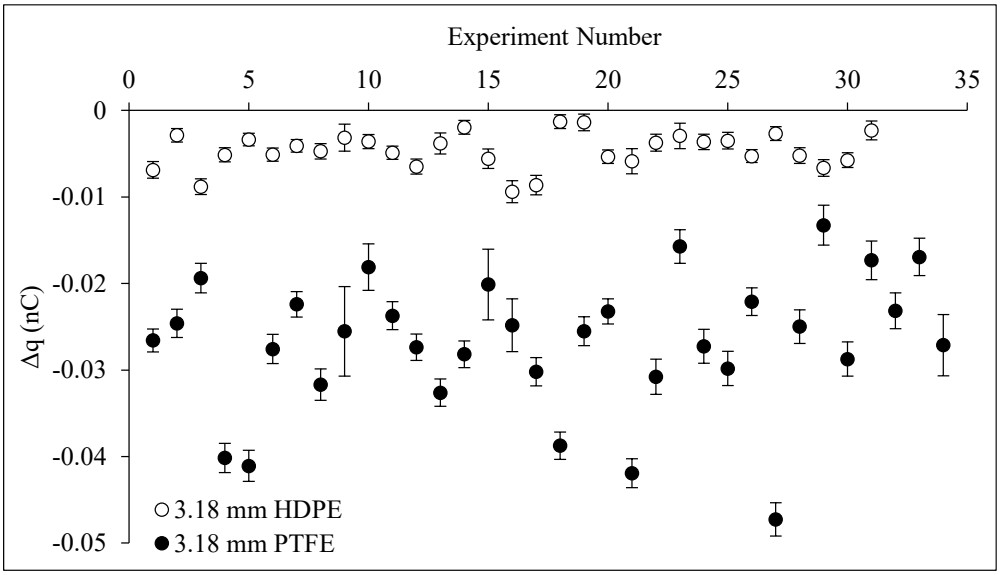

Figure 3-5: Charge generated on HDPE and PTFE particles by a single plate collision.

Figure 3-6 compares the average charge saturation values of the same-sized spherical particles as well as two of the LLDPE resins, #4 and #5. The error bars here represent one standard deviation. These two resins were selected for the comparison as they are the closest in size to the 3.18 mm HDPE and PTFE particles; one of them is slightly smaller while the other is slightly larger. It was observed that the 3.18 mm HDPE particle charged more than both LLDPE particles, which implies the size difference between HDPE and the larger LLDPE was not significant enough relative to other material properties. It is also known that HDPE tends to have a higher Young's Modulus

than LLDPE, and according to Eq. 3-3 in the numerical model, this means HDPE should charge less than LLDPE if all other properties were equal. Therefore, it can be concluded that the work function for LLDPE is lower than HDPE.

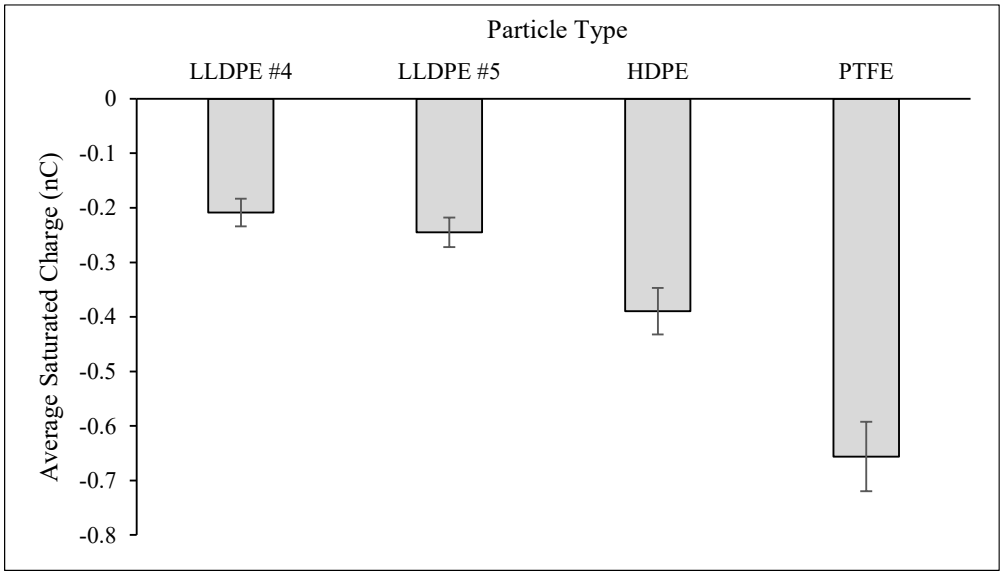

Figure 3-6: Average saturated charge for various particle types.

3.4.4. Effect of particle size

Single contact charging tests were first performed with PTFE at two different sizes; by normalizing for the surface area, as shown in Figure 3-7, it was observed that the charge generation readings strongly overlapped for the two particle sizes. The amount of charge generated a single contact is thus directly proportional to the surface area of the particle. Repeated contact experiments of the LLDPE resins have shown similar results; Figure 3-8 shows the average measured charge per surface area of the LLDPE resins. Each particle consistently generated more charge than those that were a smaller size, and normalizing the data for surface area resulted in overlapping of the charge values. The spread of the normalized charge values increased with increasing number of collisions, though the averaged charge values of each resin at any given number of collisions fell within one standard deviation for almost every resin.

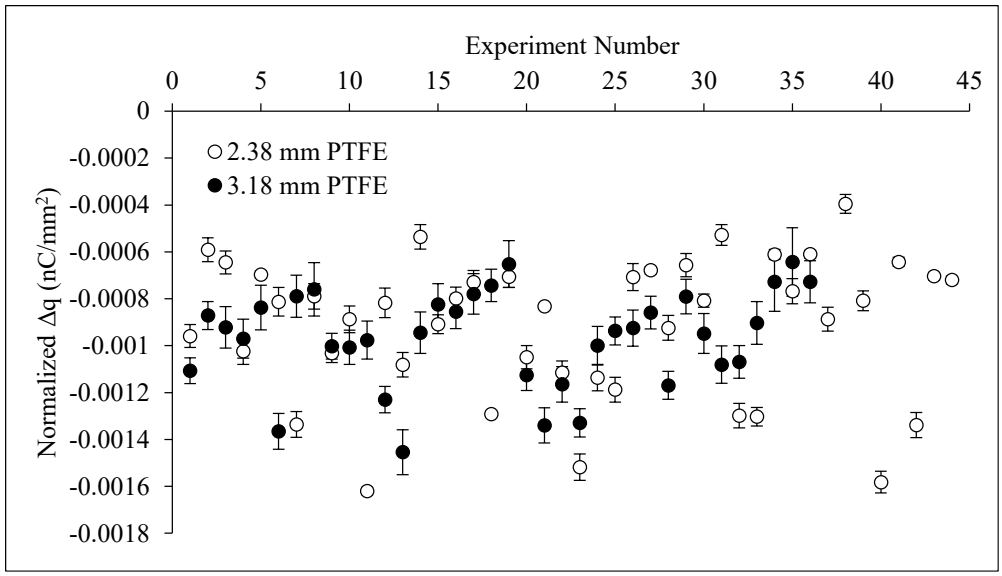

Figure 3-7: Charge generated by 2.38 and 3.18 mm PTFE spheres after a single metal collision normalized by surface area.

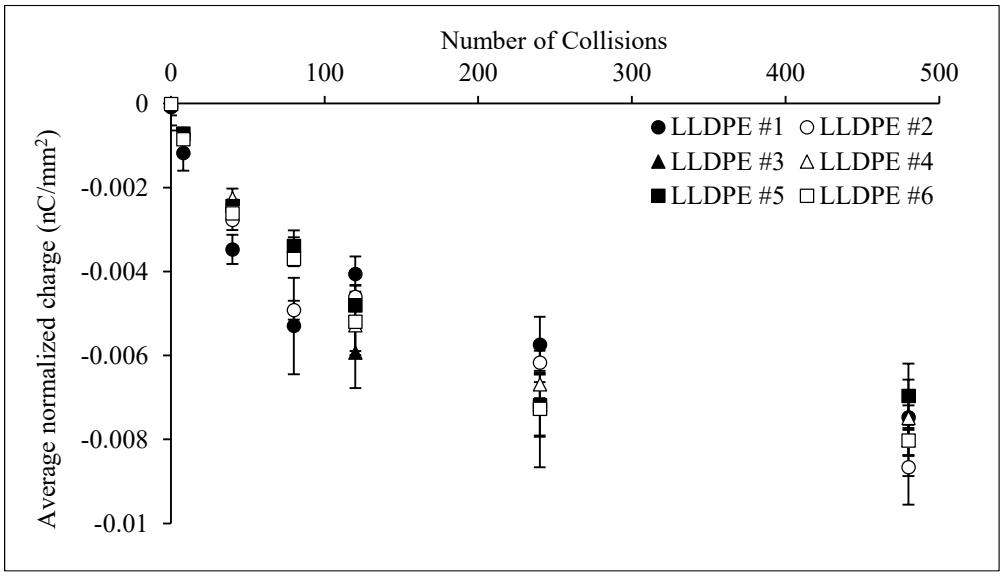

Figure 3-8: Average charge normalized by surface area of various sizes of LLDPE resins with increasing number of particle-wall collisions.

Plotting the average measured charge saturation value of the LLDPE particles against their respective surface areas, as shown in Figure 3-9, revealed a linear trend with an R^2 value of 0.98. It could therefore be used to calculate the charge saturation point of the LLDPE resins that fall within the surface area range tested in this study.

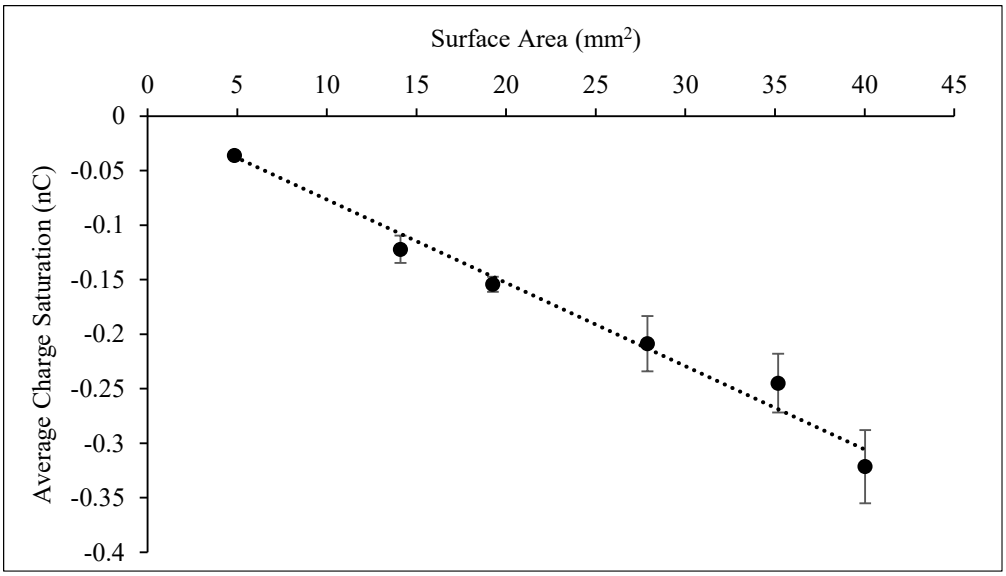

Figure 3-9: Average charge saturation of LLDPE resins with increasing surface area.

3.4.5. Application of the numerical model

For all cases, the charge generated over increasing number of collisions clearly followed the decreasing exponential form, which was the expected charging trend of particles experiencing repeated particle-wall collisions. The numerical model developed for particle-wall charging is therefore applicable for simulating the charge generation experienced by LLDPE resin in the given size range. Starting from an initial charge of zero, Eq. 3-4 was used with a guessed C and q_∞ to update the particle charge after every collision. Figure 3-10 presents the fitted numerical solution to the experimental data for the resins' average particle charge at increasing number of collisions. The error bars represent one standard deviation. The fitting criteria to obtain the optimal C and q_∞ values for the model was the minimization of the sum of errors between measured and the numerical data points. Table 3-2 summarizes the numerically parameters that provided the best fit to the experimental data for each LLDPE particle. A concern for the numerical model presented in this work is that the charge saturation values, which was provided for each case, should not be affected by particle size according to Eq. 3-6; only the interaction coefficient should be affected. However, the effect of particle size is clearly apparent from these experiments. In order to reflect the increase in charge saturation in proportion to the surface area, Eq. 3-6 must be modified in the future to consider the linear equation obtained from Figure 3-9. Overall, the model was successful in reproducing the charging trend observed in the experiments.

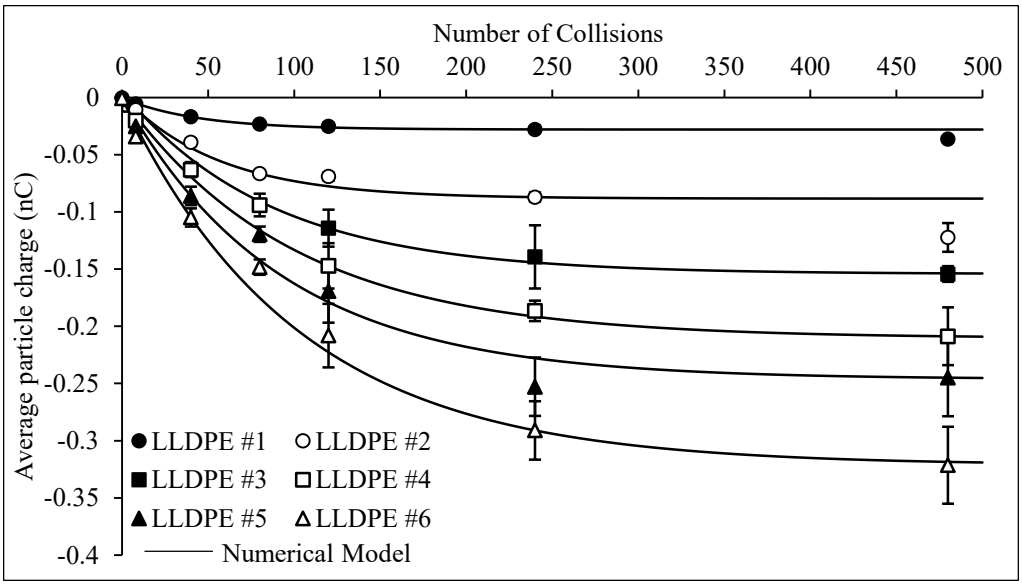

Figure 3-10 Fitting the numerical model to the experimental data for particle charging of various sizes of LLDPE resins due to repeated wall collisions.

Table 3-2: Summary of numerical model parameters and error compared to the experimental data.

Particle	Surface Area (mm^2)	Numerical q_∞ (nC)	Interaction Coefficient (nC)	Maximum Error	Sum of Errors
LLDPE #1	4.8	-0.028	-6.28E-04	0.29	0.49
LLDPE #2	14.1	-0.088	-1.55E-03	0.38	0.67
LLDPE #3	19.3	-0.154	-1.77E-03	0.03	0.04
LLDPE #4	27.9	-0.210	-2.10E-03	0.27	0.57
LLDPE #5	35.2	-0.246	-2.65E-03	0.29	0.62
LLDPE #6	40.0	-0.321	-3.14E-03	0.38	0.60

3.4.6. Effect of impurities (experimental observation)

Contamination is a major concern when it comes to any fundamental material, chemical, or electrostatic study. In the case of identifying the charge saturation values of LLDPE resins, any impurity that interacts with the particles would certainly skew the charge generation results. Figure 3-11 shows the discrepancies noted in an experimental run performed in the preliminary stage of this work. These results should only be considered qualitatively since the contamination was not quantified.

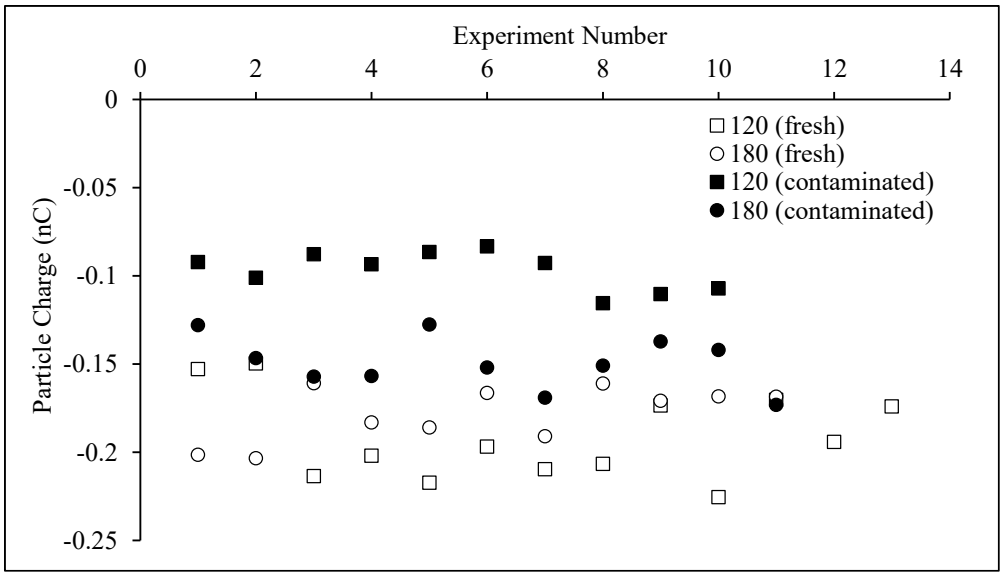

Figure 3-11: Effect of dust contamination on the charge of LLDPE #4 after 120 and 180 collisions.

The LLDPE particle used in this case was suspected to be contaminated with dust present in the laboratory, which was visually observed by the discoloration of the particle and an increase in dullness. As expected, there was an immediate change in the saturation charge for this particle. It was imperative that the particles used for such charge generation experiments are handled with care. Particularly in this study, the LLDPE resin must be tested in the same condition as they were obtained from the commercial reactor to ensure the findings are relevant. As such, it was desired for the LLDPE resin to have as minimal interaction with any form of contaminant or chemical as possible, especially since the same LLDPE resins were repeatedly used to record the charge generation over increasing number of collisions. To reduce the risk of dust contamination, the lab area was thoroughly cleaned prior to the experimental runs and a great deal of care was exercised to contain the particles in a clean manner after each run. Finally, test runs were regularly performed for different number of collisions to ensure the charge results for the LLDPE resins did not change over time. Following these precautions, the resins were deemed sufficiently uncontaminated throughout the study.

3.5. Conclusions

In summation, the mechanism for particle-wall charging of single insulative particles was analyzed and tested with single-contact and repeated-contact experiments. The single-contact experiments,

performed with spherical HDPE and PTFE particles contacting an aluminum plate, showed that particles with a larger effective work function consistently generated more charge. The amount of charge generated from a single wall contact was directly proportional to the surface area of the contacting particle. The repeated-contact experiments confirmed that the saturation charge limit also increased with the effective work function, and the surface area proportionality held true for all tested cases. A study on the effect of initial particle charge showed that particles closer to the saturation point will not charge beyond this point regardless of the number of particle-wall collisions they experience. Moreover, a particle with a known charge trend will follow the same path when starting at any initial charge.

LLDPE particles of various size were tested for their charge generation rate as well as their charge saturation limit. The charging results obtained from these experiments will aid in the simulation of electrostatic charging in commercial polyethylene gas-solid fluidized beds. These particles exhibited the decreasing exponential charging trend expected for charge generation due to particle-wall contacts. As such, the numerical model for particle-wall contact charging was successfully fitted to the experimental data. A lower saturated charge was found when a lower collision frequency was tested, implying that this LLDPE resin may be susceptible to charge relaxation. The charge generated by each LLDPE particle was consistently in proportion to its respective surface area, giving a linear trend with an R^2 value of 0.98. Dust contamination was confirmed to have a detrimental effect on the charging results, and so appropriate particle handling must be considered when performing such fundamental experiments.

References

[1] P. Mehrani, H.T. Bi, J.R. Grace, Bench-scale tests to determine mechanisms of charge generation due to particle–particle and particle–wall contact in binary systems of fine and coarse particles, Powder Technol. 173 (2007) 73–81.

[2] K.M. Forward, D.J. Lacks, R.M. Sankaran, Triboelectric charging of granular insulator mixtures due solely to particle - Particle interactions, Ind. Eng. Chem. Res. 48 (2009) 2309–2314.

[3] B.D. Fulks, S.P. Sawin, C.D. Aikman, J.M. Jenkins, Process for reducing sheeting during polymerization of alpha-olefins, US 4532311 A, 1985.

[4] W.R. Harper, The Volta Effect as a Cause of Static Electrification, Proc. R. Soc. A Math. Phys. Eng. Sci. 205(1080) (1951) 83–103.

[5] J. Lowell, A.C. Rose-Innes, Contact Electrification, Adv. Phys. 29 (1980) 947–1023.

[6] S. Matsusaka, H. Maruyama, T. Matsuyama, M. Ghadiri, Triboelectric charging of powders: A review, Chem. Eng. Sci. 65 (2010) 5781–5807.

[7] D.J. Montgomery, Static Electrification of Solids, Solid State Phys. 9 (1959) 139–197.

[8] V.J. Webers, Measurement of triboelectric position, J. Appl. Polym. Sci. 7 (1963) 1317–1323.

[9] M.W. Williams, Effect of Polymer Structure on its Triboelectric Properties, IEEE Trans. Ind. Appl. IA-12 (1976) 213–219.

[10] J. Cross, Electrostatics: Principles, Problems and Applications, Adam Hilger, Bristol, 1987.

[11] D.K. Davies, Charge generation on dielectric surfaces, J. Phys. D. Appl. Phys. 2 (1969) 307.

[12] K. Tanoue, H. Masuda, Electrostatic Separation, in: Powder Technol. Handb., 3rd ed., CRC Press LLC, 2006.

[13] G.S.P. Castle, L.B. Schein, General model of sphere-sphere insulator contact electrification, J. Electrostat. 36 (1995) 165–173.

[14] H.T. Baytekin, A.Z. Patashinski, M. Branicki, B. Baytekin, S. Soh, B.A. Grzybowski, The Mosaic of Surface Charge in Contact Electrification, Science (80-.). 333 (2011) 308–312.

[15] T. Matsuyama, H. Yamamoto, Impact charging of particulate materials, Chem. Eng. Sci. 61 (2006) 2230–2238.

[16] T. Itakura, H. Masuda, C. Ohtsuka, S. Matsusaka, The contact potential difference of powder and the tribo-charge, J. Electrostat. 38 (1996) 213–226.

[17] S. Matsusaka, H. Masuda, Electrostatics of particles, Adv. Powder Technol. 14 (2003) 143–166.

[18] A. Ema, D. Yasuda, K. Tanoue, H. Masuda, Tribo-charge and rebound characteristics of particles impact on inclined or rotating metal target, Powder Technol. 135–136 (2003) 2–13.

[19] P.M. Ireland, Triboelectrification of particulate flows on surfaces: Part I — Experiments, Powder Technol. 198 (2010) 189–198.

[20] Y. Murata, S. Kittaka, Evidence of Electron Transfer as the Mechanism of Static Charge Generation by Contact of Polymers with Metals, Jpn. J. Appl. Phys. 18 (1979) 421–421.

[21] M. Nifuku, T. Ishikawa, T. Sasaki, Static electrification phenomena in pneumatic transportation of coal, J. Electrostat. 23 (1989) 45–54.

[22] M. Nifuku, H. Katoh, A study on the static electrification of powders during pneumatic transportation and the ignition of dust cloud, Powder Technol. 135 (2003) 234–242.

[23] J. Yao, Y. Zhang, C.-H. Wang, S. Matsusaka, H. Masuda, Electrostatics of the Granular Flow

in a Vertical Pneumatic Conveying System, Ind. Eng. Chem. Res. 43 (2004) 7181–7199.

[24] S. Kittaka, N. Masui, Y. Murata, A method for measuring the charging tendency of powder in pneumatic conveyance through metal pipes, J. Electrostat. 6 (1979) 181–190.

[25] P. Mehrani, H.T. Bi, J.R. Grace, Electrostatic charge generation in gas–solid fluidized beds, J. Electrostat. 63 (2005) 165–173.

[26] A. Sowinski, L. Miller, P. Mehrani, Investigation of electrostatic charge distribution in gas–solid fluidized beds, Chem. Eng. Sci. 65 (2010) 2771–2781.

[27] J. Guardiola, V. Rojo, G. Ramos, Influence of particle size, fluidization velocity and relative humidity on fluidized bed electrostatics, J. Electrostat. 37 (1996) 1–20.

[28] F. Jalalinejad, X.T. Bi, J.R. Grace, Effect of electrostatics on freely-bubbling beds of mono-sized particles, Int. J. Multiph. Flow. 70 (2015) 104–112.

[29] J.R. Mountain, M.K. Mazumder, R.A. Sims, D.L. Wankum, T. Chasser, P.H. Pettit, Triboelectric charging of polymer powders in fluidization and transport processes, IEEE Trans. Ind. Appl. 37 (2001) 778–784.

[30] Z. Liu, X.T. Bi, J.R. Grace, Electrostatic charging behaviour of dielectric particles in a pressurized gas–solid fluidized bed, J. Electrostat. 68 (2010) 321–327.

[31] V. Rojo, J. Guardiola, A. Vian, A capacitor model to interpret the electric behaviour of fluidized beds. Influence of apparatus geometry, Chem. Eng. Sci. 41 (1986) 2171–2181.

[32] H. Watanabe, A. Samimi, Y.L. Ding, M. Ghadiri, T. Matsuyama, K.G. Pitt, Measurement of Charge Transfer due to Single Particle Impact, Part. Part. Syst. Charact. 23 (2006) 133–137.

[33] D. Boland, D. Geldart, Electrostatic charging in gas fluidised beds, Powder Technol. 5 (1972) 289–297.

[34] L. Fasso, B.T. Chao, S.L. Soo, Measurement of electrostatic charges and concentration of particles in the freeboard of a fluidized bed, Powder Technol. 33 (1982) 211–221.

[35] S. Matsusaka, M. Ghadiri, H. Masuda, Electrification of an elastic sphere by repeated impacts on a metal plate, J. Phys. D. Appl. Phys. 33 (2000) 2311–2319.

[36] J. Yao, F. Zhou, Y. Zhao, Charge generation and electrostatic equilibrium for single granules during sliding, Particuology. 29 (2016) 126–134.

[37] Y. Zhao, F. Zhou, J. Yao, Z. Ji, Electrostatic charging of single granules by repeated sliding along inclined metal plates, J. Electrostat. 87 (2017) 140–149.

[38] B.N. Cole, M.R. Baum, F.R. Mobbs, An Investigation of Electrostatic Charging Effects in High-Speed Gas-Solids Pipe Flows, Proc. Inst. Mech. Eng. Conf. Proc. 184 (1969) 77–83.

Chapter 4

Apparatus Design for Measuring Electrostatic Charge Transfer due to Particle-Particle Collisions

F. Chowdhury[a], B. Elchamaa[a], A. Sowinski[a], M. Ray[b], A. Passalacqua[b], P. Mehrani[a]

[a] Department of Chemical and Biological Engineering, University of Ottawa, 161 Louis Pasteur, Ottawa, ON, Canada, K1N 6N5
[b] Department of Mechanical Engineering, Iowa State University, 2025 Black Engineering Building Ames, IA, 50011-2161, USA

This chapter is a manuscript published in Powder Technology (2020; 361:860-866)

Abstract

A novel apparatus was designed, built and tested to study the magnitude and direction of charge transfer in particle-particle collisions of insulator particles. This design ensured that the measured change in the charge of each particle was solely due to the binary collision between the particles. The collisions were confirmed by monitoring the particle trajectories using a high frame-rate camera coupled with particle-tracking software. This apparatus can aid in understanding the charge transfer mechanisms behind particle-particle charge transfer, leading to the development of an electrostatic model to simulate particle-particle contact charging in gas-solid flows. Upon preliminary testing of this apparatus with 3.18 mm diameter polytetrafluoroethylene (PTFE) particles, it was confirmed that triboelectrification solely due to the particle-particle collision can be observed. It was found that, if the particles carry low charges relative to their charge saturation point, their initial charge before collision does not dictate the direction of charge transfer.

4.1. Introduction

The triboelectrification of insulators by contact or frictional charging is known to be an operational challenge in the polyolefin industry. Particularly in polyethylene production, gas-solid fluidized bed reactors are known to be susceptible to electrostatic charging due to the rigorous mixing of polyethylene and catalyst particles in a dry environment [1,2]. This charging phenomenon coupled with a highly exothermic polymerization reaction results in sheet formation on the reactor walls, which can eventually break off and occlude the reactor [3]. A variety of studies have been performed throughout the years to understand the particle charging tendencies within gas-solid fluidized beds, and to combat the operational challenges caused by triboelectrification [4–7]. However, the quantification of electrostatic charge generation during fluidization is still a key challenge. An alternative option to developing measurement techniques is the simulation and modeling of electrostatic charge generation in these industrial gas-solid fluidized beds, which can provide some insight on its occurrence as well as its effects.

The development of an electrostatic model for the charging of particles during gas-solid fluidization requires a fundamental understanding of their charging tendencies due to contacts with the column wall as well as between particles. The numerous studies and reviews on the triboelectrification of insulators due to particle-wall collisions have highlighted their charging behaviours, leading to the development of particle-wall charging models [8–11]. These charging models have already been applied in simulations of electrostatic charge generation in gas-solid flows [12,13]. However, particle-particle collisional charging has received limited attention due to the difficulty in performing consistent experimental studies on isolated particle-particle contacts. Understanding the charging tendencies between particles of varying physical and chemical properties is necessary for the particle-particle charging component of the electrostatic charging model for gas-solid flow simulations. As such, a novel collisional charging apparatus was designed and tested in this work, to observe the isolated charge transfer between two colliding insulators and take a step towards the development of a particle-particle charging model.

4.2. Theory

In the past, studies on electrostatic charging revolved around ranking materials in a triboelectric series, based on their relative tendency to become negatively charged [14,15]. Through this process, it was determined that the difference in work functions between two materials, including

insulators despite not having free electrons, was the driving force for triboelectric charging through electron transfer [16]. Other proposed causes of charge transfer for insulators include the transfer of surface impurities, ions or some of the material itself due to attrition [17,18]. While the dominating factor for charge transfer is still debatable, recent studies have shown that the evolution over time of the surface charge density of an inorganic solid was consistent with the electron thermionic emission model, implying that electron transfer is the dominant process for triboelectrification [19]. To explain the phenomenon of electron transfer with insulators, the surface state model was proposed where electrons can be trapped on surface sites of any insulator [20,21]. As such, a trapped electron on a high energy surface state of one material can transfer to an empty, low energy surface state of another. In agreement with this model, a study showed that the surface of insulators can be composed of both positively and negatively charged nanoscopic regions, so that the surface charge in specific regions may be larger than the net charge of the entire object [22].

A wide range of studies have observed the electrostatic charging tendencies of insulators due to particle-wall collisions, from bench-scale insulator-metal contacts [23–26] to pilot-scale pneumatic conveying [27–30] and fluidization of powders [31–35]. In addition to work function differences, other reported factors that can affect the rate of electrostatic charging include impact velocity and angle, particle size, temperature, relative humidity and initial charge [10]. The culmination of these studies gave rise to many charging models to determine Δq, the generated charge from a single collision. These models can be summarized as

$$\Delta q = C\left(1 - \frac{q_i}{q_\infty}\right) \qquad 4\text{-}1$$

where q_i is the initial charge of the particle, q_∞ is the maximum amount of charge a particle can hold (i.e. charge saturation point), and C is a parameter dependent on the various proposed relationships modeled between the particle and the contacting surface [36].

While charging models have been developed and applied in simulations for charge generation due to particle-wall contacts [13,37], some challenges arise when considering their application for particle-particle contacts. Primarily, grounded metal surfaces provide a consistent source of electrons to be transferred to the particle surface; this is not true in the case of insulator-insulator contacts. Moreover, models focusing on the difference in work functions as the driving force do

not apply when considering identical materials. Apodaca et al. [38] have concluded that random microscopic fluctuations in surface compositions can translate into macroscopic effects for contact electrification, making it difficult to predict which direction charging would occur for identical materials.

Several studies have been performed focussing on triboelectrification due to particle-particle collisions. Forward et al. [41] performed granular mixing (particle-particle collisions only) at low vacuum conditions, where they observed that binary mixtures of particles produced more charging than single-component systems. The triboelectrification of multi-particulate systems normally results in the generation of a bipolar charge distribution, where particles may become both positively and negatively charged [39]. This effect has been commonly observed and reported even in the pharmaceutical industry, with respect to both metered dose and dry powder inhalers [40]. Bilici et al. [42] studied the particle size effect on the charging of particles colliding in a fountain-like granular flow, where they found that the larger particles primarily charged positively and the smaller particles charged negatively. However, contradictory findings have been found in fluidization studies, where larger particles had negative charge while smaller particles charged positively [5]. In order to develop a particle-particle charging model, single particle-particle collisional experiments are therefore necessary to determine the specific factors and particle properties to predict the direction and magnitude of charge transfer between insulators and identical materials.

Studies performing single contact charging experiments, where one particle was dropped onto a particle resting on a plate, have shown that the magnitude of charge transfer that occurs between identical particles is dependent on the relative particle size and collision velocity [43,44]. However, particle-particle contact charging experiments between two isolated particles have yet to be studied successfully. The objective of this work is to design an apparatus that can perform isolated particle-particle collisions to study the charging tendencies of two colliding particles of similar or different materials, particle sizes, or initial charges. The findings from this setup can help in understanding the fundamental charging behaviours of particles in gas-solid flows, which can then be implemented into simulation models.

4.3. Design and Methodology

The design focus for this apparatus, shown in Figure 4-1, is to mitigate all external influence on the charge of the colliding particles, ensuring that the direction and magnitude of charge transfer is solely due to the particle-particle collision. The collisions are induced by using gas flow jets, which force the free-falling particles towards each other.

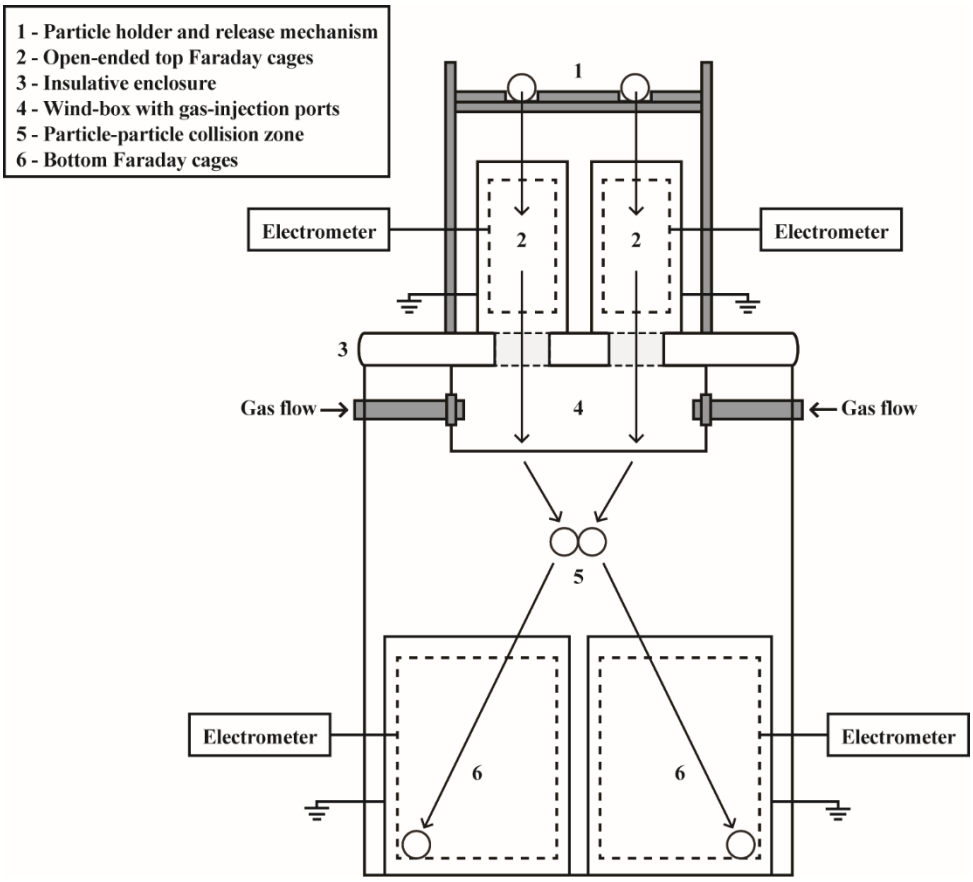

Figure 4-1: Particle-particle collision apparatus. The arrows depict the particles' pathway as they are released during a collision trial.

The apparatus uses four Faraday cages individually connected to four electrometers (Keithley 6514), to separately measure the charges on the two particles before and after their collision. Every run is monitored by a high frame-rate camera (Sony RX100 V), which records the particles' collision and subsequent drop into the bottom Faraday cages. The enclosure of the system, made of polyethylene with a clear acrylic front cover, isolates the particles from any external effects while also allowing the monitoring of the particle trajectories using the high-speed camera.

4.3.1. Apparatus Design

The apparatus can be broken down into six sections. In the first section, the two particles are placed on a modified tight-clearance stainless steel hinge, which acts as the particle holder as well as the release mechanism, as shown in Figure 4-2. Two indents on the surface of the hinge ensure that the particles are placed at the exact same position for every run. Upon releasing the mechanism, both particles simultaneously fall straight down and into the second section of the apparatus. Here, the particles free-fall into their respective Faraday cages, where their initial charges are independently measured. The top Faraday cages were built each using two hollow copper tubes placed one inside the other (the outer cup is 0.15 m tall with a 0.08 m outer diameter). They are held in place by grooves on the top surface of the enclosure (third section). The trap-door mount can be adjusted vertically to modify the drop height of the particles, to vary the free-fall velocity and/or the trajectory of the particles before and after impact. The metallic particle holder and release mechanism was grounded to mitigate the signal noise it generated on the charge measurement reading when it swung open, with the added benefit of mitigating any effect on the trajectory of the free-falling particles due to electrostatic forces.

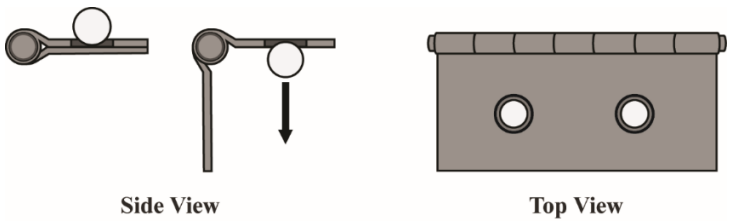

Figure 4-2: Side and top view of the particle holder and release mechanism.

The particles exit the top Faraday cages straight into the insulative enclosure, identified as the third section. The enclosure was constructed using high-density polyethylene sheets, with a removable acrylic front cover. In the fourth section within the enclosure, the free-falling particles pass through an under-mounted acrylic cylinder (0.1 m tall, 0.15 m diameter), which acts as a wind-box. The wind-box has lateral ports on two sides to house the gas nozzles – 0.0127 m (1/2”) diameter stainless steel tubing – used to push the particles towards each other. A free-fall zone below the wind-box gives the particles enough time to collide and rebound off each other. The airflow rate in the nozzles was controlled using a mass flow controller in LabVIEW. This allowed the tuning of the particle trajectories and improved the frequency of successful collisions. While a single nozzle on each side of the wind-box was sufficient, the column can also house multiple nozzles in

series for an increased effect on the trajectory, if necessary. The fifth section is the particle-particle collision zone following the wind-box. This open space needed to be long enough to give the particles time to collide and then rebound off each other. Finally, the last section is where the rebounded particles fall into separate Faraday cages for their final charge measurements. Given the element of randomness in the particle rebound trajectories, the bottom Faraday cages were fabricated using wide and deep copper cups (0.3 x 0.2 x 0.2 m for each outer cup) to ensure the particles can be captured and contained. The total height of the apparatus, from the particle holder to the base of the bottom Faraday cages, is approximately 0.8 m.

A successful collision trial requires the particles to fall straight through the mount and top Faraday cages, collide with each other below the wind-box, and then rebound into the two separate bottom Faraday cages. This could be challenging given the element of randomness currently present for the particles' trajectories, particularly due to any turbulence in the wind-box. As such, a large number of collision trials could be required to obtain statistically significant results. However, many runs can be performed quickly using this apparatus, which can compensate for cases of low collision rates. Moreover, this apparatus design allows the adjustment of the particle mount height and gas injection velocity. This can aid in maximizing the frequency of successful collisions, especially when testing particles of varying sizes and densities, and can also lead to testing different impact velocities and angles.

4.3.2. Particle Collision Detection and Tracking

Each experimental run was video-recorded using a Sony RX100 V digital camera at 920 frames per second. This was necessary to confirm if an elastic collision has occurred, and if the particles then dropped directly into their respective Faraday cages after the collision. Figure 4-3 showcases the video snapshots of two particles experiencing an elastic collision.

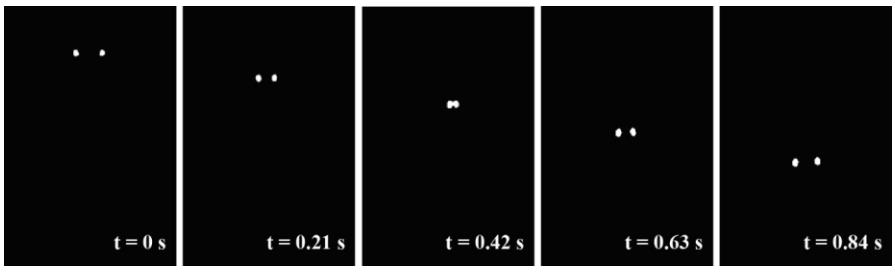

Figure 4-3: Snapshots from a particle-particle collision video, taken at 0.21 s intervals.

The recordings have shown that collisions can occur at varying angles, and in some cases the particles may simply miss each other. As such, a successful collision is identified by the sudden change in the trajectory of the two particles upon collision. This change in trajectory can be observed by applying a particle tracking method, using LabVIEW Vision, to build composite images of the falling particles, as shown in Figure 4-4. Developing such composite images also allows the calculation of the colliding particles' falling velocity, and in turn their impact velocity, for future studies.

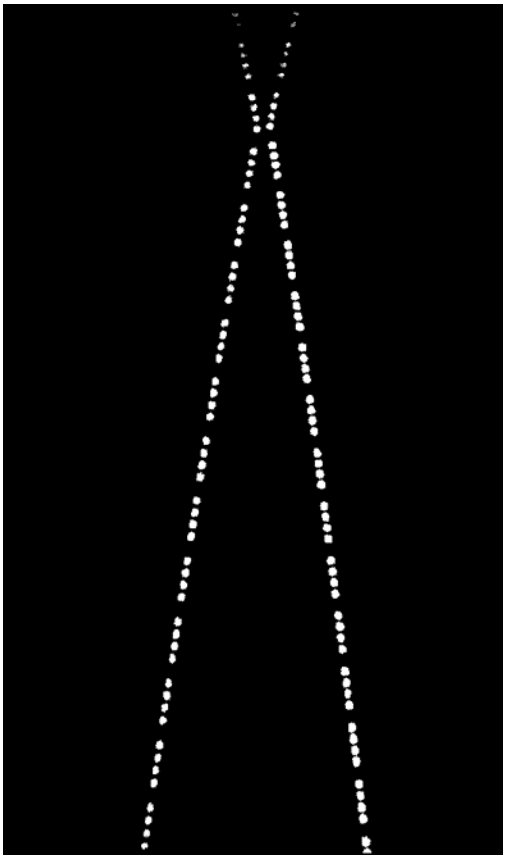

Figure 4-4: Composite image of two particles undergoing an elastic collision.

4.3.3. Charge Measurement Technique

All four Keithley 6514 electrometers in this apparatus were controlled and monitored in LabVIEW. It was programmed to simultaneously measure the charge in the four Faraday cages for the duration of a single run, using a buffered reading rate of 100 Hz. This reading rate was selected to provide a fast measuring speed, ensuring that the maximum particle charge measured

in each Faraday cage reflects the actual charge of the particle, while also minimizing the signal noise.

For each run, the baseline for the charge measurement was adjusted to 0 nC. The electrometers' noise readings can also be accounted for since they are periodic in nature and their amplitudes are negligible relative to the particle charge values. The charge signals obtained from each Faraday cage can be analyzed to determine the particles' charges before and after their collision. It should be noted that every coulomb reading by the electrometer has a measurement accuracy of *"± (Value*0.4% + 50 fC)"*. This reading error is truncated when finding the charge difference (final – initial) on a particle and should be considered when analyzing the amount of charge transferred from one particle to the other. A sample set of charge readings for one particle, detected by electrometers connected to a top and bottom Faraday cage, is shown in Figure 4-5. The reading from the top Faraday cage corresponds to the particle's initial charge, which can be characterized as an impulse as the particle passes through the cage. After the collision, the particle falls into and remains in the bottom Faraday cage, hence the particle's final charge is seen as a step-change.

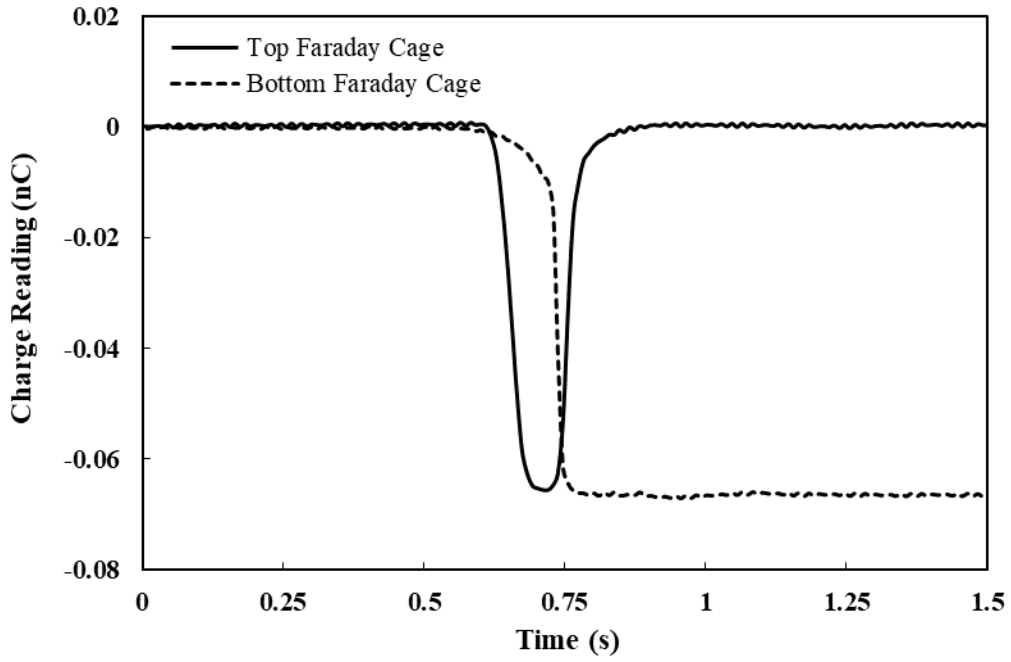

Figure 4-5: Charge readings of one particle dropping through its top Faraday cage before the particle-particle collision, and then landing in its bottom Faraday cage after the collision.

The apparatus was designed to limit any external effects on the colliding particles between the initial and final charge measurements. The only interaction the particles experience during a trial, other than their collision, is with the dry building air used inside the wind-box. It should be noted that electrometer calibration tests were performed to correct for any measurement error between the paired electrometers. It was confirmed during these calibration tests that the dry air did not have a noticeable effect on the charge of the particles. That is, the charge on the particles measured by the top Faraday cages were the same as those measured by the bottom Faraday cages.

4.4. Results and Discussion

Spherical polytetrafluoroethylene (PTFE) particles (3.18 ± 0.05 mm diameter), purchased from McMaster-Carr, were used to test the apparatus design. These particles are ideal for initial testing because PTFE is a highly electronegative material and can gain a significant amount of negative charge from metal contacts and general particle-handling. As such, combining their electronegativity and size, each of these particles can have a measurable initial charge and subsequently a measurable magnitude of charge transfer upon collision. Dry building air (relative humidity (RH) = ~0%, T = 22 °C) was used in the wind-box, and collisions were observed when the air was fed at 150 SLPM per nozzle. The experiments were performed in an ambient laboratory, where the temperature was controlled at 24 °C and the RH ranged from 43 to 49%. While this variance in the RH did not have a noticeable impact on the current results, it may be beneficial in future works to modify the apparatus to allow collisions under vacuum conditions.

The results from 70 collision trials are presented and discussed. In all trials, the initial charges of the particles were never the same value, and it was impossible to predict which of the two particles was more negatively charged prior to the experiment. As such, to simplify the analysis of the charge transfer between the two colliding particles in each trial, the paired particles were labeled based on their initial charges relative to each other, as shown in Figure 4-6. For example, in one trial where the initial charges of the paired particles were -0.06 and -0.03 nC, the particle with the greater negative charge, -0.06 nC, was labeled as *Relatively Negative (RN) Particle* whereas its paired particle, with a charge of -0.03 nC, was labeled as *Relatively Positive (RP) Particle*.

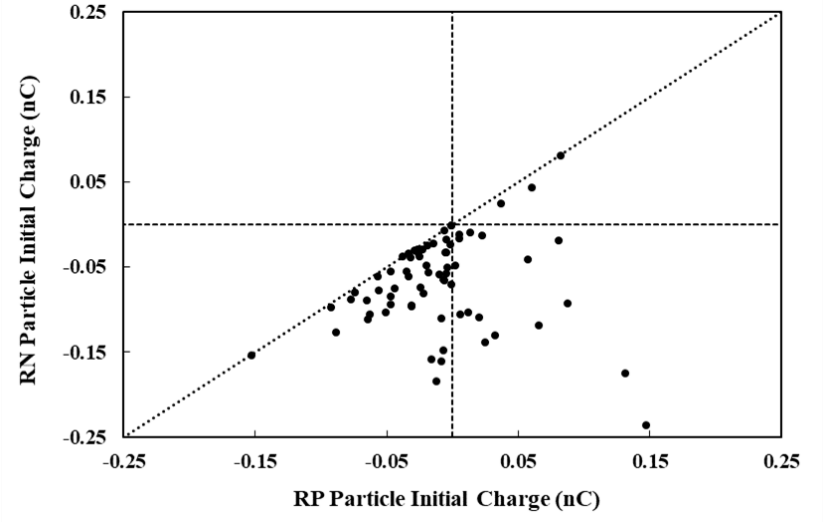

Figure 4-6: Initial charge comparison of paired particles measured for all trials.

Figure 4-7 compares the difference in charge between two particles before and after their collisions. In most cases, it was found that a particle-particle collision resulted in a small amount of charge transfer, since the difference in the particles' initial charge (before collision) was close to the same as the difference in the particles' final charge (after collision). This was expected since the effective work function difference between the two identical particles should be very close to zero – the primary driving force for charge transfer between the two particles would be their difference in initial charges.

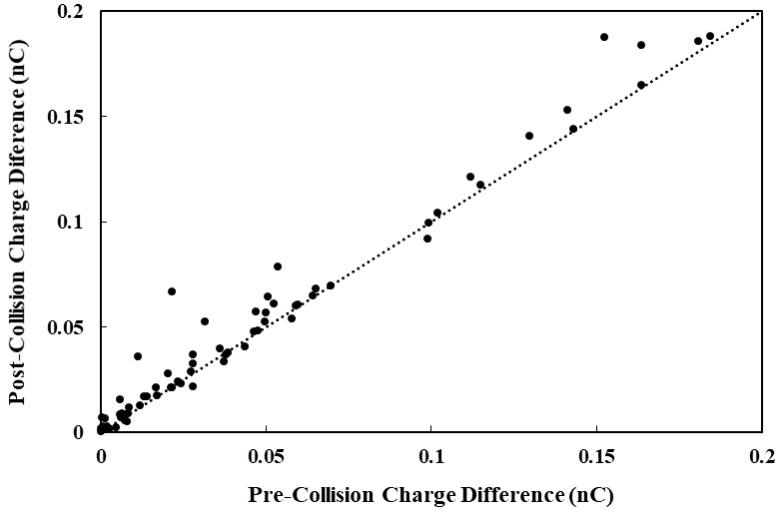

Figure 4-7: Comparing the charge differences between two particles before and after their collision.

It is expected for two objects of varying charges to move towards charge equilibrium upon collision, i.e. their difference in charge after collision should be lower than their initial charge difference. However, it is evident in Figure 4-7 that this was generally not the case; the particles tended to charge such that their charge difference grew greater after their collision. This phenomenon could be explained using the surface state model [20]. While the overall charge on one particle might be more negative than the other, the particle's localized charge at the point of impact might be more positive. As a result, the more negatively charged particle can end up gaining negative charge from the collision event. The tested PTFE particles were previously studied and their saturation charge value was determined to be approximately -0.65 nC [11]. It was shown in Figure 6 that the initial charges of the tested particles were significantly lower than their saturation point, which suggests that their low charges have a low impact on the direction of charge transfer.

Upon further analysis of these collision trials, 2 distinct charge transfer scenarios were found: conventional charging, where the colliding particles charge oppositely; and anomalous charging, where the colliding particles both charged in the same direction.

4.4.1. Conventional Charge Transfer

Conventionally, a collision between two surfaces causes charge transfer from one surface to the other. It was therefore expected from these particle-particle collisions that one particle to charge in the negative direction while the other charges oppositely in the positive direction. Moreover, if the charge transfer was solely due to the particle-particle collision, then the change in charge for both particles should be the same magnitude. Overall, 41 collision trials exhibited conventional charge transfer. However, taking the coulomb reading errors into account for each trial, it was found that 15 trials exhibited near-perfect collisional charge transfer. These ideal charge transfer trials are shown in Figure 4-8, sorted by the magnitude of the net change in charge of the paired particles.

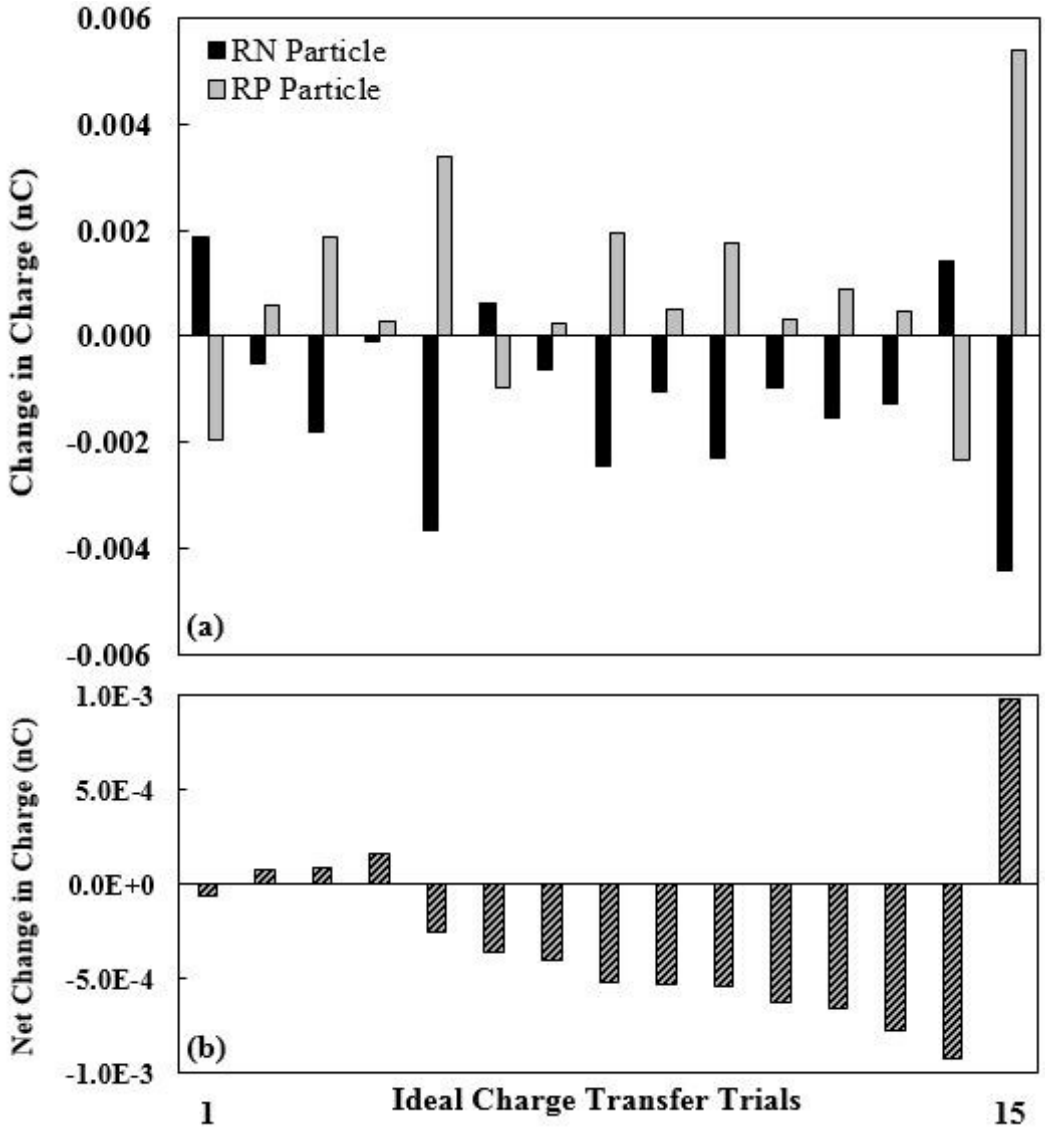

Figure 4-8: Ideal charge transfer trials where (a) the collided particles exhibited conventional charging with near-perfect collisional charge transfer; (b) the charge transfer trials were sorted by increasing discrepancy in the charging of the paired particles.

The remaining conventional charging trials, that exhibited charge transfer discrepancies beyond the truncated reading accuracy of the electrometers, are shown as imbalanced charging trials in Figure 4-9. It was observed that the imbalances in the charge transfer trials were more pronounced for larger charge transfers. At the same time, the larger charge transfers did not strictly correlate with greater initial charges, as shown in Figure 4-10. This suggests that the particles' initial charges were not the driving force for the significantly larger changes in charge. Finally, it was observed that the net charge generated after the particle-particle collision was negative in 31 of the

conventional charge transfer trials. As mentioned above, it was confirmed through calibration tests that the change in charge for the particles in this apparatus was expected to be solely due to the particle-particle collisional charge transfer. The current findings, however, suggest otherwise. Thus, it is possible that an unknown charging mechanism, in addition to particle-particle contact charging, is generating negative charge on the particles.

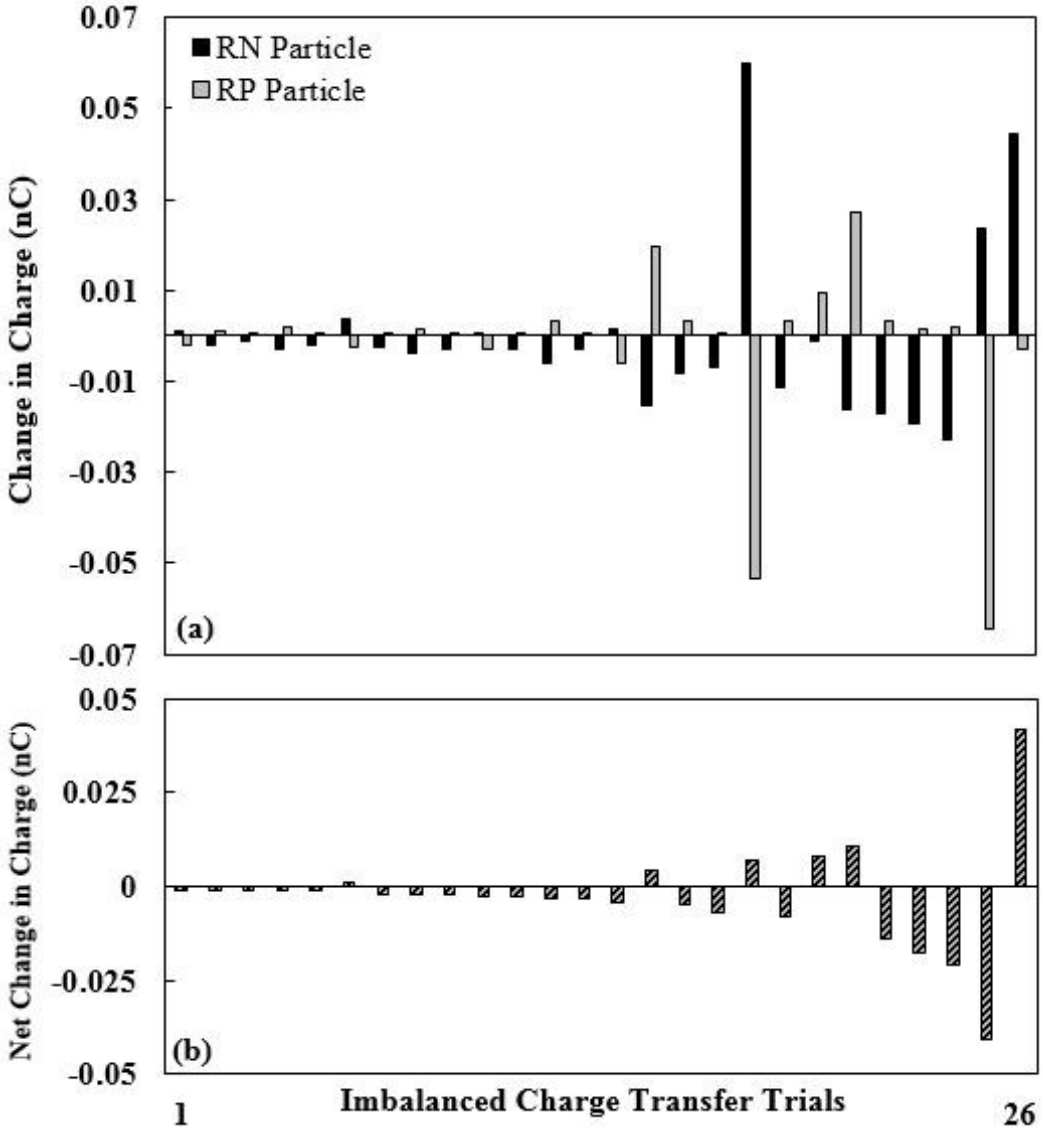

Figure 4-9: Imbalanced charge transfer trials where (a) the collided particles exhibited a charge transfer discrepancy beyond the truncated reading accuracy of the electrometers; (b) the trials were sorted by increasing net change in charge.

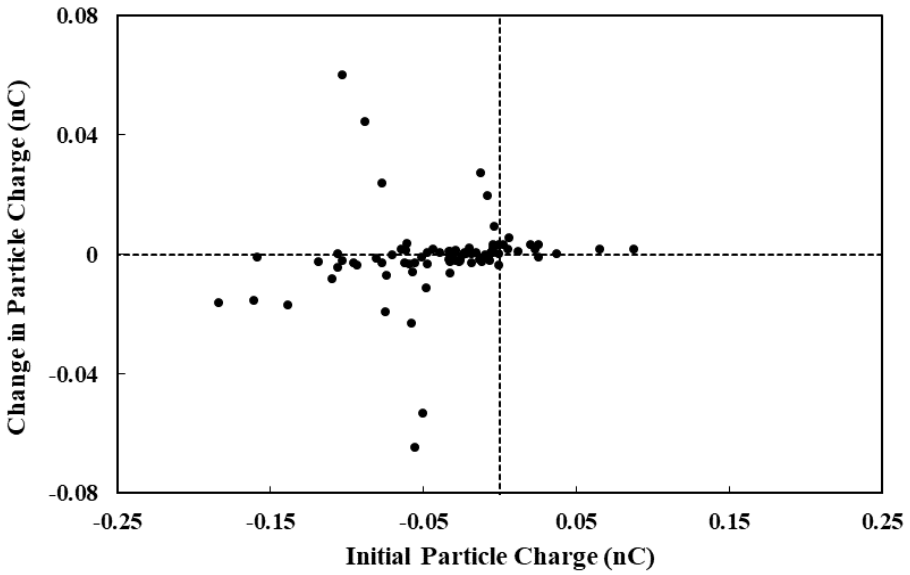

Figure 4-10: The effect of each particle's initial particle charge on its change in charge after experiencing a particle-particle collision.

4.4.2. Anomalous Charging

In addition to the imbalanced charge transfers observed in the conventional charging trials, 29 collision trials have experienced anomalous charging where both particles charged in the same direction. These trials are listed in Figure 11, sorted by the degree of negative charging experienced by the RN Particle. Anomalous charging behaviour has been observed and reported in contact experiments using inorganic materials, but were concluded to not occur in carbon-based materials such as polyethylene and PTFE [45]. It is therefore unclear why a significant portion of the collision trials experienced anomalous charging, though it is possible that this behavior is an extension of the observed conventional yet imbalanced charging trials. In both cases, the net charge generated after the particle-particle collisions tended to be negative. Given the relatively low charging magnitudes observed in the anomalous cases, it is possible that typical conventional charge transfers experienced by the colliding particles were overshadowed by the additional negative charging experienced by the particles.

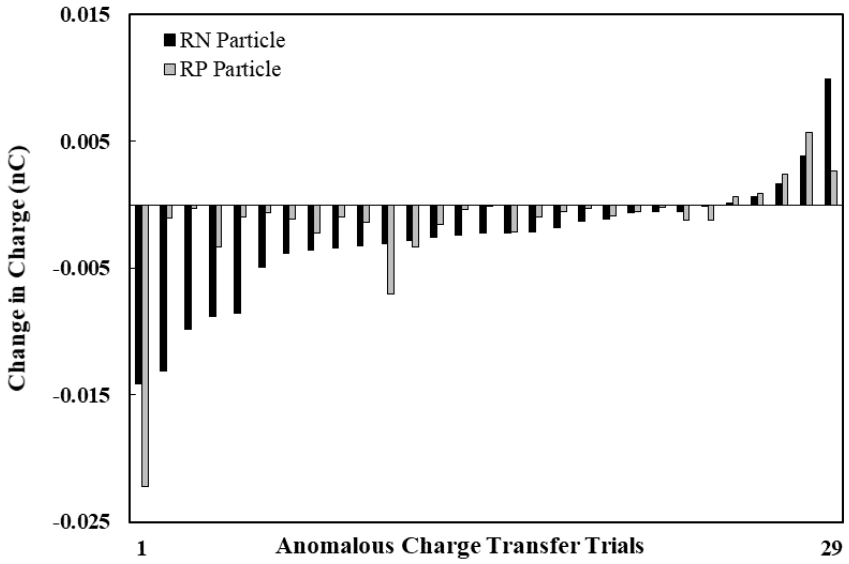

Figure 11: Anomalous charge transfer trials where the collided particles experienced charging in the same direction.

4.5. Conclusions and Future Work

In conclusion, an apparatus to study the direction and magnitude of charge transfer between two colliding particles was designed and built. This design ensured that the measured change in each particle's charge was solely due to the particle-particle interactions between the two colliding particles. The collisions were confirmed by monitoring the particle trajectories using a high frame-rate camera coupled with particle-tracking software. Upon performing preliminary tests on this apparatus with PTFE particles, it was confirmed that triboelectrification solely due to the particle-particle collision can be observed. However, additional charge generation was also observed in most collision trials, indicating that an unknown charging mechanism could also play a role in the particle-particle interaction. In some cases, this mechanism could overshadow the particle-particle charge transfer, possibly leading to the numerous anomalous charging trials observed. Further collision trials, particularly with highly charged particles, may shed some light on this charge-transfer behaviour. In most cases, the initial charge of the colliding particles did not dictate the direction of charge transfer, which held true even for the ideal charge transfer cases. Future work for this study involves testing with highly charged particles; to explore the cause of the additional charging observed in many cases, and to confirm if initial charges closer to the particles' charge saturation point have an impact on the direction of charge transfer. Finally, the apparatus must be used to test the charge transfer between polyethylene particles of varying sizes, to work towards

the objective of developing a particle-particle charging model for simulating electrostatic effects of polydisperse particles in gas-solid fluidized beds.

References

[1] F. Fotovat, X.T. Bi, J.R. Grace, Electrostatics in gas-solid fluidized beds: A review, Chem. Eng. Sci. 173 (2017) 303–334.

[2] P. Mehrani, M. Murtomaa, D.J. Lacks, An overview of advances in understanding electrostatic charge buildup in gas-solid fluidized beds, J. Electrostat. 87 (2017) 64–78.

[3] G. Hendrickson, Electrostatics and gas phase fluidized bed polymerization reactor wall sheeting, Chem. Eng. Sci. 61 (2006) 1041–1064.

[4] J.R. Chirillo, C.K.I. Kellam, P.E. McHattie, Method for reducing sheeting during polymerization of alpha-olefins, US4855370 A, (1986). https://www.google.com/patents/US4855370 (accessed August 1, 2017).

[5] A. Sowinski, L. Miller, P. Mehrani, Investigation of electrostatic charge distribution in gas–solid fluidized beds, Chem. Eng. Sci. 65 (2010) 2771–2781.

[6] D. Song, P. Mehrani, Comparison of electrostatic charge generation in gas-solid fluidized beds in turbulent versus pre-turbulent flow regime, Powder Technol. 319 (2017) 426–433.

[7] Mahdi F. Al-Adel, A. Dudley A. Saville, S. Sundaresan*, The Effect of Static Electrification on Gas−Solid Flows in Vertical Risers, Ind. Eng. Chem. Res. (2002).

[8] H. Watanabe, A. Samimi, Y.L. Ding, M. Ghadiri, T. Matsuyama, K.G. Pitt, Measurement of Charge Transfer due to Single Particle Impact, Part. Part. Syst. Charact. 23 (2006) 133–137.

[9] P.M. Ireland, Triboelectrification of particulate flows on surfaces: Part I — Experiments, Powder Technol. 198 (2010) 189–198.

[10] S. Matsusaka, H. Maruyama, T. Matsuyama, M. Ghadiri, Triboelectric charging of powders: A review, Chem. Eng. Sci. 65 (2010) 5781–5807.

[11] F. Chowdhury, A. Sowinski, M. Ray, A. Passalacqua, P. Mehrani, Charge generation and saturation on polymer particles due to single and repeated particle-metal contacts, J. Electrostat. 91 (2018) 9–15.

[12] C. Pei, D. England, S. Byard, H. Berchtold, M. Adams, C.Y. Wu, D. England, S. Byard, H. Berchtold, M. Adams, Numerical analysis of contact electrification using DEM–CFD, Powder Technol. 248 (2013) 34–43.

[13] M. Ray, F. Chowdhury, A. Sowinski, P. Mehrani, A. Passalacqua, An Euler-Euler model for mono-dispersed gas-particle flows incorporating electrostatic charging due to particle-wall and particle-particle collisions, Chem. Eng. Sci. 197 (2019) 327–344.

[14] J. Cross, Electrostatics: Principles, Problems and Applications, Adam Hilger, Bristol, 1987.

[15] M.W. Williams, Effect of Polymer Structure on its Triboelectric Properties, IEEE Trans. Ind. Appl. IA-12 (1976) 213–219.

[16] D.K. Davies, Charge generation on dielectric surfaces, J. Phys. D. Appl. Phys. 2 (1969) 307.

[17] J. Lowell, A.C. Rose-Innes, Contact Electrification, Adv. Phys. 29 (1980) 947–1023.

[18] A.F. Diaz, D. Fenzel-Alexander, An ion transfer model for contact charging, Langmuir. 9 (1993) 1009–1015.

[19] C. Xu, Y. Zi, A.C. Wang, H. Zou, Y. Dai, X. He, P. Wang, Y.-C. Wang, P. Feng, D. Li, Z.L. Wang, On the Electron-Transfer Mechanism in the Contact-Electrification Effect, Adv. Mater. 30 (2018) 1706790.

[20] G.S.P.S.P. Castle, L.B.B. Schein, General model of sphere-sphere insulator contact electrification, J. Electrostat. 36 (1995) 165–173.

[21] J. Lowell, W.S. Truscott, Triboelectrification of identical insulators. I. An experimental investigation, J. Phys. D. Appl. Phys. 19 (1986) 1273–1280.

[22] H.T. Baytekin, A.Z. Patashinski, M. Branicki, B. Baytekin, S. Soh, B.A. Grzybowski, The Mosaic of Surface Charge in Contact Electrification, Science (80-.). 333 (2011) 308–312.

[23] T. Matsuyama, H. Yamamoto, Impact charging of particulate materials, Chem. Eng. Sci. 61 (2006) 2230–2238.

[24] T. Itakura, H. Masuda, C. Ohtsuka, S. Matsusaka, The contact potential difference of powder and the tribo-charge, J. Electrostat. 38 (1996) 213–226. doi:10.1016/S0304-3886(96)00026-5.

[25] S. Matsusaka, H. Masuda, Electrostatics of particles, Adv. Powder Technol. 14 (2003) 143–166.

[26] A. Ema, D. Yasuda, K. Tanoue, H. Masuda, Tribo-charge and rebound characteristics of particles impact on inclined or rotating metal target, Powder Technol. 135–136 (2003) 2–13.

[27] M. Nifuku, T. Ishikawa, T. Sasaki, Static electrification phenomena in pneumatic transportation of coal, J. Electrostat. 23 (1989) 45–54.

[28] M. Nifuku, H. Katoh, A study on the static electrification of powders during pneumatic transportation and the ignition of dust cloud, Powder Technol. 135 (2003) 234–242.

[29] J. Yao, Y. Zhang, C.-H. Wang, S. Matsusaka, H. Masuda, Electrostatics of the Granular Flow in a Vertical Pneumatic Conveying System, Ind. Eng. Chem. Res. 43 (2004) 7181–7199.

[30] S. Kittaka, N. Masui, Y. Murata, A method for measuring the charging tendency of powder in pneumatic conveyance through metal pipes, J. Electrostat. 6 (1979) 181–190.

[31] P. Mehrani, H.T. Bi, J.R. Grace, Electrostatic charge generation in gas–solid fluidized beds, J. Electrostat. 63 (2005) 165–173.

[32] J. Guardiola, V. Rojo, G. Ramos, Influence of particle size, fluidization velocity and relative humidity on fluidized bed electrostatics, J. Electrostat. 37 (1996) 1–20.

[33] F. Jalalinejad, X.T. Bi, J.R. Grace, Effect of electrostatics on freely-bubbling beds of mono-sized particles, Int. J. Multiph. Flow. 70 (2015) 104–112.

[34] J.R. Mountain, M.K. Mazumder, R.A. Sims, D.L. Wankum, T. Chasser, P.H. Pettit, Triboelectric charging of polymer powders in fluidization and transport processes, IEEE Trans. Ind. Appl. 37 (2001) 778–784.

[35] Z. Liu, X.T. Bi, J.R. Grace, Electrostatic charging behaviour of dielectric particles in a pressurized gas–solid fluidized bed, J. Electrostat. 68 (2010) 321–327.

[36] M.W. Korevaar, J.T. Padding, M.A. Van der Hoef, J.A.M. Kuipers, Integrated DEM-CFD modeling of the contact charging of pneumatically conveyed powders, Powder Technol. 258 (2014) 144–156.

[37] C. Pei, C.Y. Wu, D. England, S. Byard, H. Berchtold, M. Adams, Numerical analysis of contact electrification using DEM-CFD, Powder Technol. 248 (2013) 34–43.

[38] M.M. Apodaca, P.J. Wesson, K.J.M. Bishop, M.A. Ratner, B.A. Grzybowski, Contact Electrification between Identical Materials, Angew. Chemie Int. Ed. 49 (2010) 946–949.

[39] D. Song, F. Salama, J. Matta, P. Mehrani, Implementation of Faraday cup electrostatic charge measurement technique in high-pressure gas–solid fluidized beds at pilot-scale, Powder Technol. 290 (2016) 21–26.

[40] M. Rowland, A. Cavecchi, F. Thielmann, J. Kulon, J. Shur, R. Price, Measuring The Bipolar Charge Distributions of Fine Particle Aerosol Clouds of Commercial PMDI Suspensions Using a Bipolar Next Generation Impactor (bp-NGI), Pharm. Res. 36 (2018) 15.

[41] K.M. Forward, D.J. Lacks, R. Mohan Sankaran, Methodology for studying particle–particle triboelectrification in granular materials, J. Electrostat. 67 (2009) 178–183.

[42] M.A. Bilici, J.R. Toth, R.M. Sankaran, D.J. Lacks, Particle size effects in particle-particle triboelectric charging studied with an integrated fluidized bed and electrostatic separator system, Rev. Sci. Instrum. 85 (2014).

[43] W. Hu, L. Xie, X. Zheng, Contact charging of silica glass particles in a single collision, Appl. Phys. Lett. 101 (2012) 114107.

[44] L. Xie, G. Li, N. Bao, J. Zhou, Contact electrification by collision of homogenous particles, J. Appl. Phys. 113 (2013) 184908.

[45] Y. Fang, L. Chen, Y. Sun, W.P. Yong, S. Soh, Anomalous Charging Behavior of Inorganic Materials, J. Phys. Chem. (2018).

Chapter 5

Electrostatic charging due to individual particle-particle collisions

F. Chowdhury[a], M. Ray[b], A. Passalacqua[b], P. Mehrani[a], A. Sowinski[a]

[a] Department of Chemical and Biological Engineering, University of Ottawa, 161 Louis Pasteur, Ottawa, ON, Canada, K1N 6N5
[b] Department of Mechanical Engineering, Iowa State University, 2025 Black Engineering Building Ames, IA, 50011-2161, USA

This chapter is a manuscript published in Powder Technology (2021; 381:352-365)

Abstract

The charge transferred between individual particles of varying materials (aluminum, PTFE and nylon) and sizes (3.2 – 4.8 mm) was investigated using a particle collision apparatus. The collisions were video-recorded and analyzed via a Particle Tracking Velocimetry software to determine the particles' impact velocities and angles. Glancing impacts were found to have a notable effect on charge transfer. Different-material collisions exhibited expected directions of charge transfer. Same-sized nylon collisions revealed that their charge transfer amplified the difference in the particles' initial charges in most cases. Different-sized nylon collisions suggested that size-dependent bipolar charging occurs in individual particle-particle collisions. However, the charging magnitude and direction did not correlate with their size differences, and so additional particle collision experiments with other material types and sizes are needed. This work should be considered as a steppingstone for future researchers to explore particle-particle charge transfer in their respective systems, and develop empirical particle charging models.

5.1. Introduction

Electrostatic charging is a seemingly simple phenomenon where an insulator gains or loses charge after colliding with another surface. However, progress has been slow in understanding even the most fundamental aspects of charge transfer [1]. This is partly because charge transfer is extremely sensitive to the properties and conditions of the contacting surfaces and their environments. For example, Masuda et al. (1976) discussed how charge transfer between insulators could increase drastically by simply introducing an impurity on their surface [2]. This behavior was convincingly demonstrated by Horn et al. (1993), who observed enhanced contact electrification between two silica surfaces when one was coated with a single chemisorbed monolayer [3]. More recently, Heinert et al. (2020) saw that even ambient fields can contribute to induction charging [4], suggesting that any changes to the lab environment or operation of the charging experiments could lead to unreproducible results. In addition to its sensitivity, charge transfer occurs due to a complex combination of competing contact charging mechanisms. Despite being heavily debated over the years, it remains unclear which charging mechanism dominates in triboelectrification: electron transfer [5,6], ion transfer [7,8], or material transfer [9,10]. Lacks and Shinbrot (2019) provided extensive details on the observed complexity in triboelectric charging, which, in some cases, even defied our qualitative understanding of the subject [11]. Due to the described complexity in possible charge transfer mechanisms, the electrostatic charging behaviour for a given system can only be understood by performing experiments relevant to that environment. One of these poorly understood charging behaviours is the bipolar charging of insulators observed in gas-solid flow systems. Numerous studies have shown that bipolar charging is prevalent in particle flow systems with a wide particle-sized distribution. It has been widely established that smaller particles in granular systems tend to charge negatively [12–14], although contrary findings have also been reported for specific polymers in fluidization studies [15,16]. In industrial applications such as fluidized bed reactors for polymer production, one must consider interactions between the produced polymer, catalysts, antistatic agents and any impurities present during the fluidization process. This complex mixture of particles of varying sizes could certainly alter the charging behavior than what is observed in simpler granular systems. Ultimately, the direction of charging between different-sized insulators is dependent on the properties of the colliding materials, and particularly the dominant charged species involved. It is unclear whether bipolar charging is a consequence of particle interactions in bulk flow, or if it is also prevalent in individual collisions.

Bipolar charging behaviour must therefore be studied at a fundamental level; to determine the direction of charge transfer between individual particle-particle collisions of different-sized insulators.

5.1.1. Particle-Particle Charging Experiments

In an effort to study the charging behaviour between insulative particles, several researchers have developed experimental procedures to observe particle-particle collisions and measure their change in charge. Xie et al. (2013) performed particle contact experiments where one particle was dropped onto a resting particle of the same or larger size [17]. These collisions of homogeneous particles, which ranged between 2 and 20 mm in size, revealed that the maximum magnitude of charge transfer occurred when the diameter ratio between the two particles was 0.6. While the charge on the smaller, free-falling particles was not measured, it could be deduced that these particles gained negative charge equal to the magnitude of positive charge measured for the larger particle. Bilici et al. (2014) developed an integrated fluidized bed and electrostatic separator system to induce and characterize particle charging solely due to interparticle interactions [18]. Their tests using a bidisperse mixture of soda lime glass particles showed that the smaller particles charged negatively, whereas the larger particles charged positively. In addition, the charge segregation for one particle size was strongest when its collisions were mostly with particles of the other size [18]. Waitukaitis et al. (2014) further confirmed this size-dependent charging behavior, where smaller particles charged negatively, by tracking individual grains falling and colliding in an electric field [19]. Konopka et al. (2020) performed same-material particle-particle collisions by shaking 0.8 mm to 1 mm polyethylene resin in a metal container coated with a monolayer of the same particle [20]. They observed bipolar charging on the particles, which took significantly longer to reach charge saturation than their cases of particle-metal collisions. The dependency on particle size for the bipolar charging was not considered in their study.

Our contribution to studying particle-particle charge transfer was through the development of a novel collisional charging apparatus [21]. In this apparatus, particle-particle collisions were performed using airflow to push two free-falling particles towards each other, and both particles' charges were individually measured before and after the collision. This charging technique successfully isolated the charge transfer between two particles, opening the possibility of observing the charging behaviours in various types of particle-particle collisions. It should be

noted that Kline et al. (2020) also recently developed an apparatus to measure individual particle charging due to repeated contacts between acoustically levitated sub-millimetre grains [22]. Using a very precise charge measurement technique, they measured charge transfers of approximately 0.5 fC per collision between two chemically identical polyethylene particles. The scale of these charge transfer measurements is significantly lower than what was measured in our initial experiments, where 3.2 mm polytetrafluoroethylene particles experienced charge transfers of approximately 2 pC. [21]. The greater charge transfer in our previous work could be attributed to larger particle sizes and impact velocities, and especially the difference in material type. Thus, to further investigate the effect of various properties involved in collisional charge transfer, particles of varying materials and sizes were collided together in an updated version of our particle-particle charging apparatus. The results presented in this work are part of the continued effort to observe and analyze fundamental particle-particle charging behaviours, which would ultimately aid in the development of electrostatic charging models for use in gas-solid flow simulations.

5.2. Design & Methodology

The original design of the particle-particle collision apparatus and the applied charge measurement techniques were presented in Chowdhury et al. (2020) [21]. While the schematic remained the same, an updated apparatus was built, which improved the success rate of the collision trials and allowed the collision of different-sized particles. The experimental procedure is reiterated here, with references to the sections listed on the schematic visualized in Chowdhury et al. (2020) [21]. The updates to the original design are also discussed in detail.

5.2.1. Apparatus Design

Each collision trial was initiated by loading two particles into the particle holder and release mechanism (section 1), pictured in Figure 5-1. This was a removable 0.0127 m (½ inch) thick aluminum plate, under-mounted with two sliding trapdoors, activated using pull-type solenoid actuators. Multiple plates were fabricated with two holes drilled to match the size of the particles. The plates were easily substituted to ensure that the particles of varying sizes were always resting at the same position for each trial before their release. While all the presented collision trials were dropped simultaneously, having two independent trapdoors allowed the option to perform a staggered particle drop when needed.

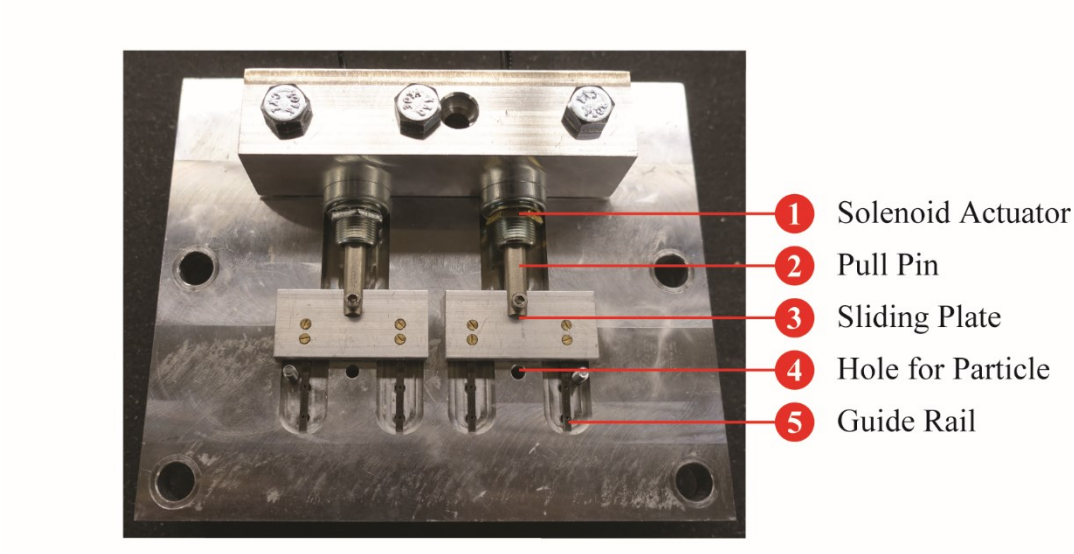

Figure 5-1: Bottom view of the particle holder and release mechanism, showcasing the two sliding trapdoors.

Upon activating the trapdoors, the particles were dropped through two open-ended Faraday cages to obtain their individual initial charges (section 2). These Faraday cages were built using two hollow copper tubes, one placed inside the other, and were held in place by grooves on the top surface of the enclosure. The outer tubes (0.15 m, 0.08 m outer diameter) were grounded while the inner tubes were connected to two separate Keithley 6514 electrometers. Once the free-falling particles entered the enclosure (section 3), they passed through an under-mounted acrylic wind-box (0.1 × 0.085 × 0.085 m). Here, the particles were pushed towards each other using air jets fed through two lateral 0.0127 m (½ inch) nozzles (section 4). The particle-particle collision zone below the wind-box (section 5) gave the particles enough time to collide and rebound off each other. A 960 FPS camera (Sony RX100 V) was focused on this zone to record the particles' movements and confirm if a collision took place. If a collision occurred, the rebounding particles fell into their respective bottom Faraday cages, where their final charges were measured by two additional Keithley 6514 electrometers (section 6). These Faraday cages were fabricated as copper cups (0.3 × 0.2 × 0.15 m for each outer cup), which were deep enough to capture the particles and wide enough to account for varying particle rebound trajectories.

All four electrometers used in this apparatus were controlled and monitored in LabVIEW. They were programmed to simultaneously detect charge signals for the duration of a single run, using a buffered reading rate of 100 Hz. The initial and final charges for each particle are used to calculate

their change in charge, ΔQ, due to the particle-particle collision. The initial charge of the particles could be minimized using a charge neutralizer, although it is logistically not possible to obtain a completely neutral initial charge due to general particle handling as well as particle-metal interactions with the particle-holder. The particle charging data were deemed usable for each collision trial when the net change in charge, ΔQ_{net}, for the two particles were sufficiently close to zero. Since these calculations require charge readings from four different electrometers, precise and accurate charge measurements were vital to minimize the truncated measurement errors. The charge measurement and signal analysis was discussed in detail in Chowdhury et al. (2020) [21]. The airflow rate in the nozzles was controlled using a mass flow controller in LabVIEW, which in turn provided control over the particle trajectories. The airflow rate was tested between 80 and 175 SLPM on each nozzle to identify the ideal conditions for collisions which may change depending on the size and density of the particles. It was found that 125 SLPM provided successful collisions for all tested combinations of particle types and sizes.

The most notable improvement to the original design was the sliding trapdoor mechanism, which automated the simultaneous release of both particles and greatly reduced the effect of electrostatic forces on their starting trajectories. Moreover, implementing the solenoid actuator made it possible to activate the trapdoor through LabVIEW, thus synchronizing the particles' release with the buffered reading of the electrometers. This not only streamlined the process of repeating collision trials but also simplified the post-processing of the charge measurement readings. Minor modifications include a reduced spacing between the two particles at the start and a longer collision zone to allow the particles ample time to rebound and fall into their separate Faraday cages. These changes to the design significantly increased the rate of successful collisions.

5.2.2. Collision Detection & Particle Tracking

The turbulence in the wind-box due to continuous gas injection, coupled with the electric field effect from the particles' initial charges, introduced an element of randomness to every collision trial. A slow-motion recording of each trial was, therefore, necessary to confirm if the particles collided and then dropped directly into separate Faraday cages. Moreover, since every particle interaction is unique, recording each trial also provided the opportunity to group the collisions based on their mode of contact. Figure 5-2 showcases the video snapshots of three collision scenarios: a clean, direct collision where the particles were at the same height at the moment of

impact; an angled collision where one particle was slightly below the other; and a tangential collision where the particles grazed each other.

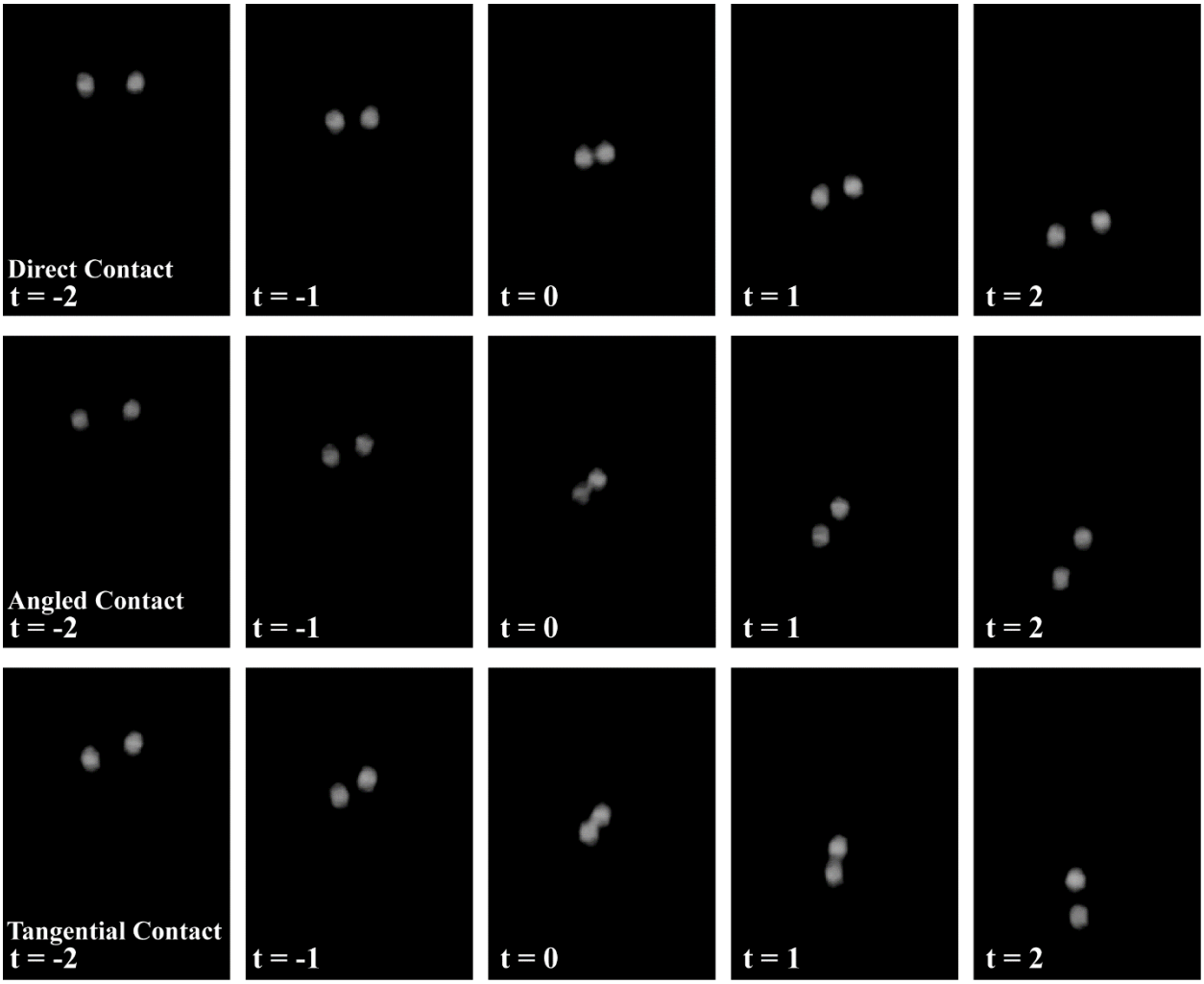

Figure 5-2: Video frames of three sample collision trials: direct contact, angled contact, and tangential contact.

Particularly for tangential collisions, the contact was confirmed by checking if there was a sudden change in the particle trajectories after their supposed impact. The trajectories were determined using PTVResearch [23], a particle tracking velocimetry (PTV) program built for MATLAB. Once the two particles were identified in a video through image analysis techniques such as binarization and thresholding, the program determined the pixel coordinates of the particle centers in each frame. Plotting these coordinates made it possible to visualize the particles' trajectories before and after their collision, and in turn determine the particles' impact angle and velocity [24].

5.2.2.1. Impact Velocity & Impact Angle

The series of coordinates obtained through PTV was used to obtain the velocity vectors of both particles before and after their collision. Given that each collision was unique, the impact angle and, in turn, the normal component of the impact velocity was drastically different for each trial. This was an important factor to consider when analyzing the charge transfer data, since normal velocity, u_N, is an independent parameter in charge transfer models [25,26]. Therefore, it may be beneficial to analyze the charge transfer data for each collision trial as a function of the normal velocity. More specifically, the Hertzian theory of contact deformation is used in charge transfer models to determine the effective contact area (S_c) of colliding surfaces as a function of u_N [27]:

$$S_c = k_s u_N^{4/5} \qquad 5\text{-}1$$

Here, k_s is 5-14. The resting particle is selected as such based on their relative mass, such that $m_2 \geq m_1$. Both particles are then rotated about the origin until the velocity of the approaching particle only exists in the x-direction.

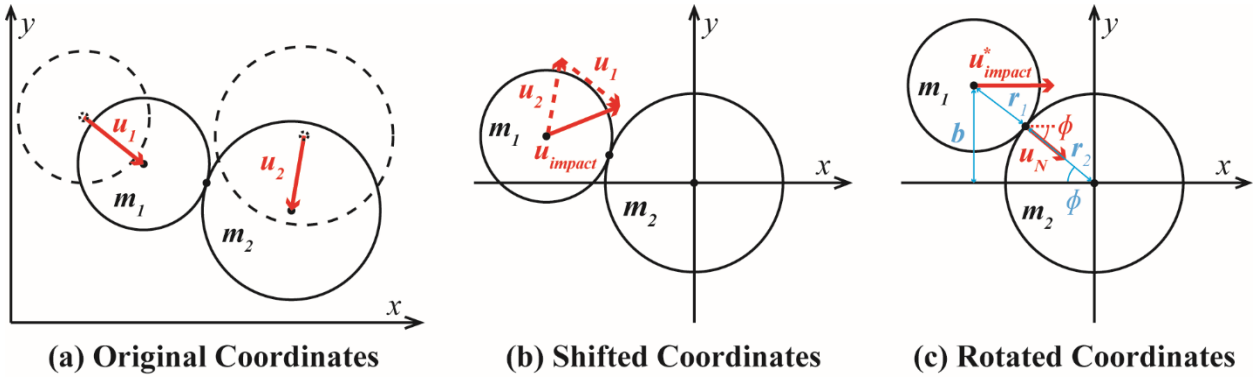

Figure 5-3: Procedure for identifying the normal velocity at the point of impact: (a) Original Coordinates: Determine the particles' cell-center coordinates as well as their velocities before collision. (b) Shifted Coordinates: Shift the coordinates of both particles and adjust the frame of reference such that the larger particle is at rest at the point of origin. (c) Rotated Coordinates: Rotate the particles about the origin until the moving particle horizontally approaches the resting particle.

This procedure simplifies the geometry of the system such that the velocity of the approaching particle represents the rotated impact velocity, u^*_{impact}, and the impact angle, ϕ, can be easily calculated:

$$\sin\phi = \frac{b}{r_1 + r_2} \quad 5\text{-}2$$

The impact parameter, b, is the vertical distance between the two particle centers and provides a numerical description of the modes of contact shown in Figure 5-2. For example, if $b = 0$ then a perfectly direct collision took place between the particles. As the value of b increases, the mode of contact becomes more angled in nature. Finally, a tangential contact occurs when $b \cong (r_1 + r_2)$, and after this point it is implied that the collision did not occur. The normal velocity at the point of impact is determined using the impact angle ϕ and the modified velocity vector:

$$u_N = u^*_{impact} cos\phi \quad 5\text{-}3$$

Although it is not considered in current charge transfer models, the tangential velocities may also be worth investigating for their contribution to charge transfer in particle-particle collisions:

$$u_T = u^*_{impact} sin\phi \quad 5\text{-}4$$

5.2.3. Materials and Operating Conditions

The particle-particle charging apparatus was used to perform a matrix of collision experiments with varying particle types and sizes. The experiments were performed primarily using smooth, spherical particles purchased from McMaster-Carr (USA). The tested materials, which ranged between 1.6 and 4.8 mm in size, included polytetrafluoroethylene (PTFE), nylon 6/6, aluminum, high-density polyethylene (HDPE), and polypropylene (PP). Particle-particle collisions were also attempted using linear low-density polyethylene (LLDPE) resins, which were previously used for repeated particle-metal contact experiments [29].

At the end of every set of collision trials, the tested particles were first rinsed with water to remove any large dust particles or impurities they may have picked up after their collision trial. They were then thoroughly cleaned with 60% ethanol solution, followed by a second round of water rinsing. The particles were then blow-dried for at least 24 hours before storage or reuse. The relative humidity (RH) of the lab environment typically ranged between 50-55%. However, dried compressed air was injected into the wind-box during the collision trials; it was assumed that the continuous flow of the ~0% RH compressed air would mitigate humidity effects on electrostatic charging. Nonetheless, the particles likely contained water molecules on their surface, which is

known to be a possible contributor to charge transfer [30,31]. As such, it may be worthwhile in future experiments to heat-dry the particles, rather than simply blow dry in ambient conditions, and then perform the collision trials in a humidity-controlled environment.

While collisions were observed for almost all tested combinations of particle types and sizes, the primary challenge was attaining a measurable value of particle-particle charge transfer. It should be noted that every Coulombic reading by Keithley 6514 electrometers has a measurement accuracy of "$\pm\ (Value * 0.4\%) + 0.05\ pC$", and the reading error is truncated when measuring the change in charge, ΔQ, for a particle before and after the collision. This means if the truncated reading error for ΔQ is greater than the value itself, then the charge measurement cannot be trusted. This situation occurred for all trials involving particle sizes smaller than 3.2 mm. Moreover, the majority of the same material collision trials, including both same-sized and different-sized collisions, did not exhibit significant charge transfer relative to their reading accuracy and so their charge measurements are not reported. This was expected behaviour based on the particle charging results from Kline et al. (2020) [22], who found that submillimetre polyethylene particles charged an order lower than what is measurable with our electrometer. Ultimately, measurable charge transfer data was successfully obtained for same-sized PTFE-PTFE, PTFE-aluminum, PTFE-nylon, and nylon-nylon collisions. Charge transfers between different-sized nylon particles were also detected for combinations of 3.2, 4.0, and 4.8 mm nylon. The material properties of all successfully tested particles, along with the tested airflow rates, are summarized in Table 5-1.

Table 5-1: Densities, sizes, and airflow rates used for all successfully tested particles.

Particle Type	Particle Density (kg/m^3)	Particle Size (mm)	Airflow Rate (SLPM)
Polytetrafluoroethylene (PTFE)	2130	3.2	100, 125, 150
Nylon 6/6	1135	3.2, 4.0, 4.8	100, 125, 150, 175
2017 Aluminum	2790	3.2	125
High-density polyethylene (HDPE)	970	3.2	125

5.2.4. Particle Charging in Airflow

If the collision trials ever exhibited a discrepancy in charge transfer beyond the truncated reading accuracy, then an external source must have contributed to the particles' charging. This was a concern that emerged from the charge transfer data for PTFE-PTFE collisions, where a significant number of cases experienced imbalanced and anomalous charge transfer [21]. The design of this

apparatus relied heavily on the notion that non-ionized airflow does not affect particle charging. However, provided that the colliding particles did not touch any other surface during the run, it could be reasoned that the airflow was responsible for this discrepancy. This was confirmed by dropping single PTFE particles through the apparatus with and without the airflow. The charge measurements were related to the particles' initial charges (Q_i), with an example shown in Figure 5-4 for 3.2 mm PTFE particles.

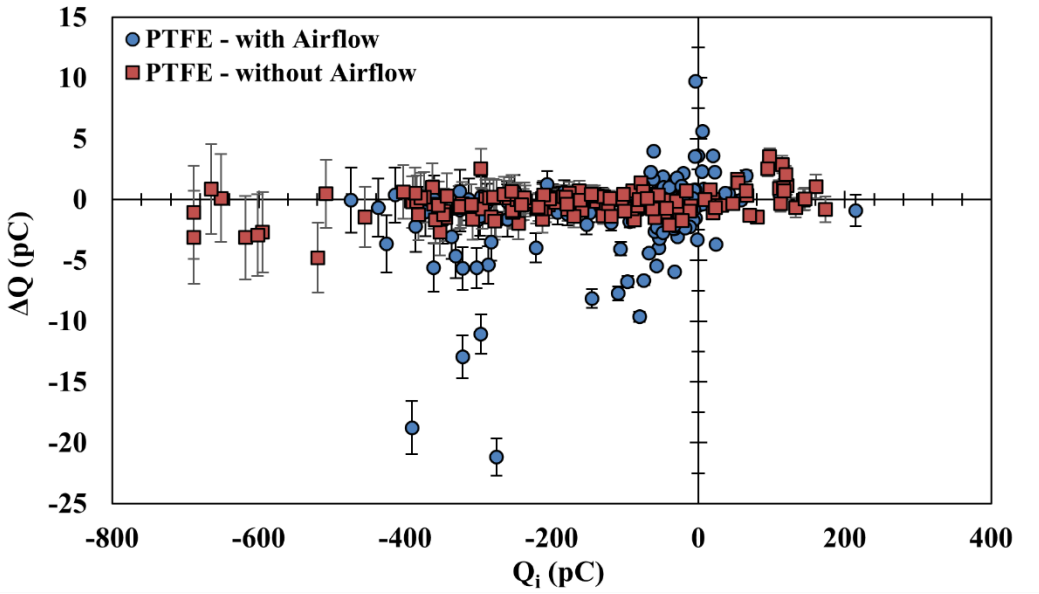

Figure 5-4: Change in particle charge as a function of initial charge for single 3.2 mm PTFE particles dropped with and without airflow.

In general, high initial charges ($|Q_i| > 200\,pC$) resulted in truncated measurement errors that would overshadow the actual charge transfer magnitudes observed from the collision trials (i.e. larger error bars with increasing initial charges). Although collisions were already rare at high initial charges, the measurement error gave another reason to avoid such trials. Thus, only lower initial charges ($|Q_i| < 200\,pC$) should be considered in the collision trials. Within this range, it was clear that PTFE did not generate charge when dropped without airflow. On the other hand, charge generation was observed in a few cases with airflow. This explains the cases of anomalous charging behaviour observed in the previous study [21], and confirms that PTFE cannot be reliably used for further experiments with this apparatus.

Since PTFE tended to charge negatively when interacting with the non-ionized airflow, its highly electronegative nature is the likely source for its electrostatic instability. Thus, less electronegative polymers such as HDPE and nylon 6/6 were selected as potential particles for the collision experiments. As shown in Figure 5-5, HDPE and nylon particles experienced much lower charge generation from the airflow interactions. Particularly for nylon, the airflow effect was minimized when $|Q_i| < 100\,pC$. It should be noted that nylon appeared to generate positive charge at relatively higher initial charges, which suggests that the mechanism for the airflow-induced charging behaviour is affected by the electronegativity of the particle.

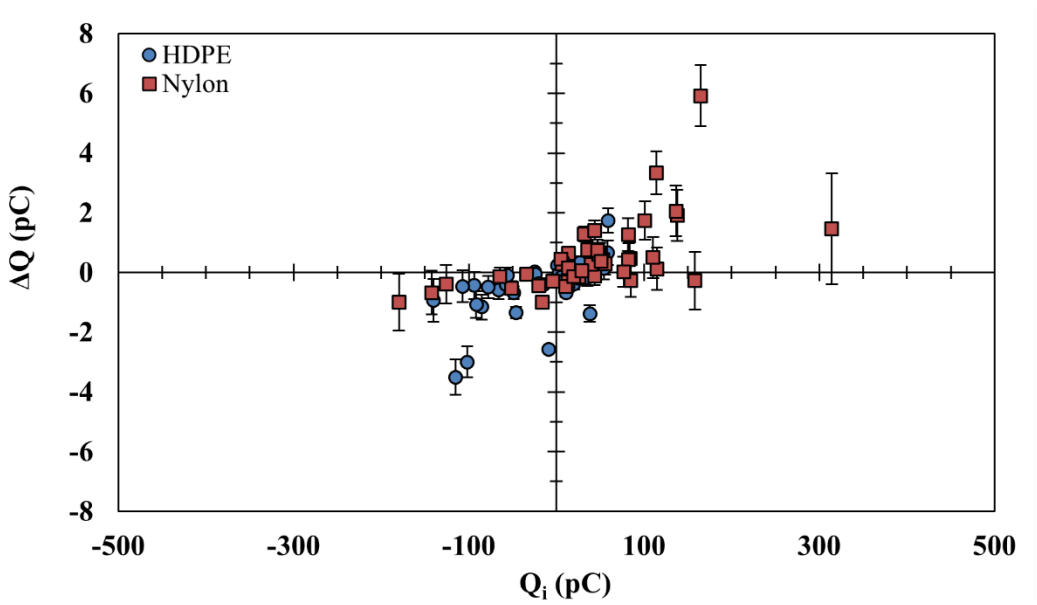

Figure 5-5: Change in particle charge as a function of initial charge for single HDPE and Nylon particles dropped with airflow.

The effect of airflow on charge transfer was an unexpected finding from this work, and a lot of focus was placed on addressing this observation as part of the development process for the collisional charging apparatus. As presented, it was clear that increasing particle charges and the presence of a sufficiently strong airflow resulted in particle charging due to gas-particle interactions. It should also be noted that this charging behaviour persisted with different sources for the airflow, including extra-dry air and nitrogen from pressurized cylinders. One possible cause for the particle charging could be due to the particles interacting with atmospheric aerosols, which are typically present in standard laboratories. These aerosols can be rigorously disturbed within the wind-box of the apparatus, and subsequently settle onto the particle if they have a sufficiently

large surface charge. Although the charging effects of airflow was minimized for this work, the phenomenon should be explored in more detail in the future.

5.2.5. Reproducibility of Charge Measurements

For the success of this apparatus, the charge transfer results for such fundamental experiments needed to be reproducible over multiple days. Thus, any cause for significant changes in the charging behaviour had to be identified and addressed. As such, all the collision trials were performed the same way, and the lab environment remained unchanged over the multiple days the experiments were performed. This also included maintaining the condition of the tested particles, which could be different based on the production batch, storage conditions, and cleaning procedure for when they are reused in collision trials. The importance of performing this procedure is showcased in Figure 5-6, which compares the magnitude of charging observed on Nylon particles in each consecutive day. Nylon particles were washed at the end of each day and were reused after at least 24 hours of drying. In Day 1, the nylon particles were used directly from storage; they were previously used for similar collision experiments and then washed and kept sealed in storage for several months. It was observed that the consecutive days of collision experiments (Day 2 and 3) exhibited lower degrees of charging than in Day 1, suggesting that the cleaning process removed dust particles or other impurities, or they modified the surface morphology or chemistry of the particles. On Day 4, a new batch of nylon particles was purchased and tested without washing and subsequently washed, dried, and reused in Day 5. These newer particles exhibited similar charging magnitudes before and after washing (Day 4 and 5) and were also comparable to the older particles after washing (Day 2 and 3).

These findings showcase the importance of ensuring that no impurities are present on the particles when studying fundamental charge transfer behaviours. It also means that for any electrostatic charging experiments performed to analyze particles from an industrial application, the particles must be kept in the exact same conditions as when they are used. Any variances in the operating conditions, surface morphology, or presence of impurities could drastically change the charging behaviour.

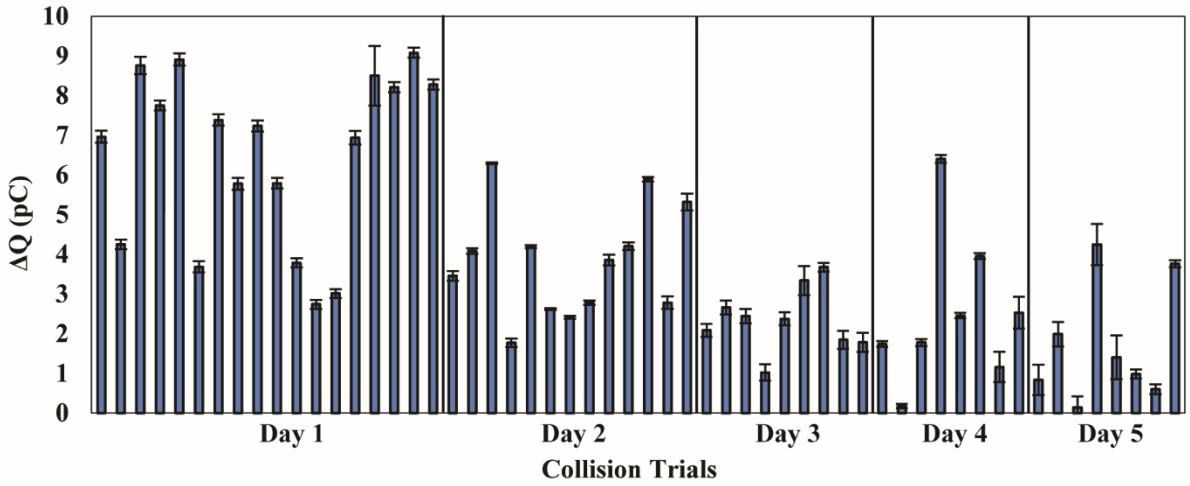

Figure 5-6: Charge transferred to 4.0 mm particles in 4.0 mm-3.2 mm nylon collision trials over multiple days. The particles were washed and blow-dried for at least 24 hours prior to their use in each day. Notes: particles were used directly from storage and not pre-washed in Day 1. Newly purchased batch of non-washed particles were used in Day 4, which were then washed, dried, and reused for Day 5.

5.3. Results & Discussion

Charge transfer data will be presented for same-sized PTFE-aluminum, PTFE-nylon, and nylon-nylon collisions; and different-sized nylon collisions using combinations of 3.2, 4.0, and 4.8 mm nylon. The effects of initial particle charge, impact velocity and impact angle will be discussed for several of these cases.

5.3.1. Different-Material Collisions

Polytetrafluoroethylene (PTFE) has been identified as a highly electronegative insulator across many documented triboelectric series for metals and insulators [32]. This means that PTFE particles should consistently gain negative charge after colliding with metals and electropositive insulators such as nylon. As such, PTFE particles were used to test the performance and validity of the particle-particle charging apparatus. Particle-particle collisions of PTFE with aluminum and nylon were performed, and, as shown in Figure 5-7, the particles consistently transferred charge in the expected direction. When comparing their charge transfer magnitudes, it was observed that the PTFE-nylon collisions, on average, transferred more charge than PTFE-Aluminum. This behaviour was also expected, since according to the triboelectric series, the work-function difference between PTFE and nylon is greater than that between PTFE and aluminum [32]. Finally,

near-perfect charge transfer between the particles was observed for most collision trials, implying that particle-particle charge transfer was successfully isolated from any other external sources of charge in this apparatus. The charge transfer results from these particle-particle collisions have confirmed the validity of the apparatus. Thus, it can be used to measure the charge transfer between identical particles as well as particles of varying sizes.

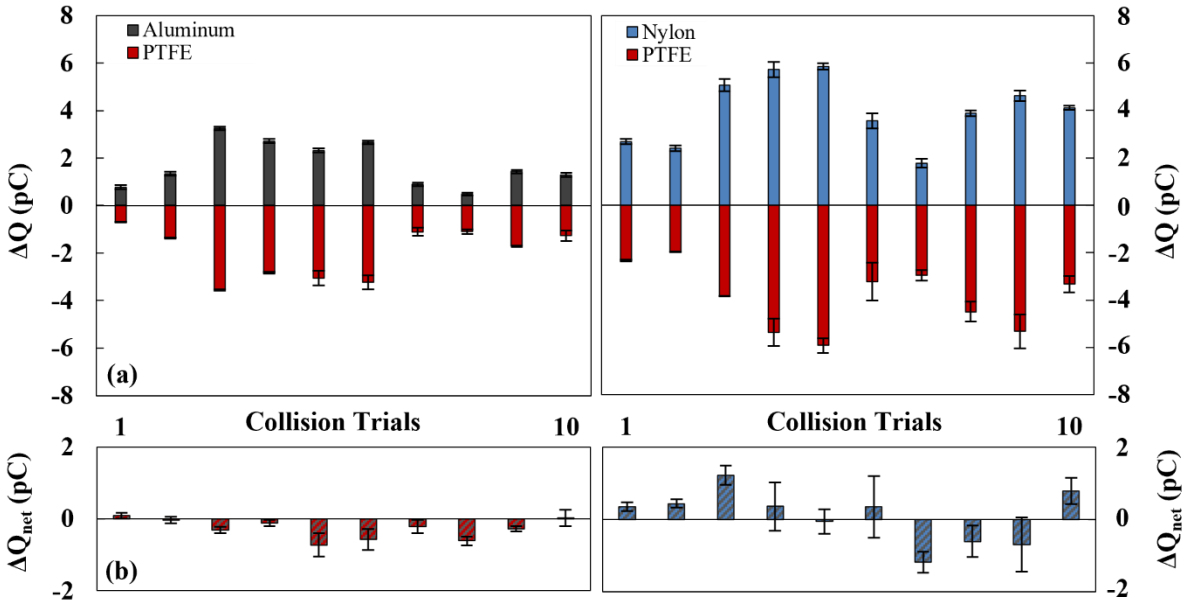

Figure 5-7: Charge transfer measurements for each particle in PTFE-Aluminum (left) and PTFE-Nylon (right) collision trials. (a) Change in charge, ΔQ, where PTFE-Nylon collisions exhibited greater charge transfer than PTFE-Aluminum collisions. (b) A net change in charge, ΔQ_{net}, close to zero implies near-perfect charge transfer between particles with negligible external influences. The error bars represent the truncated measurement errors from each electrometer.

5.3.1.1. Comparing particle-particle and particle-plate charge transfer

The PTFE-aluminum particle collision trials were compared to our previous findings of PTFE colliding with an inclined aluminum plate [29]. The particle-plate contact charging apparatus was set up in a similar manner to the particle-particle collision apparatus. The PTFE particles were dropped through an open-ended Faraday cage to obtain their initial charge. They then contacted an angled aluminum plate before bouncing into a second Faraday cage to obtain their final charge. By adjusting the drop height and the angle of the plate, the charge generated from the particle-plate contacts could be determined at varying impact velocities and angles. Particle-plate collisions were therefore performed with two drop heights, 62 and 81 cm, and for the latter case, the plate

was rotated such that the particle dropped onto it at an angle of 30, 45, and 60° off the normal. Figure 5-8 shows the average impact charge measurements, ΔQ, from the PTFE-aluminum plate collisions grouped based on their set impact angles and velocities.

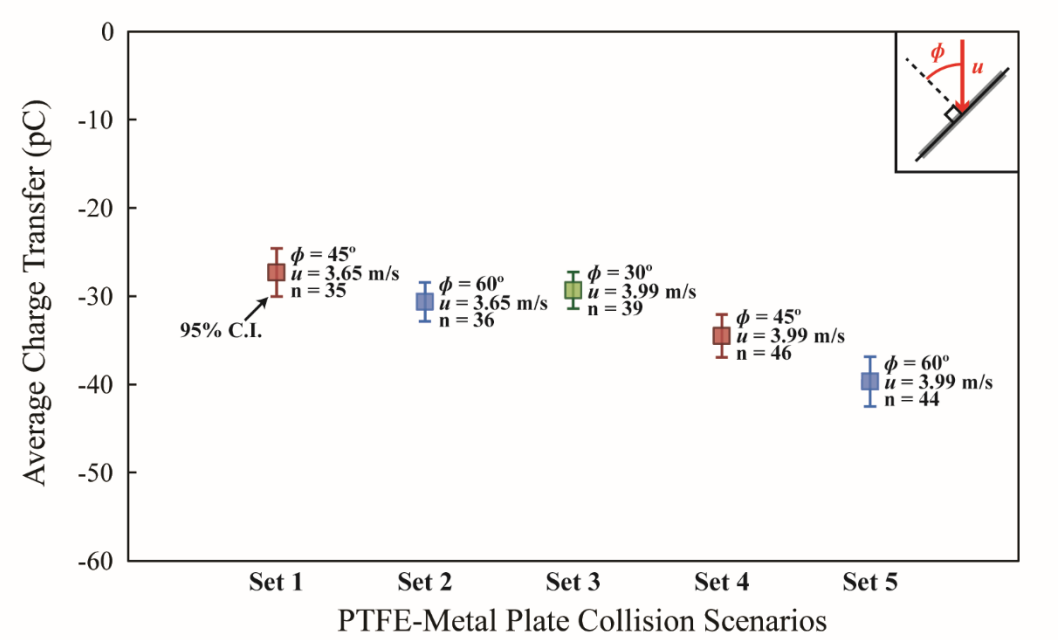

Figure 5-8: The average charge transferred to 3.2 mm PTFE particles after colliding with an inclined aluminum plate. The charge measurements are grouped by the particles' impact velocities and angles, which are defined as shown in the inset.

The particle-wall collisions show a very strong overlap in the charging data for all collision scenarios. This was expected since the small difference in drop height resulted in a minor difference in impact velocities. Nonetheless, the effect of impact velocity was still noticeable in these experiments; the charge transferred to PTFE, on average, increased with increasing impact velocity. The angle of impact also had a clear effect on the average charge transfer, where a larger impact angle or a more tangential impact resulted in increased charge transfer. To compare these findings to the particle-particle collisions of PTFE and aluminum, Figure 5-9 shows the impact charge of PTFE-aluminum particle collision trials in relation to their respective impact velocity and angle.

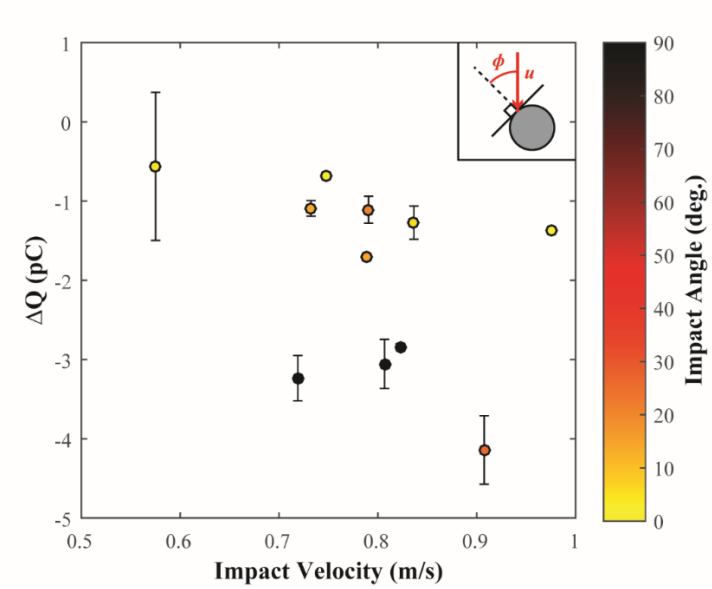

Figure 5-9: Effect of impact angle and velocity on charge transfer to PTFE due to PTFE-aluminum particle collisions. The PTFE's impact angle, ϕ, and velocity, u, are defined as shown in the inset.

Although the sample size of PTFE-aluminum collisions was small, especially when considering the variation in charge data observed in the particle-wall collisions, the effect of impact velocity and angle was already noticeable. The charge transferred to PTFE appeared to increase with increasing impact angle and velocity, similar to the behaviour seen in the particle-wall collision trials. This behaviour agrees with previous studies in particle-plate contact charging, where it was suggested that the dominant charge transfer mechanism in such cases was due to sliding and, more significantly, rolling contact [28,33]. However, most charge transfer models used in gas-solid flow simulations only consider the normal velocity to determine the degree of charge transfer, and the effect of tangential velocity is often neglected.

While the effects of impact angle and velocity on charge transfer were consistent between particle-wall and particle-particle collisions, there was still a major difference between the magnitudes of charging measured in both contact types. Charge transfer magnitudes from the PTFE-aluminum plate collisions were consistently measured at a factor of 10 higher than the particle-particle collisions. While this was partly due to the difference in the average impact velocities between both cases, a lower degree of charging due to particle-particle contacts was expected since the rate of charging from such collisions is significantly lower than charging due to particle-wall collisions [20]. However, it was worth investigating whether current charge transfer models reflect the same

difference in the degree of charge transfer between particle-wall and particle-particle collisions. In both cases, a spherical PTFE particle contacted an aluminum surface at varying velocities and angles. The primary difference, besides the aluminum surface being a spherical particle as opposed to a flat surface, was that the particle was not grounded during the trial. Nonetheless, the electric field effect from the minuscule initial charge on the aluminum particle should not affect the degree of electrostatic charging. Looking at Eq. 5-1, the constants based on the surface properties can be determined for both the particle-wall and particle-particle cases [26,34]:

$$k_{s,w} = \pi d^2 \left(\frac{5\pi}{128} \rho \frac{(1 - v^2)}{E} \right)^{2/5} \tag{5-5}$$

$$k_{s,p} = \pi \left[\frac{15\sqrt{2}}{32} \frac{m_1 m_2}{m_1 + m_2} \left(\frac{1 - v_1^2}{E_1} + \frac{1 - v_2^2}{E_2} \right) \right]^{2/5} \left(\frac{d_1 d_2}{d_1 + d_2} \right)^{4/5} \tag{5-6}$$

Here, d is the particle diameter, ρ is the particle density, m is the particle mass, v is the Poisson ratio, and E is the Young's Modulus. Applying Eqns. 5-1, 5-5, and 5-6 for PTFE and aluminum, and accounting for the fact that the normal velocities in the particle-wall collisions were approximately four times larger than the particle-particle collisions, the models predict that charging due to particle-wall collisions should be approximately 3.75 times larger than the particle-particle collisions. However, after normalizing the experimental data by the surface area of contact using the same equations, charge transfer magnitudes from the PTFE-aluminum plate collisions were roughly five times larger than the particle-particle collisions. Thus, this numerical model could be deemed sufficient in approximating the degree of charging for a single collision. However, in gas-solid flows where an innumerable number of particle-particle collisions take place, this is certainly a notable discrepancy. As such, determining the effective contact area based solely on the normal component of the impact velocity would not be sufficient in describing the magnitudes of charge transfer for both particle-wall and particle-particle collisions.

5.3.2. Same-Material Collisions

Same-sized (3.2 mm) PTFE-PTFE collisional charging results were published along with the original design of the apparatus in Chowdhury et al. (2020) [21]. It was found that if the particles initially carry low levels of charge ($|Q_i| < 200\ pC$), their initial charge before collision did not dictate the direction of charge transfer. In fact, most collision trials resulted in an amplification of

the initial charges, i.e. the particle with a relatively negative charge became more negative. It was then hypothesized that a larger difference in initial charge could drive the charge direction towards equilibrium, where the particle with a relatively negative charge became more positive. Thus, collision trials using PTFE at high particle charges were performed to test this possibility. However, two problems arose when attempting these collision trials. First, if the particles were beyond a certain threshold of initial charge ($|Q_i| > 600\ pC$), the strong electrostatic forces on the particles severely hindered their simultaneous release from the particle holder. Secondly, additional charge generation was detected on PTFE-PTFE collision trials as we had previously reported in Chowdhury et al. (2020) [21], which resulted in imbalanced or anomalous charge transfer measurements. While the mechanism for this charge generation is still unclear, the anomaly was identified to be an isolated interaction between moderate to highly charged PTFE particles and the airflow, as discussed earlier. Thus, PTFE was deemed unreliable for further collision trials and was replaced with nylon as the primary focus for particle-particle collisions. It should be noted that the nylon particles were also limited to low initial charges ($|Q_i| < 100\ pC$), since they were quite susceptible to electrostatic forces due to their lower densities. However, their particle charges were far more stable than PTFE in this apparatus, especially for particle sizes greater than 3.2 mm.

5.3.2.1. Same-Sized Collisions

Figure 5-10 presents samples of same-sized nylon-nylon collisions performed using two sizes – 3.2 mm and 4.0 mm. For each collision trial, the particles' polarities relative to each other were identified and compared to the direction of charge transfer. Various airflow rates were tested to find the ideal conditions for a collision to take place. As expected, higher flowrates were needed to push the larger particles towards each other, with 3.2 mm nylon collisions colliding the most at 100 SLPM whereas 4.0 mm particles needed at least 125 SLPM. The charge measurements in almost all collision trials did not indicate charge transfer discrepancies beyond the truncated reading accuracy of the electrometers. This was very unlike the charge readings recorded for PTFE-PTFE collisions, where more than half the collision trials exhibited imbalanced and even anomalous charge transfer behaviours [21]. Collisions between 4.0 mm nylon particles generally exhibited greater charge transfers compared to the 3.2 mm collision trials. This was expected since a larger particle diameter allows a larger contacting area for charge transfer to occur. However, the

scale of charging for both cases strongly overlapped at 125 SLPM, which is likely due to the impact velocities being proportionally lower for 4.0 mm nylon than for 3.2 mm nylon at the same flowrate.

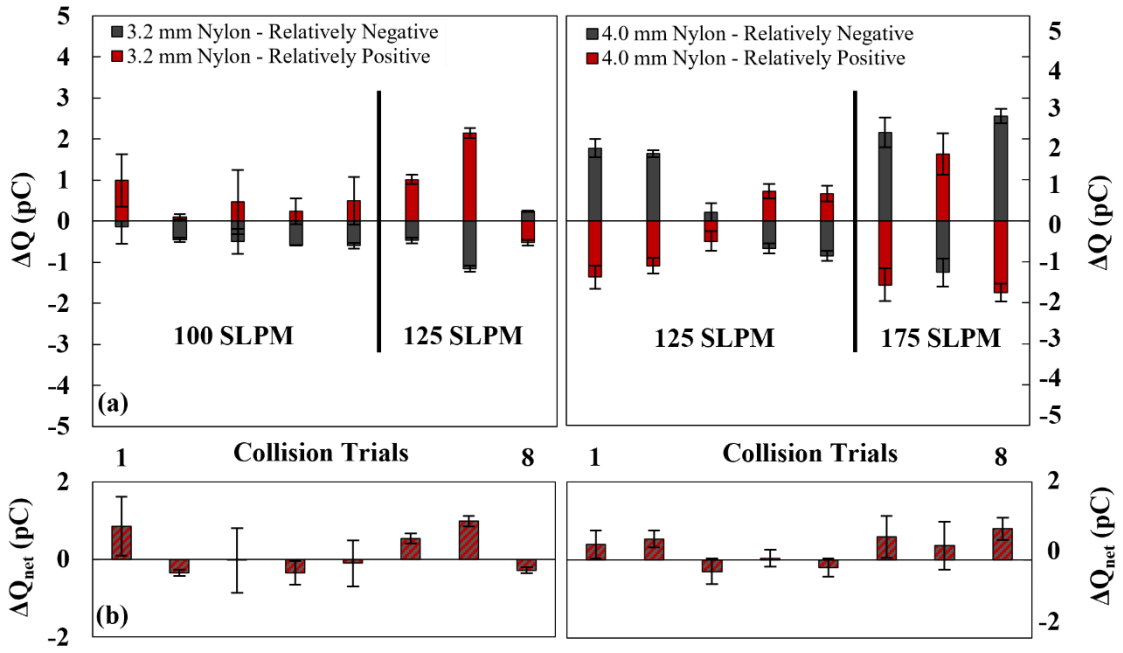

Figure 5-10: Sample of charge transfer measurements for nylon particles undergoing same-sized particle-particle collisions, using 3.2 mm (left) and 4.0 mm (right) nylon. The error bars represent the truncated measurement errors from each electrometer. Charge data is presented for two airflow rates for each set of collision trials. (a) Change in charge was higher in 4.0 mm nylon collisions than in 3.2 mm nylon collisions. (b) The net change in charge shows mostly negligible discrepancies in the charging of the paired particles.

For the 3.2 mm nylon trials, it was observed that the particles with relatively negative polarities charged more negatively after the collision in most cases. On the other hand, charge transfer in the 4.0 mm collision trials appeared to be more random and not related to the particles' relative polarity. Since charge transfer can only occur in the contacted area between two insulator particles, the direction of charge transfer is likely dictated by the localized charge difference at their contacting surfaces. This should result in random charging directions in both collision scenarios, especially since the tested particles only carried low initial charges. However, 3.2 mm nylon collisions clearly favored charge amplification as opposed to equilibrium charging, akin to the previously tested PTFE collisions [21]. This charge amplification behaviour could be explained by the iterative dipole amplification model [35]. The electric field generated by the net initial

charges could induce a dipole moment as the particles approach each other. Upon contact, the charges from the dipole moment closest to the colliding surfaces will get fully or partially neutralized, thereby amplifying the initial charges of the particles upon separation [11]. While this model is in good agreement with the results shown for 3.2 mm nylon collisions, it needs to be further explored by performing same-sized collisions with larger particle sizes and, if possible, higher net initial charges.

5.3.2.2. Different-Sized Collisions

Measurable charge transfer values were obtained using combinations of 3.2, 4.0, and 4.8 mm spherical nylon 6,6 particles. The ideal airflow rate for successful collisions, determined through trial and error, was 125 SLPM for all combinations. Nonetheless, the flow rate was adjusted, whenever possible, to obtain charge transfer readings at varying impact velocities. It should be noted that because of the turbulence in the wind-box, a fixed airflow rate did not provide consistent particle trajectories and impact velocities. Figure 5-11 presents a sample of collision trials where 3.2 mm nylon collided with 4.0 and 4.8 mm nylon, and Figure 5-12 presents the same for 4.0-4.8 mm collisions. Almost all collision trials did not indicate charge transfer discrepancies beyond the truncated reading accuracy of the electrometers; near-perfect charge transfer occurred even when different-sized particles collided. In all three collision scenarios, the initial relative polarities of the particles did not affect the direction of charge transfer. For collision trials involving 3.2 mm nylon colliding with 4.0 and 4.8 mm nylon, the smaller particle consistently charged negatively after colliding with the other two larger particles. However, this was not the case for the 4.0-4.8 mm collisions, where the smaller particle (4.0 mm) charged positively in most cases. To add to this conflicting charging behaviour, it was found that the smaller particle in 4.0-4.8 collisions charged negatively only when they experienced a tangential collision. The mode of contact did not influence the charge direction for the other collision scenarios. Nonetheless, the experiments confirmed that bipolar charging could occur with individual different-sized particle collisions, which suggests that particle size differences fundamentally play a role in collisional charging of otherwise identical particles.

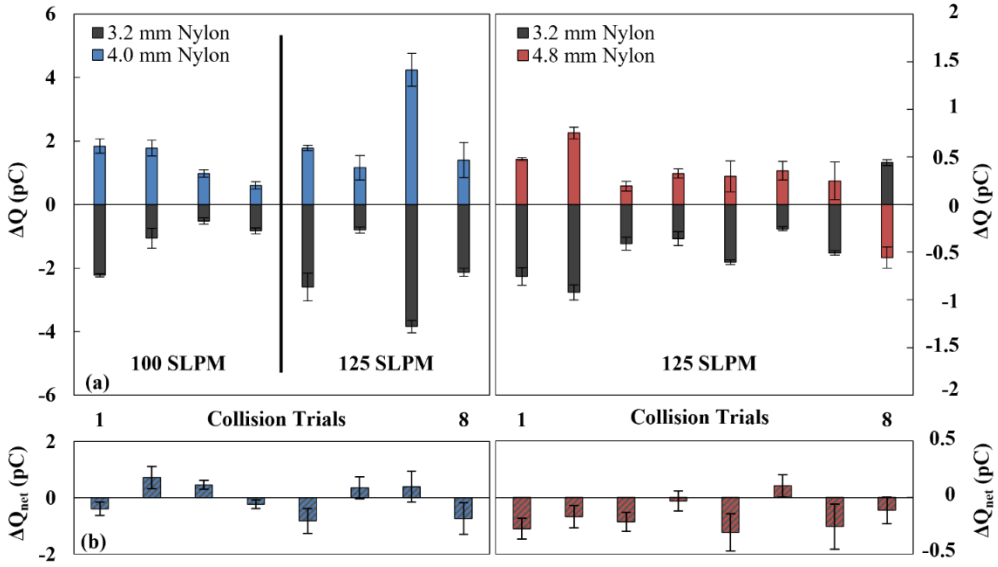

Figure 5-11: Sample particle-particle charge transfer measurements of 3.2-4.0 mm nylon collisions with the flowrates set at 100 and 125 SLPM (left), and 3.2-4.8 mm nylon collisions at 125 SLPM (right). The error bars represent the truncated measurement errors from each electrometer. Note the difference in the scale of the two plots. (a) Change in charge on 3.2 mm nylon was greater when colliding with 4.0 mm nylon than with 4.8 mm nylon. (b) The net change in charge highlighted the minor to negligible discrepancies in the charging of the paired particles.

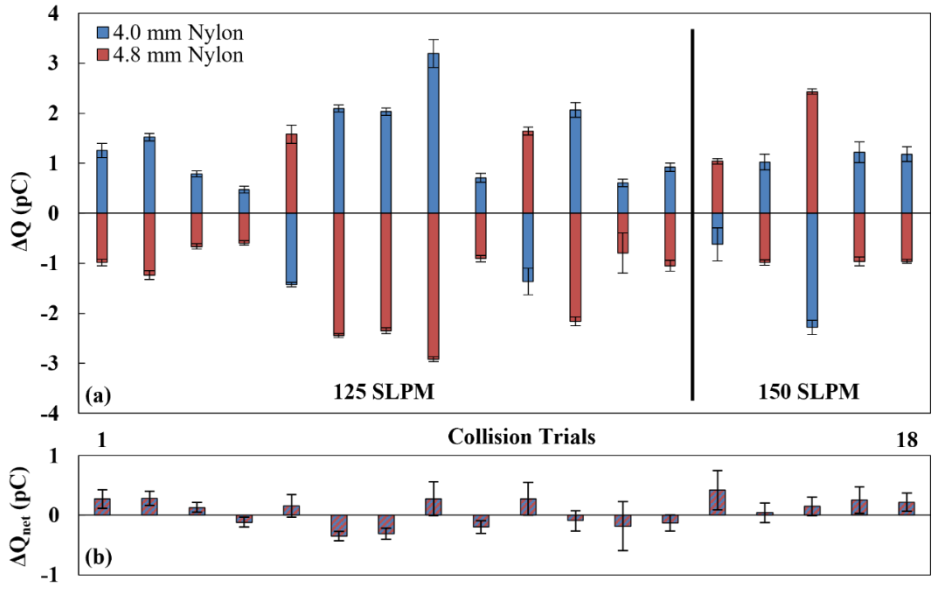

Figure 5-12: Sample Particle-particle charge transfer measurements due to collisions between 4.0 mm and 4.8 mm nylon. The error bars represent the truncated measurement errors from each electrometer. (a) 4.0 mm nylon charged positively in most collisions, contrary to previous charging direction based on particle size. Negative charging of the smaller particle was only observed for tangential contacts. (b) Near-perfect charge transfer observed for most collision trials.

5.3.2.3. Effect of Initial Charge Difference

One of the factors that should have intuitively dictated charge transfer in same-material collisions was the initial difference in particle charges, where a greater initial difference should result in a stronger drive for charge transfer towards equilibrium. Although the charge transfer results presented for same-sized particle collisions introduced the notion of charge amplification, an increased driving force for charge separation is still possible with increasing differences in initial charge [36]. The direction and magnitude of charge transfer was therefore closely examined based on the initial particle charges in all collision trials. To simplify the comparison between all the different-sized particle collision scenarios, the charge transfer observed in every collision trial was compared to the net surface charge densities of the particles prior to their collision, $\Delta\sigma_i$:

$$\Delta\sigma_i = \frac{Q_{i,1}}{\pi d_1^2} - \frac{Q_{i,2}}{\pi d_2^2} \qquad 5\text{-}7$$

A positive value for $\Delta\sigma_i$ implies that particle 1 has a relatively positive surface charge density compared to particle 2, and thence should gain negative charge after the collision. Likewise, a negative value for $\Delta\sigma_i$ suggests particle 1 should gain positive charge. However, the opposite would be true for both cases if the charge amplification model is the dominant charging mechanism. Figure 5-13 presents the charge transferred to 3.2 mm nylon particles after colliding with 3.2, 4.0 and 4.8 mm nylon as a function of $\Delta\sigma_i$, whereas Figure 5-14 presents the same for 4.0 mm nylon particles. The initial surface charge density, σ_i, of each reference particle is also color-mapped in both figures.

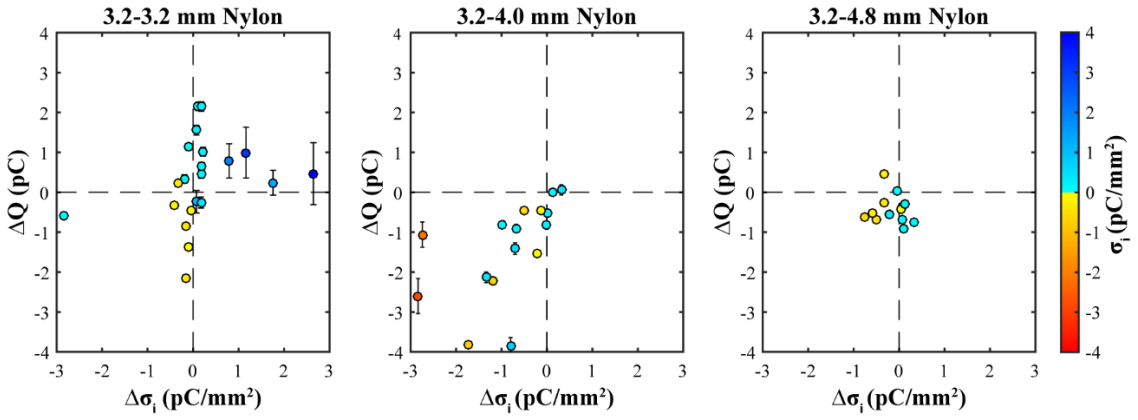

Figure 5-13: Change in particle charge on 3.2 mm nylon after colliding with 3.2, 4.0 and 4.8 mm nylon as a function of the colliding particles' net initial surface charge densities, $\Delta\sigma_i$. The initial surface charge density σ_i of the reference particle is also color-mapped for each collision trial.

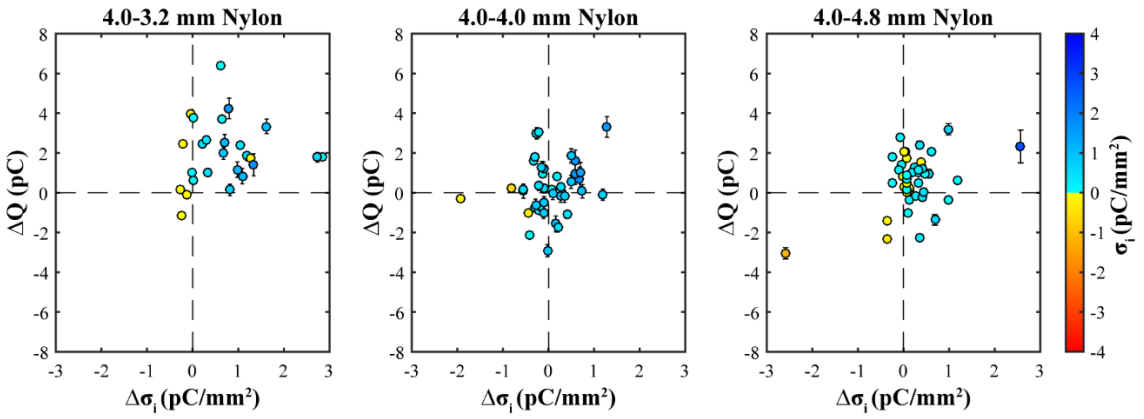

Figure 5-14: Change in particle charge on 4.0 mm nylon after colliding with 3.2, 4.0 and 4.8 mm nylon as a function of the colliding particles' net initial surface charge densities, $\Delta\sigma_i$. The initial surface charge density σ_i of the reference particle is also color-mapped for each collision trial.

These figures also reconfirmed that same-sized particle collisions exhibited both conventional charge transfer and charge amplification for 4.0 mm nylon particles, and primarily charge amplification for 3.2 mm nylon. It was also evident that the initial surface charge densities did not affect the direction of charge transfer in different-sized nylon collisions. More specifically, 3.2 mm nylon particles consistently charged negatively regardless of their relative polarity when colliding with 4.0 and 4.8 mm nylon, thereby confirming that the bipolar charging behaviour is strictly connected to the difference in particle sizes. Although 4.0 mm nylon mostly charged positively in both different-sized collision scenarios, there are some cases in the 4.0-4.8 mm collision trials where the 4.0 mm nylon particles charged negatively. This discrepancy in the direction of charge transfer did not appear to be affected by the difference in initial surface charge densities, suggesting that the charging behaviour was influenced by other factors such as particle size difference, impact angle or impact velocity.

It should be noted that the magnitude of charge transfer was generally not affected by the net initial surface charge densities, i.e. the range of charge transfer values did not correlate with increasing separation of charge densities. This behaviour can be explained by the non-uniform distribution of charge on the particle surfaces, resulting in a large variance in the degree of charge transfer regardless of the initial charges. The particles' localized charge at the contact area should then dictate the direction of charge transfer especially when the particles have low surface charge concentrations. This would explain the supposed charge amplification observed in same-sized

collisions. On the other hand, the electric field generated from a sufficiently large net surface charge between the particles should promote conventional charge transfer in particle-particle collisions. However, the effect of highly pre-charged particles could not be studied in these experiments, as it was found that the particles with a greater magnitude of initial charge consequently had a higher measurement error. Given the low range of the measured charge transfer, this limits the reliability of the measurements to collision trials with initial charge densities less than approximately 3 pC/mm^2. As such, charge transfers for highly pre-charged particles could not be reliably tested in these particle-particle collision experiments.

5.3.2.4. Effect of Impact Velocity & Angle

Another factor that dictates the degree of collisional charge transfer is the force of impact between the two particles. A stronger collision should result in greater charge transfers since the induced elastic deformation of the particles would expose more of their surfaces for charge transfer. One possibility for the lower charge transfers observed with larger particle sizes could be that the larger particles experienced relatively weaker collisions at a given flowrate. Considering Eq. 5-1, weaker particle-particle collisions would reduce the effective contact area between the two particles, reducing the charge transfer. In addition to weaker collisions, the angle of impact could play a role. When two different-sized particles are resting in the particle holder, their centers will be off-set from each other by Δr. Since the particles were always released simultaneously, an angled collision is more likely to occur with increasing particle-size differences. In turn, the collision would become more tangential, which could affect the overall charging of the particles.

The combination of the element of randomness introduced by the wind-box and the vertical off-set in different-sized particle combinations resulted in a small range of uncontrolled impact velocities and angles. Given the complex charge transfer observations discussed above, the collision trials were further analyzed based on these two parameters. The charge transferred to 3.2 mm nylon in all of its collision trials were compared to their respective impact velocities and angles, as shown in Figure 5-15. The same is shown for 4.0 mm particles in Figure 5-16. The impact velocities were found to range between 0.6 m/s and 2.3 m/s, and the impact angles ranged from 0° (direct collision) and 90° (tangential collision). The impact velocities strongly overlapped for all collision scenarios, though on average the collisions with smaller particles had slightly higher impact velocities. Most of the collisions occurred at impact angles less than ~35°. For cases

with impact angles above ~50°, the particles experienced a glancing contact and continued to move in the same direction, albeit with modified trajectories.

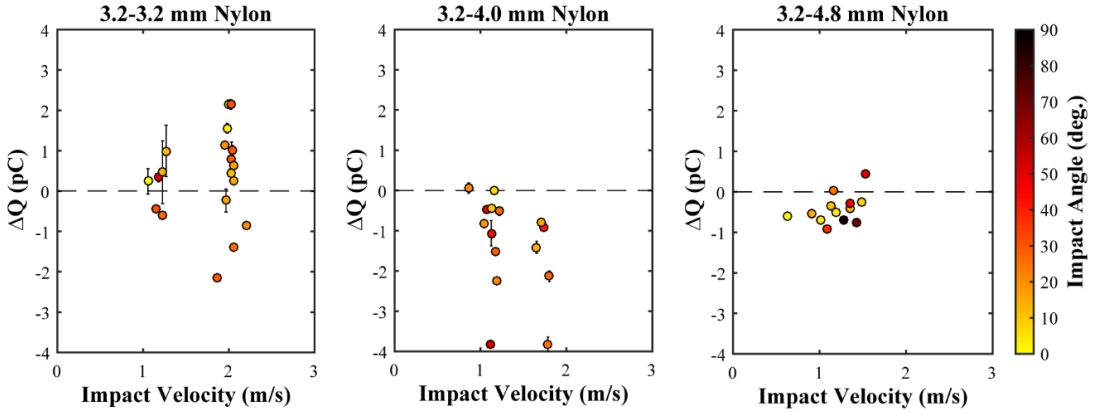

Figure 5-15: Change in particle charge on 3.2 mm nylon after colliding with 3.2, 4.0 and 4.8 mm nylon as functions of impact velocity and angle.

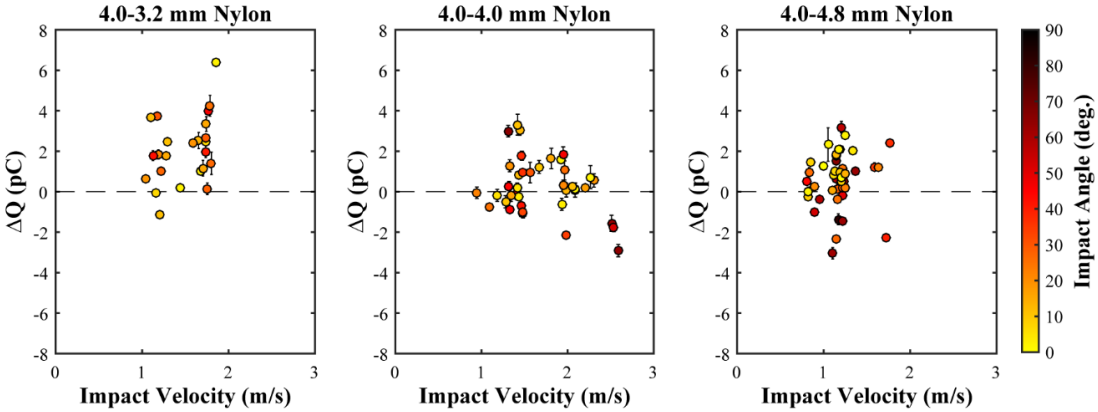

Figure 5-16: Change in particle charge on 4.0 mm nylon after colliding with 3.2, 4.0 and 4.8 mm nylon as functions of impact velocity and angle.

Overall, the charge transfer magnitudes did not have a clear trend in terms of their impact velocity. A spread in the degree of charge transfer was expected given the complex interactions of initial charges, mode of contact, and availability of high-energy sites in the colliding surfaces. With all these parameters possibly affecting the magnitude and direction of charging, the small range of impact velocities may not have a significant influence on the charge transfer. One notable observation made from these collision trials was that high degrees of charge transfer were possible through tangential collisions. The greatest charge transfer generally occurred when the impact velocity had contributions from both the normal and tangential velocity components. It should also

be noted from Figure 5-16 that some of the tangential collisions in 4.0-4.8 mm nylon trials resulted in negative charging of 4.0 particles. This charging behaviour should not be ignored since their charge transfer was measured at magnitudes comparable to the rest of the 4.0-4.8 mm collision trials. Once again, tangential contacts had a significant influence in particle-particle charging, and thus their contribution needs to be considered in charge transfer models.

5.3.3. Summary of Particle-Particle Charge Transfer

Figure 5-17 summarizes the results of all the particle-particle collision scenarios, where the charge transfer data is averaged for each collision scenario and presented in terms of the amount of elementary charge transferred per contact area (as calculated using Eq. 5-1). Given the strong overlap in the confidence intervals in all collision scenarios, it is difficult to evaluate how the different collision scenarios affected the charge transfer magnitudes. The low statistical confidence is first attributed to the fact that individual particle-particle collisions do not exhibit strong charge transfers, at least relative to particle-wall collisions as presented above. Secondly, the particles exhibited a wide range of charge transfer magnitudes at any given initial charge difference, impact velocity and angle. This is likely due to the non-uniform distribution of the already low initial surface charge densities. As such, it may still be worth comparing the average charge transfer magnitudes for each collision scenario. On average, the PTFE-aluminum collisions resulted in lower charging than the PTFE-nylon collisions of the same particle size. As mentioned, this coincides with the materials' work function differences between each other. Amongst the same-material collision scenarios, 4.0-4.0 mm nylon collisions on average exhibited higher charge transfers than the 3.2-3.2 mm collisions, even after normalizing for contact area. 4.0-3.2 mm nylon collisions exhibited the highest charge transfer, while 4.8-3.2 mm collisions exhibited the lowest – slightly lower than the charging observed in 3.2-3.2 mm collisions. At first glance 4.8-4.0 mm nylon collisions may appear to have the lowest average charge transfer, but one should consider that this is the only collision scenario with a significant number of collision trials that experienced charge transfers in both directions.

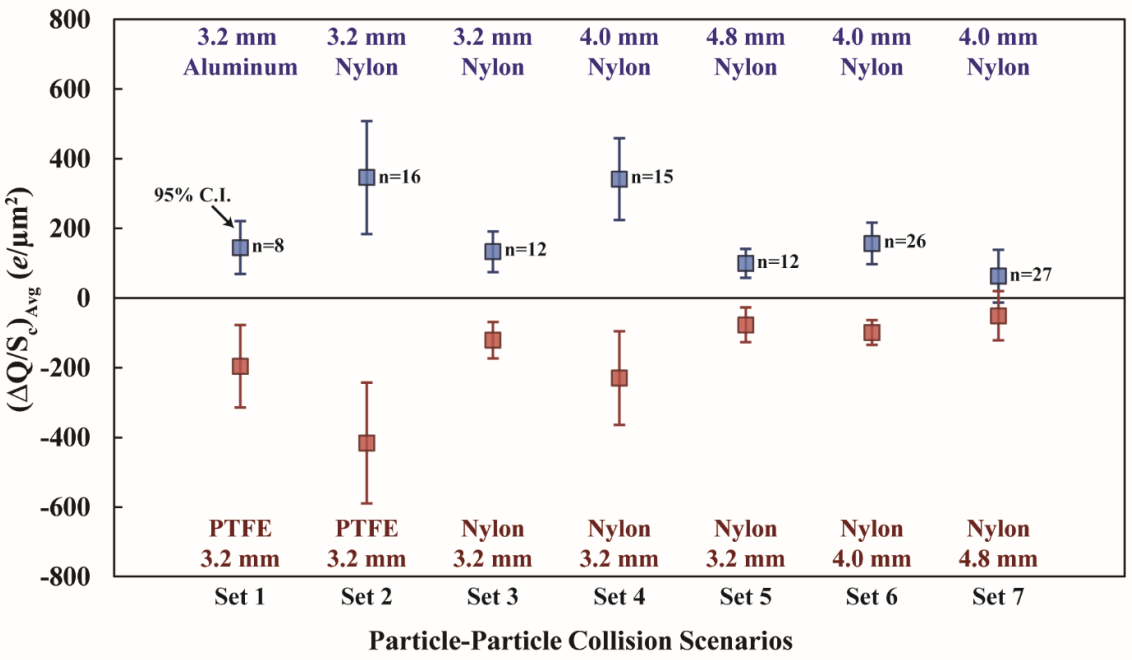

Figure 5-17: Average charge transferred per contact area for all particle-particle collision scenarios, where n is the number of collision trials tested for every scenario. The data points in each set were determined by grouping the particles based on their material type and particle size and averaging their charge transfer values. For the identical particle-particle collision scenarios, the particles from each trial were instead grouped based on their charge transfer direction.

Although the range of charge transfer measurements in all collision trials resulted in low statistical confidence in terms of the magnitude of charge, most collision scenarios with varying material type or particle size showcased a strong statistical confidence in terms of the direction of charge transfer. However, it remains unclear why varying the particle size had an effect on the nylon particles' direction and magnitude of charge transfer, and why this effect did not correspond with increasing particle sizes. Particularly for 4.8-4.0 mm nylon collisions, it was unexpected to find that the larger particle mostly charged negatively unlike the rest of the cases. One possible reason for this behaviour could be that the particles acquired slight variances in their surface chemistry during the production process, which would dictate the direction of charge transfer. For a clearer picture of the bipolar charging behaviour, additional particle collision experiments should be performed with other material types and sizes, preferably using particles produced in a single batch with a wide particle-size distribution.

5.4. Conclusions

An updated version of the particle-particle contact charging apparatus was used to obtain charge transfer measurements for a matrix of particle collisions. The apparatus was extensively tested to ensure that reliable charge transfer measurements were obtained. For example, the airflow used in the wind-box was found sometimes to influence the charge generated on PTFE particles but had a negligible effect on HDPE and nylon 6/6 particles when used with sufficiently low initial charges ($|Q_i| < 100\ pC$). Moreover, the charge transfer data was reproducible as long as the tested particles were washed before their reuse, which provided similar results as colliding a fresh batch of particles. All collision trials were recorded using a slow-motion camera and analyzed via PTV to determine each particle pair's impact velocity and angle. The video analysis identified the mode of contact experienced by the particles, be it a direct, angled, or tangential collision.

Measurable charge transfer was observed and presented for same-sized PTFE-aluminum, PTFE-nylon, and nylon-nylon collisions, as well as different-sized nylon collisions. The different-material collisions confirmed that the apparatus provided reasonable results; PTFE particles consistently charged negatively when colliding with aluminum and nylon particles. Near-perfect charge transfer was observed for almost all collision trials, where the charge gained on one particle was equal to the charge lost by the other. The PTFE-nylon collisions also exchanged more charge than the PTFE-aluminum collisions, which agrees with all three materials' relative ranking in the triboelectric series.

The charge transfer magnitudes in PTFE-aluminum particle-particle collisions, accounting for effective contact areas calculated using the normal impact velocities, were roughly 5 times lower than those measured in past PTFE-aluminum particle-plate collisions. This factor is slightly larger than what current charge transfer models account for, likely due to the exclusion of the tangential component. This is confirmed by the fact that the impact angle for each collision was found to be directly proportional to the degree of charge transfer in both particle-particle and particle-plate collisions. These findings suggest that the tangential component of the impact velocity needs to be included in current charge transfer models for all collision types. Currently, most particle charging models developed for gas-solid flows only consider the normal component of the impact velocity [26,37,38]. Given these experimental results, the tangential component of all collisions should also be considered when simulating electrostatic charging.

Same-sized nylon particle collisions using 3.2 mm and 4.0 mm particles revealed that the transferred charge did not always move towards equilibrium, but instead causes an increased separation of particle charges. Particularly for 3.2 mm collisions, the particles' difference in initial charges was amplified in almost all collision trials. This suggests that the charge transfer in identical particle collisions may be caused by the neutralization of the induced dipole moments between the colliding particles. However, given the low initial charges of the tested particles, this charging behaviour could also be attributed to the non-uniform distribution of charge on the particle surfaces. For different-sized nylon collision trials, the charge transfer direction was independent of the particles' initial charges and consistently favored one particle size over another. Based on the magnitudes and direction of charging, it appeared that the nylon particles' apparent electronegativities did not correlate with their particle sizes. Additional particle collision experiments, with other material types and sizes, are therefore necessary in understanding the connection between particle size and charge direction. Ultimately, this work is a steppingstone for future researchers to explore particle-particle charge transfer in their respective systems, and to develop empirically accurate particle-particle charging models.

References

[1] C. Pounder, The quest for a charging mechanism to the end of the 19th century, J. Electrostat. 3 (1977) 389–394.

[2] H. Masuda, T. Komatsu, K. Iinoya, The static electrification of particles in gas-solids pipe flow, AIChE J. 22 (1976) 558–564.

[3] R.G. Horn, D.T. Smith, A. Grabbe, Contact electrification induced by monolayer modification of a surface and relation to acid-base interactions, Nature. 366 (1993) 442–443.

[4] C. Heinert, R.M. Sankaran, D.J. Lacks, Electrostatic charge generation on material surfaces from the evaporation of liquids, J. Electrostat. 105 (2020) 103450.

[5] S. Kittaka, N. Masui, Y. Murata, A method for measuring the charging tendency of powder in pneumatic conveyance through metal pipes, J. Electrostat. 6 (1979) 181–190.

[6] Z.L. Wang, A.C. Wang, On the origin of contact-electrification, Mater. Today. 30 (2019) 34–51.

[7] A.F. Diaz, J. Guay, Contact charging of organic materials: Ion vs. electron transfer, IBM J. Res. Dev. 37 (1993) 249–259.

[8] L.S. McCarty, G.M. Whitesides, Electrostatic Charging Due to Separation of Ions at

Interfaces: Contact Electrification of Ionic Electrets, Angew. Chemie Int. Ed. 47 (2008) 2188–2207.

[9] M.W. Williams, Triboelectric charging of insulators - Mass transfer versus electrons/ions, J. Electrostat. 70 (2012) 233–234.

[10] H.T. Baytekin, A.Z. Patashinski, M. Branicki, B. Baytekin, S. Soh, B.A. Grzybowski, The mosaic of surface charge in contact electrification, Science (80-.). 333 (2011) 308–312.

[11] D.J. Lacks, T. Shinbrot, Long-standing and unresolved issues in triboelectric charging, Nat. Rev. Chem. 3 (2019) 465–476.

[12] D.J. Lacks, A. Levandovsky, Effect of particle size distribution on the polarity of triboelectric charging in granular insulator systems, J. Electrostat. 65 (2007) 107–112.

[13] H. Zhao, G.S.P. Castle, I.I. Inculet, The measurement of bipolar charge in polydisperse powders using a vertical array of Faraday pail sensors, J. Electrostat. 55 (2002) 261–278.

[14] D. Song, P. Mehrani, Comparison of electrostatic charge generation in gas-solid fluidized beds in turbulent versus pre-turbulent flow regime, Powder Technol. 319 (2017) 426–433.

[15] W.O. Moughrabiah, J.R. Grace, X.T. Bi, Electrostatics in gas–solid fluidized beds for different particle properties, Chem. Eng. Sci. 75 (2012) 198–208.

[16] A. Sowinski, L. Miller, P. Mehrani, Investigation of electrostatic charge distribution in gas–solid fluidized beds, Chem. Eng. Sci. 65 (2010) 2771–2781.

[17] L. Xie, G. Li, N. Bao, J. Zhou, Contact electrification by collision of homogenous particles, J. Appl. Phys. 113 (2013) 184908.

[18] M.A. Bilici, J.R. Toth, R.M. Sankaran, D.J. Lacks, Particle size effects in particle-particle triboelectric charging studied with an integrated fluidized bed and electrostatic separator system, Rev. Sci. Instrum. 85 (2014).

[19] S.R. Waitukaitis, V. Lee, J.M. Pierson, S.L. Forman, H.M. Jaeger, Size-dependent same-material tribocharging in insulating grains, Phys. Rev. Lett. 112 (2014) 1–5.

[20] L. Konopka, S. Jantač, M. Vrzáček, M. Svoboda, J. Kosek, Triboelectric charging of polyethylene powders: Comparison of same-material and different-material contributions to the charge build-up, Powder Technol. 367 (2020) 713–723.

[21] F. Chowdhury, B. Elchamaa, M. Ray, A. Sowinski, A. Passalacqua, P. Mehrani, Apparatus design for measuring electrostatic charge transfer due to particle-particle collisions, Powder Technol. 361 (2020) 860–866.

[22] A.G. Kline, M.X. Lim, H.M. Jaeger, Precision measurement of tribocharging in acoustically levitated sub-millimeter grains, Rev. Sci. Instrum. 91 (2020) 023908.

[23] J. Higham, PTVResearch, (2020). https://github.com/jonnyhigham/PTVResearch (accessed August 24, 2020).

[24] W.D. Fullmer, J.E. Higham, C.Q. LaMarche, A. Issangya, R. Cocco, C.M. Hrenya, Comparison of velocimetry methods for horizontal air jets in a semicircular fluidized bed of Geldart Group D particles, Powder Technol. 359 (2020) 323–330.

[25] S. Matsusaka, M. Ghadiri, H. Masuda, Electrification of an elastic sphere by repeated impacts on a metal plate, J. Phys. D. Appl. Phys. 33 (2000) 2311–2319.

[26] M. Ray, F. Chowdhury, A. Sowinski, P. Mehrani, A. Passalacqua, Eulerian modeling of charge transport in bi-disperse particulate flows due to triboelectrification, Phys. Fluids. 32 (2020) 023302.

[27] S.P. Timoshenko, Theory of Elasticity, 3rd ed., McGraw-Hill, 1934.

[28] A. Ema, D. Yasuda, K. Tanoue, H. Masuda, Tribo-charge and rebound characteristics of particles impact on inclined or rotating metal target, Powder Technol. 135–136 (2003) 2–13.

[29] F. Chowdhury, A. Sowinski, M. Ray, A. Passalacqua, P. Mehrani, Charge generation and saturation on polymer particles due to single and repeated particle-metal contacts, J. Electrostat. 91 (2018) 9–15.

[30] S. Pence, V.J. Novotny, A.F. Diaz, Effect of Surface Moisture on Contact Charge of Polymers Containing Ions, Langmuir. 10 (1994) 592–596.

[31] P.S. Gil, D.J. Lacks, Humidity transforms immobile surface charges into mobile charges during triboelectric charging, Phys. Chem. Chem. Phys. 21 (2019) 13821–13825.

[32] J. Cross, Electrostatics: Principles, Problems and Applications, Adam Hilger, Bristol, 1987.

[33] P.M. Ireland, Triboelectrification of particulate flows on surfaces: Part I — Experiments, Powder Technol. 198 (2010) 189–198.

[34] J. Kolehmainen, A. Ozel, S. Sundaresan, Eulerian modelling of gas-solid flows with triboelectric charging, J. Fluid Mech. 848 (2018) 340–369.

[35] T. Siu, J. Cotton, G. Mattson, T. Shinbrot, Self-sustaining charging of identical colliding particles, Phys. Rev. E - Stat. Nonlinear, Soft Matter Phys. 89 (2014) 1–7.

[36] T. Shinbrot, M. Rutala, H. Herrmann, Surface contact charging, Phys. Rev. E. 96 (2017) 032912.

[37] C. Pei, C.-Y. Wu, D. England, S. Byard, H. Berchtold, M. Adams, DEM-CFD Modeling of Particle Systems with Long-Range Electrostatic Interactions, Am. Inst. Chem. Eng. J. 61 (2015) 1792–1803.

[38] H. Grosshans, M. V. Papalexandris, Numerical study of the influence of the powder and pipe properties on electrical charging during pneumatic conveying, Powder Technol. 315 (2017) 227–235.

Chapter 6

Evaluating the electrostatic charge transfer model for particle-particle interactions

F. Chowdhury[a], M. Ray[b], A. Passalacqua[b], P. Mehrani[a], A. Sowinski[a]

[a] Department of Chemical and Biological Engineering, University of Ottawa, 161 Louis Pasteur, Ottawa, ON, Canada, K1N 6N5
[b] Department of Mechanical Engineering, Iowa State University, 2025 Black Engineering Building Ames, IA, 50011-2161, USA

This chapter is a manuscript under review in the Journal of Electrostatics (ID: ELSTAT-S-21-00078)

Abstract

The particle-particle charging model currently used in computational studies of gas-solid flows was evaluated on its ability to predict the electrostatic charge transfer in individual particle collisions measured in atmospheric conditions. Three particle-particle collision scenarios were analyzed: different material particle collisions (3.2 mm PTFE-aluminum and PTFE-nylon), same material and same sized particle collisions (3.2 mm and 4.0 mm nylon), and same material and different sized particle collisions (4.0-3.2 mm and 4.0-4.8 mm nylon). Although the work function difference term in the model should have a dominating effect on both the magnitude and direction of charge transfer, the experiments showed similar magnitudes even for same-material collisions. Thus, preliminary collision experiments are necessary to obtain the appropriate charging efficiency term and to identify the non-zero work function difference that could exist due to the presence of impurities or chemical defects present on particle surfaces. While the model correctly predicted the direction of charge transfer in different-material collisions, it was unable to capture the charging behaviours observed in same-material particle collisions, such as charge amplification and size-dependent bipolar charging. The question remains as to how to incorporate these mechanisms into the particle-particle charging model to better represent the charging behaviours in real systems, especially those with dense granular flows.

6.1. Introduction

Electrostatic charging is known to be prevalent in many gas-solid flow systems. The large frequency of particle-wall and particle-particle collisions in such systems can lead to highly charged granular flows, which in turn can cause operational challenges such as wall fouling and particle agglomeration. In some scenarios, such as flow in grain silos, it can even lead to hazardous spark discharges and dust explosions. As such, the electrostatic charging behaviour of insulative powders has been extensively studied over the years in various gas-solid flow systems, such as fluidized beds [1] and pneumatic conveying systems [2,3]. As a part of this research effort, computational fluid dynamic (CFD) simulations of gas-solid flows have also been performed that consider the effect of electrostatic charging [4–7].

The charge transfer models implemented into CFD models can be broken down into two components: particle-wall charge transfer and particle-particle charge transfer. Particle-wall charging behaviour was extensively studied in numerous bench-scale experimental studies [8–14], and a charge transfer model, named the condenser model [9], was confirmed to provide a reasonable representation of particle-wall charging behaviour. Variations of the condenser model were therefore implemented into the abovementioned CFD studies to simulate charging due to both particle-wall and particle-particle collisions. However, particle-particle charging observed in bulk particle systems [15–18], and more recently in individual particle collisions [19–21], showed complex particle-particle charging mechanisms such as charge amplification [22,23] and size-dependent bipolar charging [24–26], which are not represented in the condenser model.

The particle-particle charging model requires further development to accurately represent the phenomenon in CFD studies of gas-solid flows. The first crucial step for this is to achieve good agreement between the measured and modelled charge transfer values for isolated particle collisions. In an earlier work, we conducted individual particle-particle collision experiments using particles of varying sizes and materials and observed their charging behaviour [27]. As such, the aim of this work is to use the charge transfer data from these experiments to evaluate the particle-particle charging model. Along with the material and electrostatic properties of the relevant particles, the particles' initial charge and impact velocity will also be used in the model as unique input parameters for every collision trial.

6.1.1. Particle-particle charge transfer model

The change in particle charge due to a particle-particle collision is expressed as follows [28]:

$$\frac{dQ_1}{d\boldsymbol{n}_c} = -\frac{dQ_2}{d\boldsymbol{n}_c} = k_c \left[\frac{\varepsilon_0 \varepsilon_r}{z_0} V_c + \frac{Q_{i,2}}{\pi d_2^2} - \frac{Q_{i,1}}{\pi d_1^2} + \varepsilon_0 \varepsilon_r \boldsymbol{E_c} \right] S_p \tag{6-1}$$

where k_c is the charging efficiency, ε_0 is the permittivity of vacuum, ε_r is the relative permittivity of the medium, V_c is the work function difference between the particle and the wall, z_0 is the critical gap for electron transfer, Q_i is the particle's charge prior to collision, $\boldsymbol{E_c}$ is the electric field acting on the collision point, and S_p is the contact area between the two particles. The particle-particle charge transfer model assumes that each of the particles will exchange an equal amount of charge during the collision. Moreover, the particle charges are assumed to be equally distributed over the particle surface, hence their normalization over surface area. The total contact area is estimated using the Hertzian theory of contact deformation between two spherical particles [29]:

$$S_P = 1.76 \left[\frac{m_1 m_2}{m_1 + m_2} \left(\frac{1 - \nu_1^2}{E_1} + \frac{1 - \nu_2^2}{E_2} \right) \right]^{2/5} \left[\frac{d_1 d_2}{d_1 + d_2} v_N \right]^{4/5} \tag{6-2}$$

where d_i, m_i, ν_i, and E_i are the particles' diameter, density, Poisson ratio and Young's Modulus, and v_N is the normal component of the impact velocity.

The proposed particle-particle charge transfer model does not consider the tangential component of the impact velocity, which would contribute to sliding or rolling contact between the particles. Past studies on sliding and rolling contact charging have shown that, between the two modes of contact, rolling contact exposes a much larger contacting surface area leading to significantly greater charge transfer between the surfaces [10,30]. The additional contact area due to rolling can be estimated as follows [31]:

$$S_R = 2 v_T \Delta t_c \sqrt{S_P / \pi} \tag{6-3}$$

where v_T is the tangential component of the impact velocity, Δt_c is the duration of the contact, and S_P is the contact area calculated in Eq. 6-2. The duration of the contact can also be obtained from Hertzian theory:

$$\Delta t_c = 2.93 \left[\frac{m_1 m_2}{m_1 + m_2} \left(\frac{1 - \nu_1^2}{E_1} + \frac{1 - \nu_2^2}{E_2} \right) \right]^{2/5} \left[\frac{d_1 d_2}{d_1 + d_2} v_N \right]^{-1/5} \tag{6-4}$$

Considering both the normal and tangential impact velocities, the total contact area should therefore be the summation of Eqns. 6-2 and 6-3.

$$S_c = S_P + S_R \tag{6-5}$$

where S_c is the total contact area, including both the normal and tangential components of the impact velocity. This modification for the total contact area calculation was evaluated in this study.

6.2. Model Evaluation

In an earlier work we designed a particle-particle collision apparatus such that the measured charge transfer between two particles was solely due to their collision [20]. This apparatus was used to test collisions between particles of varying material types and sizes [27]. In this work, each tested collision scenario will be assessed using the charge transfer model to confirm whether the predicted charging behavior agrees with the measured charge transfer data. The material and electrostatic properties of the tested particles were obtained from literature [32] and are listed in Table 6-1. Since each particle-particle collision occurred in an electrostatically isolated environment, with no other particles present in the system, the electric field term in the model was set to zero. The critical gap value, z_0, is typically argued to range between 1.0 and 100 nm [33], and in this study a value of 1 nm used. The selected value will only have an impact on collisions between surfaces with different effective work functions. Ultimately, the charge efficiency term k_c was used to set the modeled charge transfer values in the same magnitude range as the experimental data. Charge transfer behavior between two surfaces can vary immensely due to differences in the surface chemistry, particle shape, surface roughness, or even environmental conditions such as relative humidity, temperature, and the medium in which the collision took place (i.e., in air, nitrogen, vacuum, etc.). Thus, preliminary triboelectrification experiments will always be necessary to identify the appropriate value for k_c for any given system to account for variations brought about by the complex interaction between possible charge transfer mechanisms. In this work, the k_c of every collision data set was selected to minimize the sum of squares of the error between the measured and modelled charge magnitudes of every collision trial.

Table 6-1: Particle properties and model parameters used in the charge transfer model.

Particle Type	Particle Size (mm)	Particle Mass (mg)	Poisson Ratio (-)	Young's Modulus (GPa)	Work Function (eV)
Polytetrafluoroethylene (PTFE)	3.2	36.8	0.46	0.599	4.26
Aluminum-2017 alloy	3.2	47.2	0.33	72.4	4.20
Nylon-6/6	3.2, 4.0, 4.8	19.0, 37.2, 63.5	0.40	3.72	4.08
Model Parameter	$\boldsymbol{\varepsilon_0}$ (pC/V·mm)	$\boldsymbol{\varepsilon_r}$ (-)	$\boldsymbol{z_0}$ (nm)	$\boldsymbol{E_c}$ (V/mm)	$\boldsymbol{k_c}$ (-)
Value	0.008855	1.0006	1.0	0	*varies*

6.2.1. Rolling contact area

To analyze the inclusion of the rolling contact area (Eq. 6-3) in the model, the total contact area was calculated both with and without the effect of particle rolling between PTFE and nylon spheres of the same particle size (3.2 mm diameter). This was one of the tested cases in the particle-particle collision experiments referenced in this study [27]. It was observed in that work that increasing contact angles, resulting in a lower normal impact velocity, did not notably affect the degree of charge transfer. In some cases, a tangential or glancing impact resulted in greater charge transfer than head-on collisions [27]. Figure 6-1 shows the calculated contact area for these particle-particle collisions plotted as a function of impact velocity at varying contact angles. It is evident that the calculated contact area due to rolling has a strong impact on the total contact area between particles. In fact, angled collisions could result in a greater total contact area than head-on collisions beyond a certain impact velocity. This threshold velocity value would differ based on the size and material properties of the colliding particles. In the experimental trials for PTFE-nylon collisions, the maximum observed impact velocity was approximately 1.5 m/s, which according to Figure 6-1, resulted in similar total contact areas for 0, 30, and 45° collisions. These findings suggest that the rolling contact area should be included in the particle-particle charge transfer model, and thus will be considered in the following applications of the model for individual particle-particle collisions.

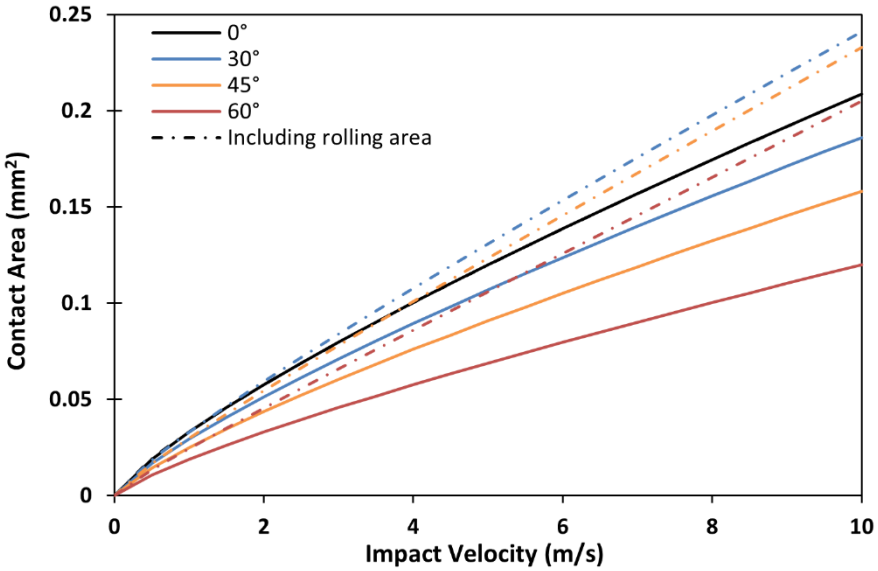

Figure 6-1: Contact area in particle-particle collisions as a function of impact velocity at varying contact angles. The dashed lines represent the total contact area when including particle rolling.

6.2.2. Different-material, same-sized particle collisions

The first collision scenario from the experimental work was the charge transfer between PTFE spheres individually colliding with aluminum and nylon 6/6 spheres [27]. All the particles in these collision trials were the same size at 3.2 mm diameter. Given the identical particle size and the absence of any other particle at the time of the collision, the charge transfer model for this scenario can be simplified to

$$\frac{dQ_1}{d\boldsymbol{n}_c} = -\frac{dQ_2}{d\boldsymbol{n}_c} = k_c\left[\frac{\varepsilon_0\varepsilon_r}{z_0}V_c + \frac{Q_{i,2} - Q_{i,1}}{\pi d^2}\right]S_c \qquad 6\text{-}6$$

The degree of charge transfer to PTFE in each collision trial, ΔQ, was predicted with this model using the particles' measured initial charges, their measured impact velocity and angle, and finally the material and electrostatic properties listed in Table 6-1 [32]. The effective work function difference is assumed to be a constant for a given collision scenario. The value for k_c was set to 0.188 and 0.061 for the 3.2 mm same-sized PTFE-aluminum and PTFE-nylon particle collisions, respectively. To observe the charging trend predicted by the model for different material collisions, a surface area plot was created for PTFE-nylon collisions using Eq. 6-6, as shown in Figure 6-2.

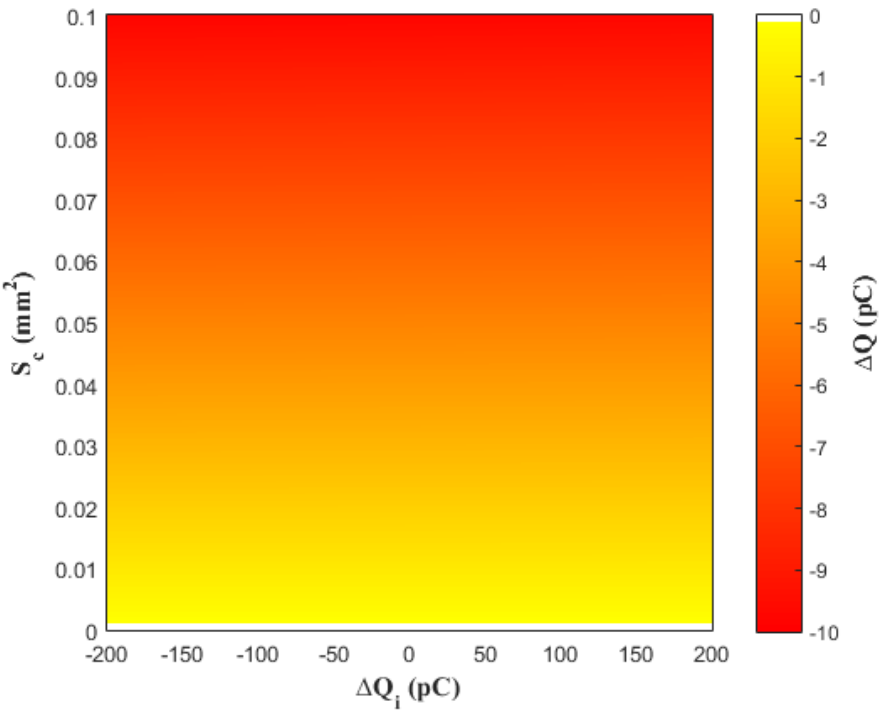

Figure 6-2: Surface plot of the charge transferred, ΔQ, as a function of the contact area, S_c, and the difference in initial charges, ΔQ_i, as described in Eq. 6-6 and using input parameters based on 3.2 mm same-sized PTFE-nylon collisions.

It is evident from the surface plot that the degree of charging did not change with the net initial charge; the effective work function difference had a dominant effect on the direction of charge transfer, and the magnitude of charging was directly proportional to the contact area. Figure 6-3 was plotted to compare the actual charge transfer measurements from each collision trial to the predicted values from Eq. 6-6, using the initial charge difference, impact angle, and impact velocity as input parameters. In the experiments, PTFE was measured to gain negative charge from the particle-particle collisions. This was predicted by the charge transfer model due to PTFE having a greater work function value than both aluminum and nylon. In addition, the model shows that PTFE-nylon collisions are expected to transfer more charge than PTFE-aluminum collisions since the work function difference for the former is greater than in the latter. Although the experimental findings showed a range of overlapping charge transfer values for both collision scenarios, PTFE-nylon did exhibit higher charge transfer magnitudes than PTFE-aluminum. In comparison, the predicted charge transfer data points were static relative to the range of measured data.

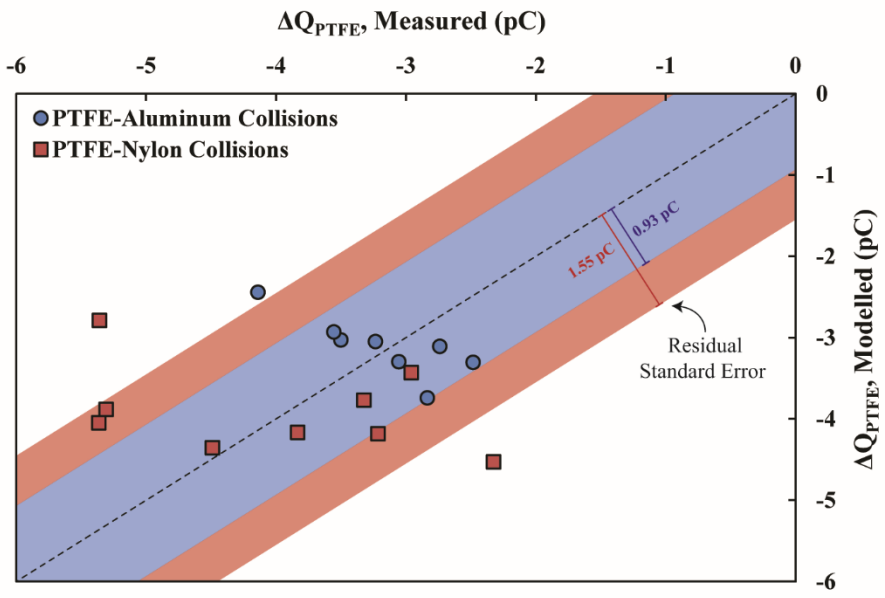

Figure 6-3: Comparing the experimentally measured change in charge for PTFE, ΔQ_{PTFE}, with that calculated using the charge transfer model. k_c values of 0.188 and 0.061 were used for PTFE-Aluminum (blue) and PTFE-nylon (red) collisions, respectively, to minimize their residual standard errors visualized along the 45 degree line.

As mentioned above, the consistency in the predicted values is due to the dominating effect of the work function difference term in the model. However, the work function alone did not dictate the degree of charging in the experiments, and so other factors need to be identified and emphasized in the model that could cause this range of charge transfer. Figure 6-4 presents the same charge transfer data in terms of the colliding particles' initial charge difference. The observed range of initial charge differences had a negligible influence on the charge transfer between different materials for both the modelled and measured results. However, as shown in Figure 6-5, the model predicts that a greater surface area of contact yields higher charge transfers which was not consistently observed for the measured data. The residuals between the modelled and measured data were generally lower for PTFE-aluminum collisions than for PTFE-nylon collisions, which was likely due to electron mobility on the metal surface. This suggests that the non-uniform distribution of charge on an insulator surface may have caused the range of charge transfer magnitudes in the experimental results. It would explain why a larger contact area did not always result in greater charge transfer in the experiments. Thus, the assumption of a uniform charge distribution on the particles may need to be reconsidered.

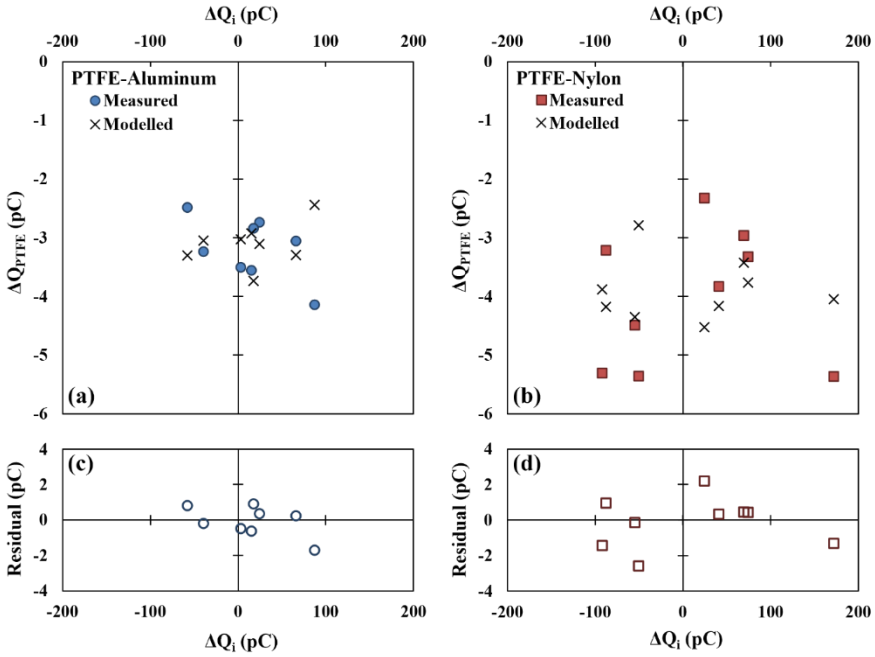

Figure 6-4: The effect of the initial charge difference, ΔQ_i, on the measured and modelled charge data for PTFE in (a) PTFE-Aluminum and (b) PTFE-Nylon collisions. The residual plots highlight the discrepancies between the measured and modelled data for each (c) PTFE-Aluminum and (d) PTFE-Nylon collision trial.

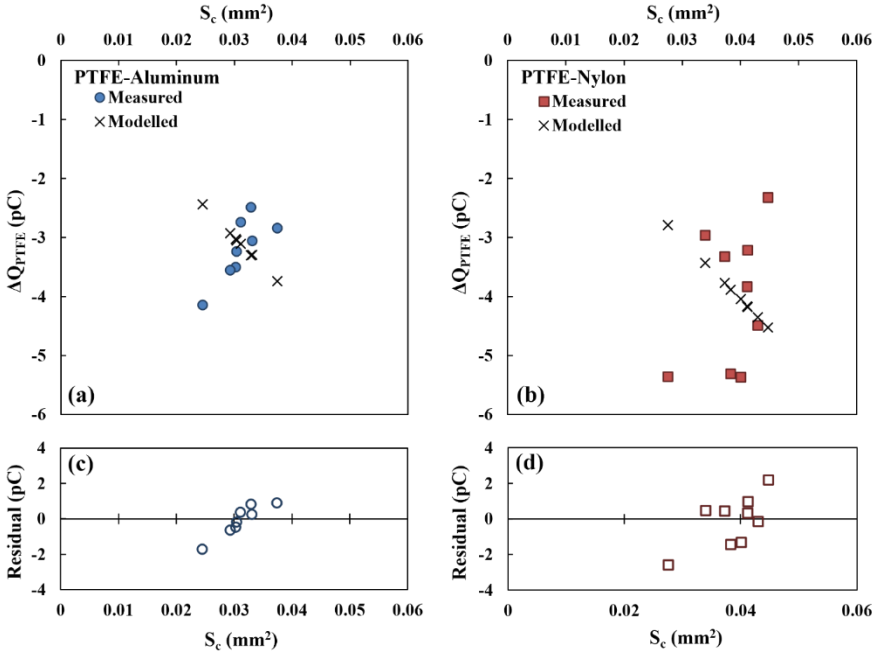

Figure 6-5: The effect of the surface area of contact, S_c, on the measured and modelled charge data for PTFE in (a) PTFE-Aluminum and (b) PTFE-Nylon collisions. The residual plots highlight the discrepancies between the measured and modelled data for each (c) PTFE-Aluminum and (d) PTFE-Nylon collision trial.

6.2.3. Same-material, same-sized particle collisions

The second scenario is the charge transfer between particles of identical material and size. Two cases were tested for this scenario using nylon-6/6 spheres with particle sizes of 3.2 mm and 4.0 mm diameter. The work function difference between identical materials should be zero, and as the collision trials were still isolated the particles are not influenced by any additional electric fields. The model suggests that the sole driving force for charge transfer in this scenario is the difference in initial particle charges:

$$\frac{dQ_1}{d\boldsymbol{n}_c} = -\frac{dQ_2}{d\boldsymbol{n}_c} = k_c\left[\frac{Q_{i,2} - Q_{i,1}}{\pi d^2}\right]S_c \qquad 6\text{-}7$$

The charging efficiency values used in the model for the 3.2 mm and 4.0 mm same-sized nylon particle collisions were 13.08 and 25.01, respectively. According to Eq. 6-7, charge transfer will always tend towards thermal equilibrium such that the particle with the relatively more negative initial charge will charge positively, and vice versa. This behaviour is illustrated in the surface plot shown in Figure 6-6, which used input parameters for 3.2 mm same-sized nylon particle collisions.

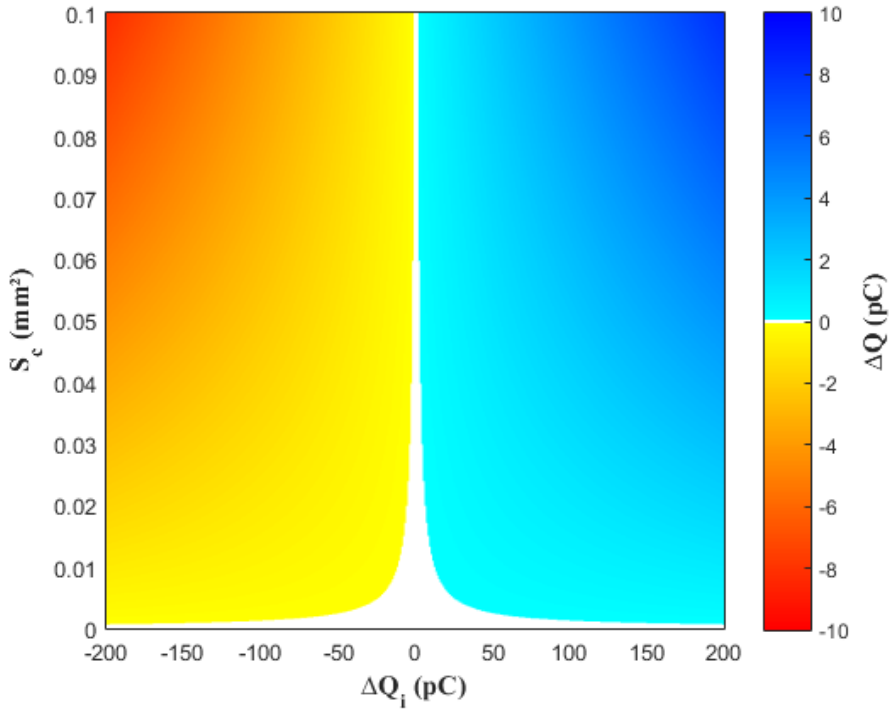

Figure 6-6: Surface plot of the charge transferred, ΔQ, as a function of the contact area, S_c, and the difference in initial charges, ΔQ_i, as described in Eq. (7) and using input parameters based on 3.2 mm same-sized nylon particle collisions.

To confirm whether this behaviour held true in the experimental results, Figure 6-7 compares the predicted and actual charge transfer to the particles with a relatively more negative initial charge. As expected, the model consistently showed positive charging for these particles. However, experimental results show the opposite is true in almost all cases for 3.2-3.2 mm nylon collisions and in roughly half of the 4.0-4.0 mm collisions; the initial particle charge differences can become amplified after a collision.

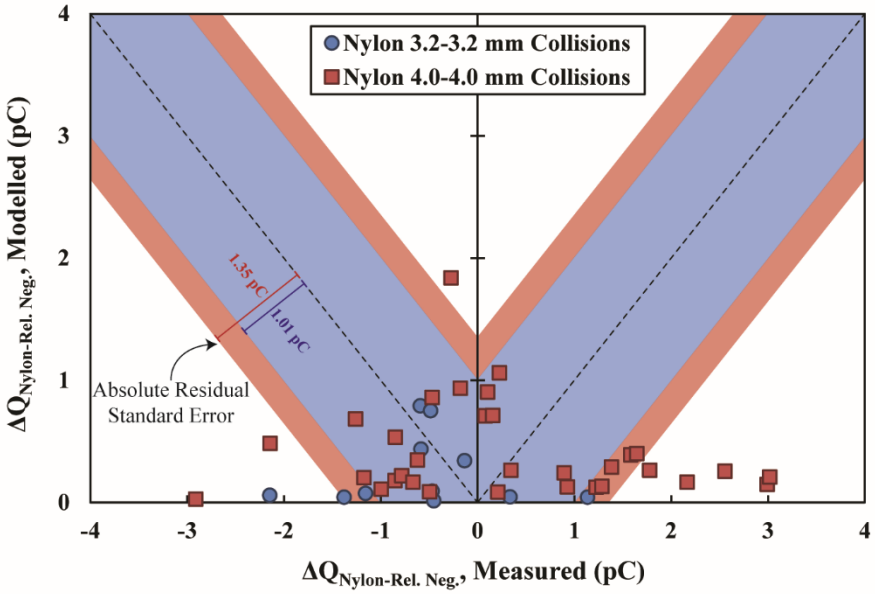

Figure 6-7: Comparing the experimentally measured charge transferred to nylon particles with a relatively negative initial charge with that calculated using the charge transfer model. While the model predicted positive charging for particles with a relatively negative initial charge, experimental data showed both positive and negative charging. Focusing on the magnitude of charge transfer instead of its direction, k_c values of 0.188 and 0.061 were respectively used for the 3.2 mm (blue) and 4.0 mm (red) same-sized nylon particle collisions to minimize their absolute residual standard errors.

The charge transfer predicted by the model tended to be much lower than what was measured. At the same time, the model also predicted higher charge transfers when the actual measurements were closest to zero. It should be noted that the charging efficiencies used for these collision trials are a factor of 100-1000 times greater than what was used for the different material collision trials, further illustrating how much the work function term dominates in the charge transfer model. Figure 6-8 explores this behaviour by looking at the effect of initial charge, which is presented in logarithmic scale to provide a clearer comparison of the modelled and measured data. It was

expectedly observed that the model predicted greater charge transfer with a greater difference in initial charge, which was not reflected in experiments. The discrepancy could be due to the abovementioned non-uniform distribution of charge; the charge differences localized to the contacting area would have the strongest effect on the magnitude of charge transfer.

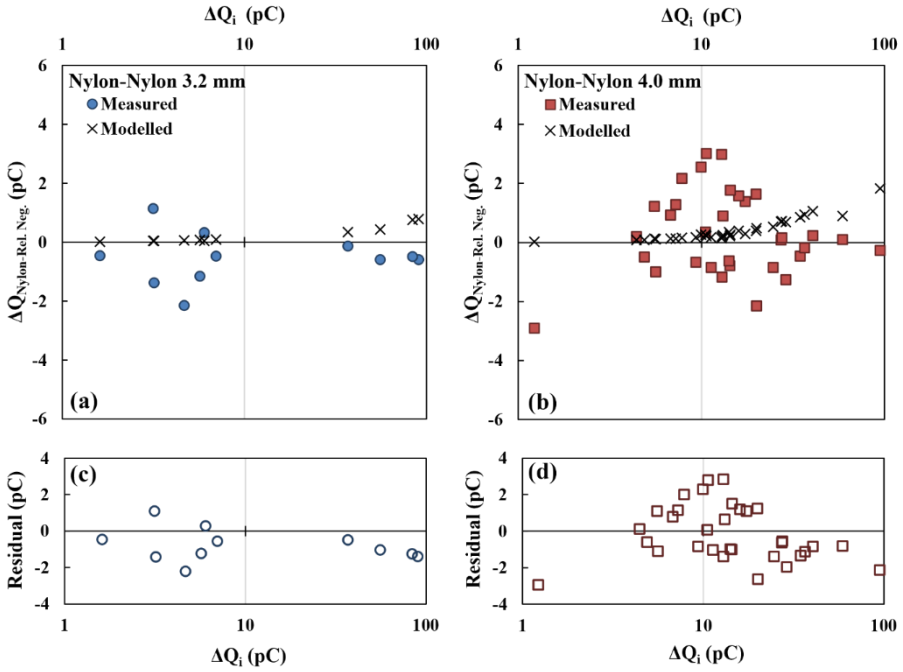

Figure 6-8: The effect of the initial charge difference, ΔQ_i, on the measured and modelled charge data for nylon particles with a relatively negative initial charge in (a) 3.2 mm and (b) 4.0 mm same-sized nylon particle collisions. Presented in logarithmic scale. The residual plots highlight the significant discrepancies between the measured and modelled data for each (c) 3.2 mm and (d) 4.0 mm collision trial.

Although the experimental results from these same-material collisions showed a lower maximum charge transfer magnitude, the values were still of the same scale as the different-material collisions. This does not align with the charging efficiencies needed to fit the model with the experimental data, suggesting that other influential factors were not considered in the model. For example, the work function term may not be exactly zero for the same-material collisions due to the presence of impurities or chemical and structural defects on real particles. This could explain why, as seen in Figure 6-9, the experimental results for 3.2-3.2 mm nylon collisions showed higher charge transfer magnitudes with larger contact areas, whereas the model predicted very little charge transfer for the same collisions due to the low initial charge differences on those particles

(Figure 6-8). This affirms the need to perform triboelectric studies on all studied particles to observe their charging behaviours and determine their appropriate modeling parameters prior to their simulation.

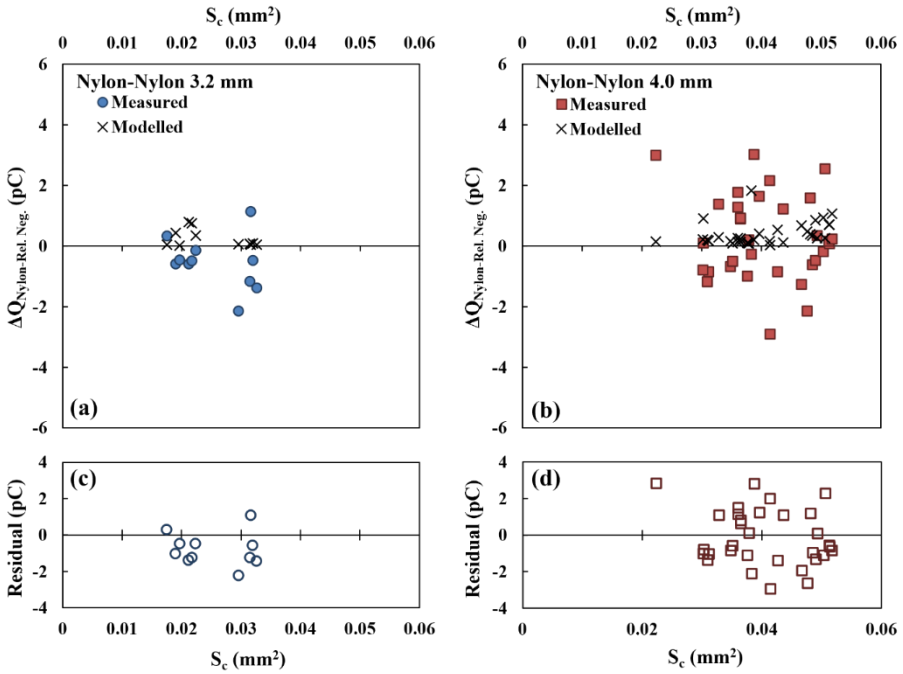

Figure 6-9: The effect of the surface area of contact, S_c, on the measured and modelled charge data for nylon particles with a relatively negative initial charge in (a) 3.2 mm and (b) 4.0 mm same-sized nylon particle collisions. The residual plots highlight the significant discrepancies between the measured and modelled data for each (c) 3.2 mm and (d) 4.0 mm collision trial.

6.2.4. Same-material, different-sized collisions

The final examined scenario is the charge transfer between chemically identical nylon-6/6 particles but with different particle sizes. More specifically, 4.0 mm nylon particles were collided with 3.2 and 4.8 mm nylon particles. Again, the work function difference should be zero since the particles remain chemically identical and the electric field term is zero since the particle collision is isolated:

$$\frac{dQ_1}{d\boldsymbol{n}_c} = -\frac{dQ_2}{d\boldsymbol{n}_c} = k_c\left[\frac{Q_{i,2}}{\pi d_2^2} - \frac{Q_{i,1}}{\pi d_1^2}\right]S_c \qquad 6\text{-}8$$

The charging efficiency was set to 64.33 for the 4.0-3.2 mm nylon collisions, and 46.98 for the 4.0-4.8 mm nylon collisions. Similar to Eq. 6-7, charge transfer using Eq. 6-8 will always tend towards electrical equilibrium, except the magnitude and direction of charge transfer is now

dependent on the initial surface charge densities, σ_i. This behaviour is showcased in the surface plot shown in Figure 6-10, which used input parameters for 4.0-3.2 mm nylon collisions.

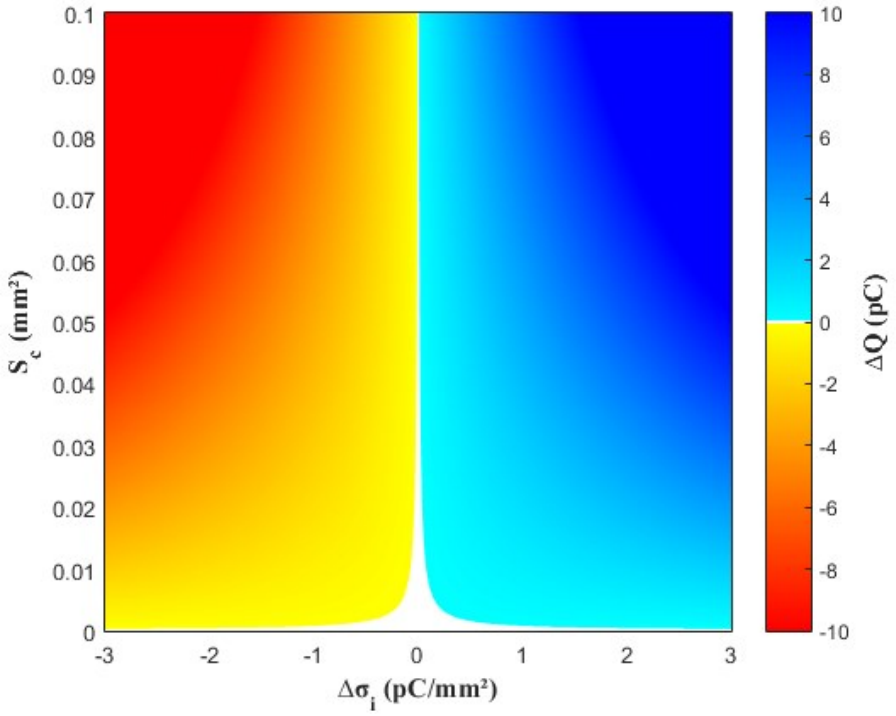

Figure 6-10: Surface plot of the charge transferred, ΔQ, as a function of the contact area, S_c, and the difference in initial surface charge densities, $\Delta\sigma_i$, as described in Eq. 6-8 and using input parameters based on 4.0-3.2 mm nylon collisions.

The primary finding from the experimental results of different-size collisions was that the direction of charge transfer was strongly influenced by particle size. Considering only the surface charge densities, a possible contributor to this size-dependent bipolar charging behaviour is that, provided with a sufficiently large difference in particle size, the larger particle can have a greater net charge but a lower charge density. This would allow for the accumulation of either positive or negative charge on the larger particle leading to bipolar charging behaviour, though eventually an equilibrium would be reached between the two surface charge densities. However, as shown in Figure 6-11, there are major disagreements between the model and the experimental results for the direction of charge transfer. 4.0 mm nylon particles charged positively in the majority of its collisions with both the smaller and larger particle sizes, whereas the model predicted primarily negative charging for 4.0 mm nylon in both collision scenarios.

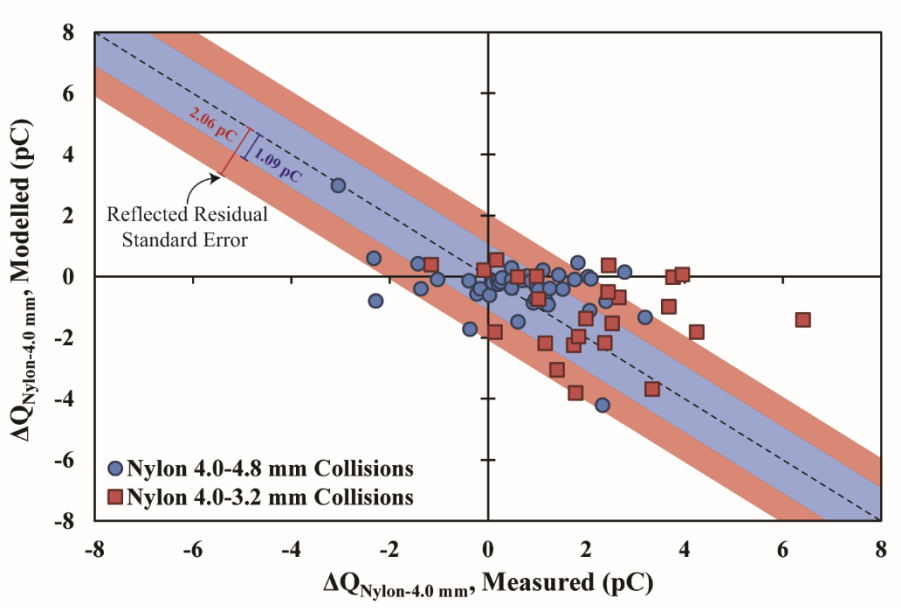

Figure 6-11: Comparing the experimentally measured charge transferred to 4.0 mm nylon particles with that calculated using the charge transfer model. The model generally predicted charge transfer in the opposite direction of the experimental data. Focusing on the magnitude of charge transfer instead of its direction, k_c values of 64.33 and 46.98 were respectively used for the 4.0-4.8 mm (blue) and 4.0-3.2 mm (red) nylon collisions to minimize their reflected residual standard errors.

Figure 6-12 further shows that the 4.0 mm nylon particles had a greater negative charge density than their colliding counterparts in most collision trials. The measured data presented positive charging for these trials whereas the model predicted negative charging. For the few cases where the 4.0 mm nylon particles had a greater positive charge, the experiments still exhibited positive charging which agreed with the model trends. Although the direction of charge transfer is largely not in agreement between the measured and modelled data, there is at least good agreement between the magnitudes of charge transfer. This was more clearly observed in Figure 6-13, where the wide range of charge transfer magnitudes for the measured and modelled data somewhat mirrored each other about the x-axis. Thus, size-dependent bipolar charging behaviour which is evident in the experiments is not properly considered in the particle-particle charging model, though the factors that affect the actual magnitude of charge transfer may not need significant adjustments.

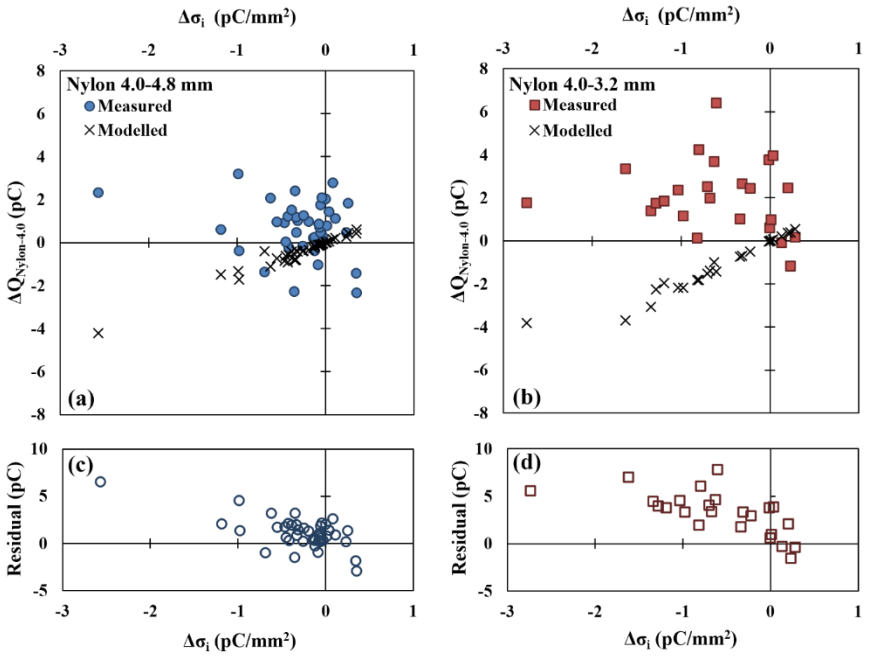

Figure 6-12: The effect of the difference in initial surface charge density, $\Delta\sigma_i$, on the measured and modelled charge data for 4.0 mm nylon particles in (a) 4.0-4.8 mm and (b) 4.0-3.2 mm nylon collisions. The residual plots highlight the significant discrepancies between the measured and modelled data for each (c) 4.0-4.8 mm and (d) 4.0-3.2 mm collision trial.

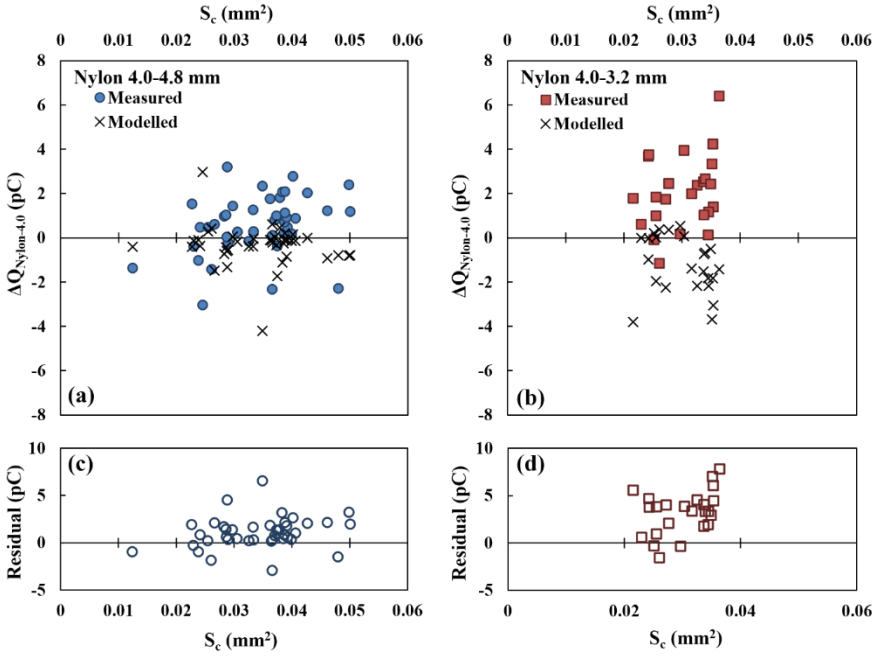

Figure 6-13: The effect of the surface area of contact, S_c, on the measured and modelled charge data for 4.0 mm nylon particles in (a) 4.0-4.8 mm and (b) 4.0-3.2 mm same-sized nylon particle collisions. The residual plots highlight the significant discrepancies between the measured and modelled data for each (c) 4.0-4.8 mm and (d) 4.0-3.2 mm collision trial.

6.3. Conclusion

The particle-particle charge transfer model currently used in gas-solid flow simulation studies [7] was tested to confirm its ability to predict the charging transfer behaviour observed in recent individual particle-particle collisions experiments [27]. Three distinct collision scenarios were considered: collisions between same-sized particles made of different materials, collisions between particles of the same material and size, and collisions between particles of the same material but different sizes. The magnitude and direction of charge transfer in these collision scenarios were analyzed based on the particles' work function differences, initial charges, and the contact area calculated using both the normal and tangential components of the observed impact velocity. It should be noted that this evaluation was performed using a single source of individual particle-particle collisions that provided all the necessary input parameters for the model. As such, the charging behaviours, and the model itself, should be re-evaluated in the future as additional studies are performed by other researchers.

The particle-particle charge transfer model was found to be most effective when considering collisions between particles of different materials. In this scenario, the work function difference between the colliding particles dictates the magnitude and direction of charge transfer, with a negligible influence from the initial particle charges. However, experimental studies of PTFE-aluminum and PTFE-nylon collisions showed that each collision could result in a range of charge transfer magnitudes regardless of their initial particle charges and contact areas. This behaviour may be attributed to the non-uniform distribution of charge on the surface of insulator particles. Nonetheless, the model can be used to simulate the charging in multi-component granular mixtures if a probability density function for the charge transferred per contact area is experimentally determined for the desired different-material collisions.

For isolated same-material collisions, the work function and electric field terms in the particle-particle charging model are negligible. As such, the charge transfer direction is only dictated by the difference in surface charge densities, and the particles were expected to equilibrate their charges. However, the experimental results of same-sized nylon particle collisions showed the prevalence of charge amplification behaviour that cannot be predicted by this model. Moreover, an influence must exist beyond the difference in surface charge densities to emulate the size-dependent bipolar charging behaviour observed by many researchers. According to previous

studies on particle-particle charging, collisions between different-sized particles of the same material generally led to the larger particle charging positively and the smaller particle charging negatively [34]. However, the charging results of different-sized nylon collisions discussed here show that this is not necessarily true for all cases [27]. It is insufficient to simply assume that the direction of charge transfer is dictated by particle size; the size of a particle should not be directly related to the material's electronegativity. Thus, additional factors need to be considered in the model, such as a non-zero work function difference due to the presence of impurities or chemical/surface defects. In addition, if a non-uniform charge distribution is assumed on the particle surfaces, then the charged species on the particles not involved in the charge transfer could induce an electric field at the contact point, thereby influencing the degree and direction of charging.

Ultimately, the current particle-particle charging model does not sufficiently consider collisions between particles made of the same material, and especially not particles of the same material and varying sizes. Beyond these limitations, the model could accurately predict charge transfer assuming the exact work function difference and initial charges on the contacting surfaces is known. These parameters are impractical to determine in real systems, especially those with dense granular flows. Thus, the question remains as to how the complex particle-particle charging behaviours observed in experimental studies can be better, and more practically, represented by a particle-particle charging model.

References

[1] P. Mehrani, M. Murtomaa, D.J. Lacks, An overview of advances in understanding electrostatic charge buildup in gas-solid fluidized beds, J. Electrostat. 87 (2017) 64–78.

[2] M. Nifuku, H. Katoh, A study on the static electrification of powders during pneumatic transportation and the ignition of dust cloud, Powder Technol. 135 (2003) 234–242.

[3] M. Taghavivand, B. Elchamaa, A. Sowinski, P. Mehrani, Study of electrostatic charging of single particles during pneumatic conveying, Powder Technol. 355 (2019) 242–250.

[4] C. Pei, C.Y. Wu, M. Adams, DEM-CFD analysis of contact electrification and electrostatic interactions during fluidization, Powder Technol. 304 (2016) 208–217.

[5] H. Grosshans, M. V. Papalexandris, Direct numerical simulation of triboelectric charging in particle-laden turbulent channel flows, J. Fluid Mech. 818 (2017) 465–491.

[6] J. Kolehmainen, A. Ozel, S. Sundaresan, Eulerian modelling of gas-solid flows with

triboelectric charging, J. Fluid Mech. 848 (2018) 340–369.

[7] M. Ray, F. Chowdhury, A. Sowinski, P. Mehrani, A. Passalacqua, An Euler-Euler model for mono-dispersed gas-particle flows incorporating electrostatic charging due to particle-wall and particle-particle collisions, Chem. Eng. Sci. 197 (2019) 327–344.

[8] T. Itakura, H. Masuda, C. Ohtsuka, S. Matsusaka, The contact potential difference of powder and the tribo-charge, J. Electrostat. 38 (1996) 213–226.

[9] S. Matsusaka, M. Ghadiri, H. Masuda, Electrification of an elastic sphere by repeated impacts on a metal plate, J. Phys. D. Appl. Phys. 33 (2000) 2311–2319.

[10] A. Ema, D. Yasuda, K. Tanoue, H. Masuda, Tribo-charge and rebound characteristics of particles impact on inclined or rotating metal target, Powder Technol. 135–136 (2003) 2–13.

[11] H. Watanabe, M. Ghadiri, T. Matsuyama, Y.L. Ding, K.G. Pitt, H. Maruyama, et al., Triboelectrification of pharmaceutical powders by particle impact, Int. J. Pharm. 334 (2007) 149–155.

[12] P.M. Ireland, Triboelectrification of particulate flows on surfaces: Part I — Experiments, Powder Technol. 198 (2010) 189–198.

[13] J. Yao, S. Ge, Y. Zhao, S. Cong, C.H. Wang, N. Li, Investigation of granule electrostatic charge generation with normal stress effect, Adv. Powder Technol. 27 (2016) 2094–2101.

[14] F. Chowdhury, A. Sowinski, M. Ray, A. Passalacqua, P. Mehrani, Charge generation and saturation on polymer particles due to single and repeated particle-metal contacts, J. Electrostat. 91 (2018) 9–15.

[15] M.A. Bilici, J.R. Toth, R.M. Sankaran, D.J. Lacks, Particle size effects in particle-particle triboelectric charging studied with an integrated fluidized bed and electrostatic separator system, Rev. Sci. Instrum. 85 (2014).

[16] K.M. Forward, D.J. Lacks, R. Mohan Sankaran, Methodology for studying particle-particle triboelectrification in granular materials, J. Electrostat. 67 (2009) 178–183.

[17] S.R. Waitukaitis, V. Lee, J.M. Pierson, S.L. Forman, H.M. Jaeger, Size-dependent same-material tribocharging in insulating grains, Phys. Rev. Lett. 112 (2014) 1–5. doi:10.1103/PhysRevLett.112.218001.

[18] L. Konopka, S. Jantač, M. Vrzáček, M. Svoboda, J. Kosek, Triboelectric charging of polyethylene powders: Comparison of same-material and different-material contributions to the charge build-up, Powder Technol. 367 (2020) 713–723.

[19] L. Xie, G. Li, N. Bao, J. Zhou, Contact electrification by collision of homogenous particles, J. Appl. Phys. 113 (2013) 184908.

[20] F. Chowdhury, B. Elchamaa, M. Ray, A. Sowinski, A. Passalacqua, P. Mehrani, Apparatus design for measuring electrostatic charge transfer due to particle-particle collisions, Powder

Technol. 361 (2020) 860–866.

[21] A.G. Kline, M.X. Lim, H.M. Jaeger, Precision measurement of tribocharging in acoustically levitated sub-millimeter grains, Rev. Sci. Instrum. 91 (2020) 023908.

[22] A. Mehrotra, F.J. Muzzio, T. Shinbrot, Spontaneous separation of charged grains, Phys. Rev. Lett. 99 (2007) 058001.

[23] T. Shinbrot, M. Rutala, H. Herrmann, Surface contact charging, Phys. Rev. E. 96 (2017) 032912.

[24] H. Zhao, G.S.P. Castle, I.I. Inculet, A.G. Bailey, Bipolar charging of poly-disperse polymer powders in fluidized beds, IEEE Trans. Ind. Appl. 39 (2003) 612–618.

[25] D. Song, Study of Electrostatic Charging and Particle Wall Fouling in a Pilot-scale Pressurized Gas-Solid Fluidized Bed up to Turbulent Flow Regime, (2017).

[26] M. Rowland, A. Cavecchi, F. Thielmann, J. Kulon, J. Shur, R. Price, Measuring The Bipolar Charge Distributions of Fine Particle Aerosol Clouds of Commercial PMDI Suspensions Using a Bipolar Next Generation Impactor (bp-NGI), Pharm. Res. 36 (2018) 15.

[27] F. Chowdhury, M. Ray, A. Passalacqua, P. Mehrani, A. Sowinski, Electrostatic charging due to individual particle-particle collisions, Powder Technol. (2020).

[28] S. Matsusaka, H. Masuda, Electrostatics of particles, Adv. Powder Technol. 14 (2003) 143–166.

[29] S.P. Timoshenko, Theory of Elasticity, 3rd ed., McGraw-Hill, 1934.

[30] P.M. Ireland, Triboelectrification of particulate flows on surfaces: Part II—Mechanisms and models, Powder Technol. 198 (2010) 189–198.

[31] M.W. Korevaar, J.T. Padding, M.A. Van der Hoef, J.A.M. Kuipers, Integrated DEM-CFD modeling of the contact charging of pneumatically conveyed powders, Powder Technol. 258 (2014) 144–156.

[32] MatWeb, Material Property Data, (2020). http://www.matweb.com/ (accessed October 28, 2020).

[33] J. Lowell, Contact electrification of metals, J. Phys. D. Appl. Phys. 8 (1975) 53–63.

[34] D.J. Lacks, T. Shinbrot, Long-standing and unresolved issues in triboelectric charging, Nat. Rev. Chem. 3 (2019) 465–476.

Chapter 7

A review on modeling approaches for the electrostatic charging of particles

F. Chowdhury[a], M. Ray[b], A. Sowinski[a], A., P. Mehrani[a*], Passalacqua[b]

[a] Department of Chemical and Biological Engineering, University of Ottawa, 161 Louis Pasteur, Ottawa, ON, K1N 6N5, Canada
[b] Department of Mechanical Engineering, Iowa State University, 2025 Black Engineering Building, Ames, IA, 50011-2161, USA

This chapter is a manuscript under review in Powder Technology (ID: POWTEC-D-20-03376R1)

Abstract

Triboelectrification and its underlying mechanisms have been studied over several decades to provide us with deterministic tools which can predict the occurrence of such phenomenon. This has also produced many charge transfer models that have been validated by some experiments and contradicted by others. However, certain trends have emerged which provide insight for a general charge evolution model. Variations produced by impact conditions and solids surface properties have been discussed in greater detail in recent years and their effects need to be modeled as well. Of particular interest is the occurrence of bipolar charging in insulative particle systems. While models can predict such behavior with suitable work function differences, justifying this for particles of the same material is not obvious. Aside from discrete models, simulation setup and parameters used have also significant impact on outcomes. These factors and their implications are reviewed in this paper while highlighting shortcomings that need to be addressed.

7.1. Introduction

In gas-solid flow systems, particles can gain electrostatic charge through particle-wall and particle-particle collisions. This phenomenon, known as triboelectrification, has proven to be beneficial in some applications, such as powder coating [1] and electro-spraying [2]. However, it was also confirmed to be detrimental for several industrial processes. For example, in polyethylene production the generation of electrostatic charge in fluidized bed reactors has been identified as the cause for wall sheeting events [3], which can disrupt production by forcing frequent reactor shutdowns. In the pharmaceutical industry, uncontrolled electrostatic charging was found to impede the homogenous blending of active pharmaceutical ingredients [4], resulting in the production of lower quality drugs. In powder handling processes, such as the pneumatic conveying of coal, poor control of triboelectrification could result in dust explosions due to electrostatic discharge [5]. The electrostatic charging of particles is inherent in all gas-solid flow systems, and not addressing it may lead to undesired, and sometimes unexpected, consequences.

With the goal of mitigating the effects of triboelectrification in industrial processes, researchers have conducted experimental studies for decades. Mehrani, Murtomaa and Lacks (2017) [6] compiled a comprehensive review of works pertaining to electrostatic charge buildup and its effects in gas-solid fluidized beds, including fundamentals of triboelectrification and charge measurement methods. Kaialy (2016) [7] published a review on electrostatic charging and its effects in pharmaceutical processes, specifically on material properties and operating conditions associated with inhalation powder production and usage. Klinzing (2018) [8] discussed the state of research on pneumatic conveying, which included insights on electrostatics. All these reviews have shown that electrostatic charging is dependent on the complex interaction between many material and operational properties. Extensive parametric studies are therefore key in identifying the dominant charging mechanisms for a given system, which may not always be feasible to perform experimentally. As such, numerical models of electrostatic charging in gas-particle flows can help bridge these knowledge gaps in experimental studies. If developed carefully, these models can also be a cost-effective alternative to performing electrostatic charging experiments, especially when testing large-scale systems such as gas-solid fluidized bed reactors.

This review paper will discuss some of the recent findings by researchers, experimentalists, and modelers, with the objective of recognizing key aspects that need to be addressed before using

existing electrostatic models for prediction purposes. This paper is not an exhaustive list of issues that need to be addressed but connects certain relevant findings of previous works to highlight shortcomings that should be remedied in mathematical models.

7.2. Charge transfer mechanisms and models

Electrostatic charge transfer can occur when any two material surfaces contact each other. This seemingly simple phenomenon has been observed for centuries [9], but progress in understanding the mechanisms behind this process has been slow despite being extensively studied even in modern times. The greatest challenge in studying electrostatic charging is the fact that contact charging experiments can be unpredictable [10], possibly due to competing and unstable dynamic processes involved in any given contact charging event. Currently, the competing mechanisms for triboelectric charging include electron transfer, ion transfer, and material transfer. Studies have shown that the magnitude and direction of charge transfer in these mechanisms are affected by many different factors: electrostatic properties such as electronegativity and charge saturation; material properties such as elasticity, morphology and particle size; operating conditions such as temperature and relative humidity; or even the electric field acting on the surfaces before contact [11]. Considering these and many other factors, one can see the challenge in characterizing the charging behaviors observed in gas-solid flow systems where millions of particles of varying surface properties and other physical characteristics can experience charging through an inconceivable number of particle-wall and particle-particle collisions. Nonetheless, all these experimental studies over the years have led to ever-evolving proposals of charge transfer models. While it may be impossible to accurately predict the exact charge transferred in individual interactions, developing numerical models based on observed charging behaviors in gas-solid flows can provide an approximate description of the expected average behavior observed over a substantial number of encounters.

In the most simplified form, the amount of charge transferred to a particle on impact with flat, metal surfaces, can be determined as follows [12]:

$$\Delta q = c\left(1 - \frac{q_i}{q_\infty}\right) \qquad 7\text{-}1$$

Here, q_i is the particle charge before collision and q_∞ is the saturated charge value, i.e., the maximum charge the particle can accumulate for a given plate material and surrounding conditions. Here the effect of any electric field due to surrounding particles and external sources is ignored. Eq. 7-1 represents the averaged behavior based on several observations reported in literature [13–18]. These researchers have proposed various charging mechanisms between the particle and the contacting surface, which manifests as the coefficient c in Eq. 7-1 and is discussed further in the succeeding sections. Variations on c adapted by some researchers are listed in Table 7-1. These model variations all depict the same charge generation behavior: the total charge per particle grows towards an equilibrium value with an exponentially decaying growth rate. The primary difference between these models lies on the how the charge saturation point is defined. For example, the charge saturation density or the saturation charge is predetermined in all equations except the one of [13] where it is indirectly calculated in the ratio $\frac{\varepsilon_0}{z\tau}$.

Table 7-1: Various proposed relationships for the general charge transfer equation.

Relationship	Reference
$c = \sigma_\infty A_{max}(v_n)$	[12]
$c = \frac{\varepsilon_0}{z\tau} A_{max}(v_n)$	[13]
$c = aq_\infty;$ $\frac{dq}{dt} = a(q_\infty - q_i)$	[14]

7.2.1. Condenser model

One of the widely proposed and tested charge transfer models for metal-metal or metal-insulator collisions is the *condenser (or capacitor) model* [17]. This model assumes that electron transfer is the chief mode of charge exchange and it was proposed that the contact region between a particle and a flat surface can be regarded as a capacitor, as shown in Figure 7-1 [19]. The initial condenser model was conceptualized by Cheng and Soo (1970) [20] while determination of the condenser capacitance from the contact area and the cut-off distance was provided by Cole et. al. (1969) [21]. The model was extended to include the effect of image charge and pre-charge as well [21,22]. The model of Matsusaka et. al. (2000) [17] considers these effects as well and shows how the charge

evolution equation reaches the form of Eq. 7-1, which corroborates exceptionally well with their experimental findings.

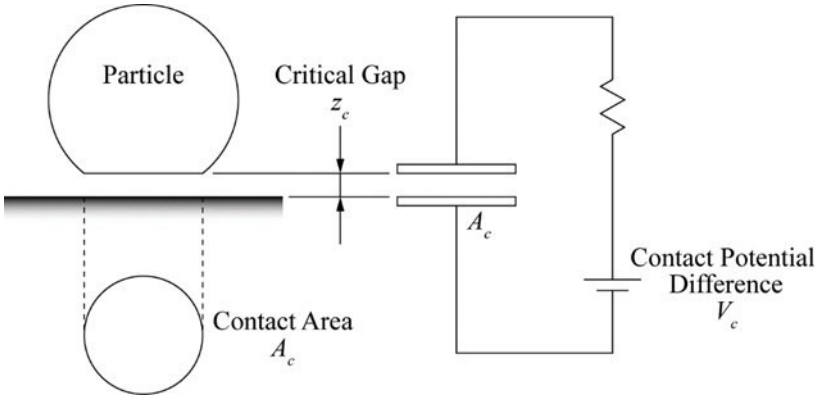

Figure 7-1: Condenser model schematic (Adapted from [19]).

The amount of charge transferred to the particle per collision event, $\frac{dq}{dn}$, is given by [17]:

$$\frac{dq}{dn} = k_c CV \tag{7-2}$$

where k_c is the charging efficiency, C is the capacitance between the two surfaces and V is the total potential difference, which includes the effects of work function difference (V_c), image (V_{im}) and space charges (V_{sp}), and any external field (V_{ex}):

$$V = V_c - V_{im} - V_{sp} + V_{ex} \tag{7-3}$$

The electric potential due to image charge is determined from the charge of the particle in consideration, whereas the potential due to spatial charge considers all the surrounding particles. The capacitance C is defined as:

$$C = \frac{A\varepsilon_0\varepsilon_r}{z_c} \tag{7-4}$$

where A is the maximum area of contact between the interacting objects, $\varepsilon_0\varepsilon_r$ is the permittivity of the medium in between the two surfaces and z_c is the electric cut-off distance. Thus Eq. 7-2 becomes

$$\frac{dq}{dn} = k_c \frac{A\varepsilon_0\varepsilon_r}{z_c}\left(V_c - V_{im} - V_{sp} + V_{ex}\right) \tag{7-5}$$

In this model, repeated collisions will result in increasing particle charge, until a maximum charge value (saturation charge) is reached [17]. As the particle charge increases, V_{im} also increases and counteracts the influence of V_c. In the absence of spatial charge and external electric field, the charging process will stop when $V_c = V_{im}$ and hence $V = 0$ in Eq. 7-3. Thus, the number of impacts it requires to reach equilibrium is dependent on k_c and C. V_{im} is given by the following equation if it is assumed that the charge is uniformly distributed on the surface of the particle and if polarization by the particle material is neglected:

$$V_{im} = \frac{q}{4\pi\varepsilon_0\varepsilon_r d_p^2} z_c \qquad 7\text{-}6$$

Hence, in the absence of other particles and electric fields, the particle can acquire a maximum charge:

$$q_\infty = 4\pi\varepsilon_0\varepsilon_r d_p^2 \frac{V_c}{z_c} \qquad 7\text{-}7$$

In these equations, d_p is the particle diameter. After inserting Eq.'s 7-6 and 7-7 in Eq. 7-5 and rearranging the terms, it can be seen that the latter attains the same form as Eq. 7-1, with c given by:

$$c = k_c \frac{A\varepsilon_0\varepsilon_r}{z_c} V_c \qquad 7\text{-}8$$

Before moving on to discussion of other charging models, parameters which affect the condenser model will be summarized as these are relevant to other models as well.

7.2.1.1. Effective work function difference

The work function difference between two surfaces is used in the condenser model to predict the equilibrium charge, since it is assumed that the charge transfer takes place due to movement of electrons. However, electron transfer between insulator materials is theoretically unlikely due to the large energy gap between the electron-filled valence band on one surface and the empty conduction band on the other. As such, the electron transfer may only occur if intermediate energy states exist between the valence and conduction bands [6]. These states could be present due to structural and chemical defects on the contacting surfaces, which would be prevalent in granular

materials. Moreover, it is possible that the charge carrying species involved in the triboelectrification include loosely-bound ions on the surfaces [23], or even patches of the surfaces themselves [24]. This would explain why charge transfer can take place between seemingly identical surfaces or particles [25]. Such findings cannot be explained with a simple work function concept in the same way it can be attributed to pure substances. Thus, for a realistic simulation of electrostatic charging in a given system, the "effective" work function differences between the colliding materials need to be established through experimentation at the desired operating conditions (temperature, pressure, and humidity).

7.2.1.2. Critical gap

The critical gap (or the capacitive gap), z_c, in between the two separating surfaces is determined by the distance across which electron (or charged species) transfer can take place. This was initially assumed to be the gap (about 1 nm) across which quantum tunneling can occur [26–28]. The reasoning for this choice was opined to be the rapid increase in resistivity to electron transfer beyond this distance. This is true in vacuum, but not when a medium is present. In initial studies, the tunneling threshold was used to explain observed saturation charge values [26]. However, discrepancies were found, and it was suggested that the critical gap could also depend on the surface roughness of the two surfaces [29]. To this date, no clear consensus has been arrived at for the appropriate value for the critical gap. For modelling purposes, researchers have assumed values ranging from the tunneling threshold to distances several orders higher. These are sometimes based on values derived from experiments and in others they are chosen to predict reasonable equilibrium charge magnitudes [30–33].

7.2.1.3. Saturation charge

In triboelectrification experiments by Matsuyama and Yamamoto (1995) [34], it was noted that the saturated charge on an insulator did not vary if the metal surface was changed. As such, they argued that there is no strong correlation between work function difference and the saturation charge magnitude, and that the latter was limited by the breakdown potential of the surrounding medium. The maximum theoretical charge, in C, on a spherical particle based on Gauss' law and the electric breakdown potential of air (8.854×10^{-12} F/m) is [35]:

$$|q|_{max} = 2.64 \times 10^{-5}\left(\pi d_p^2\right)\left(\frac{3\varepsilon_r}{2+\varepsilon_r}\right). \quad 7\text{-}9$$

This value was found to be greater than the average charge density measured on the surface of insulators, thus agreeing with the concept of breakdown being the restricting factor. If surfaces were perfectly smooth and homogeneous (chemically and physically), then all materials might have the same limiting theoretical charge in a given atmosphere. However, any variation in the surface would cause a deviation from this limit.

Given the uncertainties behind both the saturation charge and the critical gap discussed above, it is prudent to not rely on the condenser model to predict the saturation charge by means of Eq. 7-7, but use the experimental values for a given combination of particle and wall material. These can be used as parameters in Eq. 7-1 for simulation models. Variations in saturated surface charge density due to difference in sizes, as well as other statistical variations should be noted as well, for usage in more advanced models in the coming years.

7.2.1.4. Surface area of contact

The surface area of impact is used to find the area over which charge transfer will take place in all insulator charging models, and for calculating the contact capacitance in the condenser model. This seems reasonable if charge remains localized within a thin layer on the surface. Based on the Hertzian theory of impact deformation [36], the maximum area of contact is proportional to the normal component of the impact velocity raised to power of 4/5. Thus, the charge transfer rate per collision could be expected to follow this proportionality if the surface charge confinement assumption is correct. This correlation has indeed been established with the charge transfer rate per collision in experiments [17]. However, the true area of contact will be different from the predicted maximum surface area since the model does not account for surface projections, or surface roughness. Surface roughness of the colliding surfaces was proven to be a relevant material property for charge generation in experimental studies [37–39]. Specifically, Yao et al. (2017) [40] found that there exists a critical roughness value that maximizes the charge generated upon contact. Since the charging average behavior follows the proportionality discussed above despite not considering surface roughness, one option to incorporate its effect would be to multiply the computed contact area with an experimentally determined surface roughness factor (which could be a function of the roughness).

If sliding or rolling is considered, which could be present for any collision event, then the total contact area in an impact event is expected to be larger than that of a normal impact. It was found through experimentation that the tangential velocity has a non-linear effect on the degree of particle charging for any given collision [41]. The charge generated by collisions steadily increased with respect to the impact angle up to 60^o, after which a sharp decrease in charging was observed. This sudden drop in charging was attributed to the fact that at the critical collision angles the contact mode changes from rolling to sliding. In fact, dropping powders down an inclined plane is a common method used by researchers for measuring electrostatic charge generation [42,43], and so are likely to experience rolling or sliding contact as the primary cause for charge transfer.

In their computational model, Korevaar et. al. (2014) [12] have assumed that a spherical particle with non-zero tangential velocity slides on the surface after impact and the additional area over which charge is transferred is the product of the contact patch area, the tangential velocity component and the duration of contact. In a different study, Ireland (2010) [44,45] also proposed a charging model for such continuous contacts based on his own experimental findings:

$$\tau \frac{dq}{dt_c} = (q_i - q_\infty)[A_c^s(1 - \phi_r) + A_c^r \phi_r] \qquad 7\text{-}10$$

where τ is the characteristic time of the charging process based on the condenser model; A_c^s and A_c^r are the total contacted area of the particle surface over the collision time interval, t_c, due to sliding and rolling, respectively; and ϕ_r is the roll fraction.

The particle dynamics of rolling and sliding; however, are often neglected when modeling gas-solid flows due to computational limitations in simulating such behaviors, especially in dense flows. Instead, it is assumed that modeling parameters can be tuned to account for the charge generation due to sliding or rolling. As such, this charging model has not yet been implemented in Computational Fluid Dynamics (CFD) models. If it is possible to find reproducible correlations between impact angle and charge transfer rate through experimentation, then those correlations must be used to formulate an empirical model for CFD simulations.

7.2.1.5. Effect of the electric field

The direction and magnitude of charge transfer depends on the local electric field at the point of separation [46]. This includes the contributions due to the charge on the separating surfaces as well

as those of any charge present in the system and any external field applied. The first is obvious and the second is encountered in most gas-solid flow applications. In single-particle experiments, only the first contribution is considered, and thus several triboelectrification equations only model the difference in charge and preclude any discrete electric field term. However, in a multi-particle system and especially in dense gas-solid flow applications, the short and long-range contributions of spatial charge contribute to the local electric field must be included. This implies that the presence of charged particles or an external field will alter the saturation charge. In systems where external fields are not present, it can be expected that the saturation charge magnitude will be lesser than the theoretical maximum. In simulations one could therefore predict that if a particle or region reaches the maximum theoretical charge before the entire system reaches thermodynamic equilibrium, further electrification of the system could lead to lowering of the particle or regional charge and hence the evolution of local charge may not be monotonic (total system charge may still evolve monotonically). Most recent computational models incorporating electrostatic charging have included the electric field term.

7.2.2. Ion transfer and material transfer models

The condenser model was derived with the assumption that electrons are the carrier species for collisional charging. However, it is believed through experimental studies that electron transfer is not energetically plausible for charging in organic, insulative materials. Instead, charge transfer in such materials is attributed to the presence of moisture and mobile ions [47,48]. In addition, the effects of material transfer and mechanochemistry on particle charging cannot be ignored [24,49]. Despite the clear evidence for ion and material transfer, there is currently a lack of numerical models based on these mechanisms that would be useful for simulating the dynamic charging behavior seen in gas-solid flows.

The net charge on two surfaces after a collision event can be related to the number of ionic functional groups present on one surface as well as the number of ions transferred between surfaces, as described in the schematic shown in Figure 7-2 [23].

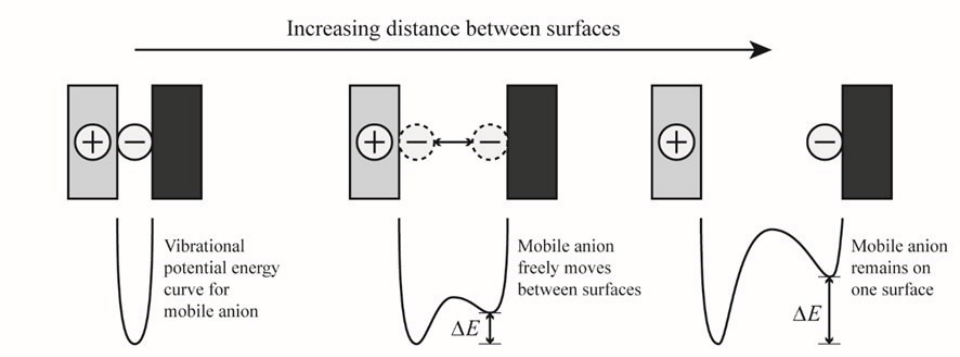

Figure 7-2: Ion transfer mechanism (Adapted from [23]).

Assuming a uniform distribution of charge on each surface, the number of transferred ions, n, required to achieve thermal equilibrium after a collision event can be estimated as follows:

$$\frac{n}{N-n} = \exp\left(-\frac{nde^2}{\varepsilon_0 kT}\right) \tag{7-11}$$

Here, N is the number of ionic functional groups present on one surface. The exponential term describes the electrostatic work required to transfer n ions between the two surfaces at a distance d and temperature T, where e is the magnitude of charge on a single ion, ε_0 is the permittivity of the vacuum, k is the Boltzmann constant [23]. In cases where a specific functional group or dissociated ion is expected to be the dominant charge transfer species, it may be necessary to develop a charge transfer model with the specific mechanism in mind. In the context of contact charging between small toner particles and large carrier beads in electrophotography, Diaz and Denzel-Alexander (1992) [50] proposed an ionic transfer model to study the presence of known mobile ions. They expressed the equilibrium charge acquired by a bead particle after colliding with n toner particles as follows:

$$q_b = n\, z\, F \left[\frac{a_b K}{a_t + a_b K}\right] \Gamma a_t \tag{7-12}$$

Here, a_b and a_t are the surface areas of the bead and toner particles, Γ is the surface ion concentration of the salt present in the toner powder, z is the valency of the ion, F is the Faraday constant, and K is the equilibrium distribution of ions between the toner particles and the bead.

To implement these ion-transfer models into CFD models for gas-solid flows, one must now consider the presence of mobile ions and how they are dynamically distributed per collision event, which may be challenging when their presence is otherwise not expected or relevant to the studied system. Nonetheless, if the equilibrium charge density can be reliably predicted based on Eq. 7-12 and if charge evolution follows an average growth rate predicted by Eq. 7-2, then these can be used in conjunction in computational models for dense flows.

7.2.3. Particle-particle charge transfer model

One commonly used charge transfer model between two colliding particles, *i* and *j*, is as follows [30]:

$$\Delta q = \frac{A\varepsilon_0\varepsilon_r}{z_c}\left(V_c - E_{ij}\cdot\frac{\mathbf{d}_{ij}}{\|\mathbf{d}_{ij}\|}z_c\right) \qquad 7\text{-}13$$

This model is based on what was proposed by Schein et. al. (1992) [51] assuming high density of surface charge carriers. Here, $\mathbf{d}_{ij}$ is the relative position vector of the centers of the two contacting particles, and E_{ij} is the electric field acting at the point of contact. The definition of the other quantities in this equation is the same as that in Eq. 7-5. In this form, when the work function difference of identical particles is zero, the charge transfer between such particles is entirely dependent on the electric field at the impact point. This electric field term accounts for the initial charges on both contacting particles as well from the surrounding particles and other external sources. Thus, Eq. 7-13 is identical to Eq. 7-5 since the electric potentials due to charge distribution and external sources are taken care of by the electric field term. Eq. 7-13 has been used in CFD-DEM studies [12,33,52–54] and also for developing closure equations in Eulerian models [55–59]. Eq. 7-14 assumes that the duration of contact is long enough so that the contact patch reaches thermodynamic equilibrium. However, if the amount of transferred charge is a small fraction of the equilibrium requirement, then one should recourse to the first inter-particle charge transfer model of Soo et. al. [20], which is a modified version of Eq. 7-13:

$$\Delta q = \frac{A\varepsilon_0\varepsilon_r}{z_c}\left(V_c - E_{ij}\cdot\frac{\mathbf{d}_{ij}}{\|\mathbf{d}_{ij}\|}z_c\right)h\Delta t. \qquad 7\text{-}14$$

Here h is a function of the conductance of the particles and the characteristic charge transfer lengths, and Δt is the duration of contact calculated using the Hertzian theory [36].

7.2.3.1. Dipole amplification mechanism

The particle charging model described in Eq. 7-13 suggests that for the same material, the contact patch will tend to neutralize the charge on the two surfaces. However, experimental studies with identical material collisions have shown that this might not always be the case. Chowdhury et al. (2020) [25] measured the charge transferred between two same-sized chemically identical PTFE particles, using a particle-particle collision apparatus, and found that the charge difference between the colliding particles usually increased after their collision. This behavior may be attributed to the fact that the charge on insulators is not uniformly distributed, and so the net charge transferred could be unpredictable especially at low charges. Alternatively, Shinbrot et al. (2008) [60] proposed the dipole amplification model to explain this charging behavior. As shown in Figure 7-3, the electric field generated between two approaching particles induces dipole moments of opposite polarities for each particle. The dipoles are fully or partially neutralized upon the particles' collision, thereby amplifying the actual initial charges and further strengthening the electric field between the particles upon separation. The dipole amplification model was confirmed through experimental studies [61,62], and provides a possible explanation for bipolar charging between particles made up of the same material. Thus, the particle-particle charge transfer model needs further development to also consider this phenomenon.

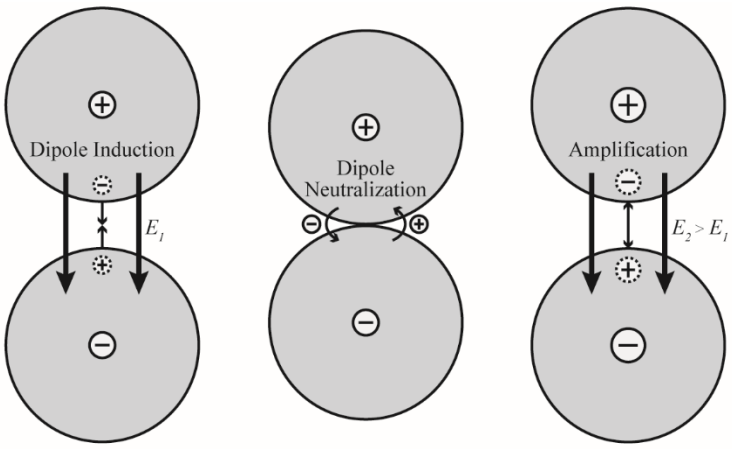

Figure 7-3: Dipole amplification model (adapted from [11]).

7.2.4. Charge relaxation model

Electrons can jump across larger gaps when the electric field strength exceeds the breakdown threshold of the surrounding medium. Breakdown can also occur in the bulk of the material of the separating surfaces (under common circumstances, their dielectric strength is usually higher than that of the surrounding medium) [34]. Thus, the largest distance across which charge transfer can take place is not a fixed value but varies with the material, the fluid medium, and the local electric field strength. This theory was suggested by Matsuyama and Yamamoto (1997) [63] in their *charge relaxation* model.

The model suggests that after a collision, some of the transferred charge may be dissipated during the separation process [64]. Figure 7-4 shows the mechanism for this model, which applies the Paschen curve to calculate the air breakdown potential between a wall and a particle as a function of pressure of air and distance between them. If the charge transferred to the particle is high enough to make the potential curve intersect the Paschen curve, then some of the charge will dissipate after a certain separation distance due to dielectric breakdown. This dissipation will continue till the potential curve of the particle follows the Paschen curve tangentially. Thereafter, as the potential curve diverges from the Paschen curve on further separation, a residual charge will remain on the surface. Therefore, the maximum surface charge density a particle can sustain is dictated by the dielectric breakdown of the surrounding medium, although it may be determined by the breakdown threshold of the particle material if it is lower. Obviously, if the potential curve of the particle surface after separation remains below the Paschen curve at any distance, then ionization is not expected.

In their experiments, Matsuyama and Yamamoto (1995) [34] observed that the magnitude of equilibrium charge on polymer particles did not change for different metal targets. However, the equilibrium charge declined with increasing dielectric constant of the polymer material, likely due to varying degrees of polarization by the polymer. These observations augment the argument made in favor of charge relaxation, which would not be present in vacuum. This also explains why the condenser model fails to predict the equilibrium charge in atmospheric conditions.

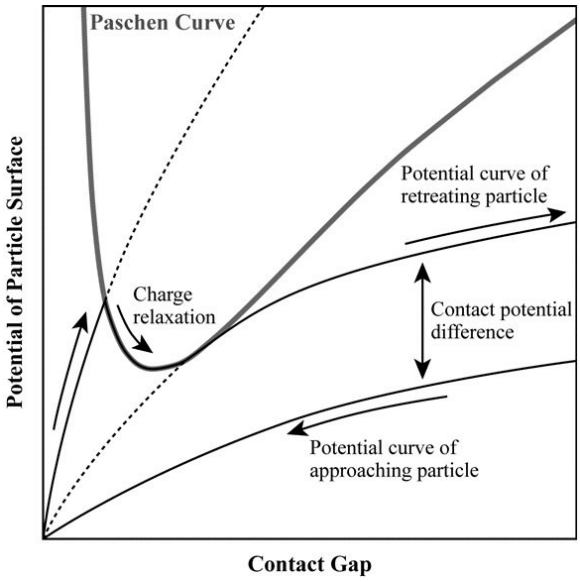

Figure 7-4: Mechanism of charge relaxation during separation (adapted from [19]).

The concept of charge relaxation has been used for CFD-DEM simulations by previous researchers [12,15]. In both of these works, it was assumed that the contact patch acquires saturation (or equilibrium) charge during the first impact. This can happen if the saturation charge in vacuum is much larger than that in ambient conditions and if the charge transferred during the contact duration is large enough to cause gaseous breakdown. Korevaar et. al. (2014) [12] have shown that under these assumptions, the charge relaxation model converges to that described by Eq. 7-1. As has been mentioned in Table 7-1, the charge transferred in a single collision in their model is proportional to the saturation charge density σ_{sat} (which is assumed to be a constant) and the area A_c^* over which charge transfer takes place:

$$\Delta q = \sigma_{sat} A_c^* \tag{7-15}$$

A_c^* is calculated as follows:

$$A_c^* = \alpha A_{hertz}\left(1 - \frac{A_{totalChargedAreaOfParticle}}{A_{totalAreaOfParticle}}\right), \tag{7-16}$$

where that the term in bracket approximates the fraction of the area which is uncharged. This is an oversimplified first order approximation since this is possible only for a uniformly charged sphere. However, ensemble averaging using a non-uniform charged sphere would lead to the same

expression. A_{hertz} is the contact area determined from the Hertzian model as has been discussed previously and α accounts for additional contact due to rolling and sliding [12]. Since σ_{sat} is a constant, Eqns. 7-15 and combine to give Eq. 7-16, which has the same form as Eq. 7-1 with $c = \alpha A_{hertz}$.

$$\Delta q = \alpha A_{hertz}\left(1 - \frac{q_{particle}}{q_{\infty}}\right) \tag{7-17}$$

This model equation is simplistic and has the advantage that it only requires knowledge of the saturation charge density and the charging rate, both of which can be obtained experimentally. Thus, no guesswork is needed for deciding on the parameters of the condenser model. The other advantage is that the underlying charge carrier need not be confirmed for every material or system if charge relaxation determines the saturation charge.

7.3. Gas-solid flow models with electrostatic effects

Computational Fluid Dynamics (CFD) models have been developed over the years to simulate gas-solid flow systems, as summarized in reviews for CFD studies in fluidized beds [65] and pneumatic conveying systems [66]. However, CFD model development specific to charge transfer is a relatively newer avenue of research. Most of the work in this regard has been done using the Computational Fluid Dynamics-Discrete Element Method (CFD-DEM) method which treats the gas and solid phases as Eulerian and Lagrangian phases, respectively [12,33,52–54]. Recently, the Two-Fluid Model (TFM), which describes the behavior of the solid phase as a Eulerian phase, has gained traction due to lower computational costs [55–59]. The gas phase in both these schemes is described by the mass and momentum transport equations:

$$\frac{\partial}{\partial t}\left(\alpha_g \rho_g\right) + \nabla \cdot \left(\alpha_g \rho_g \mathbf{U}_g\right) = 0 \tag{7-18}$$

$$\frac{\partial}{\partial t}\left(\alpha_g \rho_g \mathbf{U}_g\right) + \nabla \cdot \left(\alpha_g \rho_g \mathbf{U}_g \otimes \mathbf{U}_g\right) = \nabla \cdot \tau_g - \alpha_g \nabla p + \alpha_g \rho_g \mathbf{g} + \mathbf{M}_{sg} \tag{7-19}$$

where α_g, ρ_g, $\mathbf{U}_g$, and τ_g are the phase fraction, thermodynamic density, velocity vector, and stress tensor of the gas phase, respectively; $\mathbf{g}$ is the gravitational acceleration vector, p is the shared pressure [67], and $\mathbf{M}_{sg}$ is the momentum exchange term between the solid and gas phase.

This description is typical for hydrodynamic models of gas-solid flows and remains unaltered with the inclusion of electrostatic effects.

7.3.1. CFD-DEM

In CFD-DEM methods, the translational and rotational motions of each individual particle in the solid phase is determined using Newton's second law of motion:

$$m_p \frac{d\mathbf{U}_p}{dt} = \mathbf{F}_g + \mathbf{F}_{\nabla p} + \mathbf{F}_D + \mathbf{F}_C + \mathbf{F}_{el} \tag{7-20}$$

$$I \frac{d\boldsymbol{\omega}_p}{dt} = \mathbf{T} \tag{7-21}$$

where m_p, $\mathbf{U}_\mathrm{p}$, I, and $\boldsymbol{\omega}_p$ are the particle's mass, velocity, moment of inertia, and angular velocity, respectively. $\mathbf{T}$ is the torque acting on the particle due to translational and rotational moments, and the series of $\mathbf{F}$ terms represent the forces acting on the particle due to gravitational, pressure gradients, drag, collisional, and electrostatic forces.

Assuming a uniform distribution of charge on the surface of every particle, and a negligible magnetic field strength in gas-solid flow systems, the electrostatic force acting on a particle i due to its electric interaction with its surrounding particles is governed by Coulomb's law as follows:

$$\mathbf{F}_{el,i} = \sum_{j \neq i} \mathbf{F}_{el,ij} = \sum_{j \neq i} \frac{q_i q_j}{4\pi\varepsilon_\mathrm{r}\varepsilon_0 \left\|\mathbf{r}_{ij}\right\|^2} \frac{\mathbf{r}_{ij}}{\left\|\mathbf{r}_{ij}\right\|} \tag{7-22}$$

where $\mathbf{F}_{el,ij}$ is the electrostatic force from particle i having charge q_i to particle j having charge q_j, $\mathbf{r}_\mathrm{ij}$ is the vector joining the two particle centers and $\left\|\mathbf{r}_{ij}\right\|$ is its magnitude. The electrostatic force can also be expressed in terms of the electric field acting on the particle, $\mathbf{E}_i$, and the gradient of the electric potential, φ_i, with respect to the position of particle i:

$$\nabla \cdot (\varepsilon_0 \varepsilon_m \nabla \varphi) = \rho_q \tag{7-23}$$

$$\mathbf{F}_{el,i} = q_i \mathbf{E}_i = -q_i \nabla_i \varphi_i \tag{7-24}$$

While Eq. 7-22 can be used to compute the exact electrostatic force acting on a given particle due to every other particle (pair-wise approach), it becomes exceedingly expensive if a large number of particles are involved since the cost scales as $O(N^2)$. A compact support or cutoff distance can be used to reduce computational cost [14,52,68], but this leads to underestimation of the long-

range interactions producing erroneous results. To remedy this shortcoming, hybrid approaches are used. One method is to divide the domain into cells and use Eq. 7-22 assuming that the total charge of all the particles in the cell is located at its centroid. This is done to compute contributions of particles from outside a cutoff distance while those inside are treated individually [69]. Alternatively, the Poisson equation (7-23) can be solved for the electric potential field after approximating the volumetric charge density ρ_q (total charge/total volume) in each cell/element and applying relevant boundary conditions. The advantage of this approach is that curved boundaries and image charging at conducting walls are handled conveniently [70]. Eqn. 7-24 is then used to calculate the electrostatic force due to charge outside the cutoff distance while those within are treated pair-wise. If the cutoff distance is larger than the cell size, then any duplicate contributions should be subtracted [70]. The computational cost for both of these hybrid approaches scale as O(NM), where M is the number of cells [70]. As M<N, this reduces simulation cost considerably.

The benefit of using CFD-DEM is that charge transfer to a solid particle can be computed by directly using the experimental charging models. Pei et al. (2016) [33] used their 2D CFD-DEM model to study electrostatic charging in small-scale fluidized bed (5x35 mm conductive column, 2500 insulative particles of 100 μm diameter and varying work functions) and found that the particle system became more charged with increasing superficial gas velocities (25-100 m/s). Moreover, particle collisions of different materials/work functions resulted in binary charge and formed agglomerates. Kolehmainen et al. (2017) [53] also implemented charge transfer into their 3D slugging fluidized bed simulation (3 mm diameter and 96 mm height conductive column, 38,410 polyethylene particles of 150 μm diameter), and observed bimodal charge distributions, particle fouling, and reduced bed height oscillations with increasing work function differences between the wall and the particles. This is an important consideration in any gas-solid flow system, since multi-component systems or even the presence of impurities could have a large impact in the charge generation rate. Simulating the gas-solid flow system with a single “pure” component should result in much lower charging rates than what is observed experimentally. Korevaar et al. (2014) [12] performed CFD-DEM channel flow simulations (2x2x20 mm conductive column, 100,000 insulative particles of 60 μm diameter) and included a charge generation model. They showed that image charges induced onto the channel walls have a profound effect on the spatial

distribution of particles, and subsequently their degree of triboelectrification. Sufficiently charged particles are unable to escape the attraction of the image charges, and consequently experience charging due to repeated wall collisions. For dense particle loads, the interaction between a particle and the image charges of other particles should also be included [12]. Grosshans and Papalexandris (2017) [54] performed direct numerical simulations of charging in particle-laden turbulent channel flows. In their study, it was observed that both particle charging and migration from the walls was strongly promoted by increasing particle loadings as well as increasing particle Stokes numbers, Stk. For example, when $Stk = 2$, a low particle loading (40,000 particles) resulted in charge build-up at the walls but limited charge transport into the bulk of channel due to low particle migration. On the other hand, a large particle loading (400,000 particles) allowed the charge to migrate away from the walls due to inter-particle charge diffusion [54].

7.3.2. Two-fluid models

While CFD-DEM modeling is well established to estimate the electrostatic forces and its effects in small-scale gas-solid flow systems, their resource cost prohibits usage in industrial scale systems. As such, Two-Fluid Models (TFM) have been developed to model large-scale, poly-dispersed gas-solid flows. The solid phase transport equations in TFM are described in a similar fashion to the gas phase, with the addition of the particle pressure p_s and the electrostatic force term $\boldsymbol{F}_{el}$ [71]:

$$\frac{\partial}{\partial t}(\alpha_s \rho_s) + \nabla \cdot (\alpha_s \rho_s \mathbf{U}_s) = 0 \qquad 7\text{-}25$$

$$\frac{\partial}{\partial t}(\alpha_s \rho_s \mathbf{U}_s) + \nabla \cdot (\alpha_s \rho_s \mathbf{U}_s \otimes \mathbf{U}_s) = \nabla \cdot \tau_s - \alpha_s \nabla p - \nabla p_s + \alpha_s \rho_s \mathbf{g} - \mathbf{M}_{sg} + \mathbf{F}_{el} \qquad 7\text{-}26$$

The solid-phase properties such as the particle pressure and viscosity, which are needed to calculate the stress tensor, are determined using the kinetic theory of granular flow [72–74]. The electrostatic force is now determined using Eq. 7-23 with the electric potential determined from the Poisson equation (Eq. 7-24).

TFM schemes cannot be used to predict the charge of each individual particle, but the averaged charge over a cell volume. Thus, the rate of charge transfer between elements/volumes is determined using the charge transport equation [72]:

$$\frac{\partial}{\partial t}(\alpha_s \rho_s \langle q \rangle) + \nabla \cdot (\alpha_s \rho_s \langle \mathbf{c} q \rangle) = m_s \mathbb{C}(q) \qquad 7\text{-}27$$

where $\langle q \rangle$ is the mean particle charge density, and $\mathbb{C}(q)$ is the mean collisional rate of change of particle charge due to binary inter-particle collisions [56], which is obtained from the solution of collision integrals as explained by Ray et. al. (2019, 2020) [56,58]. Expressions for $\mathbb{C}(q)$ were also derived by other researchers for monodisperse [55,59] and bidisperse cases [75]. The second term on the left-hand side of Eq. 7-27 includes the contribution due to advection as well as self- (kinetic) diffusion, which was derived by making assumptions on higher order moments [55,56,58,59]. This term was shown to be significant in dilute flows [59] and was also required to predict the wall fouling thickness and charge magnitudes seen in experiments [56].

Ray et al. (2019) [56] performed 2D TFM simulations of a mono-dispersed gas-solid fluidized bed (0.1x1.27 m conductive column) using an established electrostatic charge transfer model and compared the results to past experimental findings by Sowinski et al. (2015) [76] of a pilot-scale polyethylene fluidized bed. Their model predicted that larger particles have lower proclivity of wall fouling and that polyethylene particles larger than 1 mm would not stick to the wall. Their simulations also validated the order of magnitude of charge in different regions of the bed (at the wall and away from it). For wall fouling to occur, the electrostatic force that drives a particle towards the wall must produce enough frictional resistance to counteract the influence of other forces (gravitational, drag, inter-particle friction) acting on it. With this in mind, simulations can be used to predict the time needed for enough charge to build up in the system when wall fouling starts occurring. Other works [55,57–59,75] have used idealized nondimensional domains to illustrate possibilities of their models but have not been utilized to validate or predict experimental observations.

Although TFM is considerably cheaper than DEM methods and can simulate large scale models much more efficiently, there are several limitations which need to be considered. In scenarios with wall fouling, the current TFM stress models are numerically unstable and unreliable to simulate stationary particle layers. Also, in polydisperse cases, there is a limit to how many separate size bins can be simulated. Each of these bins need their individual transport equations for charge, mass, and momentum. A single transport equation for every physical property which considers a continuous size distribution would be ideal, although this would be extremely cumbersome to

model. In this regard, DEM is convenient since every particle can have different individual properties. This is essential when modeling bipolar charge diffusion or considering interaction between particles of opposite charge. The latter cannot be simulated in a single cell/element using TFM. Knowledge of charge variance and inclusion of agglomeration and breakage kernels can assist but uncertainties will still persist.

7.4. Considerations for future electrostatic models

Significant progress was made in recent years for modelling charge transfer between insulators, which proved beneficial in their application in gas-solid flow simulations. Nonetheless, the complex nature of triboelectrification is still being studied, and the current charging models must evolve as new discoveries are made. As such, this section will explore charging behaviors and relevant parameters that may need to be added to improve the current electrostatic models for gas-solid flow simulations.

7.4.1. Finite duration of contact during impacts

Eulerian and Lagrangian models used for simulating triboelectrification assume that the duration of contact between particles is infinitesimally small. Thus, impulse exchange is instantaneous and is dependent on the incident relative velocity vector and the coefficient of restitution. The impact dynamics are then dictated by normal reaction forces and there is no dependence on the body force or cohesive forces at the point of contact. Recently, Klahn et. al. (2020) [77] have shown that electrostatic and van der Waals forces alter the impact dynamics and lead to agglomeration of particles and layering on a wall surface. Depending on the net impulse that is exchanged, the particles may undergo anything between a perfectly elastic to a perfectly inelastic collision as has been displayed in Figure 7-5. The first series of snapshots (Figure 7-5) at the top show the collision outcome between two perfectly elastic particles but with a substantial magnitude of van der Waals force. This is similar to the last (bottom) case where cohesive forces are absent but the partly inelastic nature of contact leads to similar result. The case in the middle shows the effect of combining both cohesive interaction and inelastic impact ($0<e<1$) which leads to a perfectly inelastic outcome. Replacing the van der Waals force with electrostatic forces will have similar implications if the latter is attractive. If the particles electrically repulse each other, it will lead to other intriguing outcomes, where the particles may not make contact at all. Hence, this work has

shown that resolving the contact dynamics and following its temporal evolution is crucial to allow large interparticle forces to manifest.

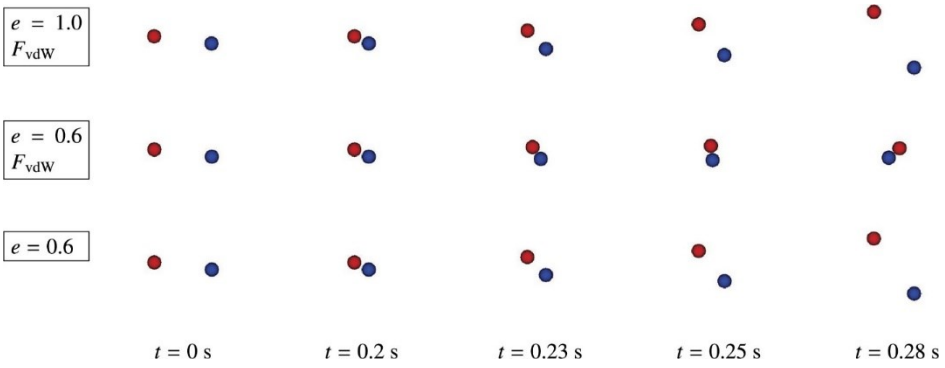

Figure 7-5: Variation in collision outcome with coefficient of restitution [77].

Particularly important in fluidized beds is the kinetic behavior of particles near the wall of the fluidization column with a high enough charge to stick and initiate wall layer formation. These particles are expected to have no granular energy which lends stability to the static layer, as shown in Figure 7-6. In recent simulations [32,56], this was not possible because the particles did not come to a complete rest in any situation. To understand the implications of this shortcoming, one could imagine throwing a highly magnetized disk ($e < 1$) at a ferromagnetic wall. Without body forces contributing to the net impulse change during contact, the disk would bounce off the wall, get attracted to it again and keep repeating this process with decaying impact velocity, but will never be fully stationary.

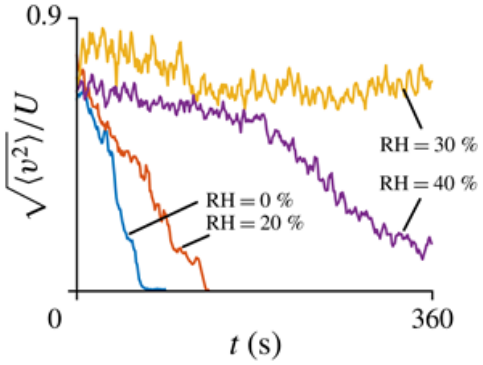

Figure 7-6: Residual particle velocity at the wall of a fluidized bed with relative humidity [32]

In Eulerian simulations, a charged static layer should not have any granular energy. This layer should not be charged further by the wall since no diffusion (since there is no granular energy) or advection is present. In the two-fluid model implementations used in Ray et al. (2019) [56], a stationary wall acts as a sink of granular energy, but it does not dissipate it completely. The surrounding gas and solid phases will act as sources of this energy and thus the layer will have intermittent contact with the wall and a certain residual velocity will always remain. This was also observed in the CFD-DEM model implementation used by Sippola et al. (2018) [32], as shown in Figure 7-7. This can be remedied if the momentum and kinetic energy fluxes at the boundaries consider finite duration of contact and include the body force in determining the total change of impulse.

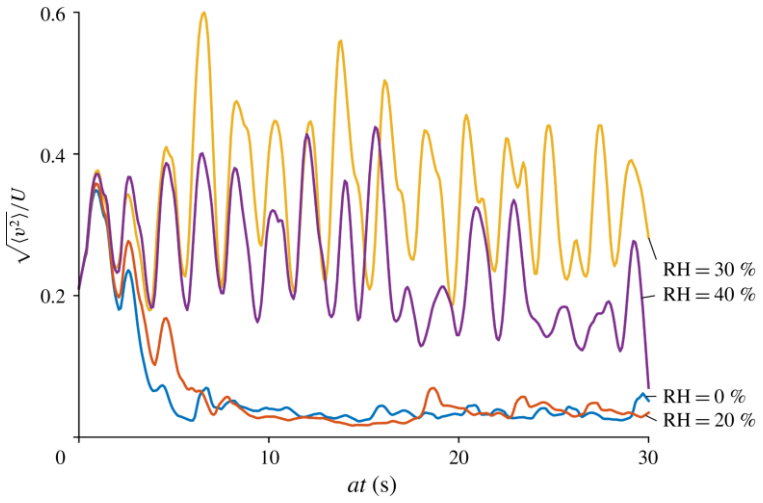

Figure 7-7: Temporal variation of residual velocity at the wall (simulation results for different relative humidity) [32]

The finite duration of contact can be calculated using the Hertzian model, which approximates it to be a function of the normal component of incident velocity. The collision integrals can then be evaluated in a manner similar to what was done for deriving charge diffusion coefficients [55,56]. This is an essential step that needs closure before researchers proceed with more simulations and predictions. One may be tempted to parameterize the value of e as a function of the relative body force to reproduce agreeable results. However, its utility would be limited, and a general interaction model as discussed above would be more beneficial.

7.4.2. Nonuniform surface charge density

The charge on an insulator surface is not distributed uniformly even in the absence of external polarization (like conductors). Baytekin et al. (2011) [24] showed that while an insulative surface can have a net positive or net negative charge, it supports a random *mosaic* of oppositely charged nanoscopic regions. Even when the total charge is near saturation, the insulator cannot be expected to possess a uniform surface charge density due to physical and chemical inhomogeneities discussed earlier. Thus, for a neutral particle, only the patch that comes in contact may gain or lose charge. Then, when this particle undergoes a second impact, a different region may make contact and exchange charge. Alternatively, the same patch, which was charged during the first impact, may also be in partial contact with the surface and may gain or lose charge to some degree. Based on these assumptions, Grosshans et al. (2017) [78] suggested a model where the particle surface was divided into a number of discrete subregions. Each of the subregions could then reach the same saturation charge density. This model was used to explain the scatter observed in experimental results by Matsuyama and Yamamoto (1995) [79], where it was shown how the non-uniform model could lead to more variation in charge transferred in second and successive impacts (Figure 7-8).

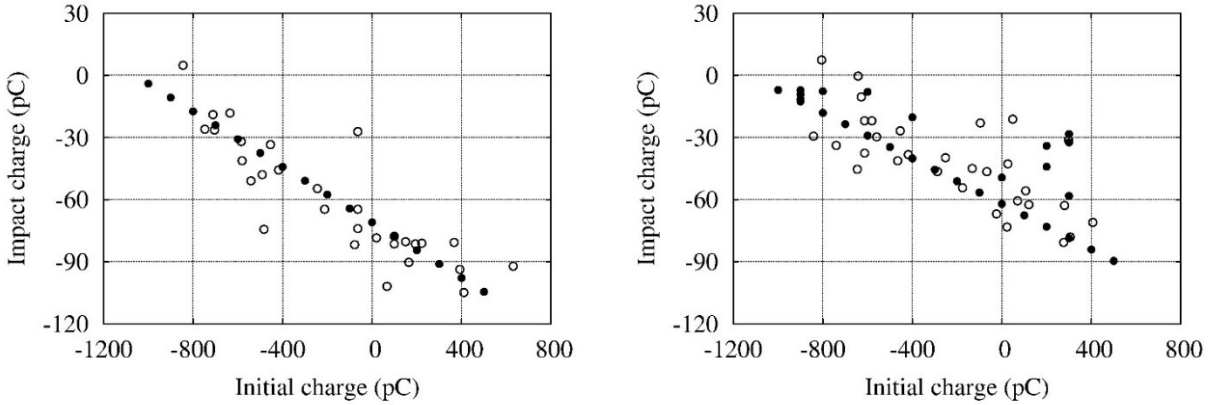

Figure 7-8: Non-uniform charge transfer as a function of initial charge (The open circles are experimental results of Matsuyama and Yamamoto [79], and the solid circles are simulation predictions by Grosshans et al. [78]).

The model by Grosshans et al. [78] was then used to demonstrate the non-monotonic rate of charge transfer in successive impacts between a PTFE particle and a brass plate. They found that if the number of discrete regions was greater than 100, then the particles reached the same asymptotic

saturated charge limit of the uniform charging model (Figure 7-9(a)). However, during successive impacts, the charge transfer rate was not uniform. There are quite a few impacts where no charge was transferred at all (Figure 7-9(b)).

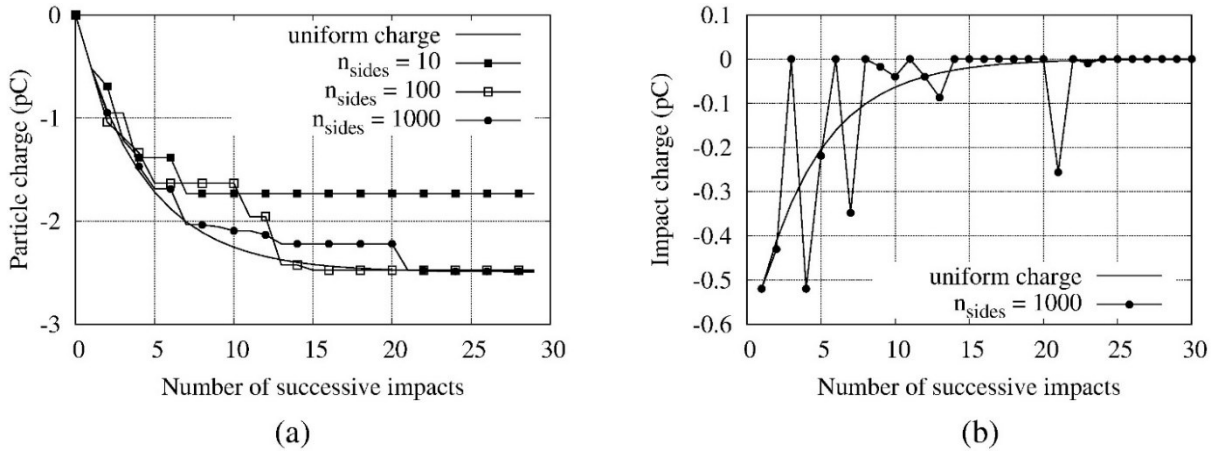

Figure 7-9: Evolution of particle charge due to non-uniform charging (copied from [78]).

In realistic situations in dense fluidized beds, there are several hundred collisions every second which would diminish the non-uniformity of the surface charge. Thus, the mean charging rate may be expected to be similar to that derived from the uniform surface charge assumption. In Eulerian models, the averaged quantities are derived from the interaction of hundreds/thousands of particles. Here also the large number of collisions would imply that even if the order of particle charge is less than saturation, the averaged behavior of an element/volume would be similar to if all the particles had uniform charge. CFD-DEM simulations of small-scale systems could verify these conjectures.

In pneumatic conveying, the dense flow assumptions would not be valid since the particles may not encounter many collisions and their charge may be significantly lower than saturation even at the outlet(s). Here the use of CFD-DEM models in conjunction with the non-uniform surface charge model could be required to simulate the entire system. In such scenarios, the rotational motion of the particles must also be considered as it could dictate the charge distribution on the particle surface and the rotational momentum itself may be governed by the dipole moment of the particles.

7.4.3. Bipolar charging of granular materials

Granular materials involved in gas-solid flows can range between being complex multi-component mixtures, which is the case in many fluidized bed reactors, to being single-component materials of similar structures and sizes generally used in controlled experimental studies. Bipolar charging is possible in all granular materials due to differences in chemical compositions, physical and dielectric properties, and presence of impurities. Numerous triboelectrification studies have also shown that the direction of charge transfer is directly affected by differences in particle size [48,80–83]. It is unclear whether the effect of particle size is related to the dipole amplification mechanism discussed above. Especially in gas-solid flow systems with particles of a single material composition, the electric field effect alone cannot explain the observed size-dependent bipolar charging behavior [84]. Most of these studies have shown that, for a variety of granular materials, the smaller particles in a single-component system charge negatively while the larger particles charge positively. Although the net charge in the system would remain close to neutral, the segregation of particle charge based on particle-size can have a strong impact in gas-solid flows. Particularly in gas-solid fluidized beds, fine particles can leave the system through elutriation, which would alter the net charge left behind in the bed. Thus, bipolar charging due to particle-size differences must be considered in future model implementations.

It should be noted that the direction of charge transfer is not consistent with respect to the size difference for all granular materials. For example, when performing fluidization tests with the same metallic column on two different commercial polyethylene resins, Sowinski et al. (2010) [76] reported that the fines of one type of polyethylene resin had acquired a positive charge, whereas Song et al. (2017) [85] found the fines of the other acquired negative charge. Hence, the factors that would affect the direction and magnitude of charging based on particle-size differences need to be determined experimentally for any given granular material.

To implement the effect of particle-size distribution on charging, one option is to use a probability density function (PDF) of the particle charge measured through experiments. A PDF can be created following any kind of particle charging process by using an electrostatic separator to collect particles of different polarities and charge magnitudes into a series of Faraday cages. Provided that the charge data of the granular material was collected at the appropriate operating conditions, the PDF would help account for all the unknown factors that would influence bipolar charging in the

specified system. As an example, Konopka et. al. (2020) [86] created PDFs using an electrostatic separator to present the charge distribution of polyethylene particles from their particle-particle collision experiments, as shown in Figure 7-10. They found that the particles had heterogenous tribocharging properties which promoted bipolar charging, though it was not confirmed whether the behavior was affected by differences in particle size. Salama et al. (2013) [87] also used an electrostatic separator and reported a bipolar charge distribution on the polyethylene particles that fouled their fluidized bed column wall. This observation led to the theory of formation of layers of alternating polarity on the wall [88]. The sizes of the particles collected in each Faraday cage after the separator was also measured, but no consistent difference was found between them. If some correlation would have been observed here, then a conclusive comment on the dependence on particle size could have been made. In any case, it could at least be said that in a fluidized bed, particles of similar sizes can possess charges of opposite polarity although there could be a size dependence for outcomes of discrete collisions.

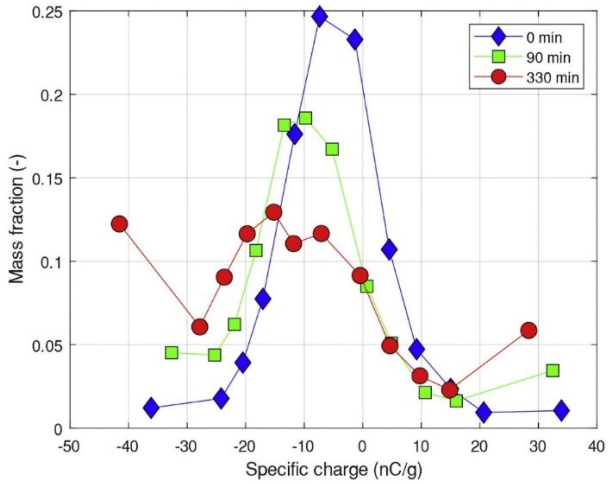

Figure 7-10: Temporal evolution of charge in a box coated with PE particles (copied from [86]).

7.4.3.1. Bipolar charging in simulations

In fluidized beds the column wall acts as a source for charging the particles. As the particles gain charge, the electric potential grows inside the bed and counteracts the further diffusion of charge. Steady state should be attained when the electric current due to gradient of charge and gradient of electric potential balance each other. This is summarized by Eq. 7-28 which is obtained by assuming steady-state conditions with no advective transport of charge in a general monodisperse scenario. However, at any location during fluidization, charge is continually being exchanged and

some amount of advection (time-averaged advection may be constant) is always present with the exception at the wall if a stable static layer forms. This will cause oscillations in charge at any location. In a region of small gradient of charge, a sudden large oscillation of electric field can even change the polarity for a certain period.

$$K_q \nabla^2 q + K_e \nabla^2 V \approx 0 \qquad 7\text{-}28$$

In their CFD-DEM simulations, Kolehmainen et. al. (2017) [31] and Sippola et. al. (2018) [32] have discussed some observations caused by the long-range interaction of the electric field. In their simulations with monodisperse particles, they found that some amount of bipolar charging is always present. This tendency varies with the equilibrium charge-to-mass ratio (Figure 7-11) as well as the charging acceleration factor (Figure 7-12). The former can lead to high electric fields in certain regions producing temporal and spatial oscillations of charge while the latter may produce fluctuations at rates faster than the relaxation time of the system. The acceleration factor was used, not for predicting the actual rate of evolution of bed charge, but to reduce the simulation time consumed to reach equilibrium [31,32]. If this factor is reduced to that which mimics the actual electrification rate in the fluidized bed, the volume of regions in the bed or the fraction of particles having opposite polarity may diminish and become negligible, even for high charge-to-mass ratios. This attenuation is illustrated in Figure 7-12.

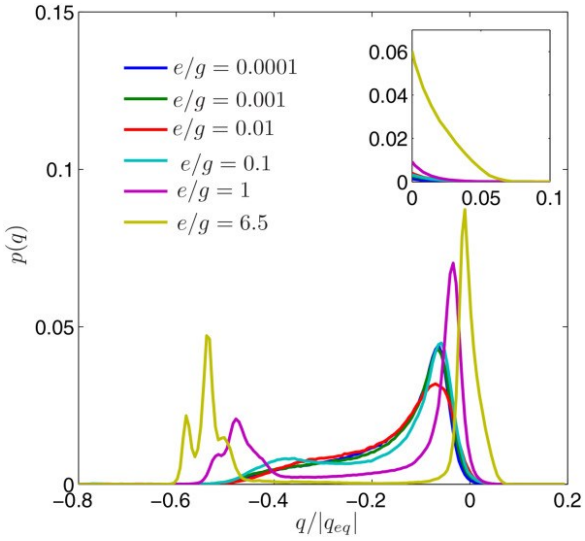

Figure 7-11: Distribution of charge for different equilibrium charge-to-mass ratios [31] (a charging acceleration factor of 12.86 was used).

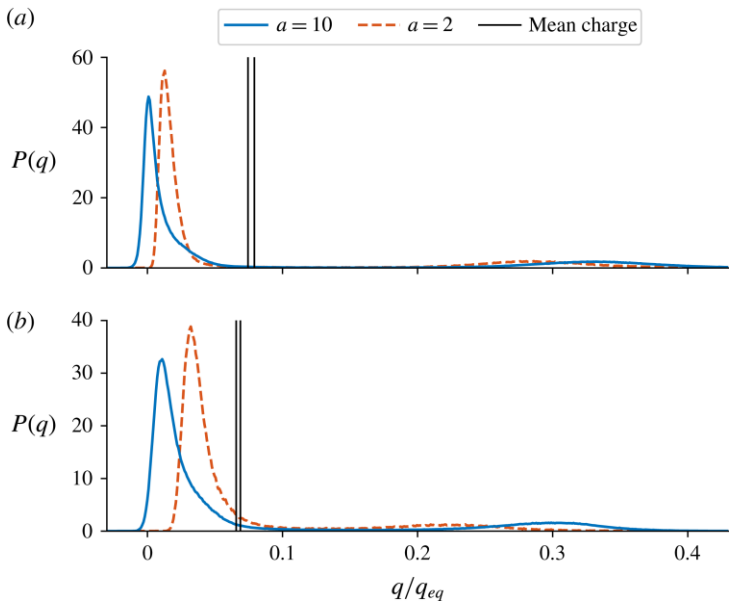

Figure 7-12: Distribution of charge for different equilibrium charge-to-mass ratios a) e/g = 8, b) e/g = 4, and charging acceleration factors *a* [32].

In our earlier work in this area we observed bipolar charging in 1-D non-hydrodynamic bidisperse simulations [58]. This occurred, whenever the two particle sizes were different regardless of the relative volume fraction. This was explained using Eq. 7-29 which is an analogous version of Eq. 7-30, but for bidisperse case. Here the gradients of charge of both the particle phases, where each phase represent a particle size, as well as the electric potential are competing. Depending on the final solution of this equation, one of the charge gradients can be large enough in magnitude so that at a certain location there is a reversal of polarity. If the Poisson equation is used, Eq. 7-29 can be written as Eq. 7-30. Here the phase having the larger diffusion coefficient will lead the electrification process, but it will produce a steeper gradient for the other phase and can reverse its polarity. This is shown in Figure 7-13, where both the phases are of the same material but different sizes and hence different saturation charge. Near the wall region, both phases (Figure 7-13(a)) have the same polarity as that of the net charge (volume averaged charge) in the bed (Figure 7-13(b)). However, there is crossover of polarity for phase 2 (Figure 7-13(c)). This was also seen when the volume fraction was varied [58].

$$K_{qi}\nabla^2 q_i + K_{qj}\nabla^2 q_i + K_e\nabla^2 V \approx 0 \qquad 7\text{-}29$$

$$K_{qi}\nabla^2 q_i + K_{qj}\nabla^2 q_i \approx K_{eq}\left(\alpha_i q_i + \alpha_j q_j\right) \qquad 7\text{-}30$$

The result of a laboratory scale simulation would be different especially since the hydrodynamics would be playing a role as well. The inter-particle charging model itself could be inaccurate but the overall model could still summarize to a form similar to Eqs. 7-29 and 7-30 and the same mathematical arguments would hold. Using this model, no bipolarity was observed when same properties were used for both the phases, thus emulating a monodisperse case. Thus, the acceleration factor along with the hydrodynamics was invoking bipolarity in the monodisperse cases discussed before.

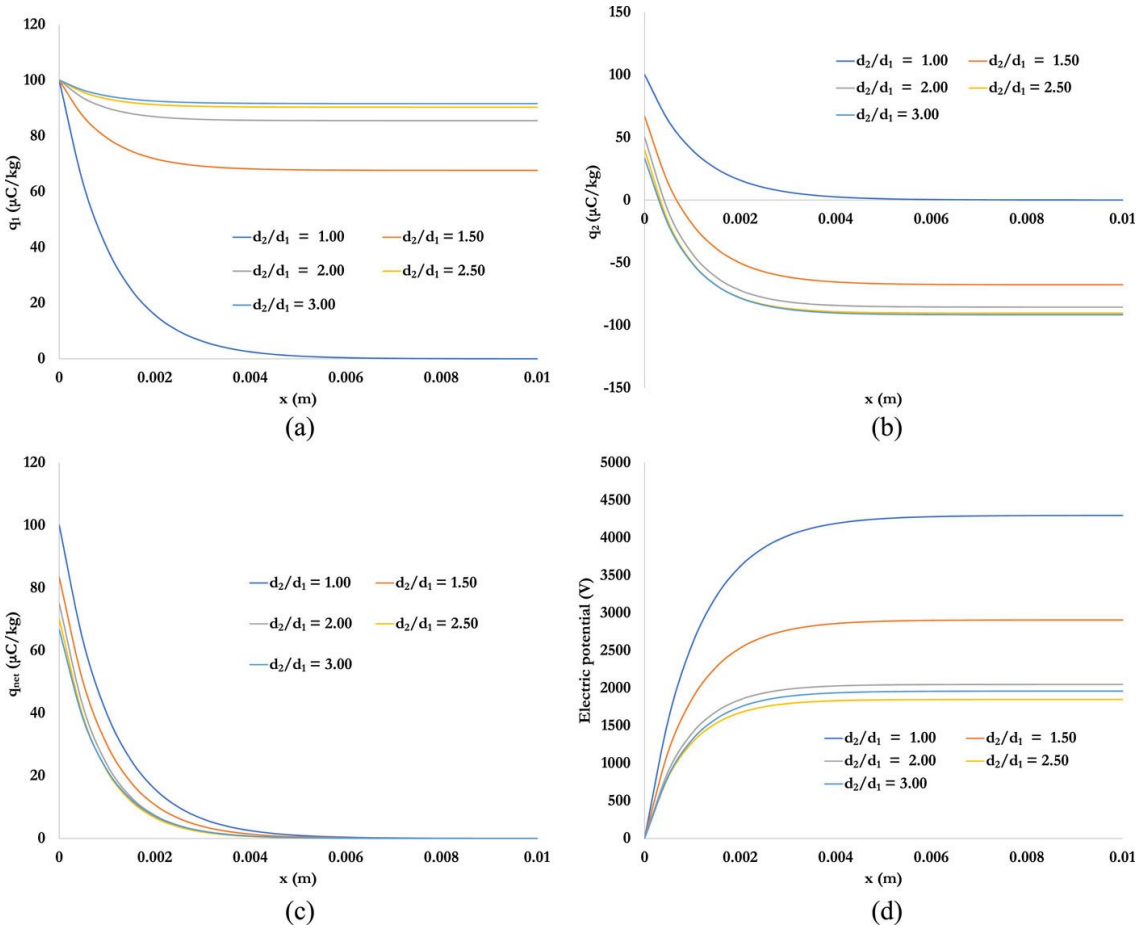

Figure 7-13: Bipolar charging when diameter ratio is varied (volume fraction = 0.3 for both particle phases) [58].

7.4.4. Operating conditions of gas-solid flow systems

The hydrodynamics of a gas-solid flow system both affects and is affected by triboelectrification. Particularly in gas-solid fluidization, maintaining the hydrodynamics in the fluidized bed is an important aspect of the process where rigorous mixing is generally desired. The inter-particle and

particle-wall collisions brought about by the particle mixing could result in electrostatic charging, and in turn the bed hydrodynamics may change due to agglomeration, wall fouling, and even due to changes in gas bubble behavior [89,90]. Parameters such as temperature, pressure, moisture content (or relative humidity), gas velocity and particle size distribution are known to have significant effects on fluidized bed hydrodynamics, which in turn impacts electrostatic charging [6,91–93]. At the same time, particle size and impact velocity are already considered in charging models, while parameters such as moisture content and temperature are currently not considered even though they are known to directly affect charge transfer between insulators [19]. The operating conditions and factors that impact both the hydrodynamics and triboelectrification in gas-solid flow systems should either be explicitly included in the charge transfer models or assumed to be sufficiently handled by the hydrodynamic models. For example, the relative humidity in a gas-solid fluidized bed is usually not included as a parameter in CFD models, even though it is known to have a complex relationship with particle charging as well as bed hydrodynamics [32,94]. If the relative humidity can vary in the gas-solid flow system, then its impact on the degree of triboelectrification should be considered in both the charging and the hydrodynamic model.

7.5. Summary and Outlook

Charging models are the most important components in the development of CFD models for simulating triboelectrification of insulative materials. The mechanisms explaining these models have undergone substantial deliberations and modifications over the last several decades which started in favor of electron transfer but is currently inclined more towards ion transfer. The charging behavior of insulative particles; however, follows a general trend with exponentially decaying growth rate tending to an asymptotic value known as the saturation charge. The saturation value which was initially thought to be dependent on the effective work function difference, is currently said to be dictated by the dielectric properties of the surrounding medium and/or that of the particle material. The surface area of contact is currently estimated using the Hertzian impact model and considers the physical properties of the colliding materials and the normal component of the impact velocity. However, this estimation needs to be corrected to also consider colliding materials' surface roughness as well as the tangential component of the impact velocity, which is connected to sliding and/or rolling contacts.

CFD-DEM models which are most used for simulations of triboelectrification in gas-solid flow systems have considerably evolved to estimate the electric field and electrostatic forces with improved accuracy and efficiency and have also incorporated sustained contact of particles with walls and other particles. The latter is particularly significant in wall fouling simulations where particles can become stationary and form agglomerates with other particles. CFD-DEM models treat the fluid as a continuous phase and the particle phase as a Lagrangian phase. These simulations are computationally expensive for particle systems in industrial systems and for simulating small laboratory systems for longer durations. Hence, most of the results reported using this method have been generated using large charge acceleration factors which reduce the equilibration time by two or three orders.

Eulerian models can model much larger systems with fewer resources and are currently gaining interest due to this reason. Some researchers have derived Eulerian transport equations for both monodisperse and bi-disperse particle systems and have used these to predict experimental results as well. Like CFD-DEM simulations, sustained contact needs to be modeled at least for particle-wall interactions for obtaining stable wall fouling results. Continued development of Eulerian models is needed to simulate bi-disperse and poly-disperse gas-solid flows to predict the charging behavior in complex, multi-component industrial-scale systems.

The models for electrostatic charging in gas-solid flows has evolved over the years. Nonetheless, as highlighted in this review, there are many aspects that need further investigation for both electrostatic charging and its implementation into CFD models. For example, operating conditions such as temperature, pressure, and moisture content are crucial factors that impact both the hydrodynamics and triboelectrification in gas-solid flow systems. These factors will need to be considered in charging as well as hydrodynamic models. Finite duration of impact and sustained contact should be modeled in all triboelectric simulations if wall fouling and particle agglomeration are to be accurately predicted and their effect on bed hydrodynamics is to be observed. The need for monitoring the exact charge distribution on a particle depends on the application and may be essential in dilute flows with small residence times. Effort needs to be exerted particularly in finding suitable expressions for modeling bipolar charging between particles made of the same material since it has been observed in all kinds of systems and scenarios. In this regard, the dipole amplification mechanism has given one of the possibilities for explaining

this phenomenon, although it remains unclear whether it plays a direct role in the size-dependent bipolar charging behavior observed in granular materials.

References

[1] W. Kleber, B. Makin, Triboelectric powder coating: A practical approach for industrial use, Particulate Science and Technology. 16 (1998) 43–53. https://doi.org/10.1080/02726359808906783.

[2] A. Jaworek, A.T. Sobczyk, Electrospraying route to nanotechnology: An overview, Journal of Electrostatics. 66 (2008) 197–219. https://doi.org/10.1016/j.elstat.2007.10.001.

[3] R.O. Hagerty, M.E. Muhle, A.K. Agapiou, C.-T.I. Kuo, M.G. Goode, F.D. Hussein, R.B. Pannell, J.F. Szul, Method for Controlling Sheeting in Gas Phase Reactors, 2005/0148742 A1, 2011.

[4] Y. Pu, M. Mazumder, C. Cooney, Effects of electrostatic charging on pharmaceutical powder blending homogeneity, Journal of Pharmaceutical Sciences. 98 (2009) 2412–2421. https://doi.org/10.1002/jps.21595.

[5] M. Nifuku, H. Katoh, A study on the static electrification of powders during pneumatic transportation and the ignition of dust cloud, Powder Technology. 135 (2003) 234–242. https://doi.org/10.1016/S0032-5910(03)00163-3.

[6] P. Mehrani, M. Murtomaa, D.J. Lacks, An overview of advances in understanding electrostatic charge buildup in gas-solid fluidized beds, Journal of Electrostatics. 87 (2017) 64–78. https://doi.org/10.1016/j.elstat.2017.03.005.

[7] W. Kaialy, A review of factors affecting electrostatic charging of pharmaceuticals and adhesive mixtures for inhalation, International Journal of Pharmaceutics. 503 (2016) 262–276. https://doi.org/10.1016/j.ijpharm.2016.01.076.

[8] G.E. Klinzing, A review of pneumatic conveying status, advances and projections, Powder Technology. 333 (2018) 78–90. https://doi.org/10.1016/j.powtec.2018.04.012.

[9] C. Pounder, The quest for a charging mechanism to the end of the 19th century, Journal of Electrostatics. 3 (1977) 389–394. https://doi.org/10.1016/0304-3886(77)90119-X.

[10] D.J. Lacks, The Unpredictability of Electrostatic Charging, Angewandte Chemie International Edition. 51 (2012) 6822–6823. https://doi.org/10.1002/anie.201202896.

[11] D.J. Lacks, T. Shinbrot, Long-standing and unresolved issues in triboelectric charging, Nature Reviews Chemistry. 3 (2019) 465–476. https://doi.org/10.1038/s41570-019-0115-1.

[12] M.W. Korevaar, J.T. Padding, M.A. Van der Hoef, J.A.M. Kuipers, Integrated DEM-CFD modeling of the contact charging of pneumatically conveyed powders, Powder Technology. 258 (2014) 144–156. https://doi.org/10.1016/j.powtec.2014.03.020.

[13] K. Tanoue, H. Tanaka, H. Kitano, H. Masuda, Numerical simulation of tribo-electrification of particles in a gas–solids two-phase flow, Powder Technology. 118 (2001) 121–129. https://doi.org/10.1016/S0032-5910(01)00302-3.

[14] M.D. Hogue, C.I. Calle, P.S. Weitzman, D.R. Curry, Calculating the trajectories of triboelectrically charged particles using Discrete Element Modeling (DEM), Journal of Electrostatics. 66 (2008) 32–38. https://doi.org/10.1016/j.elstat.2007.08.007.

[15] S. Matsusaka, H. Masuda, Electrostatics of particles, Advanced Powder Technology. 14 (2003) 143–166. https://doi.org/10.1163/156855203763593958.

[16] S. Watano, Mechanism and control of electrification in pneumatic conveying of powders, in: Chemical Engineering Science, Pergamon, 2006: pp. 2271–2278. https://doi.org/10.1016/j.ces.2005.05.008.

[17] S. Matsusaka, M. Ghadiri, H. Masuda, Electrification of an elastic sphere by repeated impacts on a metal plate, Journal of Physics D: Applied Physics. 33 (2000) 2311–2319. https://doi.org/10.1088/0022-3727/33/18/316.
[18] F. Chowdhury, A. Sowinski, M. Ray, A. Passalacqua, P. Mehrani, Charge generation and saturation on polymer particles due to single and repeated particle-metal contacts, Journal of Electrostatics. 91 (2018) 9–15. https://doi.org/10.1016/j.elstat.2017.11.004.
[19] S. Matsusaka, H. Maruyama, T. Matsuyama, M. Ghadiri, Triboelectric charging of powders: A review, Chemical Engineering Science. 65 (2010) 5781–5807. https://doi.org/10.1016/j.ces.2010.07.005.
[20] L. Cheng, S.L. Soo, Charging of Dust Particles by Impact, Journal of Applied Physics. 41 (1970) 585–591. https://doi.org/10.1063/1.1658717.
[21] B.N. Cole, M.R. Baum, F.R. Mobbs, An Investigation of Electrostatic Charging Effects in High-Speed Gas-Solids Pipe Flows, Proceedings of the Institution of Mechanical Engineers, Conference Proceedings. 184 (1969) 77–83. https://doi.org/10.1243/PIME_CONF_1969_184_082_02.
[22] H. Masuda, T. Komatsu, K. Iinoya, The static electrification of particles in gas-solids pipe flow, AIChE Journal. 22 (1976) 558–564. https://doi.org/10.1002/aic.690220320.
[23] L.S.S. McCarty, G.M.M. Whitesides, Electrostatic Charging Due to Separation of Ions at Interfaces: Contact Electrification of Ionic Electrets, Angewandte Chemie International Edition. 47 (2008) 2188–2207. https://doi.org/10.1002/anie.200701812.
[24] H.T. Baytekin, A.Z. Patashinski, M. Branicki, B. Baytekin, S. Soh, B.A. Grzybowski, The mosaic of surface charge in contact electrification, Science. 333 (2011) 308–312. https://doi.org/10.1126/science.1201512.
[25] F. Chowdhury, B. Elchamaa, M. Ray, A. Sowinski, A. Passalacqua, P. Mehrani, Apparatus design for measuring electrostatic charge transfer due to particle-particle collisions, Powder Technology. 361 (2020) 860–866. https://doi.org/10.1016/j.powtec.2019.11.013.
[26] W.R. Harper, The Volta Effect as a Cause of Static Electrification, Proceedings of the Royal Society A: Mathematical, Physical and Engineering Sciences. 205 (1951) 83–103. https://doi.org/10.1098/rspa.1951.0019.
[27] W.R. Harper, Contact and Frictional Electrification, 1967.
[28] J. Lowell, A.C. Rose-Innes, Contact electrification, Advances in Physics. 29 (1980) 947–1023. https://doi.org/10.1080/00018738000101466.
[29] J. Lowell, Contact electrification of metals, Journal of Physics D: Applied Physics. 8 (1975) 53.
[30] J.C.C. Laurentie, P. Traoré, L. Dascalescu, Discrete element modeling of triboelectric charging of insulating materials in vibrated granular beds, Journal of Electrostatics. 71 (2013) 951–957. https://doi.org/10.1016/j.elstat.2013.08.001.
[31] J. Kolehmainen, A. Ozel, C.M. Boyce, S. Sundaresan, Triboelectric charging of monodisperse particles in fluidized beds, AIChE Journal. 63 (2017) 1872–1891. https://doi.org/10.1002/aic.15541.
[32] P. Sippola, J. Kolehmainen, A. Ozel, X. Liu, P. Saarenrinne, S. Sundaresan, Experimental and numerical study of wall layer development in a tribocharged fluidized bed, Journal of Fluid Mechanics. 849 (2018) 860–884. https://doi.org/10.1017/jfm.2018.412.
[33] C. Pei, C.-Y. Wu, M. Adams, DEM-CFD analysis of contact electrification and electrostatic interactions during fluidization, Powder Technology. 304 (2016) 208–217. https://doi.org/10.1016/j.powtec.2016.08.030.
[34] T. Matsuyama, H. Yamamoto, Charge relaxation process dominates contact charging of a particle in atmospheric conditions, Journal of Physics D: Applied Physics. 28 (1995) 2418–2423. https://doi.org/10.1088/0022-3727/28/12/005.

[35] P. Jiang, H. Bi, S.-C. Liang, L.-S. Fan, Hydrodynamic behavior of circulating fluidized bed with polymeric particles, AIChE Journal. 40 (1994) 193–206. https://doi.org/10.1002/aic.690400202.
[36] Timoshenko, Theory of elasticity, McGraw-Hill, 1987.
[37] J. Yao, S. Cong, Y. Zhao, C.H. Wang, Z. Ji, Investigation of granular surface roughness effect on electrostatic charge generation, Advanced Powder Technology. 28 (2017) 2003–2014. https://doi.org/10.1016/j.apt.2017.04.001.
[38] S. Karner, M. Maier, E. Littringer, N.A. Urbanetz, Surface roughness effects on the tribo-charging and mixing homogeneity of adhesive mixtures used in dry powder inhalers, Powder Technology. 264 (2014) 544–549. https://doi.org/10.1016/j.powtec.2014.03.040.
[39] J.C. Angus, I. Greber, Tribo-electric charging of dielectric solids of identical composition, Journal of Applied Physics. 123 (2018) 174102. https://doi.org/10.1063/1.5024742.
[40] Y. Zhao, F. Zhou, J. Yao, Z. Ji, Electrostatic charging of single granules by repeated sliding along inclined metal plates, Journal of Electrostatics. 87 (2017) 140–149. https://doi.org/10.1016/j.elstat.2017.04.002.
[41] A. Ema, D. Yasuda, K. Tanoue, H. Masuda, Tribo-charge and rebound characteristics of particles impact on inclined or rotating metal target, Powder Technology. 135–136 (2003) 2–13. https://doi.org/10.1016/S0032-5910(03)00153-0.
[42] J. Peltonen, M. Murtomaa, J. Salonen, Measuring electrostatic charging of powders on-line during surface adhesion, Journal of Electrostatics. 93 (2018) 53–57.
[43] J. Wu, J. Yao, Y. Zhao, The effects of granular velocity and shape factors on the generation of polymer-metal electrostatic charge, Journal of Electrostatics. 82 (2016) 22–28. https://doi.org/10.1016/j.elstat.2016.05.001.
[44] P.M. Ireland, Triboelectrification of particulate flows on surfaces: Part II—Mechanisms and models, Powder Technology. 198 (2010) 189–198. https://doi.org/10.1016/j.powtec.2009.11.008.
[45] P.M. Ireland, Triboelectrification of particulate flows on surfaces: Part I — Experiments, Powder Technology. 198 (2010) 189–198. https://doi.org/10.1016/j.powtec.2009.11.017.
[46] J. Lowell, The effect of an electric field on contact electrification, Journal of Physics D: Applied Physics. 14 (1981) 1513.
[47] J.A. Wiles, M. Fialkowski, M.R. Radowski, G.M. Whitesides, B.A. Grzybowski, Effects of surface modification and moisture on the rates of charge transfer between metals and organic materials, Journal of Physical Chemistry B. 108 (2004) 20296–20302. https://doi.org/10.1021/jp0457904.
[48] S.R. Waitukaitis, V. Lee, J.M. Pierson, S.L. Forman, H.M. Jaeger, Size-dependent same-material tribocharging in insulating grains, Physical Review Letters. 112 (2014) 1–5. https://doi.org/10.1103/PhysRevLett.112.218001.
[49] M. Sow, R. Widenor, A. Kumar, S.W. Lee, D.J. Lacks, R.M. Sankaran, Strain-Induced Reversal of Charge Transfer in Contact Electrification, Angewandte Chemie International Edition. 51 (2012) 2695–2697. https://doi.org/10.1002/anie.201107256.
[50] A.F. Diaz, D. Fenzel-Alexander, An ion transfer model for contact charging, Langmuir. 9 (1993) 1009–1015. https://doi.org/10.1021/la00028a021.
[51] L.B. Schein, M. LaHa, D. Novotny, Theory of insulator charging, Physics Letters A. 167 (1992) 79–83. https://doi.org/10.1016/0375-9601(92)90630-5.
[52] Y. Yang, C. Zi, Z. Huang, J. Wang, M. Lungu, Z. Liao, Y. Yang, H. Su, CFD-DEM investigation of particle elutriation with electrostatic effects in gas-solid fluidized beds, Powder Technology. 308 (2016) 422–433. https://doi.org/10.1016/j.powtec.2016.12.032.

[53] J. Kolehmainen, A. Ozel, C.M. Boyce, S. Sundaresan, Triboelectric charging of monodisperse particles in fluidized beds, AIChE Journal. 63 (2017) 1872–1891. https://doi.org/10.1002/aic.15541.
[54] H. Grosshans, M.V. Papalexandris, Direct numerical simulation of triboelectric charging in particle-laden turbulent channel flows, Journal of Fluid Mechanics. 818 (2017) 465–491. https://doi.org/10.1017/jfm.2017.157.
[55] J. Kolehmainen, A. Ozel, S. Sundaresan, Eulerian modelling of gas–solid flows with triboelectric charging, Journal of Fluid Mechanics. 848 (2018) 340–369. https://doi.org/10.1017/jfm.2018.361.
[56] M. Ray, F. Chowdhury, A. Sowinski, P. Mehrani, A. Passalacqua, An Euler-Euler model for mono-dispersed gas-particle flows incorporating electrostatic charging due to particle-wall and particle-particle collisions, Chemical Engineering Science. 197 (2019) 327–344. https://doi.org/10.1016/j.ces.2018.12.028.
[57] J. Kolehmainen, L. Ceresiat, A. Ozel, S. Sundaresan, 110th Anniversary: Effect of System Size on Boundary-Driven Contact Charging in Particulate Flows, Ind. Eng. Chem. Res. 58 (2019) 17980–17990. https://doi.org/10.1021/acs.iecr.9b03437.
[58] M. Ray, F. Chowdhury, A. Sowinski, P. Mehrani, A. Passalacqua, Eulerian modeling of charge transport in bi-disperse particulate flows due to triboelectrification, Physics of Fluids. 32 (2020) 023302. https://doi.org/10.1063/1.5140473.
[59] C. Montilla, R. Ansart, O. Simonin, Modelling of the mean electric charge transport equation in a mono-dispersed gas–particle flow, Journal of Fluid Mechanics. 902 (2020). https://doi.org/10.1017/jfm.2020.577.
[60] T. Shinbrot, T.S. Komatsu, Q. Zhao, Spontaneous tribocharging of similar materials, Epl. 83 (2008) 24004. https://doi.org/10.1209/0295-5075/83/24004.
[61] R. Yoshimatsu, N.A.M. Araújo, G. Wurm, H.J. Herrmann, T. Shinbrot, Self-charging of identical grains in the absence of an external field, Scientific Reports. 7 (2017) 39996. https://doi.org/10.1038/srep39996.
[62] T. Siu, J. Cotton, G. Mattson, T. Shinbrot, Self-sustaining charging of identical colliding particles, Physical Review E - Statistical, Nonlinear, and Soft Matter Physics. 89 (2014) 1–7. https://doi.org/10.1103/PhysRevE.89.052208.
[63] T. Matsuyama, H. Yamamoto, Charge-relaxation process dominates contact charging of a particle in atmospheric condition: II. The general model, Journal of Physics D: Applied Physics. 30 (1997) 2170–2175. https://doi.org/10.1088/0022-3727/30/15/008.
[64] T. Matsuyama, H. Yamamoto, Impact charging of particulate materials, Chemical Engineering Science. 61 (2006) 2230–2238. https://doi.org/10.1016/j.ces.2005.05.003.
[65] M.J.H. Khan, M.A. Hussain, Z. Mansourpour, N. Mostoufi, N.M. Ghasem, E.C. Abdullah, CFD simulation of fluidized bed reactors for polyolefin production – A review, Journal of Industrial and Engineering Chemistry. 20 (2014) 3919–3946. https://doi.org/10.1016/J.JIEC.2014.01.044.
[66] S. Kuang, M. Zhou, A. Yu, CFD-DEM modelling and simulation of pneumatic conveying: A review, Powder Technology. 365 (2020) 186–207. https://doi.org/10.1016/j.powtec.2019.02.011.
[67] D.A. Drew, L.A. Segel, Averaged Equations for Two-Phase Flows, Studies in Applied Mathematics. 50 (1971) 205–231. https://doi.org/10.1002/sapm1971503205.
[68] M.A. Hassani, R. Zarghami, H.R. Norouzi, N. Mostoufi, Numerical investigation of effect of electrostatic forces on the hydrodynamics of gas–solid fluidized beds, Powder Technology. 246 (2013) 16–25. https://doi.org/10.1016/j.powtec.2013.05.007.

[69] C. Pei, C.-Y. Wu, D. England, S. Byard, H. Berchtold, M. Adams, DEM-CFD modeling of particle systems with long-range electrostatic interactions, AIChE Journal. 61 (2015) 1792–1803. https://doi.org/10.1002/aic.14768.
[70] J. Kolehmainen, A. Ozel, C.M. Boyce, S. Sundaresan, A hybrid approach to computing electrostatic forces in fluidized beds of charged particles, AIChE Journal. 62 (2016) 2282–2295. https://doi.org/10.1002/aic.15279.
[71] R.G. Rokkam, R.O. Fox, M.E. Muhle, Computational fluid dynamics and electrostatic modeling of polymerization fluidized-bed reactors, Powder Technology. 203 (2010) 109–124. https://doi.org/10.1016/j.powtec.2010.04.002.
[72] J.T. Jenkins, S.B. Savage, A theory for the rapid flow of identical, smooth, nearly elastic, spherical particles, Journal of Fluid Mechanics. 130 (1983) 187–202. https://doi.org/10.1017/S0022112083001044.
[73] J.T. Jenkins, F. Mancini, Balance Laws and Constitutive Relations for Plane Flows of a Dense, Binary Mixture of Smooth, Nearly Elastic, Circular Disks, Journal of Applied Mechanics. 54 (1987) 27–34. https://doi.org/10.1115/1.3172990.
[74] J.T. Jenkins, F. Mancini, Kinetic theory for binary mixtures of smooth, nearly elastic spheres, Physics of Fluids A: Fluid Dynamics. 1 (1989) 2050–2057. https://doi.org/10.1063/1.857479.
[75] L. Ceresiat, J. Kolehmainen, A. Ozel, Charge Transport Equation for Bidisperse Rapid Granular Flows with Nonequipartitioned Fluctuating Kinetic Energy, (n.d.) 32.
[76] A. Sowinski, L. Miller, P. Mehrani, Investigation of electrostatic charge distribution in gas–solid fluidized beds, Chemical Engineering Science. 65 (2010) 2771–2781. https://doi.org/10.1016/j.ces.2010.01.008.
[77] E. Klahn, H. Grosshans, An accurate and efficient algorithm to model the agglomeration of macroscopic particles, Journal of Computational Physics. 407 (2020) 109232. https://doi.org/10.1016/j.jcp.2020.109232.
[78] H. Grosshans, M.V. Papalexandris, A model for the non-uniform contact charging of particles, Powder Technology. 305 (2017) 518–527. https://doi.org/10.1016/j.powtec.2016.10.024.
[79] T. Matsuyama, H. Yamamoto, Electrification of single polymer particles by successive impacts with metal targets, IEEE Transactions on Industry Applications. 31 (1995) 1441–1445. https://doi.org/10.1109/28.475738.
[80] F. Sharmene Ali, M. Adnan Ali, R. Ayesha Ali, I.I. Inculet, Minority charge separation in falling particles with bipolar charge, Journal of Electrostatics. 45 (1998) 139–155. https://doi.org/10.1016/S0304-3886(98)00044-8.
[81] H. Zhao, G.S.P. Castle, I.I. Inculet, The measurement of bipolar charge in polydisperse powders using a vertical array of Faraday pail sensors, Journal of Electrostatics. 55 (2002) 261–278. https://doi.org/10.1016/S0304-3886(01)00209-1.
[82] L. Xie, G. Li, N. Bao, J. Zhou, Contact electrification by collision of homogenous particles, Journal of Applied Physics. 113 (2013) 184908. https://doi.org/10.1063/1.4804331.
[83] M.A. Bilici, J.R. Toth, R.M. Sankaran, D.J. Lacks, Particle size effects in particle-particle triboelectric charging studied with an integrated fluidized bed and electrostatic separator system, Review of Scientific Instruments. 85 (2014). https://doi.org/10.1063/1.4897182.
[84] D.J. Lacks, R.M. Sankaran, Triboelectric charging in single-component particle systems, Particulate Science and Technology. 34 (2016) 55–62. https://doi.org/10.1080/02726351.2015.1043676.
[85] D. Song, P. Mehrani, Comparison of electrostatic charge generation in gas-solid fluidized beds in turbulent versus pre-turbulent flow regime, Powder Technology. 319 (2017) 426–433. https://doi.org/10.1016/j.powtec.2017.07.013.

[86] L. Konopka, S. Jantač, M. Vrzáček, M. Svoboda, J. Kosek, Triboelectric charging of polyethylene powders: Comparison of same-material and different-material contributions to the charge build-up, Powder Technology. 367 (2020) 713–723. https://doi.org/10.1016/J.POWTEC.2020.04.029.
[87] F. Salama, A. Sowinski, K. Atieh, P. Mehrani, Investigation of electrostatic charge distribution within the reactor wall fouling and bulk regions of a gas–solid fluidized bed, Journal of Electrostatics. 71 (2013) 21–27. https://doi.org/10.1016/j.elstat.2012.11.002.
[88] D. Song, P. Mehrani, Mechanism of particle build-up on gas-solid fluidization column wall due to electrostatic charge generation, Powder Technology. 316 (2017) 166–170. https://doi.org/10.1016/j.powtec.2017.01.031.
[89] F. Jalalinejad, X.T. Bi, J.R. Grace, Effect of electrostatic charges on single bubble in gas-solid fluidized beds, International Journal of Multiphase Flow. 44 (2012) 15–28. https://doi.org/10.1016/j.ijmultiphaseflow.2012.03.008.
[90] J. Sun, J. Wang, Y. Yang, Z. Zhu, Effects of external electric field on bubble and charged particle hydrodynamics in a gas–solid fluidized bed, Advanced Powder Technology. 26 (2015) 563–575. https://doi.org/10.1016/j.apt.2015.01.006.
[91] G. Hendrickson, Electrostatics and gas phase fluidized bed polymerization reactor wall sheeting, Chemical Engineering Science. 61 (2006) 1041–1064. https://doi.org/10.1016/j.ces.2005.07.029.
[92] W.O. Moughrabiah, J.R. Grace, X.T. Bi, Effects of pressure, temperature, and gas velocity on electrostatics in gas-solid fluidized beds, Industrial and Engineering Chemistry Research. 48 (2009) 320–325. https://doi.org/10.1021/ie800556y.
[93] J. Guardiola, V. Rojo, G. Ramos, Influence of particle size, fluidization velocity and relative humidity on fluidized bed electrostatics, Journal of Electrostatics. 37 (1996) 1–20. https://doi.org/10.1016/0304-3886(96)00002-2.
[94] A. Giffin, P. Mehrani, Effect of gas relative humidity on reactor wall fouling generated due to bed electrification in gas-solid fluidized beds, Powder Technology. 235 (2013) 368–375.

Chapter 8

Conclusions and Recommendations

The triboelectrification of solids in gas-solid flow systems is an on-going concern in many industrial processes. Researchers in both academia and industry are driven to reduce its negative impacts on the productivity and safety of their systems. This interest has led to meaningful discoveries on charge transfer behaviours which have yet to be fully defined in quantifiable forms. As computing technologies continue to improve, CFD simulations have become an excellent predictive tool for analyzing industrial-scale gas-solid flow systems, and a cost-effective alternative to performing preliminary pilot-scale studies. As such, for the benefit of the electrostatics research community and invested industrial partners, experimental investigations into the triboelectrification of solids was a necessary next step to develop an accurate electrostatic charge transfer model and then implement it into CFD models of gas-solid flows. This thesis presented the beginnings, significant progress, and outlook on this on-going research interest, providing a steppingstone for the complete development of an Euler-Euler two-fluid model for electrostatic charging in poly-dispersed gas-solid flows.

8.1. Conclusions

A charge transport model was developed to include the phenomenon of triboelectrification in an Euler-Euler two-fluid model for mono-disperse particles. This model incorporated a particle-wall charging component which was derived based on boundary conditions developed for the hydrodynamic model [1]. The particle-particle charging component was represented through a charge diffusion model for mono-disperse particles, based on the collisional theory of rapid particle flows [2]. Both these components used the condenser model to determine the degree of charge transfer [3]. An expression for the charge-velocity covariance was also derived to consider the effect of self-diffusion in the charge transport model, which had a significant contribution to the charge diffusion rate. Employing the charge transport model in conjunction with the Eulerian two-fluid model, the electrostatic charging and wall fouling behaviour of a gas-solid fluidized bed of polyethylene particles was simulated with emphasis on the effect of particle size. The dimensions of the bed (1.27 m height, 0.1 m diameter), fluidization parameters (1.5 U_{mf}, atmospheric conditions), and the range of averaged particle sizes (362 – 855 μm) used in the

simulation were the same as that used in past experiments [4], whose results were used for the model validation.

Based on the simulation results, the wall flux boundary condition imposes a steep gradient at the wall, which initiates charge diffusion into the fluidized bed. During fluidization, gradients of granular temperature and particle charge density diffuse the charge and cause an increase in the total bed charge as well as the potential energy of the system. This resulted in an increase of the electric field strength which acts as a resistance to the charge diffusion into the bed, eventually leading to a dynamic equilibrium for charging. At the end of the fluidization, the simulated charge-to-mass ratios of the wall particles were in good agreement with the corresponding values for the wall-fouling particles in the experiments. Moreover, the degree of wall fouling diminished with increasing particles, which was also consistent with the experiments. However, the thickness of the wall fouling was notably lower in the simulations for all tested cases, likely caused by the unipolar charging of the fluidized bed as opposed to the bipolar charging behaviour usually observed in experiments due to particle size differences. As such, the electrostatic model was extended to consider bi-dispersed particulate flow systems. 1-D simulation results using this model predicted bipolar charging behaviour when the particles had different sizes, even though they were made of the same material (Appendix A). This phenomenon was driven by the net electric field produced by the charges accumulating on the particles.

To confirm the validity of the charge transfer model for use in the CFD model, experimental studies were performed for both particle-wall and particle-particle collisions. The mechanism for particle-wall charging of single insulative particles was analyzed and tested with single-contact and repeated-contact experiments. The single-contact experiments, performed with spherical HDPE and PTFE particles contacting an aluminum plate, showed that particles with a larger effective work function consistently generated more charge. The amount of charge generated from a single wall contact was also directly proportional to the surface area of the contacting particle. The repeated-contact experiments confirmed that the saturation charge limit also increased with the effective work function, and the surface area proportionality held true for all tested cases, including the charge saturation points for commercial LLDPE resins. A study on the effect of initial particle charge showed that particles closer to the saturation point will not charge beyond this point regardless of the number of particle-wall collisions they experience. Moreover, a particle

with a known charging trend will follow the same path when starting at any initial charge. These observations confirmed the viability of the condenser model to predict charge generation in gas-solid fluidized beds due to particle-wall collisions and provided a means to obtain the charge saturation values of polyethylene resins as a function of particle size.

For the case of particle-particle charging, a novel apparatus was designed and built to study the direction and magnitude of charge transfer between two colliding particles. This bench-scale experiment was the first of its kind, and the apparatus design ensured that the measured change in each particle's charge was solely due to the particle-particle interactions between the two colliding particles. The collisions were confirmed by monitoring the particle trajectories using a high frame-rate camera. Coupled with a particle-tracking velocimetry program, each collision video was analyzed to determine the particles' mode of contact (direct, angled, or tangential), and subsequently their impact angles and velocities. Measurable and near-perfect charge transfer, where the charge gained on one particle was equal to the charge lost by the other, was observed for same-sized PTFE-aluminum, PTFE-nylon, PTFE-PTFE and nylon-nylon collisions, as well as different-sized nylon collisions. The charge transfer magnitudes in PTFE-aluminum particle-particle collisions, after accounting for the effective contact areas calculated using the normal impact velocities, were roughly 5 times lower than those measured in the abovementioned PTFE-aluminum particle-wall collisions. Moreover, the impact angle for each collision was found to be directly proportional to the degree of charge transfer in both particle-particle and particle-plate collisions. These findings suggested that the tangential component of the impact velocity should also be included in current charge transfer models for all collision types.

The different-material collisions further confirmed the viability of the apparatus, as PTFE particles consistently charged negatively when colliding with aluminum and nylon particles. The PTFE-nylon collisions also exchanged more charge than the PTFE-aluminum collisions, which agreed with their expected directions of charge transfer based on the particles' effective work functions. Same-sized particle collisions using 3.2 mm PTFE, 3.2 mm nylon, and 4.0 mm nylon particles revealed that the transferred charge did not always move towards equilibrium, but instead caused an increased separation of particle charges. Particularly for 3.2 mm collisions, the particles' difference in initial charges was amplified in almost all collision trials. The charge transfer in identical particle collisions may therefore be caused by the neutralization of the induced dipole

moments between the colliding particles. However, given the low initial charges of the tested particles, this charging behaviour could also be attributed to the non-uniform distribution of charge on the particle surfaces. For different-sized nylon collision trials, the charge transfer direction was independent of the particles' initial charges and consistently favored one particle size over another. Thus, the size-dependent bipolar charging behaviour was not only due to the electric field acting on the particles, as was observed in the abovementioned bi-disperse simulations, but also caused by individual particle-particle collisions.

The experimental data from the particle-particle collisions such as the initial charges, impact velocities, and impact angles were used as input parameters for the charging model. These modeled charge transfer values were compared to the measured charge data for various collision scenarios. This investigation highlighted the missing components in the charging model that needs to be determined particularly for particle-particle collisions. Specifically, the model must consider a size-dependent bipolar charging mechanism, a charge amplification mechanism for identical particles, and a non-uniform distribution of the initial particle charges.

8.2. Recommendations for Future Work

The electrostatics and CFD modeling research communities have been quite active in recent years respectively to investigate the electrostatic charging behaviour between insulative particles and to develop electrostatic models for both Euler-Lagrange and Euler-Euler simulation studies. Coupled with the insights and the expertise in these research areas gained over the years, recent advancements in charge transfer studies were carefully reviewed and discussed in this thesis. As such, the following recommendations are proposed for the future work of this project as well as the overall research of electrostatic modeling of gas-solid flows:

1. Continue improving the design of the particle-particle collision apparatus and continue performing experiments with the goal of developing an empirical particle-particle charging model. Some recommendations to attain this goal are as follows:
    a. Design for higher impact velocities to obtain a greater range of values for a better analysis of its effect on charge transfer. This would involve either using stronger air flows in the current system or modifying the dropping mechanism entirely.

b. Utilize a more precise measurement technique to determine the degree of particle-particle charging in smaller particles, and especially in polyethylene resins which were not measurable using the current system. Moreover, any improvements on the design to allow a wider range of initial particle charges to be tested would be valuable for the empirical model.
c. Consider the effect of the laboratory environment on particle charging, especially the charging phenomenon observed with airflow. An isolated system in a controlled clean room could eliminate factors such as humidity and air particulates that may have affected the measured charge transfer data. An automated particle feeding system could also streamline the experimental procedure, and limit the potential inconsistencies brought about by manual interactions with the particles.

2. Continue the development on the Euler-Euler two-fluid model to achieve the ultimate goal of performing industrial-scale simulations studies of electrostatic charging in dense, poly-dispersed gas-solid fluidized beds. Also, address the shortcomings of the charge transfer model, the simulation setup and input parameters recently highlighted by researchers in electrostatics and CFD modeling communities. The specific objectives are:
    a. Identify a suitable method to consider charge amplification between identical particles, the bipolar charging behaviour between particles of different sizes, and the non-uniform charge distribution on particle surfaces and its effect on charge transfer. A possible solution to consider these factors is to determine the probability density functions for charge on bulk powders, correlated with their size, obtained at various times. This data can help identify the bipolarity and dispersion of charge regardless of the particle-size distribution the number of components in the mixture.
    b. Modify the charge transfer models to incorporate the abovementioned empirical charging model, and implement the developed bidisperse charge transport equation into the Eulerian model and validate it using simulations of laboratory-scale fluidized beds.
    c. Expand the bidisperse equation to the polydisperse case, which would allow the simulation of both wide particle-size distributions and multicomponent systems.

References

[1] P.C. Johnson, R. Jackson, Frictional-collisional constitutive relations for granular materials, with application to plane shearing, J. Fluid Mech. 176 (1987) 67–93.

[2] J.T. Jenkins, S.B. Savage, A theory for the rapid flow of identical, smooth, nearly elastic, spherical particles, J. Fluid Mech. 130 (1983) 187–202.

[3] S. Matsusaka, M. Ghadiri, H. Masuda, Electrification of an elastic sphere by repeated impacts on a metal plate, J. Phys. D. Appl. Phys. 33 (2000) 2311–2319.

[4] A. Sowinski, A. Mayne, P. Mehrani, Effect of fluidizing particle size on electrostatic charge generation and reactor wall fouling in gas–solid fluidized beds, Chem. Eng. Sci. 71 (2012) 552–563.

Appendix A
Eulerian modeling of charge transport in bi-disperse particulate flows due to triboelectrification

M. Ray[a], F. Chowdhury[b], A. Sowinski[b], P. Mehrani[b], A. Passalacqua[a,]

[a] Department of Chemical and Biological Engineering, University of Ottawa, 161 Louis Pasteur, Ottawa, ON, Canada, K1N 6N5
[b] Department of Mechanical Engineering, Iowa State University, 2025 Black Engineering Building Ames, IA, 50011-2161, USA

This appendix is a manuscript published in Physics of Fluids (2020; 32(2):023302).

Abstract

A Eulerian model to describe the behavior of electrically charged particles, which considers charge separation and transfer between particles of two separate species, is developed using the kinetic theory of granular flows (KTGF). A transport equation for the charge of each particle species is obtained, incorporating the effect of the charge-velocity correlation. Closures for the collisional diffusion of charge and for the charge-velocity covariance are obtained. The developed model is applied to steady-state simulations in a one-dimensional domain with no advection, neglecting momentum transport and assuming a constant granular temperature for the solid species. While this is only a preliminary test of the model, which will require further validation, the results show the prediction of bipolar charging when the particles have different sizes, even though they are made of the same material. This phenomenon is analyzed and is shown to be driven by the electric field produced by the charge accumulated on the particles.

A.1. Introduction

An ongoing challenge encountered in several practical processes such as gas-solid fluidization, mixing, drying and coating of non-conductive granular materials as well as in several reactive processed such as polymerization is the generation of electrostatic charges, which can greatly hinder the process productivity and may pose safety risks. Electrostatic charging occurs in gas-solid fluidized beds due to particle-particle and particle-wall contacts, also known as triboelectrification [1–3]. Specifically, in polyethylene production, where ethylene gas is used to produce polyethylene via catalytic polymerization in a gas-solid fluidized bed reactor [4], triboelectrification results in highly charged polymer and catalyst particles to adhere to the reactor walls. The adhered particles quickly melt and fuse together due to the heat released by the exothermic polymerization reaction, leading to the formation of large sheets that can ultimately force reactor shutdowns for clean-up operations [5].

Numerous experimental studies were performed in the past to understand the effects of electrostatic charge on gas-solid fluidized beds [6,7], including wall fouling tendencies [8–10] and changes in bubble and bed behaviors [11–13]. However, modeling work on electrostatic charge generation and its effects in gas-particle flows has only recently seen substantial progress. Hassani et al. (2013) developed a Euler-Lagrange model to study the effect of electrostatic forces on the hydrodynamics of fluidization, and found that mono-charged particles resulted in smaller bubble sizes and greater bed voidage, which was in agreement with experimental results found by Bokkers et al. (2004). In addition, bipolar charges resulted in a neutral net charge governing the hydrodynamics of the system. Yang et al. (2016) also investigated the effect of electrostatic charge using a Euler-Lagrange model with non-varying charge, but specifically on particle elutriation. Jalalinejad et al. (2015) used a Euler-Euler model to study the influence of electrostatic charge of mono-sized glass beads on bubble behavior in freely bubbling fluidized beds. Recently, Grosshans and Papalexandris (2017) used fully resolved Direct Numerical Simulation (DNS) to study charge diffusion of particles in turbulent channel flow. Rokkam et al. (2010a; 2010b) developed a Euler-Euler model for a pilot-scale gas-solid fluidized bed to study the electrostatic effect of particles with fixed charges. Using simulation conditions based on the experimental investigation by Sowinski et al. (2010), the model was able to reproduce similar trends in particle segregation and

entrainment due to the electrostatic forces in the fluidized bed [22]. These simulations precluded charge transfer between particles and between particles and wall, thus neglecting collisional diffusion of charge. Kinetic diffusion was also neglected in their work. For a more realistic representation of these systems, a model accounting for charge separation is needed to describe the triboelectric charge transfer due to collisions, some of which were proposed in the literature, as summarized below.

Schein et al. (1992) suggested a charging model, based on the surface state theory, where the charge exchanged between two surfaces per unit area of contact is such to neutralize the work function difference. Matsuyama and Yamamoto (1995, 2006) proposed the charge relaxation model, which suggests that the charge transfer between two colliding bodies is completed after their separation. This is based on the assumption that when the two particles separate, charge flows back in the direction opposite to when the particles were in contact, and is determined by the Paschen curve. Ireland (2010) put forward a particle-wall charging model that considers contact time, velocity, and the mode of contact (i.e. bouncing, sliding, and rolling), as these determine the quantity of charge transferred in each collision. Matsusaka and Masuda (2003), whose work is based on previous literature [28,29], adopted the condenser model, which suggests that the contact region between two bodies can be regarded as a capacitor. Thus, a short contact time is sufficient to experience charge transfer. The maximum area of the capacitor in such collisions depends on the impact velocity according to the Hertzian theory [30]. Under this model, repeated particle-wall contacts cause the particle to reach a maximum charge value, known as *saturation charge* [31]. Korevaar et al. (2014) proposed a contact charging model based on the condenser model for pneumatically conveyed powders in a Euler-Lagrange CFD-DEM framework. Their simulations revealed the significant influence of particle-wall interactions on both the spatial distribution of powder in the duct and the acquired charge of the particles [32]. Pei et al. (2016, 2015, 2013) also performed several CFD-DEM studies using the condenser model. They observed that particles of different material properties can acquire charges of opposite polarity and form agglomerates, which can result in de-fluidization at low superficial gas velocities [34]. Moreover, their study on long-range electrostatic interactions implied that even long-range electric field contributions are necessary for accurate modeling of charged particle systems [35]. Laurentie et al. (2013) incorporated in their DEM implementation the charging model of Schein et al. (1992), at the high

density limit of surface state theory, which is similar to the particle-particle charging model of Soo (1971). The model assumed that the charge transfer is not only dependent on the effective work function of the two contacting bodies, but also on the total electric field acting at the contact point [36]. Similar to the model of Matsusaka et al. (2000) , they used the Hertzian model [30] to compute the maximum area of contact at collision. The charge transfer model of Laurentie et al. (2013) was adopted by Kolehmainen et al. (2016) for the CFD-DEM simulation of laboratory-scale vibrated granular beds and fluidized beds. These studies revealed that bed height oscillations in small fluidized beds of mono-charged particles decreases with increasing charge due to the lateral segregation of particles. The average charge in their cases also reached an equilibrium state at a value much lower than expected based on the work function difference [38].

As reviewed above, Euler-Lagrange models have gained some traction for simulating triboelectrification and its effects in laboratory-scaled gas-solid flows. However, very few works have been published modeling charge generation in gas-solid flows using a Euler-Euler framework [39,40]. A monodisperse Euler-Euler model was formulated and used for simulation of a lab-scale fluidized bed of polyethylene particles by Ray et al. (2019). In their work, charge transfer due to particle-wall collisions was modeled assuming the mechanism of charge separation as described by the model of Matsusaka et al. (2000) and formulating a boundary condition for charge transfer at walls compatible with the boundary conditions for the velocity and the granular temperature of Johnson and Jackson (1987). Similarly, charge diffusion due to particle-particle collisions was accounted for based on the kinetic theory of granular flow of Jenkins and Savage (1983), and the charging model of [36]. This Euler-Euler model was validated against the experimental results of a pilot-scale fluidized bed study [9], by comparing the charge density and mass fraction of particles adhering to the wall. In these experiments, a wide particle size distribution was present which was narrowed in some of the tests by sieving. In practical scenarios, a broad size distribution is to be expected and hence a polydisperse model is necessary. As a step in the direction of accounting for polydispersity, a Eulerian bi-disperse model is developed in this work. The discrete charging models of Matsusaka et al. (2000) and Laurentie et al. (2013), which already accounted for the effect of different particle sizes and work functions, were used in the formulation of the Eulerian-Eulerian model proposed in this work. Kinetic-theory based closure for the transport of particle charge due to particle-particle collisions were derived based on the kinetic theory of Jenkins and Mancini (1987) for bi-disperse granular systems. The model for particle-wall charging of Ray et

al. (2019) was adopted. One-dimensional simulations of polyethylene particles were performed without considering any mean motion of the particles. The diameter and volume fraction of the two species were varied relative to each other, and it was found that the larger particle species exhibited a bipolar behavior.

A.2. Electrostatic model

The electrostatic force on a particle having a charge q, as per the definition of Lorentz force, is:

$$\mathbf{F}_q = q(\mathbf{E} + \mathbf{v} \times \mathbf{B}), \tag{A-1}$$

where **E** is the electric field and **B** the magnetic field at the location where the particle is moving with a velocity **v**. The contribution of the latter can be neglected in the context of gas-particle flows due to the low particle velocities (much smaller than the speed of light) under consideration, and also due to negligible magnetic field strength induced by the low magnitude of electric current and rate of electric field fluctuations. Thus,

$$\mathbf{F}_q = q\mathbf{E}, \tag{A-2}$$

where

$$\mathbf{E} = -\nabla\varphi_E, \tag{A-3}$$

in which φ_E is the electric potential, solution of the Poisson equation:

$$\nabla \cdot (\varepsilon_0 \varepsilon_m \nabla\varphi_E) = \rho_q, \tag{A-4}$$

where ε_m is the relative permittivity of the mixture and ρ_q is the volumetric charge density, which for a mixture is given by

$$\rho_q = \sum_i^n N_i q_i, \tag{A-5}$$

with q_i the mean charge of a single particle and N_i the number density of species i. Gas-particle flow is not simulated in this work and therefore the effect of advection (including the effect of $\mathbf{F}_q$) is not considered. The spatial distribution of the electric field still must be determined for

estimating charge diffusion as will be discussed in the next few sections. The spatial charge distribution is then used to compute the volumetric charge density from Eq. A-5, needed to solve Eq. A-4. Thus, a coupled system of partial differential equations needs to be solved as shown in the following sections.

A.2.1. Particle charging model

A.2.1.1. Particle-wall charging

The quantity of charge exchanged between a particle and a wall, can be calculated according to the observations of Matsusaka et al., (2000), and Matsusaka and Masuda (2003):

$$\frac{dq_i}{dn_{c,w}} = -k_c \varepsilon_0 \varepsilon_r \left[\frac{V_c}{z_0}\left(1 - \frac{q_{w,i}}{q_{\infty,\mathrm{i}}}\right) + \mathbf{E}\cdot\mathbf{n}\right] S_i, \qquad \text{A-6}$$

where V_c is the difference of the work functions of the wall and the particle, k_c is the charging efficiency, ε_r is the relative electrical permittivity of the fluid medium, z_0 is the critical gap for electron transfer, $q_{w,i}$ is the particle charge, $q_{\infty,\mathrm{i}}$ is the particle saturation charge, $\mathbf{n}$ is the wall normal unit vector, and S_i is the maximum contact area during impact deformation between a spherical particle and a rigid wall. The latter is computed according to the Hertzian theory [30] as:

$$S_i = \left[\frac{\pi}{2}\left(\frac{5\sqrt{2}\pi}{32}\right)^{2/5} \mathrm{d}_\mathrm{i}^2 \left(\rho\frac{1-\nu}{E}\right)^{2/5}\right] v^{4/5} = k_{s,w,i} v^{4/5}, \qquad \text{A-7}$$

where ν, ρ and E are the Poisson ratio, density and the Young's modulus of the particle material, and v is the wall-normal component of the particle velocity. This model for particle-wall charging has been used in monodisperse simulations by Kolehmainen et al. (2018) and Ray et al. (2019), and it is adopted in this manuscript for each particle species.

A.2.1.2. Inter-particle charging

Schein et al. (1992) proposed a model to describe the exchange of charge during a collision of two particles based on the assumption that each of the particles will exchange an equal amount of charge during the collision. This model, which has been used in the previous works of Laurentie et al. (2013), Kolehmainen et al. (2018) and Ray et al. (2019), leads, for the case of two particle species *i* and *j* to the following expression for the rate of change of particle charge with the number of collisions:

$$\left(\frac{dq_i}{dn_c}\right)^b = -\left(\frac{dq_j}{dn_c}\right)^b = \left[K_v^b \phi_{ij} - K_i^b q_i + K_j^b q_j + K_{eq}^b (\mathbf{E}\cdot\mathbf{k})\right](\mathbf{c}_{ij}\cdot\mathbf{k})^{4/5}, \quad \text{A-8}$$

with

$$K_v^b = \frac{k_c k_s^b \varepsilon_0 \varepsilon_r}{z_0}, \quad \text{A-9}$$

$$K_i^b = \frac{k_c k_s^b}{\pi d_i^2}, \quad \text{A-10}$$

$$K_j^b = \frac{k_c k_s^b}{\pi d_j^2}, \quad \text{A-11}$$

$$K_{eq}^b = k_c k_s^b \varepsilon_0 \varepsilon_r, \quad \text{A-12}$$

and

$$k_s^b = \pi R_o \left(\frac{15}{8}\frac{m_i m_j}{m_i + m_j}\frac{1-\nu}{E\sqrt{R_o}}\right)^{2/5}. \quad \text{A-13}$$

The result in Eq. A-14 is based on the Hertzian theory of contact deformation between two spherical particles [30] of the same material but different sizes, where

$$R_o = \frac{d_i d_j}{2(d_i + d_j)}. \quad \text{A-14}$$

The term ϕ_{ij} in Eq. A-8 is the work function difference between materials of the two species, d_i and d_j are the particle diameters of species i and j, respectively, m_i, m_j are the particle masses, and $(\mathbf{c}_{ij}\cdot\mathbf{k})$ is the component of relative velocity along the line joining the centers of the two colliding particles, and $\mathbf{k}$ is the unit vector along that direction. The superscript b in the equations above corresponds to collisions between unlike particles. Since we also need to include the effect of the collisions between like particles, we have:

$$\left(\frac{dq_{i1}}{dn_c}\right)^m = -\left(\frac{dq_{i2}}{dn_c}\right)^m = \left[K_i^m (q_{i2} - q_{i1}) + K_{eq}^m (\mathbf{E}\cdot\mathbf{k})\right](\mathbf{c}_{i12}\cdot\mathbf{k})^{4/5}, \quad \text{A-15}$$

with

$$K_i^m = \frac{k_c k_s^m}{\pi d_i^2}, \tag{A-16}$$

$$K_{eq}^m = k_c k_s^m \varepsilon_0 \varepsilon_r, \tag{A-17}$$

and

$$k_s^m = \frac{\pi}{4}\left(\frac{5\pi}{16}\right)^{2/5} \mathrm{d_i^2} \left(\rho \frac{1-\nu}{E}\right)^{2/5}, \tag{A-18}$$

which is derived from Eq. A-13.

It is worth mentioning at this point that charge could also dissipate through charge decay [31], where particles lose charge over a period of time to the surrounding medium and reach an equilibrium. Due to this decay, rubber particles were shown to reach a lower saturation level when there was an interval of more than 10 s between consecutive collisions [31]. In a bubbling fluidized bed of 400 μm polyethylene particles, the time between collisions was shown to be less than 100 ms, and thus charge decay is ignored in this paper.

A.2.2. Particle charge transport

The transport equation for particle charge can be developed following the work of Jenkins and Savage (1983) and Jenkins and Mancini (1987) by additionally considering particle charge and particle velocity may be correlated. Thus the mean charge of the particle species i, q_i, varies according to the equation:

$$\frac{\partial}{\partial t}(N_\mathrm{i}\langle q_i\rangle) + \nabla \cdot (N_\mathrm{i}\langle \mathbf{c}_i q_i\rangle) = \mathbb{C}_{ii}(q_i) + \mathbb{C}_{ij}(q_i), \tag{A-19}$$

which can be rewritten as:

$$\frac{\partial}{\partial t}(N_\mathrm{i}\langle q_i\rangle) + \nabla \cdot (N_\mathrm{i}\langle q_i\rangle \mathbf{U}) + \nabla \cdot (N_\mathrm{i}\langle \mathbf{C}_i q_i'\rangle) = \mathbb{C}_{ii}(q_i) + \mathbb{C}_{ij}(q_i), \tag{A-20}$$

because

$$\mathbf{c}_i = \mathbf{U} + \mathbf{C}_i, \tag{A-21}$$

with the barycentric velocity $\mathbf{U}$ given by

$$\mathbf{U} = \frac{m_i N_\mathrm{i} \langle \mathbf{c}_i \rangle + m_j N_\mathrm{j} \langle \mathbf{c}_j \rangle}{m_i N_\mathrm{i} + m_j N_\mathrm{j}}, \tag{A-22}$$

where N_i, N_j are the species number densities, and $\mathbf{c}_i, \mathbf{c}_j$ are the i and j particle velocities. The remainder symbols in the previous equations are defined as follows: $\mathbb{C}_{ii}(q_i)$ and $\mathbb{C}_{ij}(q_i)$ are the collisional rate of change of q_i for collisions with particles of the same species i and with the other species j, respectively, while $\langle \mathbf{C}_i q_i' \rangle$ is the expected value of the charge-velocity covariance. Also

$$q_i = \langle q_i \rangle + q_i'. \tag{A-23}$$

A.2.3. Number density function

The single-particle number density function (NDF) $f_i(t, \mathbf{x}, \mathbf{c}_i, q_i)$ is defined in this work so that it has the same moments as a Maxwellian distribution for velocity and of a Gaussian distribution for charge:

$$\mathbf{U}_\mathrm{i} = \int_{\mathbb{R}^3} \int_{\mathbb{R}} \mathbf{c}_i f_i \, \mathrm{d}q_i \, \mathrm{d}\mathbf{c}_i, \tag{A-24}$$

$$T_i \bar{\bar{\mathrm{I}}} = (T + \theta_i) \bar{\bar{\mathrm{I}}} = m_i \int_{\mathbb{R}^3} \int_{\mathbb{R}} \mathbf{C}_i \mathbf{C}_i f_i \, \mathrm{d}q_i \mathrm{d}\mathbf{c}_i, \tag{A-25}$$

$$T = \frac{N_\mathrm{i} T_i + N_j T_j}{N_\mathrm{i} + N_j}, \tag{A-26}$$

$$\langle q_i \rangle = \int_{\mathbb{R}^3} \int_{\mathbb{R}} q_i f_i \, \mathrm{d}q_i \, \mathrm{d}\mathbf{c}_i, \tag{A-27}$$

$$\langle {q_i}'^2 \rangle = \int_{\mathbb{R}^3} \int_{\mathbb{R}} {q_i}'^2 f_i \, \mathrm{d}q_i \, \mathrm{d}\mathbf{c}_i. \tag{A-28}$$

Here $\mathbf{U}_\mathrm{i}$, T_i, $\langle q_i \rangle$ and $\langle {q_i}'^2 \rangle$ are the expected values of the velocity, granular temperature, charge and charge variance of particle i. T is the number-averaged mixture granular temperature. Additionally, the charge-velocity covariance $\langle \mathbf{C}_i {q_i}' \rangle$ is defined as follows:

$$\langle \mathbf{C}_i q_i' \rangle = \int_{\mathbb{R}^3} \int_{\mathbb{R}} \mathbf{C}_i q_i' f_i \, \mathrm{d}q_i \, \mathrm{d}\mathbf{c}_i. \tag{A-29}$$

It should be noted from hereon that the velocity fluctuations of particle 1 and charge fluctuations of particle 2 in a particle pair are not correlated, and vice versa, irrespective of whether both the particles are of the same species or different species. This implies that

$$\langle \mathbf{C}_i q'_j \rangle = \langle \mathbf{C}_j q'_i \rangle = 0. \tag{A-30}$$

Variables of particles of one species are also assumed to be independent and uncorrelated with variables of the other species, i.e.:

$$\langle M_i^a M_j^b \rangle = \langle M_i^a \rangle \langle M_j^b \rangle, \tag{A-31}$$

where M_i^a and M_j^b are, respectively, the moments of order a and b of quantities belonging to species i and species j. Thus, the two-particle PDF f^2 is such that the joint moments are products of the moments of the individual NDFs. In concise form,

$$f^2 = g_{ij} f_i f_j, \tag{A-32}$$

where g_{ij} is the radial distribution function.

A.2.4. Rate of charge diffusion due to particle-particle collisions

The average rate of change of the mean particle charge due to inter-particle collisions between two species is evaluated from the collision integrals [43,44]:

$$\mathbb{C}_{ij}(q_i) = \chi_{q_i}^b - \nabla \cdot \boldsymbol{\theta}_{q_i}^b, \tag{A-33}$$

where

$$\chi_{q_i}^b = \mathrm{d}_{ij}^2 \int_{\mathbf{c}_{12}\cdot\mathbf{k}>0} \int_{\mathbb{R}^6} \int_{\mathbb{R}^2} \left(\frac{dq_i}{dn_c}\right)^b (\mathbf{c}_{ij} \cdot \mathbf{k}) f^2 \, \mathrm{d}q_i \mathrm{d}q_j \mathrm{d}\mathbf{c}_i \mathrm{d}\mathbf{c}_j \mathrm{d}\mathbf{k}, \tag{A-34}$$

and

$$\boldsymbol{\theta}_{q_i}^b = \frac{\mathrm{d}_{ij}^3}{2} \int_{\mathbf{c}_{12}\cdot\mathbf{k}>0} \int_{\mathbb{R}^6} \int_{\mathbb{R}^2} \left(\frac{dq_i}{dn_c}\right)^b (\mathbf{c}_{ij} \cdot \mathbf{k}) \mathbf{k} f^2 \, \mathrm{d}q_i \mathrm{d}q_j \mathrm{d}\mathbf{c}_i \mathrm{d}\mathbf{c}_j \mathrm{d}\mathbf{k}, \tag{A-35}$$

in which $\mathrm{d}_{ij} = (d_i + d_j)/2$ is the average diameter of the two colliding particles.

It should be noted that in the discussion presented in the following sections to obtain closures for the collision integrals, only binary collisions are considered, while the effect of collisions involving more than two particles and of enduring particle contact are ignored. Determining these integrals requires the substitution of the inter-particle charging model from the previous section. To such purpose, we use the modified one-particle PDFs which are obtained through Taylor series expansion about the mid-point between the centers of the two colliding particles [42] as follows:

$$f_i^e = f_i \left[1 - \frac{\mathrm{d}_{ij}}{2} (\mathbf{k} \cdot \nabla) \ln f_i + \cdots \right], \tag{A-36}$$

$$f_j^e = f_j \left[1 + \frac{\mathrm{d}_{ij}}{2} (\mathbf{k} \cdot \nabla) \ln f_j + \cdots \right]. \tag{A-37}$$

Including the effect of a finite particle size in this manner allows the effect of the collisional diffusion flux due to the gradient of charge to be incorporated in the model closure. Based on these considerations, the modified two-particle PDF becomes [42,43]:

$$f^2 = g_{ij} f_i^e f_j^e = g_{ij} f_i f_j \left[1 + \frac{\mathrm{d}_{\mathrm{ij}}}{2} (\mathbf{k} \cdot \nabla) \ln \frac{f_j}{f_i} + \cdots \right], \tag{A-38}$$

where

$$\begin{aligned} (\mathbf{k} \cdot \nabla) \ln \frac{f_j}{f_i} = {} & \frac{{q'_j}^2}{2\langle {q'_j}^2 \rangle^2} \left(\mathbf{k} \cdot \nabla \langle {q'_j}^2 \rangle\right) - \frac{{q'_i}^2}{2\langle {q'_i}^2 \rangle^2} \left(\mathbf{k} \cdot \nabla \langle {q'_i}^2 \rangle\right) - \frac{q'_j}{\langle {q'_j}^2 \rangle} \left(\mathbf{k} \cdot \nabla \langle q_j \rangle\right) \\ & + \frac{q'_i}{\langle {q'_i}^2 \rangle} (\mathbf{k} \cdot \nabla \langle q_i \rangle) + \cdots, \end{aligned} \tag{A-39}$$

where terms involving gradients of granular temperatures and phase volume fractions, and divergence of the barycentric velocity were neglected, consistently with what done in the rest of this work. This is justified observing that the gradient of species charge is a few orders of magnitude higher than the neglected terms, particularly near the wall region [40], which majorly contributes for charge transport in dense granular flows such as those encountered in the systems of interest to the applications mentioned in the introduction. Specifically, this assumption is valid for charging of insulator particles because of their low permittivity. It will be shown in the Appendix that such assumptions allow a convenient form of the charge-velocity covariance to be formulated as well.

The radial distribution function g_{ij} in Eq. A-38 is given [43] as:

$$g_{ij} = \frac{1}{1-2\alpha_{ij}} + \frac{3\mathrm{d_i}\mathrm{d_j}}{\mathrm{d_{ij}}}\frac{\varepsilon}{\left(1-2\alpha_{ij}\right)^2} + 2\left(\frac{\mathrm{d_i}\mathrm{d_j}}{\mathrm{d_{ij}}}\right)^2\frac{\varepsilon^2}{\left(1-2\alpha_{ij}\right)^3}, \tag{A-40}$$

where α_{ij} is the average volume fraction of the two species and:

$$\varepsilon = \frac{2}{3}\pi\left(N_\mathrm{i}\mathrm{d_i^2} + N_\mathrm{j}\mathrm{d_j^2}\right). \tag{A-41}$$

Similarly,

$$g_{ii} = \frac{1}{1-2\alpha_{ij}} + 3\mathrm{d_i}\frac{\varepsilon}{\left(1-2\alpha_{ij}\right)^2} + 2\mathrm{d_i^2}\frac{\varepsilon^2}{\left(1-2\alpha_{ij}\right)^3}. \tag{A-42}$$

A.2.5. Derivation of charge-velocity covariance $\langle \boldsymbol{C_i q_i}' \rangle$

The closure term for the charge-velocity covariance can be obtained by considering the transport equation for $\langle \mathbf{c_i} q_i \rangle$ as follows:

$$\begin{aligned}\frac{\partial}{\partial t}\left(N_i\langle \mathbf{c_i} q_i\rangle\right) + \nabla\cdot\left(N_i\langle \mathbf{c_i}\mathbf{c_i} q_i\rangle\right) \\ = \mathbb{C}_{ii}(\mathbf{c_i} q_i) + \mathbb{C}_{ij}(\mathbf{c_i} q_i) + N_i\left\langle\frac{\partial \mathbf{c_i} q_i}{\partial \mathbf{c_i}}\frac{\mathrm{d}\mathbf{c_i}}{\mathrm{dt}}\right\rangle + N_i\left\langle\frac{\partial \mathbf{c_i} q_i}{\partial q_i}\frac{\mathrm{d}q_i}{\mathrm{dt}}\right\rangle,\end{aligned} \tag{A-43}$$

which, if we ignore all time derivatives, reduces to

$$\nabla\cdot\left(N_i\langle \mathbf{c_i}\mathbf{c_i} q_i\rangle\right) = \mathbb{C}_{ii}(\mathbf{c_i} q_i) + \mathbb{C}_{ij}(\mathbf{c_i} q_i). \tag{8-1}$$

Treating the divergence of terms containing $\mathbf{U}$ and gradients of $\alpha_\mathrm{i}, \rho_\mathrm{i}, T_i$ as negligible compared to gradients of $\langle q_i \rangle$, and also considering the particle temperature and charge variance to be uncorrelated gives:

$$\begin{aligned}\nabla\cdot\left(N_i\langle \mathbf{c_i}\mathbf{c_i} q_i\rangle\right) &= \nabla\cdot\left(N_i\mathbf{U}\langle \mathbf{c_i} q_i\rangle\right) + \nabla\cdot\left(N_i\langle \mathbf{C}_i\mathbf{c_i} q_i\rangle\right) \\ &= \nabla\cdot\left(N_i\langle q_i\rangle\langle \mathbf{C}_i\mathbf{C}_i\rangle\right) = N_i\frac{T_i}{m_i}\nabla\langle q_i\rangle.\end{aligned} \tag{A-44}$$

Hence, we have:

$$\mathbb{C}_{ii}(\mathbf{c_i} q_i) + \mathbb{C}_{ij}(\mathbf{c_i} q_i) = N_i\frac{T_i}{m_i}\nabla\langle q_i\rangle. \tag{8-2}$$

Evaluating the integrals A-29, we obtain:

$$\langle \mathbf{C}_i q_i' \rangle = \frac{-T_i \nabla \langle q_i \rangle}{\left\{ m_i g_{ij} N_j \mathrm{d}_{\mathrm{ij}}^2 M_j (1+e) \left[\left(\frac{4\pi m_{ij} T}{m_i m_j} \right)^{\frac{1}{2}} \left(1 - \frac{\theta_i + \theta_j}{T} \right) \right. \right.}$$

$$+ \frac{3}{\sqrt{2}} \left(\frac{\pi}{m_{ij} T m_i m_j} \right)^{\frac{1}{2}} \left(m_i \theta_i + m_j \theta_j \right)$$

$$\left. \left. + 2\sqrt{2\pi} \left(\frac{m_{ij} T}{m_i m_j} \right)^{\frac{3}{2}} \frac{1}{T^2} \left(m_i M_j^2 \theta_i + m_j M_i^2 \theta_j \right) \right] \right.$$

$$\left. + \frac{1}{2} m_i g_{ii} N_i \mathrm{d}_i^2 (1+e) \left(\frac{4\pi T_i}{m_i} \right)^{\frac{1}{2}} \right\} \qquad \text{A-45}$$

where

$$m_{ij} = m_i + m_j, \qquad \text{A-46}$$

$$M_i = \frac{m_i}{m_{ij}}, \qquad \text{A-47}$$

and

$$M_j = \frac{m_j}{m_{ij}}. \qquad \text{A-48}$$

A.2.6. Charge transport equation with wall boundary conditions

Evaluating the collision integrals (Eqns. A-34 and A-35) gives us the following form for the charge transport equation:

$$\frac{\partial}{\partial t} (N_{\mathrm{i}} \langle q_i \rangle) + \nabla \cdot (N_{\mathrm{i}} \langle q_i \rangle \mathbf{U}) = N_c(q_i) - \nabla \cdot \mathbf{q}_i \qquad \text{A-49}$$

where the non-advective charge flux is:

$$\mathbf{q}_i = N_i\langle \mathbf{C}_i q_i' \rangle - 2^{\frac{9}{10}}\sqrt{\pi} g_{ii} N_i^2 \mathrm{d_i^3}\Gamma\left(\frac{2}{5}\right)\left(\frac{2T_i}{m_i}\right)^{\frac{9}{10}}\left(\frac{7}{90}K_{eq}^m \nabla\varphi_E + \frac{19}{180}K_i^m \mathrm{d_i}\nabla\langle q_i\rangle\right)$$
$$- 2^{\frac{9}{10}}\sqrt{\pi} g_{ij} N_i N_j \mathrm{d_{ij}^3}\Gamma\left(\frac{2}{5}\right)\left(\frac{m_{ij}T}{m_i m_j}\right)^{\frac{9}{10}}\left\{K_{eq}^b \nabla\varphi_E\left[\frac{7}{90}\left(1 - \frac{\theta_i + \theta_j}{T}\right)\right.\right.$$
$$\left. + \frac{7}{60}\left(\frac{m_i\theta_i + m_j\theta_j}{m_{ij}T}\right) + \frac{14}{75}\left(\frac{m_i M_j^2\theta_i + m_j M_i^2\theta_j}{T^2}\right)\right]$$
$$\left. + \frac{19}{360}\left(K_i^b \nabla\langle q_i\rangle + K_j^b \nabla\langle q_j\rangle\right)\mathrm{d_{ij}}\right\}, \tag{A-50}$$

and

$$N_c(q_i) = 2^{\frac{9}{10}}\sqrt{\pi} g_{ij} N_i N_j \mathrm{d_{ij}^2}\Gamma\left(\frac{2}{5}\right)\left(\frac{m_{ij}}{m_i m_j}T\right)^{\frac{9}{10}}$$
$$\times\left\{\left(-K_i^b\langle q_i\rangle + K_j^b\langle q_j\rangle\right)\left[\frac{56}{95}\left(1 - \frac{\theta_i + \theta_j}{T}\right) + \frac{32}{95}\left(\frac{m_i\theta_i + m_j\theta_j}{m_{ij}T}\right)\right.\right.$$
$$\left. + \frac{672}{475}\left(\frac{m_{ij}\left(m_i M_j^2\theta_i + m_j M_i^2\theta_j\right)}{m_i m_j T}\right)\right]$$
$$+ \frac{56}{95}\left(\frac{m_{ij}}{m_i m_j}T\right)^{-4/5}\left(K_i^b\langle \mathbf{C}_i q_i'\rangle - K_j^b\langle \mathbf{C}_j q_j'\rangle\right)\cdot\left(\mathbf{v}_i - \mathbf{v}_j\right)$$
$$\left. + \frac{56}{95}\left(-M_i K_i^b\langle \mathbf{C}_i q_i'\rangle + M_j K_j^b\langle \mathbf{C}_j q_j'\rangle\right)\left(\frac{M_i\mathbf{v}_i + M_j\mathbf{v}_j}{T}\right)\right\}, \tag{A-51}$$

with

$$\mathbf{v}_i = \mathbf{U}_i - \mathbf{U} \tag{A-52}$$

and

$$\mathbf{v}_j = \mathbf{U}_j - \mathbf{U}. \tag{A-53}$$

Eq. A-51 is a second-order partial differential equation involving $\langle q_i\rangle$, $\langle q_j\rangle$ and φ_E. The corresponding charge transport equation for $\langle q_j\rangle$ can be obtained by replacing *i* with *j* and *j* with *i* in equations A-51-A-53. These two transport equations along with the Poisson equation for the electric potential (Eq. A-4) define the entire electrostatic model. The wall is assumed to be either

grounded or insulated, resulting in $\varphi_E = 0$ or $\nabla\varphi_E = 0$, respectively. The wall boundary condition for $\langle q_i \rangle$ is the same reported in Ray et al. (2019) and is given by

$$q_{w,i} = q_{\infty,\mathrm{i}} \left[1 + \frac{z_0}{V_{c,i}} \left(\mathbf{E} + \frac{\mathbf{q}_{i,wall}}{k_{w,i}} \right) \cdot \mathbf{n} \right], \tag{A-54}$$

where

$$k_{w,i} = \frac{12}{35\sqrt{\pi}} 2^{\frac{9}{10}} g_{ii} N_i \Gamma\left(\frac{2}{5}\right) \left(\frac{T_i}{m_i}\right)^{\frac{9}{10}} k_c k_{s,w,i} \varepsilon_0 \varepsilon_r. \tag{A-55}$$

and $\mathbf{q}_{i,wall}$ is the non-advective diffusion flux at the wall from Eq. A-52. Boundary conditions can be obtained for $\langle q_j \rangle$ by replacing *i* with *j* in Eqns. A-56 and A-57.

A.3. Simulation results and discussion

A simple 1-D domain representing the width of the fluidized bed was chosen for solving the equations at steady state, in order to simply show what might be expected when the electrostatic model would be coupled with the hydrodynamic model. The coupled steady-state PDEs are solved in Wolfram Mathematica 12.0 using the automatic integrator NDSolve [45], which adapts the choice of the integrator to address the stiffness of the set of PDEs. This approach is particularly required in the charge diffusion of insulating particles since steep gradients are expected near the wall boundary. To resolve these large gradients, a high accuracy in the calculations is required, consequently the working precision (number of digits maintained during the calculation) was set to 50. Allowing Mathematica to automatically choose the precision causes it to use the lowest precision of the specified parameters, which maybe insufficient for determining converged solutions.

The one-dimensional domain has a width of 0.1 m, which is the same as was used in the monodisperse simulations [40], and the phases have no mean velocity. The saturation charge density varies inversely with the particle diameter as per the findings of Chowdhury et al. (2018). The material properties of both the particle species are shown in Table A-1. Even though the hydrodynamics are not simulated, an arbitrary value of the granular temperature was required to perform the calculations. A uniform value of $3 \cdot 10^{-12}$ kg-m^2/s^2 based on bubbling fluidization

simulations of 362 μm particles [40], was assigned to both particle species. The charging efficiency also needed specification and although this has not been validated against transient charge diffusion, a value of $1 \cdot 10^{10}$ (a value of $4 \cdot 10^{11}$ was used in Ray et al. (2019)) was used to obtain a reasonable thickness of the particle layer at the wall without imposing too much difficulty on the numerical method in resolving steep gradients. This was beneficial as a large set of converged solutions could be obtained in the parametric study through iteration without user intervention. The work function V_c has a magnitude of -0.9 eV, as in Ray et al. (2019).

Table A-1: Material properties and parameter values.

Mass density	Young's modulus	Poisson's ratio	Coefficient of restitution	Relative permittivity	V_c	z_0	k_c
(kg/m^3)	(MPa)	-	-	-	(eV)	(nm)	
935	150	0.5	0.8	2.25	-0.9	1.0	$1 \cdot 10^{10}$

In this article, we have studied the effect of the variation of the relative diameters of the two particle species and their volume fractions. Some commonalities for the simulation parameters are mentioned here first. The diameter of particles of species 1 particle is fixed at 400 μm, while that of species 2 is varied. The total volume fraction of the two particle species is always 0.6, or in other words the void fraction is held constant at 0.4. The variation of maximum electric potential and average particle charge density with diameter ratio and volume fraction is shown as surface plots in Figure . The average charge density is the volume averaged charge density of both the particle species.

(a) (b)

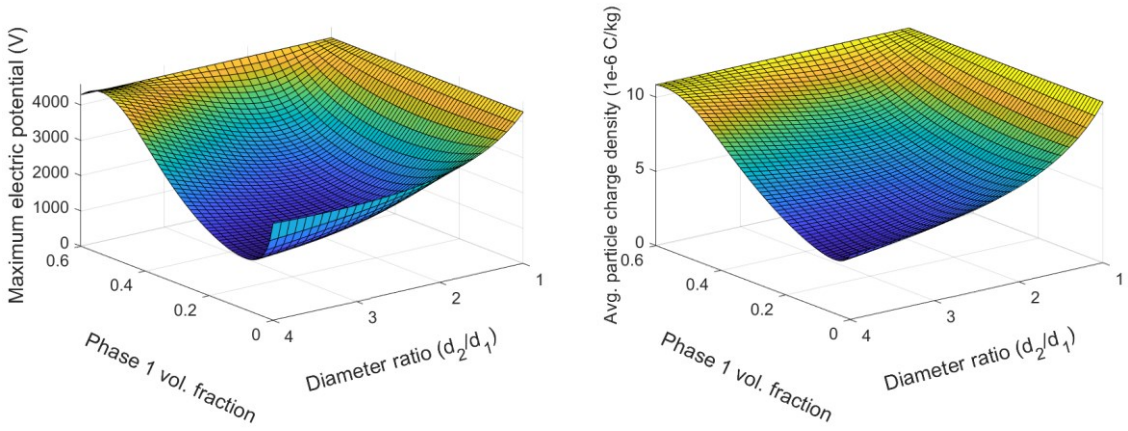

Figure A-1: Variation of a) maximum electric potential and b) average particle charge density, with phase volume fraction and diameter ratio (color represents the magnitude of the quantity reported on the vertical axis).

In Figure A-1, the axes corresponding to a diameter ratio of 1.0 and volume fraction of species 1 of 0.6 represent monodisperse scenarios with only species 1 being present, and therefore no variation is seen along these axes. The maximum electric potential has at least one inflection point with increasing volume fraction of species 2 for constant diameter ratios (Figure A-1a). Along lines of constant volume fraction, it has no, one or more inflection points as the particle diameter ratio changes. The average particle charge density also shows similar variation along lines of constant volume fraction (Figure A-1b). For constant diameter ratios, a monotonically decreasing trend is observed with increasing volume fraction of species 2. These variations are also seen in Figure A-2 and Figure A-3, where the profiles of electrostatic variables are shown along the x-direction near the wall region (boundary layer) up to 0.01 m. Figure A-2 illustrates results for fixed volume fractions ($\alpha_1 = 0.3$, $\alpha_2 = 0.3$) and varying diameter ratio of the two species, while Figure A-3 does the same for fixed sizes ($d_1 = 400$ μm, $d_2 = 800$ μm) and varying volume fraction.

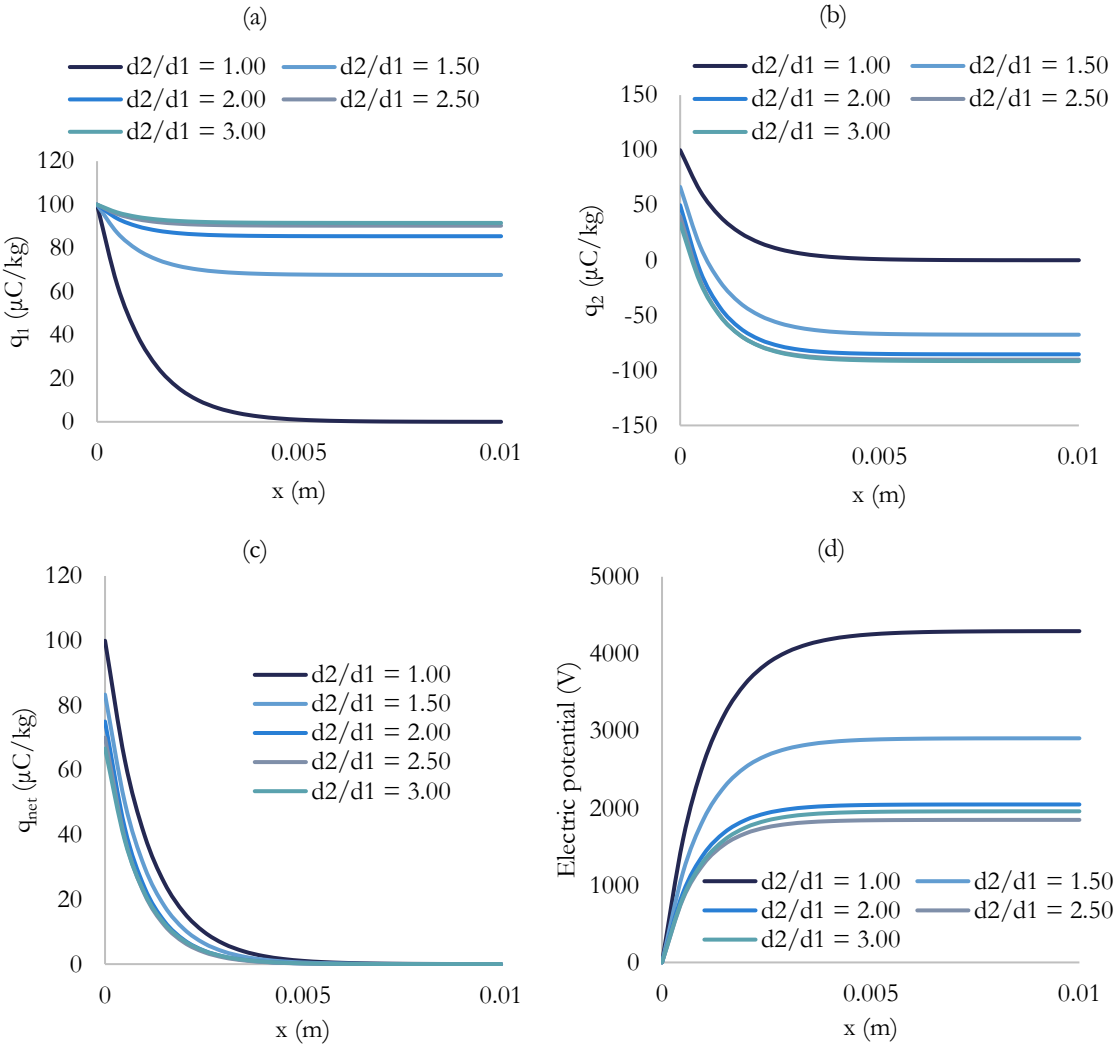

Figure A-2: Comparison of profiles of a) species 1 particle charge density, b) species 2 particle charge density, c) average charge density and d) electric potential near the wall region, when the diameter of species 2 particles is varied.

At the wall, the phase charge density is saturated, and it decreases away from the wall for both species (Figure A-2a-b, Figure A-3a-b). With increasing diameter ratio, the gradient gets shallower for species 1 and steeper for species 2 (Figure A-2a-b). As a result, the polarity of species 2 particles changes after a certain distance from the wall (when diameters are different) (Figure A-2b). The distance at which this happens gets shorter with increasing diameter ratio. This shows the capability of the model of predicting bipolar charging even without any work function difference between species. Even though the charge of species 2 is high in magnitude, it is neutralized by a similar magnitude of opposite charge of species 1, resulting in negligible average

charge density away from the wall region (Figure A-2c). The average charge density is smaller at every point in the x-direction for a higher diameter ratio (Figure A-2c), which explains the trend in Figure b. The maximum electric potential has a minimum somewhere in between d_2 = 800 µm and d_2 = 1200 µm (Figure A-2d), which was also seen in Figure A-1a. Moreover, the potential is either lower or higher at every location along the x-axis when comparing profiles of any of the diameter ratios (Figure A-2d).

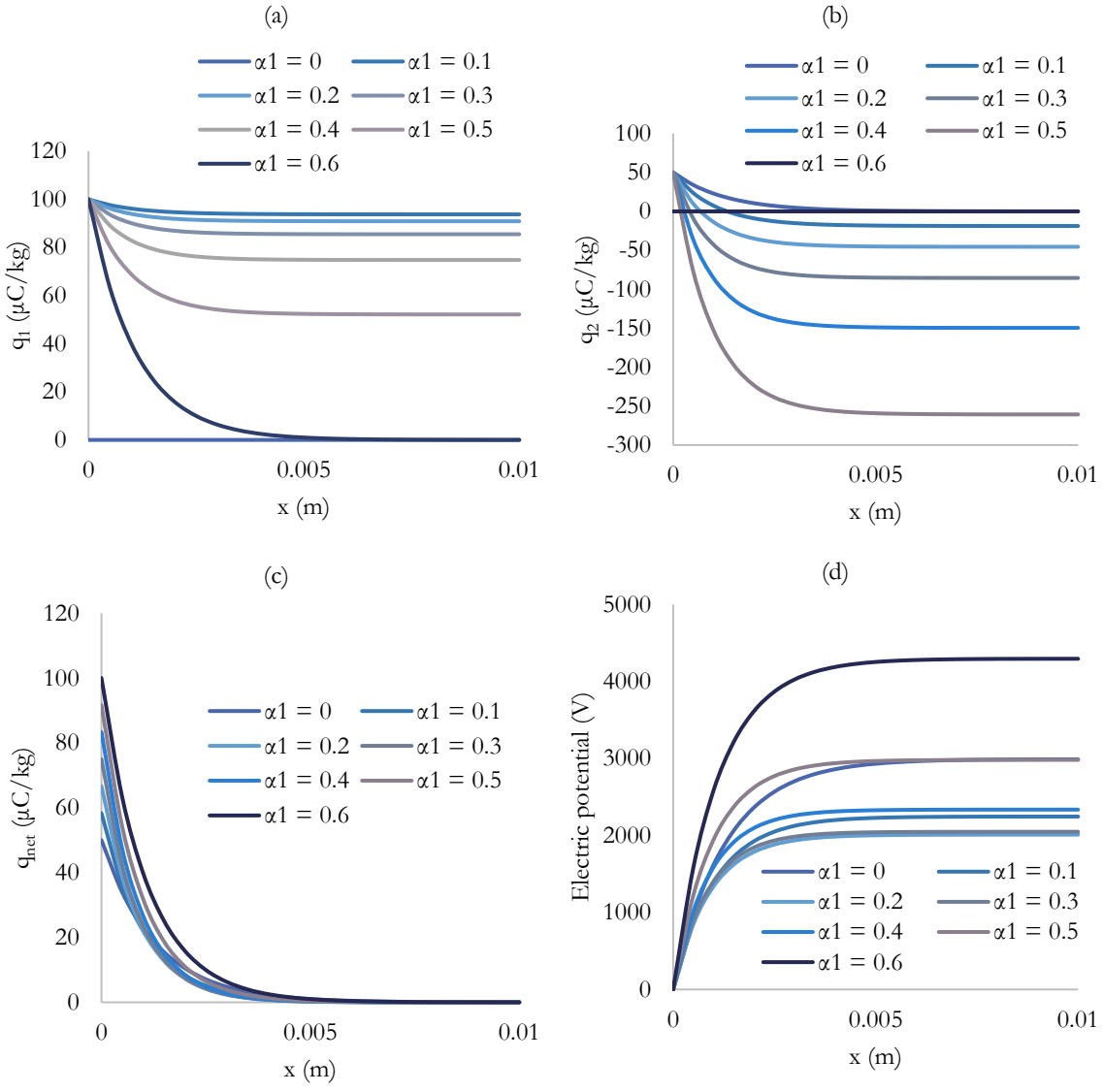

Figure A-3: Comparison of profiles of a) species 1 particle charge density, b) species 2 particle charge density, c) average charge density and d) electric potential near the wall region, when the phase volume fractions are varied.

When the particle diameters are kept fixed (d_1 = 400 μm, d_2 = 800 μm) and the volume fractions are varied maintaining $\alpha_1 + \alpha_2 = 0.6$, the simulations predict that gradients of both species charge densities gets steeper as the volume fraction of species 1 (smaller diameter) is increased (Figure A-3a-b). Bipolar charging is again observed, and the distance from the wall, where the polarity reverses gets shorter with increasing α_1 (Figure A-3b), due to steeper gradients. The average charge density at the wall (Figure A-3c) is more with larger α_1, since the saturation charge density of species 1 is higher. The maximum electric potential showed an inflection between $\alpha_1 = 0.1$ and $\alpha_1 = 0.3$ (Figure A-3d), as was seen in Figure a as well.

A.3.1. Bipolar charging

Bipolar charging is observed in the simulations presented in this work when the diameters of the two species are not the same, even for small volume fractions of one of the species. Bipolar charging of powders made of the same material has been reported in previous literature [47–50] among others. In most cases, the smaller particles tended to have negative average charge while the larger ones acquired positive average charge. Previous works have tried to explain this in terms of particle-size correction of the work function and effective capacitance of the colliding particles as well as the dependence of surface roughness and shape [51] on particle size. The former two impose a negligible effect while the last one could be assumed to be not system independent [51]. Lacks et. al. [52,53] explained the preferential negative charging of smaller particles with their trapped electron model, which assumes that electrons are transferred from higher energy states on one particle to lower energy states on the other particle. Since smaller particles have less surface area, they are assumed to possess lower number of high energy electrons that could be transferred to the larger particles in comparison to the number of high energy electrons that can be supplied by the larger particles to the smaller ones. This was proposed to be causing bipolar charging, with smaller particles ending up with negative polarity. However, it was also mentioned that it is possible for a redistribution of electrons between lower energy levels of the two colliding particles as well reversal of electron transfer due to the electric field produced by the surface charges, both of which could negate the bipolar intensity [52]. Furthermore, their model fails to explain the positive charging of smaller particles in experiments [48]

The trends of electrification (Figure A-1 and Figure A-3) are neither monotonic nor obvious and do not naturally explain bipolar charging. To further understand this, we needed to see how the

diffusivity is varying at different diameter ratios and volume fractions. For the parameters used in this work, it was seen that Eq. A-51 could be approximately written, for the two species, as

$$D_{qi}\nabla^2\langle q_i\rangle + D_{\varphi i}\nabla^2\varphi_E + \cdots = 0 \qquad \text{A-56}$$

and

$$D_{qj}\nabla^2\langle q_j\rangle + D_{\varphi j}\nabla^2\varphi_E + \cdots = 0, \qquad \text{A-57}$$

where the other terms are neglected due to their much lower orders of magnitude. Therefore, these can be rewritten as

$$\nabla^2\langle q_i\rangle + \frac{D_{\varphi i}}{D_{qi}}\nabla^2\varphi_E = 0 \qquad \text{A-58}$$

and

$$\nabla^2\langle q_j\rangle + \frac{D_{\varphi j}}{D_{qj}}\nabla^2\varphi_E = 0. \qquad \text{A-59}$$

The diffusivity ratio $\frac{D_{\varphi i}}{D_{qi}}$ dictates the relative slopes of $\langle q_i\rangle$ and φ_E. A higher diffusivity ratio will lead to steeper charge density profiles, and the same argument holds between $\frac{D_{\varphi j}}{D_{qj}}$ and $\langle q_j\rangle$ as well. This implies that bipolar charging in these simulations is being driven by the electric field that develops due to the evolution of particle charge. The possibility of an external field driving bipolar charging had been discussed before [51] but it did not explicitly mention the role of the inherent electric field produced by the charge accumulated in the bed. The diffusivity ratios have been plotted as a function of the phase volume fraction and diameter ratios in Figure A-4. The ratio $D_{\varphi i}/D_{qi}$ decreases monotonically (Figure A-4a) with increasing volume fraction of species 2 as well diameter ratio. Thus, $\nabla\langle q_i\rangle$ is also expected to have lowering of magnitude and is confirmed by Figure A-1a and Figure A-2a, where $\langle q_i\rangle$ falls off less rapidly from the wall. The diffusivity ratio of species 2 $D_{\varphi j}/D_{qj}$ diminishes monotonically (Figure A-4b) with increasing volume fraction of species 2 and similarly $\nabla\langle q_j\rangle$ is expected to be lower. This effect is asserted in Figure A-3b. With increasing diameter ratio however, an inflection is obtained between $d_2/d_1 = 2.0$ and $d_2/d_1 = 3.0$. This is not affirmed at first glance from Figure A-2b, since the magnitude of charge seems to be reducing with higher ratios. A close inspection (Figure A-2b) shows that the magnitude of $\nabla\langle q_j\rangle$ is indeed higher at the wall for $d_2/d_1 = 2.0$ than the other ratios. The illusion of an overall

monotonic reduction manifests from the lower charge density at the wall for larger diameters (Figure A-2b), since the saturation density is inversely proportional to the diameter.

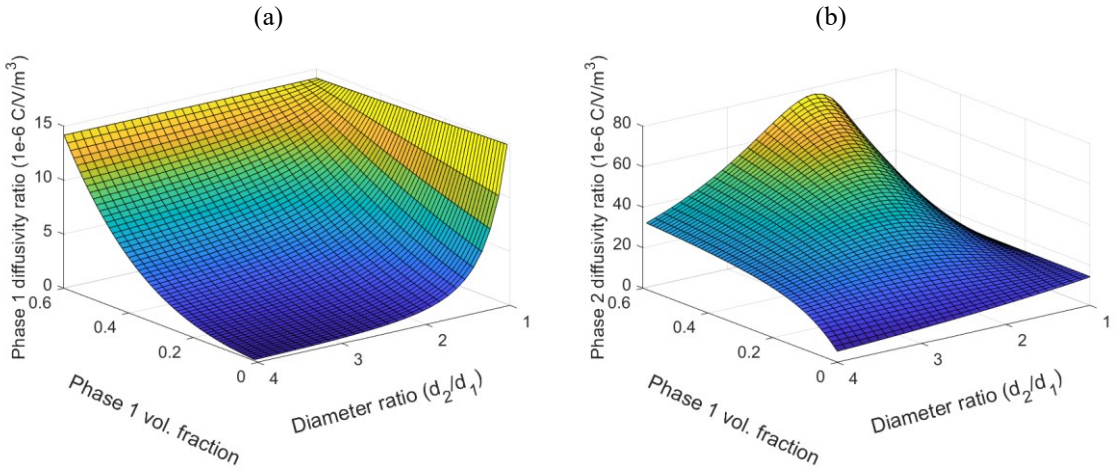

Figure A-4: Variation of diffusivity ratio of a) species 1 and b) species 2, with phase volume fraction and diameter ratio (color represents the magnitude of the quantity reported on vertical axis).

The variations in the slopes of $\langle q_i \rangle$ and $\langle q_j \rangle$ lead to bipolar charging as seen in the plots. Physically however, this would mean that particles of the two species will tend to move in opposite directions under the influence of the electrostatic force, given by Eq. A-2, unless the electric field is null at that location. This is verified in Figure A-5 (b, d), where large forces act on particles of species 2 in certain regions. Since the magnitude of species 2 charge is greater for higher diameter ratios and species 1 volume fractions, the same is seen for the electrostatic force as well. For every scenario, species 1 particles experience an electrostatic force only towards the wall, which is the same as was seen in monodisperse simulations. This would be balanced by the kinetic and, if accounted by the model, by frictional normal stress acting away from the wall for particles on that boundary. In bubbling fluidized beds, the pressure from the center of the bed is insufficient to do so and thus the particles of species 2 would be expected to be transported to the center of the bed. Thus, either of the following or both may be expected. Firstly, some particles of species 2 may acquire positive charge and migrate to form a region that is predominantly positively charged near the center of the bed. Secondly, particles of both species may acquire such an amount of charge to have no electric field in regions having opposite polarities for the two species. Given the findings of this paper, it

would be very interesting to see the results when the hydrodynamic model is coupled, which will provide a more reliable validation of the capability of the model of predicting bipolar charging.

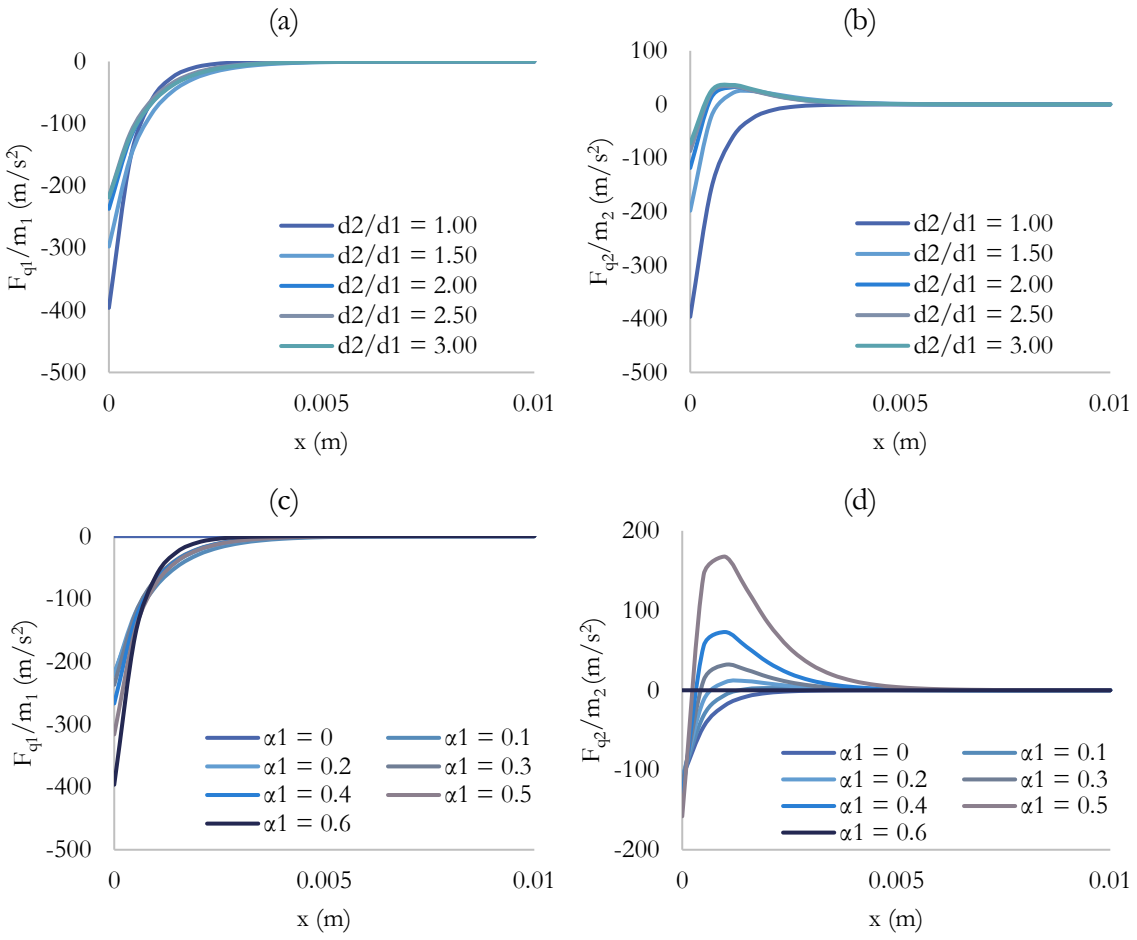

Figure A-5: Comparison of electrostatic force profiles of a) species 1 and b) species 2 particles when diameter ratio is varied, and of c) species 1 and d) species 2 particles when volume fraction is varied.

A.4. Conclusion

A Eulerian model for charge separation and transport in bi-disperse hard spheres has been obtained in this work. The discrete charging models [23,31] were adopted to describe the evolution of the particle charge due to individual collisions, similarly to what done by Ray et al. (2019). Closures for the inter-particle charge transport were obtained based on the kinetic theory of Jenkins and Mancini (1987). The effect of charge-velocity covariance on charge transport was considered. The behavior of the resulting transport equations was investigated through a parametric study in a one-

dimensional problem representing the width of an experimental fluidization column. In this case, the species had no mean velocity and hydrodynamics was not simulated, but a uniform granular temperature was assumed for both particle species. The same material properties were assigned to the two species, while the size and volume fractions were treated as the varying parameters. Bipolar charging was predicted when the two species had different sized particles, for any volume fraction. This was mainly attributed to the differences of diffusivity ratio of the two species. The smaller particles had the same polarity in every case and in all regions of the domain, whereas the larger particles exhibited opposite polarity. However, investigation of the electrostatic force acting on the larger particles showed that this would lead to the movement of these particles towards the center of the bed and would therefore yield a spatial charge distribution different from that shown in this paper. Demonstrative prediction thus necessitates coupling of the bi-disperse hydrodynamic model and execution of full-scale simulations, which will be performed in future work. It is interesting to note that even though the surface state theory-based model of Schein et al. (1992) does not predict bipolar charging in the absence of work function difference or an externally applied electric field, the model in conjunction with the charge transport (A-51, A-53) and Poisson (A-4) equations shows that it is possible. The bipolar charging phenomenon predicted by the simulations was being driven by the resultant electric field due to the charge on the particles. The results indicate that the polarity of the particles is dependent on the expected polarity of a monodisperse particle phase, which is determined by the work function difference between the particle and wall material. If the particle material tends to charge positively, then the smaller particles are expected to have the same polarity and the larger particles could charge negatively, and vice versa. This could be a possible explanation in some cases as to why smaller particles do not always end up charging negatively or positively, and the same idea holds for the larger particles.

Appendix - Derivation of the charge transport equation

The transport of solid particle charge due to collisional and kinetic diffusion is explained here in greater detail. The charge transport equation for particle species *i* was given by

$$\frac{\partial}{\partial t}(N_{\mathrm{i}}\langle q_i\rangle) + \nabla\cdot(N_{\mathrm{i}}\langle q_i\rangle\mathbf{U}) + \nabla\cdot(N_{\mathrm{i}}\langle\mathbf{C}_i q_i'\rangle) = \mathbb{C}_{ii}(q_i) + \mathbb{C}_{ij}(q_i). \qquad \text{A-60}$$

Here $\mathbb{C}_{ii}(q_i)$ and $\mathbb{C}_{ij}(q_i)$ are the collision integrals corresponding to collisions with particles of the same species i and with the other species j, respectively. The following formula for the expected value of products of central moments was used frequently in the evaluation of such integrals:

$$\langle a_i a_j a_k a_l \rangle = \langle a_i a_j \rangle \langle a_k a_l \rangle + \langle a_i a_k \rangle \langle a_j a_l \rangle + \langle a_i a_l \rangle \langle a_j a_k \rangle. \quad \text{A-61}$$

Here a_i, a_j, a_k, a_l can be individual variables raised to real powers or even constant values (e.g. substitute 1 for one of a variable if there are less than 4 variables). If a pair, a_i, a_j is such that a_i and a_j are independent of each other, then the expected value is simply the product of the individual moments, i.e.

$$\langle a_i a_j \rangle = \langle a_i \rangle \langle a_j \rangle. \quad \text{A-62}$$

However, if they are correlated, then there is the additional covariance term:

$$\langle a_i a_j \rangle = \langle a_i \rangle \langle a_j \rangle + \langle a'_i a'_j \rangle. \quad \text{A-63}$$

Derivation of $\langle \mathrm{C}_i q_i' \rangle$

Based on the assumptions of sections A.2.5, the transport equation for $\langle \mathbf{C}_i q_i' \rangle$ reduced to (Eq. (8-2))

$$\mathbb{C}_{ii}(\mathbf{c}_i q_i) + \mathbb{C}_{ij}(\mathbf{c}_i q_i) = N_i \frac{T_i}{m_i} \nabla \langle q_i \rangle, \quad \text{A-64}$$

where

$$\mathbb{C}_{ij}(\mathbf{c}_i q_i) = \boldsymbol{\chi}^b_{\mathbf{c}q} - \nabla \cdot \bar{\bar{\theta}}^b_{\mathbf{c}q}, \quad \text{A-65}$$

with

$$\boldsymbol{\chi}^b_{\mathbf{c}q} = \mathrm{d}_{\mathrm{ij}}^2 \int_{\mathbf{c}_{12}\cdot\mathbf{k}>0} \int_{\mathbb{R}^6} \int_{\mathbb{R}^2} \left(\frac{d\mathbf{c}_i q_i}{dn_c} \right)^b (\mathbf{c}_{ij} \cdot \mathbf{k}) f^2 \, \mathrm{d}q_i \mathrm{d}q_j \mathrm{d}\mathbf{c}_i \mathrm{d}\mathbf{c}_j \mathrm{d}\mathbf{k}, \quad \text{A-66}$$

and

$$\bar{\bar{\theta}}^b_{\mathbf{c}q} = \frac{\mathrm{d}_{\mathrm{ij}}^3}{2} \int_{\mathbf{c}_{12}\cdot\mathbf{k}>0} \int_{\mathbb{R}^6} \int_{\mathbb{R}^2} \left(\frac{d\mathbf{c}_i q_i}{dn_c} \right)^b (\mathbf{c}_{ij} \cdot \mathbf{k}) \mathbf{k} f^2 \, \mathrm{d}q_i \mathrm{d}q_j \mathrm{d}\mathbf{c}_i \mathrm{d}\mathbf{c}_j \mathrm{d}\mathbf{k}. \quad \text{A-67}$$

Here

$$\left(\frac{d\mathbf{c}_i q_i}{dn_c}\right)^b = q_i\left(\frac{d\mathbf{c}_i}{dn_c}\right)^b + \mathbf{c}_i\left(\frac{dq_i}{dn_c}\right)^b + \left(\frac{dq_i}{dn_c}\right)^b\left(\frac{d\mathbf{c}_i}{dn_c}\right)^b, \tag{A-68}$$

$$\left(\frac{d\mathbf{c}_i}{dn_c}\right)^b = -\left(\frac{d\mathbf{c}_j}{dn_c}\right)^b = \frac{1}{2}(1+e)\big(\mathbf{c}_{ij}\cdot\mathbf{k}\big)\mathbf{k}, \tag{A-69}$$

and

$$\left(\frac{dq_i}{dn_c}\right)^b = -\left(\frac{dq_j}{dn_c}\right)^b = \left[K_v^b\emptyset_{ij} - K_i^b q_i + K_j^b q_j + K_{eq}^b(\mathbf{E}\cdot\mathbf{k})\right]\big(\mathbf{c}_{\mathrm{ij}}\cdot\mathbf{k}\big)^{4/5}. \tag{A-70}$$

Now

$$\mathbb{C}_{ii}(\mathbf{c}_i q_i) = \boldsymbol{\chi}_{\mathbf{c}q}^m - \nabla\cdot\theta_{\mathbf{c}q,}^m \tag{A-71}$$

with

$$\boldsymbol{\chi}_{\mathbf{c}q}^m = \frac{\mathrm{d}_{\mathrm{ii}}^2}{2}\int\limits_{\mathbf{c}_{12}\cdot\mathbf{k}>0}\int\limits_{\mathbb{R}^6}\int\limits_{\mathbb{R}^2}\left[\left(\frac{d\mathbf{c}_{i1}q_{i1}}{dn_c}\right)^m + \left(\frac{d\mathbf{c}_{i2}q_{i2}}{dn_c}\right)^m\right](\mathbf{c}_{i12}\cdot\mathbf{k})f^2\mathrm{d}q_{i1}\mathrm{d}q_{i2}\mathrm{d}\mathbf{c}_{i1}\mathrm{d}\mathbf{c}_{i2}\mathrm{d}\mathbf{k} \tag{A-72}$$

and

$$\theta_{\mathbf{c}q}^m = \frac{\mathrm{d}_{\mathrm{ii}}^3}{2}\int\limits_{\mathbf{c}_{12}\cdot\mathbf{k}>0}\int\limits_{\mathbb{R}^6}\int\limits_{\mathbb{R}^2}\left(\frac{d\mathbf{c}_{i1}q_{i1}}{dn_c}\right)^m \times \big(\mathbf{c}_{ij}\cdot\mathbf{k}\big)\mathbf{k}f^2\,\mathrm{d}q_{i1}\mathrm{d}q_{i2}\mathrm{d}\mathbf{c}_{i1}\mathrm{d}\mathbf{c}_{i2}\mathrm{d}\mathbf{k}, \tag{A-73}$$

where

$$\left(\frac{d\mathbf{c}_{i1}q_{i1}}{dn_c}\right)^m = q_{i1}\left(\frac{d\mathbf{c}_{i1}}{dn_c}\right)^m + \mathbf{c}_{i1}\left(\frac{dq_{i1}}{dn_c}\right)^m + \left(\frac{dq_{i1}}{dn_c}\right)^m\left(\frac{d\mathbf{c}_{i1}}{dn_c}\right)^m, \tag{A-74}$$

$$\left(\frac{d\mathbf{c}_{i2}q_{i2}}{dn_c}\right)^m = q_{i2}\left(\frac{d\mathbf{c}_{i2}}{dn_c}\right)^m + \mathbf{c}_{i1}\left(\frac{dq_{i2}}{dn_c}\right)^m + \left(\frac{dq_{i2}}{dn_c}\right)^m\left(\frac{d\mathbf{c}_{i2}}{dn_c}\right)^m, \tag{A-75}$$

$$\left(\frac{d\mathbf{c}_{i1}}{dn_c}\right)^m = -\left(\frac{d\mathbf{c}_{i2}}{dn_c}\right)^m = \frac{1}{2}(1+e)(\mathbf{c}_{i12}\cdot\mathbf{k})\mathbf{k}, \tag{A-76}$$

and

$$\left(\frac{dq_{i1}}{dn_c}\right)^m = -\left(\frac{dq_{i2}}{dn_c}\right)^m = \left[K_i^m(q_{i2} - q_{i1}) + K_{eq}^m(\mathbf{E}\cdot\mathbf{k})\right](\mathbf{c}_{i12}\cdot\mathbf{k})^{4/5}. \quad \text{A-77}$$

For practical applications:

$$\langle \mathbf{c}_i \left(\frac{dq_i}{dn_c}\right)^b \rangle \ll \langle q_i \left(\frac{d\mathbf{c}_i}{dn_c}\right)^b \rangle \quad \text{A-78}$$

and

$$\langle \mathbf{c}_{i1} \left(\frac{dq_{i1}}{dn_c}\right)^m \rangle \ll \langle q_{i1} \left(\frac{d\mathbf{c}_{i1}}{dn_c}\right)^m \rangle. \quad \text{A-79}$$

The order of magnitude of $d\mathbf{c}_i/dn_c$ is same as that of $\mathbf{c}_i$, while that of dq_i/dn_c is at least two orders lower than q_i as per Eqns. A-70 and A-77 and experimental values of k_c [46]. This justifies the arguments of Eqns. A-78 and A-79.

Hence terms containing $\left(\frac{dq_i}{dn_c}\right)^b$ and $\left(\frac{dq_{i1}}{dn_c}\right)^m$ are neglected. Therefore:

$$\left(\frac{d\mathbf{c_i}q_{\boldsymbol{i}}}{dn_c}\right)^b \approx q_i \left(\frac{d\mathbf{c}_i}{dn_c}\right)^b, \quad \text{A-80}$$

$$\left(\frac{d\mathbf{c}_{i1}q_{i1}}{dn_c}\right)^m \approx q_{i1} \left(\frac{d\mathbf{c}_{i1}}{dn_c}\right)^m, \quad \text{A-81}$$

$$\left(\frac{d\mathbf{c}_{i2}q_{i2}}{dn_c}\right)^m \approx q_{i2} \left(\frac{d\mathbf{c}_{i2}}{dn_c}\right)^m. \quad \text{A-82}$$

Using the assumptions of Section A.2.3 and the two-particle PDF given by Eqns. A-32 and A-40, such that only source term contributions are included and collisional fluxes are neglected, the associated integrals yield:

$$\mathbb{C}_{ij}(\mathbf{c_i}q_i) = \boldsymbol{\chi}^b_{\mathbf{c}q} = g_{ij}N_iN_j\mathrm{d}_{\mathrm{ij}}^2M_j(1+e)\left[\sqrt{2\pi}\left(\frac{2m_{ij}T}{m_im_j}\right)^{\frac{1}{2}}\left(1-\frac{\theta_i+\theta_j}{T}\right)\right.$$
$$+\frac{3}{\sqrt{2}}\sqrt{\pi}\left(\frac{1}{m_{ij}Tm_im_j}\right)^{\frac{1}{2}}\left(m_i\theta_i+m_j\theta_j\right) \qquad \text{A-83}$$
$$\left.+2\sqrt{2\pi}\left(\frac{m_{ij}T}{m_im_j}\right)^{\frac{3}{2}}\frac{1}{T^2}\left(m_iM_j^2\theta_i+m_jM_i^2\theta_j\right)\right],$$

and

$$\mathbb{C}_{ii}(\mathbf{c_i}q_i) = \boldsymbol{\chi}^m_{\mathbf{c}q} = g_{ii}N_i^2\mathrm{d}_{\mathrm{i}}^2\frac{1}{2}(1+e)\sqrt{2\pi}\left(\frac{2T_i}{m_i}\right)^{\frac{1}{2}}. \qquad \text{A-84}$$

Note that $\boldsymbol{\chi}^m_{\mathbf{c}q}$ could have been obtained from $\boldsymbol{\chi}^b_{\mathbf{c}q}$ by replacing terms having subscript *j* with *i* and then simplifying algebraically. In the preceding section, terms with superscript *b* and *m* correspond to encounters between particles of different species and of the same phase respectively.

Collisional diffusion of $\langle q_i \rangle$

To solve Eq. A-60, we also need to evaluate the integral

$$\mathbb{C}_{ij}(q_i) = \chi^b_{q_i} - \nabla\cdot\boldsymbol{\theta}^b_{q_i}, \qquad \text{A-85}$$

where

$$\chi^b_{q_i} = \mathrm{d}_{\mathrm{ij}}^2\int\limits_{\mathbf{c}_{12}\cdot\mathbf{k}>0}\int\limits_{\mathbb{R}^6}\int\limits_{\mathbb{R}^2}\left(\frac{dq_i}{dn_c}\right)^b\left(\mathbf{c}_{ij}\cdot\mathbf{k}\right)f^2\,\mathrm{d}q_i\mathrm{d}q_j\mathrm{d}\mathbf{c}_i\mathrm{d}\mathbf{c}_j\mathrm{d}\mathbf{k}, \qquad \text{A-86}$$

and

$$\boldsymbol{\theta}^b_{q_i} = \frac{\mathrm{d}_{\mathrm{ij}}^3}{2}\int\limits_{\mathbf{c}_{12}\cdot\mathbf{k}>0}\int\limits_{\mathbb{R}^6}\int\limits_{\mathbb{R}^2}\left(\frac{dq_i}{dn_c}\right)^b\left(\mathbf{c}_{ij}\cdot\mathbf{k}\right)\mathbf{k}f^2\,\mathrm{d}q_i\mathrm{d}q_j\mathrm{d}\mathbf{c}_i\mathrm{d}\mathbf{c}_j\mathrm{d}\mathbf{k}. \qquad \text{A-87}$$

Using the two-particle PDF given by Eqns. A-38-A-40, results in:

$$\chi_{q_i}^b = 2^{\frac{9}{10}}\sqrt{\pi}g_{ij}N_iN_j\mathrm{d}_{\mathrm{ij}}^2\Gamma\left(\frac{2}{5}\right)\left(\frac{m_{ij}T}{m_im_j}\right)^{\frac{9}{10}}\Bigg\{\left(-K_i^b\langle q_i\rangle + K_j^b\langle q_j\rangle\right)\left[\frac{56}{95}\left(1-\frac{\theta_i+\theta_j}{T}\right)\right.$$
$$\left.+\frac{32}{95}\left(\frac{m_i\theta_i+m_j\theta_j}{m_{ij}T}\right)+\frac{672}{475}\left(\frac{m_{ij}\left(m_iM_j^2\theta_i+m_jM_i^2\theta_j\right)}{m_im_jT}\right)\right]$$
$$+\frac{56}{95}\left(K_i^b\langle\mathbf{C}_iq_i'\rangle - K_j^b\langle\mathbf{C}_jq_j'\rangle\right)\cdot\left(\mathbf{v}_i-\mathbf{v}_j\right)\left(\frac{m_{ij}T}{m_im_j}\right)^{-4/5} \qquad \text{A-88}$$
$$+\frac{56}{95}\left(-M_iK_i^b\langle\mathbf{C}_iq_i'\rangle + M_jK_j^b\langle\mathbf{C}_jq_j'\rangle\right)\cdot\left(\frac{M_i\mathbf{v}_i+M_j\mathbf{v}_j}{T}\right)+K_{eq}^b\mathbf{E}_q$$
$$\left.\cdot\frac{\Gamma\left(\frac{2}{5}\right)}{\Gamma\left(\frac{9}{10}\right)}\left[\frac{6}{5\sqrt{2}}\left(\mathbf{v}_i-\mathbf{v}_j\right)\left(\frac{m_{ij}T}{m_im_j}\right)^{-1/2}+\frac{7}{180}\nabla\ln\frac{\langle q'_j{}^2\rangle}{\langle q'_i{}^2\rangle}\mathrm{d}_{\mathrm{ij}}\right]\right\},$$

and

$$\boldsymbol{\theta}_{q_i}^b = 2^{\frac{9}{10}}\sqrt{\pi}g_{ij}N_iN_j\mathrm{d}_{\mathrm{ij}}^3\Gamma\left(\frac{2}{5}\right)\left(\frac{m_{ij}T}{m_im_j}\right)^{\frac{9}{10}}\Bigg\{K_{eq}^b\mathbf{E}\left[\frac{7}{90}\left(1-\frac{\theta_i+\theta_j}{T}\right)\right.$$
$$\left.+\frac{7}{60}\left(\frac{m_i\theta_i+m_j\theta_j}{m_{ij}T}\right)+\frac{14}{75}\left(\frac{m_iM_j^2\theta_i+m_jM_i^2\theta_j}{T^2}\right)\right]$$
$$+\frac{19}{720}\nabla\ln\frac{\langle q'_j{}^2\rangle}{\langle q'_i{}^2\rangle}\left(-K_i^b\langle q_i\rangle+K_j^b\langle q_j\rangle\right)\mathrm{d}_{\mathrm{ij}} \qquad \text{A-89}$$
$$\left.+\frac{19}{360}\left(K_i^b\nabla\langle q_i\rangle+K_j^b\nabla\langle q_j\rangle\right)\mathrm{d}_{\mathrm{ij}}\right\}.$$

If we replace the terms having subscript *j* with subscript *i* and perform algebraic simplification, we arrive at the following expressions for the same species collisions:

$$\chi_{q_i}^m = 0 \qquad \text{A-90}$$

and

$$\boldsymbol{\theta}_{q_i}^m = 2^{\frac{9}{10}}\sqrt{\pi}g_{ii}N_i^2\mathrm{d}_{\mathrm{i}}^3\Gamma\left(\frac{2}{5}\right)\left(\frac{2T_i}{m_i}\right)^{\frac{9}{10}}\left(\frac{7}{90}K_{eq}^m\mathbf{E}+\frac{19}{180}K_i^m\nabla\langle q_i\rangle\mathrm{d}_{\mathrm{i}}\right). \qquad \text{A-91}$$

Deriving expression for charge variance $\langle q'_i{}^2\rangle$

Equations A-88 and A-89 can only be solved if the charge variance distribution is known. Thus, the species i (and species j) charge variance transport given by:

$$\frac{\partial}{\partial t}\left(N_i\langle {q'_i}^2\rangle\right) + \nabla\cdot\left(N_i\langle \mathbf{c}_i {q'_i}^2\rangle\right) = \mathbb{C}_{ii}\left({q'_i}^2\right) + \mathbb{C}_{ij}\left({q'_i}^2\right) + N_i\langle\frac{\partial {q'_i}^2}{\partial \mathbf{c}_i}\frac{\mathrm{d}\mathbf{c}_i}{\mathrm{dt}}\rangle + N_i\langle\frac{\partial {q'_i}^2}{\partial q_i}\frac{\mathrm{d}q_i}{\mathrm{dt}}\rangle, \tag{A-92}$$

needs to be solved as well. If we assume that ${q'_i}^2$ is not dependent on $\mathbf{c}_i$ and that $\langle {q'_i}^2\rangle$ is a quasi-steady variable, we get:

$$\nabla\cdot\left(N_i\langle \mathbf{c}_i {q'_i}^2\rangle\right) = \mathbb{C}_{ii}\left({q'_i}^2\right) + \mathbb{C}_{ij}\left({q'_i}^2\right), \tag{A-93}$$

and

$$\nabla\cdot\left(N_i\langle \mathbf{c}_i {q'_i}^2\rangle\right) = \nabla\cdot\left(N_i\mathbf{U}\langle {q'_i}^2\rangle\right) + \nabla\cdot\left(N_i\langle \mathbf{C}_i {q'_i}^2\rangle\right). \tag{A-94}$$

We further assume that $\mathbf{C}_i$ and ${q'_i}^2$ are uncorrelated and neglect divergence of terms having $\mathbf{U}$ as before. Thus, all we are left with is:

$$\mathbb{C}_{ii}\left({q'_i}^2\right) + \mathbb{C}_{ij}\left({q'_i}^2\right) = 0, \tag{A-95}$$

where

$$\mathbb{C}_{ij}\left({q'_i}^2\right) = \chi^b_{{q'_i}^2} - \nabla\cdot\boldsymbol{\theta}^b_{{q'_i}^2}, \tag{A-96}$$

such that

$$\chi^b_{{q'_i}^2} = \mathrm{d}_{\mathrm{ij}}^2 \int_{\mathbf{c}_{12}\cdot\mathbf{k}>0}\int_{\mathbb{R}^6}\int_{\mathbb{R}^2}\left(\frac{d{q'_i}^2}{dn_c}\right)^b (\mathbf{c}_{ij}\cdot\mathbf{k}) f^2\,\mathrm{d}q_i\mathrm{d}q_j\mathrm{d}\mathbf{c}_i\mathrm{d}\mathbf{c}_j\mathrm{d}\mathbf{k}, \tag{A-97}$$

and

$$\boldsymbol{\theta}^b_{{q'_i}^2} = \frac{\mathrm{d}_{\mathrm{ij}}^3}{2} \int_{\mathbf{c}_{12}\cdot\mathbf{k}>0}\int_{\mathbb{R}^6}\int_{\mathbb{R}^2}\left(\frac{d{q'_i}^2}{dn_c}\right)^b (\mathbf{c}_{ij}\cdot\mathbf{k})\mathbf{k} f^2\,\mathrm{d}q_i\mathrm{d}q_j\mathrm{d}\mathbf{c}_i\mathrm{d}\mathbf{c}_j\mathrm{d}\mathbf{k}, \tag{A-98}$$

where

$$\left(\frac{dq'_i{}^2}{dn_c}\right)^b = 2q'_i\left(\frac{dq_i}{dn_c}\right)^b + \left[\left(\frac{dq_i}{dn_c}\right)^b\right]^2. \tag{A-99}$$

As previously assumed in Eqns. A-78-A-82, we ignore $\left(\frac{dq_i}{dn_c}\right)^{2b}$ and using the 2-particle PDF given by Eqns. A-38-A-40, the two integrals A-97 and A-98 give us:

$$\begin{aligned}\chi^b_{q'_i{}^2} = {} & 2^{\frac{9}{10}}\sqrt{\pi}g_{ij}N_iN_j\mathrm{d}_{\mathrm{ij}}^2\Gamma\left(\frac{2}{5}\right)\left(\frac{m_{ij}T}{m_im_j}\right)^{\frac{9}{10}}\Bigg\{-K_i^b\langle q'_i{}^2\rangle\left[\frac{56}{95}\left(1-\frac{\theta_i+\theta_j}{T}\right)\right. \\ & \left.+\frac{32}{95}\left(\frac{m_i\theta_i+m_j\theta_j}{m_{ij}T}\right)+\frac{672}{475}\left(\frac{m_{ij}\left(m_iM_j^2\theta_i+m_jM_i^2\theta_j\right)}{m_im_jT}\right)\right] \\ & +\frac{56}{95}\langle\mathbf{C}_iq_i{}'\rangle\left[\left(\frac{m_{ij}T}{m_im_j}\right)^{-4/5}\left(\mathbf{v}_i-\mathbf{v}_j\right)\left(K_i^b\langle q_i\rangle-K_j^b\langle q_j\rangle\right)\right. \\ & \left.-\left(\frac{M_i\mathbf{v}_i+M_j\mathbf{v}_j}{T}\right)\left(M_iK_i^b\langle q_i\rangle+M_jK_j^b\langle q_j\rangle\right)\right]+\frac{7}{90}K_{eq}^b\mathbf{E}\cdot\nabla\langle q_i\rangle\mathrm{d}_{\mathrm{ij}}\Bigg\},\end{aligned} \tag{A-100}$$

and

$$\begin{aligned}\boldsymbol{\theta}^b_{q'_i{}^2} = {} & \frac{19}{360}2^{\frac{9}{10}}\sqrt{\pi}g_{ij}N_iN_j\mathrm{d}_{\mathrm{ij}}^4\Gamma\left(\frac{2}{5}\right)\left(\frac{m_{ij}T}{m_im_j}\right)^{\frac{9}{10}}\Big[\left(-K_i^b\langle q_i\rangle+K_j^b\langle q_j\rangle\right)\nabla\langle q_i\rangle \\ & +\frac{3}{2}K_i^b\nabla\langle q'_i{}^2\rangle-\frac{K_i^b}{2}\langle q'_i{}^2\rangle\nabla\ln\langle q'_j{}^2\rangle\Big].\end{aligned} \tag{A-101}$$

If we again substitute terms having subscript *j* with subscript *i* and simplify, we arrive at the following expressions for the monodisperse collisions:

$$\chi^m_{q'_i{}^2} = g_{ii}N_i^2\mathrm{d}_{\mathrm{i}}^2\times 2^{\frac{9}{10}}\sqrt{\pi}\Gamma\left(\frac{2}{5}\right)\left(\frac{2T_i}{m_i}\right)^{\frac{9}{10}}\left[-\frac{56}{95}K_i^m\langle q'_i{}^2\rangle+\frac{7}{90}\mathrm{d}_{\mathrm{i}}K_{eq}^m\mathbf{E}\cdot\nabla\langle q_i\rangle\right] \tag{A-102}$$

and

$$\boldsymbol{\theta}^m_{q'_i{}^2} = \frac{19}{360}g_{ii}N_i^2\mathrm{d}_{\mathrm{i}}^4 2^{\frac{9}{10}}\sqrt{\pi}\Gamma\left(\frac{2}{5}\right)\left(\frac{2T_i}{m_i}\right)^{\frac{9}{10}}K_i^m\nabla\langle q'_i{}^2\rangle. \tag{A-103}$$

Without simplifying to exact terms, we can see that $\langle q'_i{}^2\rangle$ is composed as:

$$\langle {q'}_i^{\,2}\rangle = A\nabla\langle q_i\rangle + B\nabla\langle q_i\rangle\cdot\nabla V_q + C\nabla^2\langle q_i\rangle + D\nabla^2\langle {q'}_i^{\,2}\rangle + E\nabla^2\langle {q'}_j^{\,2}\rangle, \quad \text{A-104}$$

where the coefficients A, B, C, D, E are composed of constants and variables. The transport equation for $\langle q_i\rangle$ includes terms involving $\langle {q'}_i^{\,2}\rangle$ such as $\nabla^2\langle {q'}_i^{\,2}\rangle$, $\nabla^2\langle {q'}_j^{\,2}\rangle$, $\nabla\langle {q'}_i^{\,2}\rangle\cdot\nabla V_q$ and $\nabla\langle {q'}_i^{\,2}\rangle\cdot\nabla V_q$ which can be ignored if we do not include any term having an order higher than $\nabla^2\langle q_i\rangle$ or $\nabla^2\langle q_j\rangle$. Thus, $\chi_{q_i}^b$ and $\boldsymbol{\theta}_{q_i}^b$ can be rewritten to not include any contribution from charge variances $\langle {q'}_i^{\,2}\rangle$ or $\langle {q'}_j^{\,2}\rangle$ as

$$\begin{aligned}\chi_{q_i}^b = 2^{\frac{9}{10}}\sqrt{\pi}g_{ij}N_iN_j\mathrm{d}_{\mathrm{ij}}^2\Gamma\left(\frac{2}{5}\right)\left(\frac{m_{ij}T}{m_im_j}\right)^{\frac{9}{10}}\Bigg\{&\left(-K_i^b\langle q_i\rangle + K_j^b\langle q_j\rangle\right)\left[\frac{56}{95}\left(1-\frac{\theta_i+\theta_j}{T}\right)\right.\\ &\left.+\frac{32}{95}\left(\frac{m_i\theta_i+m_j\theta_j}{m_{ij}T}\right)+\frac{672}{475}\left(\frac{m_{ij}\left(m_iM_j^2\theta_i+m_jM_i^2\theta_j\right)}{m_im_jT}\right)\right]\\ &+\frac{56}{95}\left(\frac{m_{ij}T}{m_im_j}\right)^{-4/5}\left(K_i^b\langle\mathbf{C}_i{q_i}'\rangle - K_j^b\langle\mathbf{C}_j{q_j}'\rangle\right)\cdot\left(\mathbf{v}_i-\mathbf{v}_j\right)\\ &+\frac{56}{95}\left(-M_iK_i^b\langle\mathbf{C}_i{q_i}'\rangle + M_jK_j^b\langle\mathbf{C}_j{q_j}'\rangle\right)\cdot\left(\frac{M_i\mathbf{v}_i+M_j\mathbf{v}_j}{T}\right)\Bigg\}\end{aligned} \quad \text{A-105}$$

and

$$\begin{aligned}\boldsymbol{\theta}_{q_i}^b = 2^{\frac{9}{10}}\sqrt{\pi}g_{ij}N_iN_j\mathrm{d}_{\mathrm{ij}}^3\Gamma\left(\frac{2}{5}\right)\left(\frac{m_{ij}T}{m_im_j}\right)^{\frac{9}{10}}\Bigg\{&K_{eq}^b\mathbf{E}\left[\frac{7}{90}\left(1-\frac{\theta_i+\theta_j}{T}\right)\right.\\ &\left.+\frac{7}{60}\left(\frac{m_i\theta_i+m_j\theta_j}{m_{ij}T}\right)+\frac{14}{75}\left(\frac{m_iM_j^2\theta_i+m_jM_i^2\theta_j}{T^2}\right)\right]\\ &+\frac{19}{360}\mathrm{d}_{\mathrm{ij}}\left(K_i^b\nabla\langle q_i\rangle + K_j^b\nabla\langle q_j\rangle\right)\Bigg\},\end{aligned} \quad \text{A-106}$$

thus, rendering the charge variance equations (A-92-A-103) redundant.

References

[1] J. Cross, Electrostatics: Principles, Problems and Applications, Adam Hilger, Bristol, 1987.

[2] P. Mehrani, H.T. Bi, J.R. Grace, Electrostatic charge generation in gas–solid fluidized beds, Journal of Electrostatics. 63 (2005) 165–173.

[3] Z.L. Wang, A.C. Wang, On the origin of contact-electrification, Materials Today. (2019).

[4] D. Kunii, O. Levenspiel, Fluidization Engineering., Second, Butterworth-Heinemann, Newton, USA, 1991.

[5] G. Hendrickson, Electrostatics and gas phase fluidized bed polymerization reactor wall sheeting, Chemical Engineering Science. 61 (2006) 1041–1064.

[6] F. Fotovat, X.T. Bi, J.R. Grace, Electrostatics in gas-solid fluidized beds: A review, Chemical Engineering Science. 173 (2017) 303–334.

[7] P. Mehrani, M. Murtomaa, D.J. Lacks, An overview of advances in understanding electrostatic charge buildup in gas-solid fluidized beds, Journal of Electrostatics. 87 (2017) 64–78.

[8] R.O. Hagerty, M.E. Muhle, A.K. Agapiou, C.-T.I. Kuo, M.G. Goode, F.D. Hussein, R.B. Pannell, J.F. Szul, Method for Controlling Sheeting in Gas Phase Reactors, 2005/0148742 A1, 2011.

[9] A. Sowinski, A. Mayne, P. Mehrani, Effect of fluidizing particle size on electrostatic charge generation and reactor wall fouling in gas–solid fluidized beds, Chemical Engineering Science. 71 (2012) 552–563.

[10] A. Giffin, P. Mehrani, Effect of gas relative humidity on reactor wall fouling generated due to bed electrification in gas-solid fluidized beds, Powder Technology. 235 (2013) 368–375.

[11] J.R. Mountain, M.K. Mazumder, R.A. Sims, D.L. Wankum, T. Chasser, P.H. Pettit, Triboelectric charging of polymer powders in fluidization and transport processes, IEEE Transactions on Industry Applications. 37 (2001) 778–784.

[12] W.O. Moughrabiah, J.R. Grace, X.T. Bi, Effects of Pressure, Temperature, and Gas Velocity on Electrostatics in Gas−Solid Fluidized Beds, Industrial & Engineering Chemistry Research. 48 (2009) 320–325.

[13] K. Dong, Q. Zhang, Z. Huang, Z. Liao, J. Wang, Y. Yang, F. Wang, Experimental Investigation of Electrostatic Effect on Particle Motions in Gas-Solid Fluidized Beds, American Institute of Chemical Engineers AIChE. 61 (2015) 3628–3638.

[14] M.A. Hassani, R. Zarghami, H.R. Norouzi, N. Mostoufi, Numerical investigation of effect of electrostatic forces on the hydrodynamics of gas–solid fluidized beds, Powder Technology. 246 (2013) 16–25.

[15] G.A. Bokkers, M. van Sint Annaland, J.A.M. Kuipers, Mixing and segregation in a bidisperse gas–solid fluidised bed: a numerical and experimental study, Powder Technology. 140 (2004) 176–186.

[16] Y. Yang, C. Zi, Z. Huang, J. Wang, M. Lungu, Z. Liao, Y. Yang, H. Su, CFD-DEM investigation of particle elutriation with electrostatic effects in gas-solid fluidized beds, Powder Technology. 308 (2016) 422–433.

[17] F. Jalalinejad, X.T. Bi, J.R. Grace, Effect of electrostatics on freely-bubbling beds of mono-sized particles, International Journal of Multiphase Flow. 70 (2015) 104–112.

[18] H. Grosshans, M.V. Papalexandris, Direct numerical simulation of triboelectric charging in particle-laden turbulent channel flows, Journal of Fluid Mechanics. 818 (2017) 465–491.

[19] R.G. Rokkam, R.O. Fox, M.E. Muhle, CFD Modeling of Electrostatic Forces in Gas-Solid Fluidized Beds, The Journal of Computational Multiphase Flows. 2 (2010) 189–205.

[20] R.G. Rokkam, R.O. Fox, M.E. Muhle, Computational fluid dynamics and electrostatic modeling of polymerization fluidized-bed reactors, Powder Technology. 203 (2010) 109–124.

[21] A. Sowinski, L. Miller, P. Mehrani, Investigation of electrostatic charge distribution in gas–solid fluidized beds, Chemical Engineering Science. 65 (2010) 2771–2781.

[22] R.G. Rokkam, a. Sowinski, R.O. Fox, P. Mehrani, M.E. Muhle, Computational and experimental study of electrostatics in gas-solid polymerization fluidized beds, Chemical Engineering Science. 92 (2013) 146–156.

[23] L.B. Schein, M. LaHa, D. Novotny, Theory of insulator charging, Physics Letters A. 167 (1992) 79–83.

[24] T. Matsuyama, H. Yamamoto, Charge relaxation process dominates contact charging of a particle in atmospheric conditions, Journal of Physics D: Applied Physics. 28 (1995) 2418–2423.

[25] T. Matsuyama, H. Yamamoto, Impact charging of particulate materials, Chemical Engineering Science. 61 (2006) 2230–2238.

[26] P.M. Ireland, Triboelectrification of particulate flows on surfaces: Part II—Mechanisms and models, Powder Technology. 198 (2010) 189–198.

[27] S. Matsusaka, H. Masuda, Electrostatics of particles, Advanced Powder Technology. 14 (2003) 143–166.

[28] W. John, G. Reischl, W. Devor, Charge transfer to metal surfaces from bouncing aerosol particles, Journal of Aerosol Science. 11 (1980) 115–138.

[29] H. Masuda, T. Komatsu, K. Iinoya, The static electrification of particles in gas-solids pipe flow, AIChE Journal. 22 (1976) 558–564.

[30] Timoshenko, Theory of elasticity, McGraw-Hill, 1987.

[31] S. Matsusaka, M. Ghadiri, H. Masuda, Electrification of an elastic sphere by repeated impacts on a metal plate, Journal of Physics D: Applied Physics. 33 (2000) 2311–2319.

[32] M.W. Korevaar, J.T. Padding, M.A. Van der Hoef, J.A.M. Kuipers, Integrated DEM-CFD modeling of the contact charging of pneumatically conveyed powders, Powder Technology. 258 (2014) 144–156.

[33] C. Pei, C.Y. Wu, D. England, S. Byard, H. Berchtold, M. Adams, Numerical analysis of contact electrification using DEM-CFD, Powder Technology. 248 (2013) 34–43.

[34] C. Pei, C.-Y. Wu, D. England, S. Byard, H. Berchtold, M. Adams, DEM-CFD Modeling of Particle Systems with Long-Range Electrostatic Interactions, American Institute of Chemical Engineers Journal. 61 (2015) 1792–1803.

[35] C. Pei, C.-Y. Wu, M. Adams, DEM-CFD analysis of contact electrification and electrostatic interactions during fluidization, Powder Technology. In submiss (2016) 208–217.

[36] J.C.C. Laurentie, P. Traoré, L. Dascalescu, Discrete element modeling of triboelectric charging of insulating materials in vibrated granular beds, Journal of Electrostatics. 71 (2013) 951–957.

[37] S.L. Soo, Dynamics of charged suspensions, in: G.M. Hidy, J.R. Brock (Eds.), Topics in Current Aerosol Research, Pergamon, 1971: p. 61.

[38] J. Kolehmainen, A. Ozel, C.M. Boyce, S. Sundaresan, A hybrid approach to computing electrostatic forces in fluidized beds of charged particles, AIChE Journal. 62 (2016) 2282–2295.

[39] J. Kolehmainen, A. Ozel, S. Sundaresan, Eulerian modelling of gas–solid flows with triboelectric charging, Journal of Fluid Mechanics. 848 (2018) 340–369.

[40] M. Ray, F. Chowdhury, A. Sowinski, P. Mehrani, A. Passalacqua, An Euler-Euler model for mono-dispersed gas-particle flows incorporating electrostatic charging due to particle-wall and particle-particle collisions, Chemical Engineering Science. 197 (2019) 327–344.

[41] P.C. Johnson, R. Jackson, Frictional-collisional constitutive relations for granular materials, with application to plane shearing, Journal of Fluid Mechanics. 176 (1987) 67–93.

[42] J.T. Jenkins, S.B. Savage, A theory for the rapid flow of identical, smooth, nearly elastic, spherical particles, Journal of Fluid Mechanics. 130 (1983) 187–202.

[43] J.T. Jenkins, F. Mancini, Balance Laws and Constitutive Relations for Plane Flows of a Dense, Binary Mixture of Smooth, Nearly Elastic, Circular Disks, J. Appl. Mech. 54 (1987) 27–34.

[44] S. Chapman, T.G. Cowling, The mathematical theory of non-uniform gases, 2nd ed., Cambridge University Press, Cambridge, {U.K.}, 1961.

[45] Mathematica, Advanced Numerical Differential Equation Solving in the Wolfram Language—Wolfram Language Documentation, (2019). https://reference.wolfram.com/language/tutorial/NDSolveOverview.html.

[46] F. Chowdhury, A. Sowinski, M. Ray, A. Passalacqua, P. Mehrani, Charge generation and saturation on polymer particles due to single and repeated particle-metal contacts, Journal of Electrostatics. 91 (2018) 9–15.

[47] Huiliang Zhao, G.S.P. Castle, I.I. Inculet, A.G. Bailey, Bipolar charging of poly-disperse polymer powders in fluidized beds, IEEE Transactions on Industry Applications. 39 (2003) 612–618.

[48] F. Sharmene Ali, M. Adnan Ali, R. Ayesha Ali, I.I. Inculet, Minority charge separation in falling particles with bipolar charge, Journal of Electrostatics. 45 (1998) 139–155.

[49] S. Trigwell, N. Grable, C.U. Yurteri, R. Sharma, M.K. Mazumder, Effects of surface properties on the tribocharging characteristics of polymer powder as applied to industrial processes, IEEE Transactions on Industry Applications. 39 (2003) 79–86.

[50] H. Zhao, G.S.P. Castle, I.I. Inculet, The measurement of bipolar charge in polydisperse powders using a vertical array of Faraday pail sensors, Journal of Electrostatics. 55 (2002) 261–278.

[51] D.J. Lacks, R.M. Sankaran, Contact electrification of insulating materials, J. Phys. D: Appl. Phys. 44 (2011) 453001.

[52] N. Duff, D.J. Lacks, Particle dynamics simulations of triboelectric charging in granular insulator systems, Journal of Electrostatics. 66 (2008) 51–57.

[53] D.J. Lacks, A. Levandovsky, Effect of particle size distribution on the polarity of triboelectric charging in granular insulator systems, Journal of Electrostatics. 65 (2007) 107–112.

Appendix B
Supplemental Apparatus Images

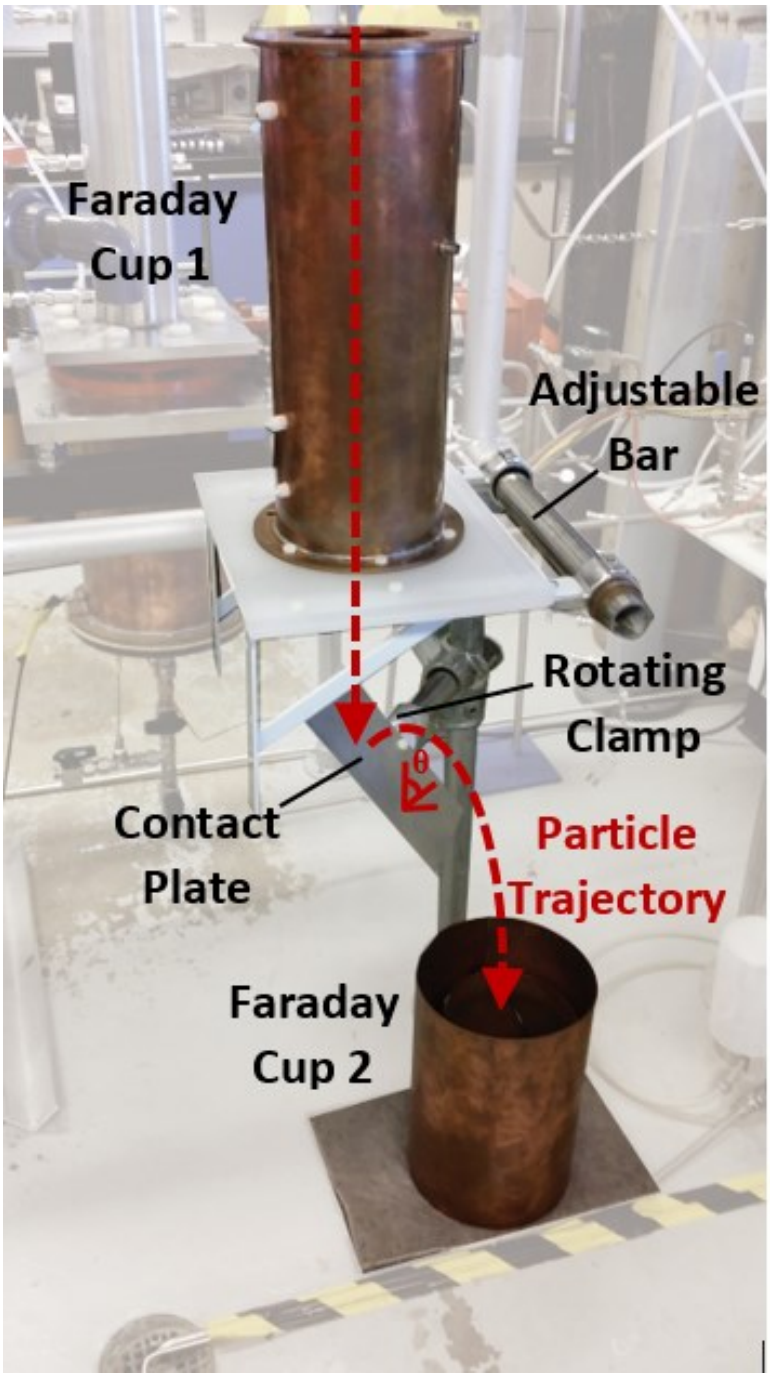

Figure B-1: Particle-wall collision apparatus.

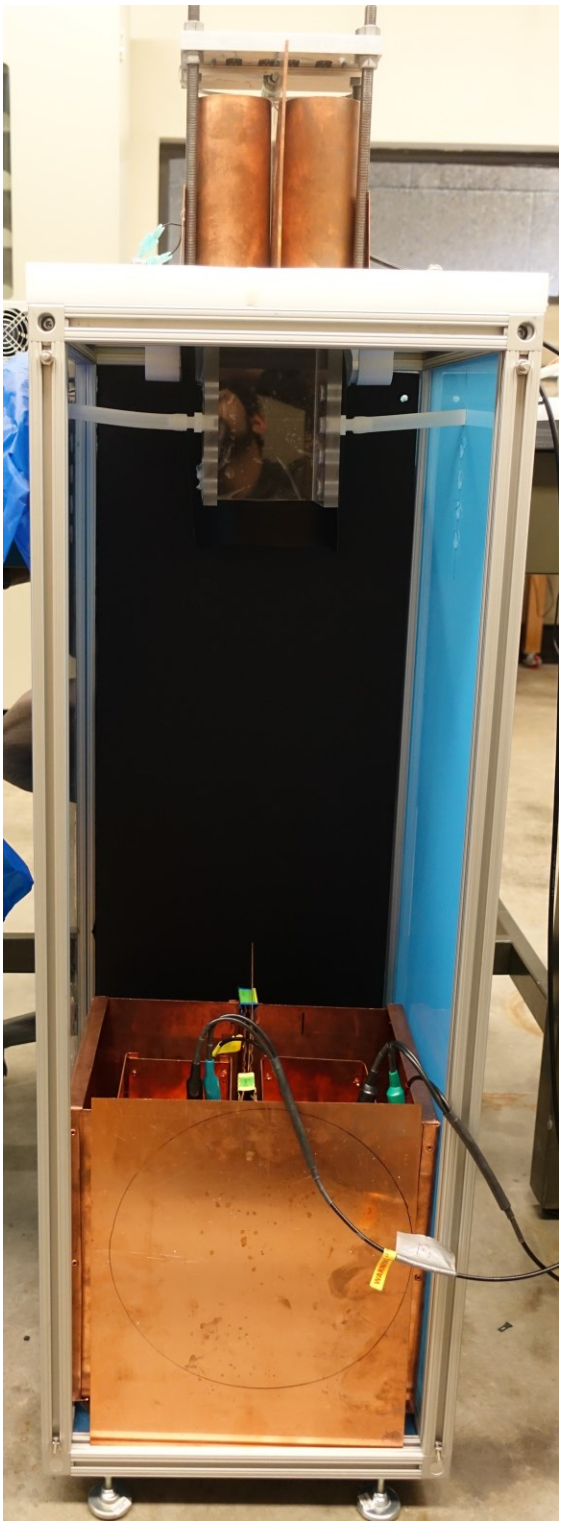

Figure B-2: Particle-particle collision apparatus.

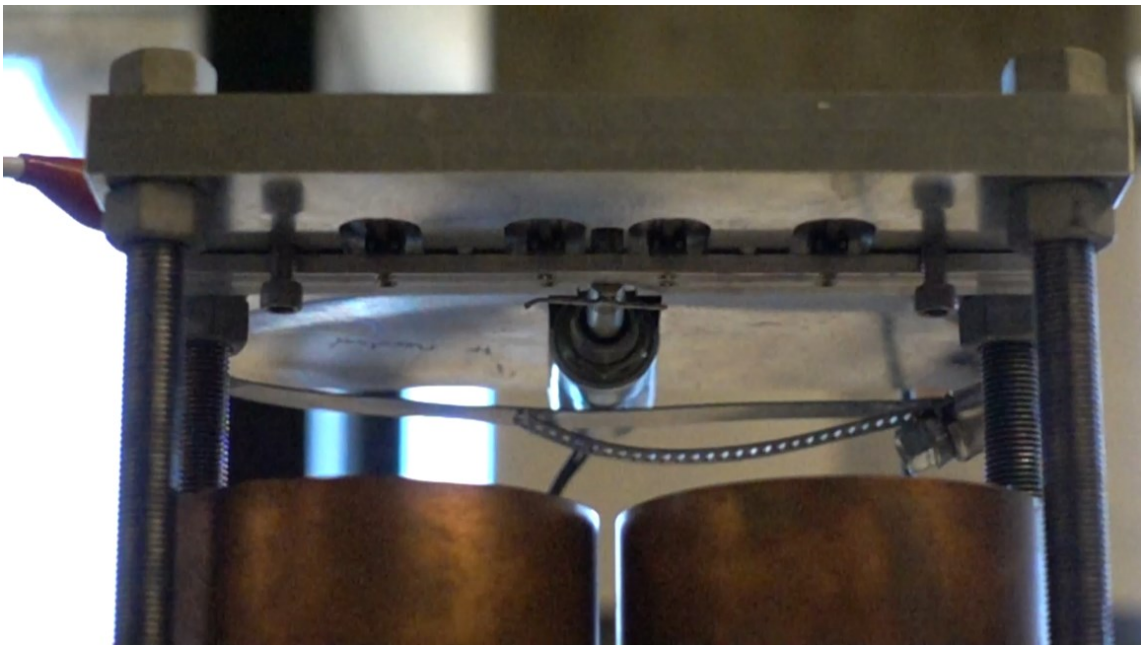

Figure B-3: Particle release mechanism; a knife gate controlled by a solenoid actuator.